AD-A166 084 PRECISION ENGINEERING - SRO 154(U) NORTH CAROLINA STATE 1/4
UNIV AT RALEIGH PRECISION ENGINEERING LAB
T A DOW ET AL JAN 86 N00014-83-K-0064

UNCLASSIFIED F/G 13/8 NL

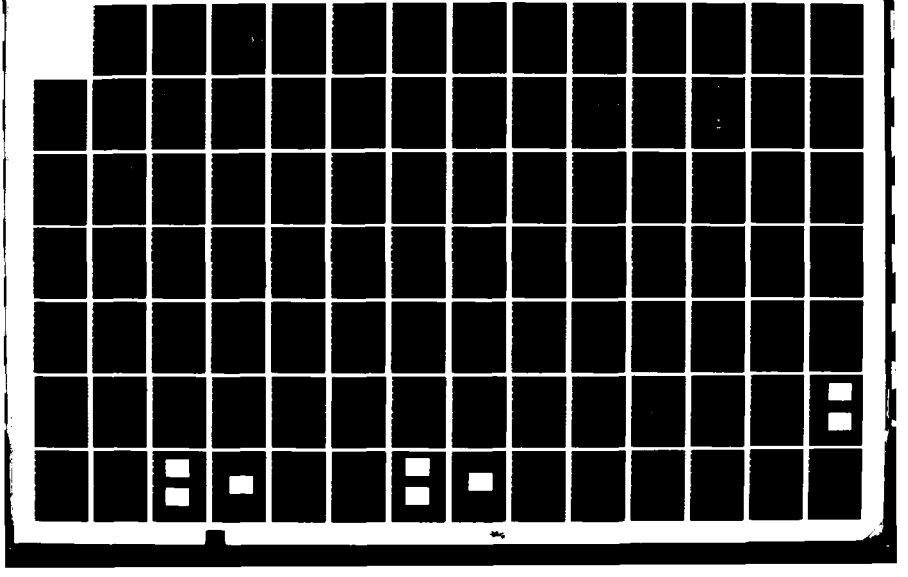

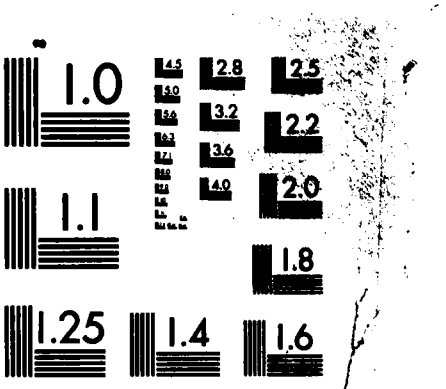

(12)

Final Report
on
Precision Engineering — SRO 154

North Carolina State University

Precision Engineering Laboratory

12

Final Report
on
Precision Engineering — SRO 154

OFFICE OF NAVAL RESEARCH
CONTRACT N00014-83-K-0064

Editor

Thomas A. Dow
Director
Precision Engineering Laboratory

Authors

Faculty

Michael D. Bryant
Thomas A. Dow
Richard F. Keltie
Clarence J. Maday
Ronald O. Scattergood
John S. Strenkowski

Graduate Students

Peter N. Blake
Thomas G. Bifano
Christopher M. Cagle
John T. Carroll, III
Peter J. Falter
James B. Gleeson
Jerrold W. Kannel
Mark S. Landy
Stephen A. Lehrman
Dan E. Luttrell
Gary L. Mitchum

Precision Engineering Laboratory Staff

C. Annie Kauffman

January 1986

TABLE OF CONTENTS

TABLE OF CONTENTS (continued)

MANAGEMENT SUMMARY

Problem

The electronics revolution, made possible by the development of the microprocessor in 1971, has significantly influenced manufacturing systems. This revolution first affected the machine tool industry in the form of numerically controlled machine tools, allowing a program to control the steps required to produce a finished part. The resulting accuracy of the part remains influenced by machine and environmental factors such as spindle runout, slide accuracy, temperature control, and machine and foundation vibration. We are now on the threshold of a new revolution; one which will utilize the speed and memory potential of VLSI and electro-optical technology to directly influence the accuracy of the final part. The ability to take advantage of this opportunity requires advances in understanding in many fields of science and engineering.

Solution

For mechanical systems, the basic principles of precision motion have long been clearly enunciated. What is new is the potential for interactive computer use in real-time feedback control, involving (1) structural stabilization of the instrument or machine; (2) movement and location of its parts; (3) processing of metrology information; and (4) positioning and stabilization of the tool/workpiece interactions in a machine tool. This can lead to a distributed, multivariable, multiloop control problem, with significant computation required in the feedback algorithm. Although the advantages of real-time control have been clear for some time, no complete machine tool or metrology system exploits this with the control of the major variables. At present open loop control is being applied, with corrections for calculated (or previously measured) estimates of systematic errors. Closed loop control automatically corrects for unpredictable errors from factors such as mechanical deflections, thermal deformation, and wear. Once in place, a system for precision manufacture can be used for less exacting tasks, offering reductions of required inspections and assuring part-to-part reproducibility, with reduced rejections. Such a system is at the heart of automated production, yet remains a research area.

Purpose

The purpose of the Precision Engineering Laboratory at North Carolina State University is to establish an ongoing research organization whose research results will be useful to the machine tool industry and related industries requiring high precision in measurement or production. The research is being conducted by faculty and graduate students at North Carolina State University. In addition to providing relevant research results, the laboratory is educating a new cadre of

engineers at the MS and PhD level with a background and experience in metrology, feedback control, and precision manufacture. The laboratory is increasing the quality and quantity of engineers and scientists trained in this important field.

Background

In December 1982, the Mechanical and Aerospace Engineering Department was granted a $1.3M contract by the Office of Naval Research (ONR) to develop a research and teaching activity in Precision Engineering. This three-year program was designed to foster development of techniques for precision manufacturing at tolerances below those attainable with current technology--techniques which will satisfy the most precise tolerance requirements. The goal was to develop adaptive learning systems that dynamically detect flaws and correct them in real-time. The program was funded through the Navy's Scientific Research Opportunity program administered by ONR's Engineering Science Directorate--Dr. Arthur Diness, Director. The objective was to bring engineering and computer science together to develop the real-time systems needed for precision manufacture and assembly.

In addition to the facility development and the specific research accomplishments, an academic program has been established in Precision Engineering. This program draws upon courses in Mechanical and Aerospace Engineering, Materials Engineering, Electrical and Computer Engineering, Mathematics, and Physics. The goal is to give the student a broad background in metrology, controls, and precision fabrication as well as specific expertise in his area of dissertation research. Three students have graduated with MS and one with a PhD degree from the program and nine other students are currently pursuing MS and PhD degrees.

During the past year, the program funding has been extended with continued ONR support and the addition of industrial affiliates. Six companies currently have committed their support including:

Eastman Kodak Company
General Motors
Lawrence Livermore National Laboratory
Los Alamos National Laboratory
Moore Special Tool, Co.
Texas Instruments, Inc.

Facilities

The Precision Engineering Laboratory, located on the campus of North Carolina State University, consists of a temperature controlled clean room, a laboratory workroom, a library/conference room, and offices for several graduate students, and a secretary. Entering its fourth year of operation, the laboratory is fully equipped with state-

of-the-art research and computational facilities. The temperature controlled clean room houses Talysurf 4 and Talystep surface profilometers, vibration isolated tables, digital storage oscilloscopes, a dual-channel FFT spectrum analyzer, a PDP-11 based digital controller, a high-speed digital controller based on the Texas Instruments TMS-320 microprocessor, an industry standard Hewlett Packard interferometry system, a Zeiss metaographic microscope, a long range microscope with video recorder for studying chip formation, several types of piezoelectric (PZT) actuators and amplifiers, and a full complement of sensors including capacitance gages, eddy current sensors, linear variable differential transformers, and accelerometers. In addition to this commercially available equipment, the laboratory has developed some of its research equipment in-house, including a laboratory-scale diamond turning machine, a tool force measurement apparatus, and a custom-designed polarized light linear interferometer.

All of the laboratory's data acquisition facilities are linked directly to a VAX 11-785 located in the Mechanical and Aerospace Engineering Department through the VT 240, VT 125, and Tektronix 4107 Graphics terminals located in the laboratory workroom. These terminals also provide direct links to the Triangle University's Computer Center (TUCC), which has an IBM 3083, and IBM 4341 and an FPS 164.

Other facilities located at North Carolina State University and available to the faculty and students include an electron microscope facility (SEM, TEM, X-ray analyzer, ion beam microprobe) and a microelectronics facility for the production of unique semiconductors and gate array chips. Instrumentation at the Microelectronics Center of North Carolina including state-of-the-art SEM has also been made available for the research program.

Technical Program Review

Measurement and Actuation

The concepts of real-time, closed-loop feedback control of a manufacturing process depend heavily on available sensors for error or motion detection and actuators for rapid positioning or correction. Therefore, an important area for study involves characterizing currently available sensors and actuators as well as the developing new designs.

Displacement Measuring Systems - The basic principles and operating characteristics of several widely used displacement sensors are presented in the first article of this section. These sensors utilize changes in eddy-current losses, inductance, capacitance, and optical interference to measure relative motion. Each has sensitivity in the microinch range and several have bandwidths above 10,000 Hz.

In addition to the commercial sensors, development has continued on the low-cost laser interferometer discussed in past reports. Modifica tions are being made to the mechanical design to facilitate set-up and

on the digital interface to improve response in a micropositioning control system.

Actuators - Unlike measurement sensors, there are few commerically available actuators capable of rapid, rigid positioning in the microinch range. Piezoelectric crystals are most commonly used but during the past year, a potentially attractive new device has been evaluated; the magnetostrictive material, Terfenol. This material changes length as a function of the magnetic field; but, when compared to previous magnetostrictive materials, has over 100x more strain potential. The results of experience with a prototype actuator design using this material are reported.

Another precision actuator is the traction drive. This device, consisting of a drive motor coupled to a traction bar through a Hertzian contact, has been used in precision positioning systems. A theoretical model of the interface was developed during the past year to calculate the elastic and non-recoverable losses in moving a static load. Design parameters for surface roughness and the influence of surface films are discussed and experimental corroboration is presented.

Real-Time Control

There are two complementary approaches to the elimination of errors in a mechanical system. The first relies on the reduction of errors by eliminating their sources. Examples of this type of error control include mounting the machine on a large granite base to minimize vibration or using an isothermal oil shower to avoid the errors induced by thermal growth. Using such error source elimination techniques, impressive precision is obtainable in open loop machine operation.

A second approach to precision control in a mechanical system is that of closed-loop feedback control. The rationale behind closed-loop control is that there are some errors which cannot be effectively eliminated at their source or else are of unknown magnitude. Examples of these types of errors include machine generated vibration, thermal distortion, and wear of machine elements. Operated open loop, the machine will produce inaccurate results when subjected to such errors. By adding feedback control, the precision of the system is increased, the effects of a variation in the system dynamics are reduced and the transient response of the system is improved. A combination of closed-loop control with careful elimination of error sources will result in a system with better precision than that obtainable by applying either approach independently.

During the past year, the concepts of closed-loop control have been applied to a number of mechanical systems. In all cases the goal has been to produce the desired response at the highest possible operating speed.

The first system involved a linear stage with a stepper motor driven lead-screw, whose accuracy has been enhanced by the addition of a piezoelectric actuator. This actuator is part of a positioning system

using feedback from a laser interferometer. The result is a system simultaneously capable of 10 in./sec. translation speed and ± 6 micro-inch (± 1 laser count) positioning accuracy. In addition to improving the resolution of the stage, the piezoelectric crystal also improves the dynamic performance by reducing the dynamic overshoot.

A general need in control system design has been a method of simulating the entire electromechanical control system. Techniques for developing a simulation of the mechanical system as well as the digital control process have been presented and corroborated with experimental results.

Determination of the characteristics of piezoelectric transducers (PZT's) is essential in the development of controllers for PZT actuated mechanical systems. Of greater importance in the design of these controllers is which characteristics can and can not be neglected. To study this problem, an analog controller was designed and built to control the position of a PZT actuated cantilever beam. The investigation showed that a system incorporating a PZT could be modeled linearly and be successfully controlled.

The control of runout motion in a rotating spindle has been addressed from two different viewpoints: the first uses a generic position sensitive controller to eliminate errors, and the second utilizes a specific PID control algorithm optimized to the dynamic characteristics of the spindle structure. The first approach was implemented without the need for an expensive sensor or microprocessor, but instead used direction information alone to reduce the runout. The second approach followed more traditional control design procedures and the final design was implemented on a PDP-11 computer. Similar accuracy in controlled runout was produced by either system but the PID controller was capable of controlling at higher rotational speeds.

A quite different approach to motion control in a dynamic structure involves active control based on power flow consideration. Control of vibratory energy is a more basic approach than that involving kinematic variables such as displacement. In addition, addressing more complicated structures at higher frequencies is possible with this technique. Over the past year, initial studies have been directed toward the formulation of the power flow concept and experimental techniques whereby such measurements can be performed.

Fabrication Technology

Precision Engineering is the study of methods of inspection and fabrication of parts to accuracies better than 10 millionths of an inch. To produce parts of this level of accuracy, a thorough understanding of all factors which effect the dimensions must be pursued. The environment (both thermal and vibration) must be steady, and the fabrication process must not induce non-uniform temperature, deformations, or residual stresses into the finished part. For this reason, better understanding of fabrication processes is necessary for the pursuit of precision parts than for conventional needs. In fact, a thorough know-

ledge of the fabrication process may be a necessary condition to produce parts that can meet the design goals.

An assessment of the technology of precision fabrication is reported. Current and potential technologies involving both material removal and addition are discussed. Much of the emphasis over the past year has involved an important precision fabrication process -- diamond turning. However, plans for the new year include the study of other fabrication processes including lapping and grinding.

Experimental Studies - A laboratory-scale diamond turning machine -- PAUL -- has been constructed and operated over the past year. This machine is capable of producing flat surfaces with a surface finish better than 0.2 microinches and total figure error less than 2 microinches. Sine wave surfaces have also been produced by driving the tool vertically with a PZT.

The diamond tool and the chips produced on the PAUL machine also received much attention over the past year. The radius of the cutting edge of the tool is an important factor to the quality of the diamond turned surface. Techniques to characterize this extremely sharp edge are discussed.

The chips produced in a cutting process provide a valuable picture of the deformation process. The picture that has evolved is one of non-uniform deformation resulting in chip structure consisting of a series of lamellae, the spacing of which is a function of the depth of cut. Micrographs of chips produced with different cutting geometries and operating conditions are described and discussed.

The forces necessary to generate plunge cuts of varying depth and tool geometry are described. These measurements were made in the PAUL machine for low cutting speeds (.05 in./sec.) and depth of cut from 100 to 900 microinches. The results indicated forces proportional to the cutting area and micrographs of the specimens showed sharply defined cuts of uniform depth with little vibration.

Analytical Studies - Each of the experimental thrusts described above was designed to provide basic understanding of the diamond turning process, which could be used to build an analytical model. Such a model is a necessary input to the control system design in the same way that the dynamics of the mechanical system is an important input. The modeling activities continued those begun during the first year of the program when a finite element model of the cutting process was developed.

A new computer model has been developed employing the finite element method within an Eulerian coordinate reference frame. This 2-D program has been applied to different metal flow problems and the results agree with previous published work. The advantage of this approach, is that the grid is fixed to the tool and as a result can be refined near the tool tip where details of the stress field are desired.

A Lagrangian finite element code (where the grid is fixed to the workpiece) has been used to study thermal effects and the occurrence of shear bands in orthogonal metal cutting. The thermal model is based on adiabatic heating from the plastic deformation and predicts the temperature distribution in the chip and workpiece. The temperature dependence of the material properties is shown to oppose work hardening and the resulting influence of residual stress in the workpiece is discussed.

Specific material properties are shown to be responsible for the occurrence of shear banding during the cutting process. Key parameters include the yield stress, strain hardening slope, peak stress value, and the slope of the subsequent strain softening due to thermal effects. Changes in material properties which define the boundary between a continuous and shear banded chip are discussed.

SECTION 1. MEASUREMENT AND ACTUATION

DISPLACEMENT MEASURING SYSTEMS

By

K. Anand
T. G. Bifano
J. T. Carroll
P. J. Falter
S. A. Lehrman

Graduate Students

And

Thomas A. Dow
Professor
Mechanical and Aerospace Engineering Department

ABSTRACT

The operating principle and characteristics of several widely used displacement sensors are discussed. These sensors utilize changes in eddy-current losses, inductance, capacitance, and optical interference to measure relative motion. The advantages and disadvantages of each drive are described and their key performance parameters are summarized below.

System	Linear range (in.)	Sensitivity* (mv/μin.)	RMS instru. noise (resolution) (μin.)	Frequency response (Hz)
Eddy Current (Bently Nevada Microprox)	.010	1.8	0.5	20,000
LVDT (Daytronics Corp)	0.001	3.3	0.5	<500
Capacitance Gage (ADE Corp.)	0.005	10	0.5	40,000
Lever-Type Gage Head (Federal Products)	.020	100	1.0	300
Interferometer (Hewlett Packard)	1600	0.6**	0.6	10,000

* Sensitivity = slope of calibrator curve for analog output
** Microinch/count @ maximum resolution

INTRODUCTION

The goal of Precision Engineering involves the inspection and fabrication of devices at the limits of measurement. Currently this means in the microinch range, but advances in metrology and sensors are certain to reduce this limit.

There are a number of techniques which can be used to measure displacements in the microinch range. These techniques utilize mechanical, electrical, or optical changes to measure relative motion. A mechanical device, the Mikrokator sold by Federal Products, uses a twisted strip to mechanically magnify the motion of the stylus by 60,000 times. Thus a microinch reading dial indicator is available. This device was not included in this section because it does not have an output which can be used in a control system.

DISPLACEMENT MEASURING DEVICES

The devices described used four different techniques to measure displacement. These include:

* eddy-current losses from a-c excited coil
* inductance change
* capacitance change
* optical interference

Each device has advantages and disadvantages which limit its application. This section of the report will describe the operating principle for each device, evaluate its performance, and discuss the most appropriate use.

1. Eddy Current Proximity Probe*

Theory of Operation:

The probes utilize the principle of impedance variation for measurements. The variations are a function of the generation and decay of eddy currents. Figure 1(a) illustrates this principle. The oscillator generates a radio frequency signal (~1 MHz). A flat coil of wire embedded in the epoxy tip acts as an antenna that radiates a small electromagnetic field into the surrounding region. When the electromagnetic field is intercepted by any conductive material, eddy currents will flow in the surface of the material. As the target surface approaches the probe tip, the magnitude of eddy currents is increased. The effect of the plate can be modeled as an equivalent inductor and resistor coupled to the coil through the electro magnetic field (i.e. mutual inductance). The effective input impedance (Z_{eff})

*Bently-Nevada Microprox

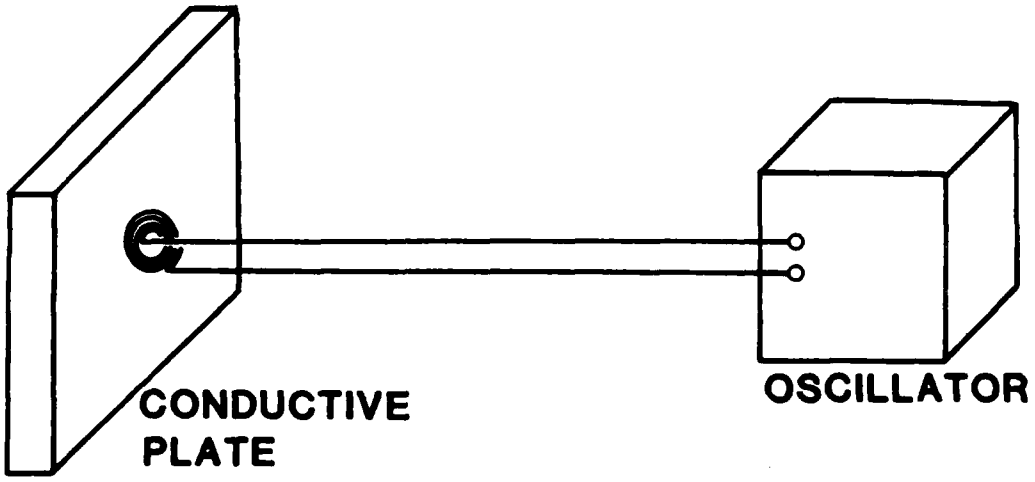

(a) Geometry of eddy-current proximity probe

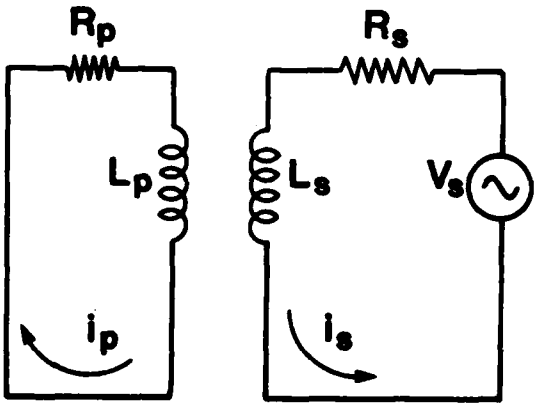

V_s = oscillator voltage

R_s = probe resistance

L_s = probe inductance

L_p = plate inductance

R_p = plate resistance

i_s = probe current

i_p = eddy current in plate

V_p = plate voltage = 0

M = mutual inductance between probe and plate

(b) Equivalent circuit of eddy-current probe

Figure 1. Operation of eddy-current proximity probe

of the probe will be a function of the impedance of the measurement circuit, the impedance of the equivalent circuit of the plate, and the mutual inductance between the probe and the plate.

The effective impedance (Z_{eff}) of the measurement circuit is defined as the supply voltage (V_s) divided by the current in the measurement circuit, i_s. The value of Z_{eff} as a function of the known circuit quantities illustrated in Figure 1(b) and is derived as follows. The plate impedance is defined as:

$$Z_p = Z_R + Z_L = (Rp + j\omega L_p) \tag{1}$$

Similarly, the probe impedance is:

$$Z_s = (R_s + j\omega L_s) \tag{2}$$

The mutual impedance for the inductive coupling is:

$$Z_m = \text{mutual impedance} = j\omega M \tag{3}$$

From Kirchoff's Law, in the measurement circuit

$$V_s = i_s Z_s + i_p Z_m \tag{4}$$

Equations (2) and (3)

$$V_s = i_s(R_s + j\omega L_s) + i_p(j\omega M). \tag{5}$$

By Kirchoff's Law in the plate

$$V_p = i_p Z_p + i_s Z_m = 0 \tag{6}$$

which becomes

$$V_p = i_p(R_p + j\omega L_p) + i_s(j\omega M) = 0 \tag{7}$$

Solving for i_p from equation (7)

$$i_p = \frac{-(j\omega M) i_s}{(R_p + j\omega L_p)} \tag{8}$$

Substituting this result into (5) yields

$$V_s = i_s \left[R_s + j\omega L_s + \frac{(\omega M)^2}{(R_p + j\omega L_p)} \right] \tag{9}$$

From which the input impedance of the circuit Z_{eff} can be found by direct substitution and rearrangement

$$Z_{eff} = \frac{V_s}{i_s} = \left(R_s + \frac{R_p M^2}{\frac{Rp^2}{\omega^2} + Lp^2} \right) + j\omega \left(L_s - \frac{L_p M^2}{\frac{Rp^2}{\omega^2} + Lp^2} \right) \qquad (10)$$

Note that M = M(d); that is, the mutual inductance depends upon the probe/plate gap. Thus, the probe input impedance varies as a function of the mutual inductance between the probe and the measured surface.

Performance

The particular eddy-current proximity probe was a high-sensitivity unit (Bently-Nevada Microprox). The output of the system has a linear range of about 0.010 in. with an initial standoff distance of 0.005-0.010 in. The actual calibration curve depends upon the material of the target. Figure 2 shows the calibration curve for three target materials: aluminum, copper, and steel. The initial standoff is different for each material, but the slope of the curves (the calibration factor) is nearly the same for each of the materials. For an aluminum target at a standoff distance of about 0.005 in., the sensitivity is 1.8 mv/microinch. The noise level on the output is approximately + 1 mV or + 0.5 μin. The manufacturer quotes an instrument bandwith of 10 kHz; that is, at 10 kHz the output voltage represents half the actual displacement.

Advantages and Disadvantages of Eddy-Current Gages

Advantages -

1) The gage can be used for dynamic measurements from d.c. to 10 kHz. They are often used to measure the motion of a rotating shaft, thus giving a clue about machine imbalance, misalignment and bearing instability.
2) Good signal to noise ratio, high level low impedance output.
3) The probe is non-contacting.
4) There are no moving parts, avoiding tribological gage difficulties.
5) The probe is rugged, and can withstand rough environments; the upper temperature limit is 350 degrees Fahrenheit.

Disadvantages -

1) Gage output is dependent on surface finish and influenced by local magnetic fields.
2) The technique is sensitive to metallurgical content of the material whose proximity is to be measured. As a result, repeatability suffers unless measurements are always made against the same target area.
3) Presence of any conductive impurities on the vicinity of the proximeter will alter the probe output characteristics.

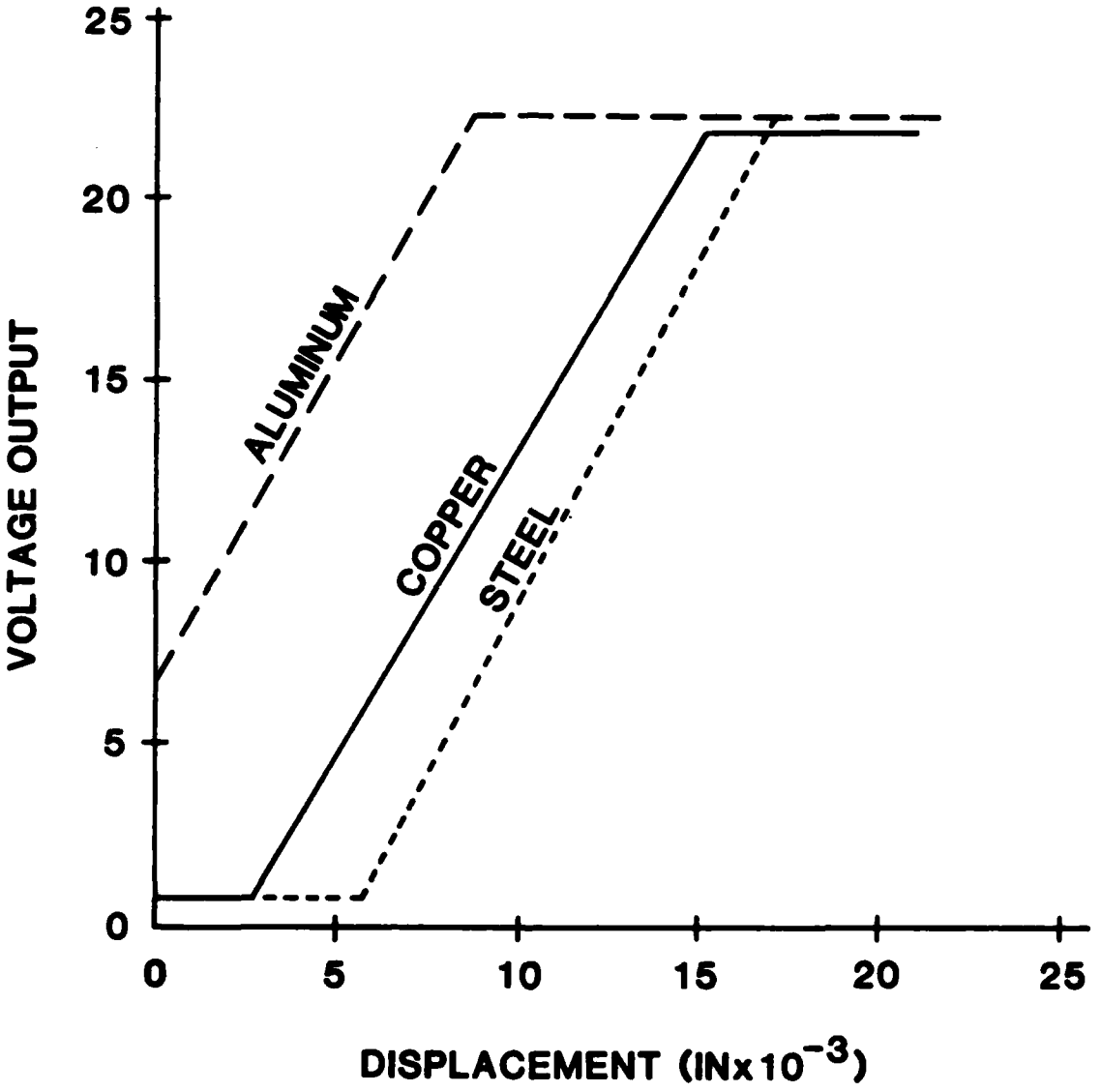

Figure 2. Calibration curves for eddy current proximity probes

2. Linear Variable Differential Transformer*

Theory of Operation

The linear variable differential transformer (LVDT) is a differential transformer consisting of a primary and two secondary magnetic coils which are wrapped around a common sliding core, as shown in Figure 3.

The primary acts to set up a magnetic field in the core. This flux is

$$\Phi = \frac{V_p}{4.44 N_p f_p} \tag{1}$$

where

N_p = number of turns in the primary

V_p = voltage of the primary

f_p = frequency of V_p

For either of the secondaries,

$$V_{s_i} = 4.44 \Phi N_{s_i} f_p \qquad i = 1,2$$

where

N_s = number of turns in the secondary

Therefore;

$$V_o = V_{s1} - V_{s2} = 4.44 \Phi f_p (N_{s1} - N_{s2}) \tag{2}$$

When the core is moved to the left N_{s2} decreases. If the coil is uniformly wound then the reduction in N_{s2} will be proportional to dx. That is,

$$dN_{s2} = -\alpha dx \tag{3}$$

where

α = number of turns per inch in the secondary coil

In order that the properties of the LVDT will be the same for dx positive and negative, the secondaries are identically wound. In this case,

$$V_o = 4.44 \Phi f_p \alpha dx \tag{4}$$

*Daytronics DS80

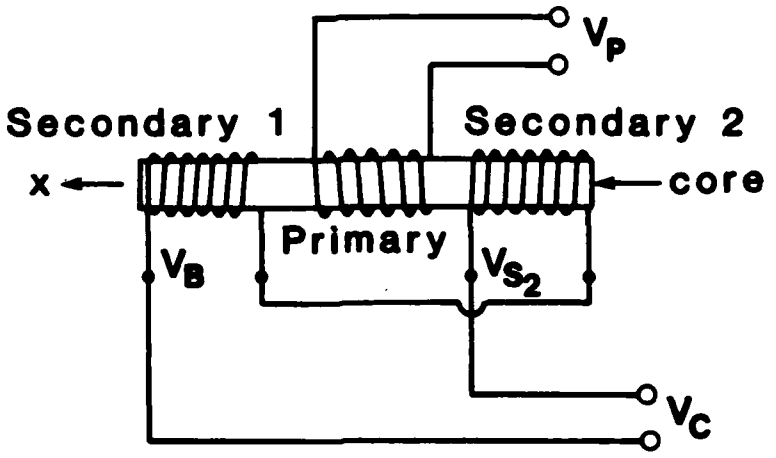

Figure 3. Geometry of linear variable differential transformer (LVDT)

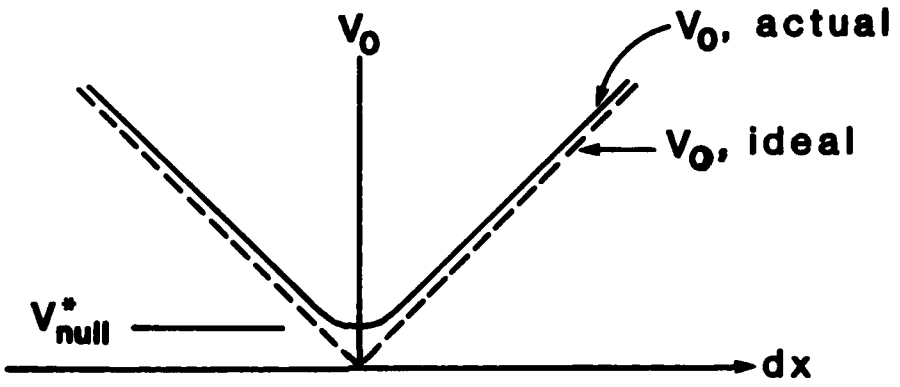

*V null is less than 0.5% of full scale. Away from the null position linearity is excellent

Figure 4. Response curve for LVDT

Equation (4) describes the behavior of an ideal LVDT. Real LVDT's are very linear, typically 0.1-0.5% of full scale. The response curve of an actual LVDT is shown in Figure 4. The voltages are shown as amplitudes in volts a.c. as a function of core position. The phase of V_o changes by 180 degrees as dx passes through zero. In this way positive and negative displacements may be resolved.

A characteristic of transformers is the formation of eddy-currents in the core. This phenomenon is reduced by increasing the frequency of the applied voltage. Eddy-currents cause heat generation and noise; for this reason d.c. voltages are not used.

Construction

The Daytronics DS80 is a subminiature LVDT capable of $\pm$ 1 mm of measurements. A cross section in Figure 5 shows its general construction. Despite its sensitivity, the DS80 is rugged with a sealed stainless steel body. The stainless not only protects the LVDT but helps to make it thermally stable.

The support rod slides in a linear ball bearing. The manufacturer claims a repeatability of 0.4 µin. for this mechanism. The rod is also spring loaded with k_s = 15 gram/mm and a nominal spring force at the null position of 70 grams. The tip is made of tungsten carbide and has a radius of 1.5 mm. This tip may be removed and replaced by any desired fixture.

Performance

The performance of the LVDT depends to a large extent on the signal conditioner used to display the output. The Daytronics 9130 drives the LVDT with a 3 V. rms, 3 kHz supply voltage and then processes the LVDT output to determine the displacement. This signal conditioning involves both AM demodulation and amplification to 5.0 V. The output is displayed on a digital display and available as an analog voltage $\pm$ 7.5 V.

A sensitivity adjustment on the signal conditions allows the sensitivity of the system to be 1, 10, or 100 times that of the LVDT. This also acts to decrease the range in a similar fashion. At sensitivity x100, one can measure $\pm$ 0.0005 in. to 0.5 µin.

The unit also has four low pass filters of 0.2, 2, 200, 500 Hz. The filter attenuates the signal to 70% at the specified frequency and by 60 dB per decade for higher frequencies. The maximum frequency measurable is less than 500 Hz.

Advantages and Disadvantages

The Daytronic LVDT system is a good choice for general small motion measurement and gaging. It is rugged, easy to use, and has excellent resolution although the rolling element bearing introduces some

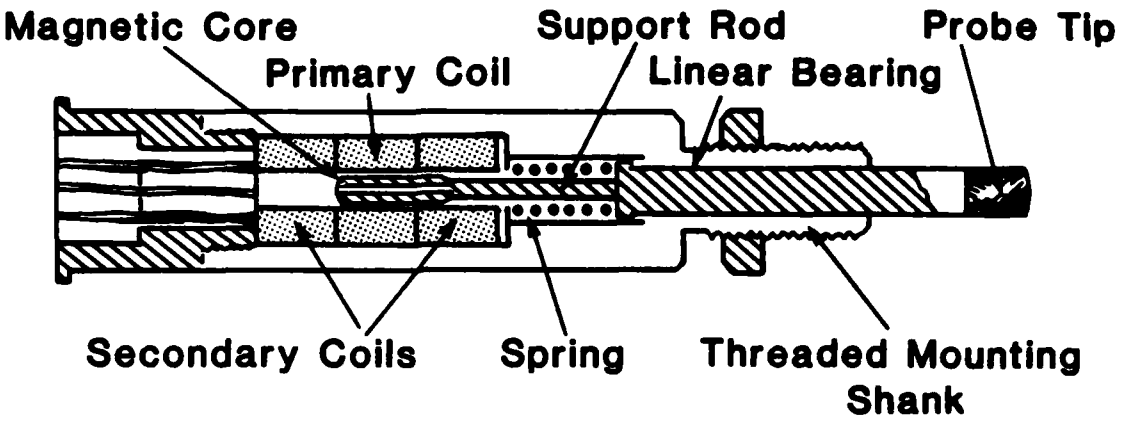

Figure 5. Construction of Daytronics DS 80 LVDT

hysteresis. It also has a short travel and cannot be electrically zeroed. The system is limited in band width due to the mechanical contact and the mass of the core but its digital output is in real engineering units so that no conversion is necessary. A further plus for this system is the low cost of approximately $2,000 for the above items and a DS80 or similar LVDT.

3. Capacitance Gage*

Theory of Operation

The surface of the probe tip contains insulating material and a sensor. During operation, the driver supplies a fixed high-frequency voltage signal to the sensor. This creates a "capacitor," with the probe sensor and target surface serving as its plates (see Figure 6). Circuitry in the probe measures the capacitance and generates a current signal that is proportional to the distance between the probe and target. (See description of capacitance gages in Second Annual Report, pg. 8). With proper conditioning, this signal also provides target velocity and acceleration parallel to the probe's axis. The measured capacitance is give by the following equation:

$$C = k\ a\ /d + C_o \qquad (1)$$

where

C = capacitance measured across the gap between the sensor and target surfaces
k = dielectric constant
A = area of the probe sensor
d = distance between the probe and target
C_o = stray capacitance

The adverse effects of stray capacitance on measurements can be minimized if probe components are selected with matching coefficients of thermal expansion. If a marginal increase in cost and complexity is acceptable, stray capacitance can be nearly eliminated by placing a guard ring around the sensor and driving it with the same voltage applied to the sensor (see Figure 7). This effectively eliminates capacitance between the sensor and the (grounded) probe housing and helps to collimate the electric field between sensor and target surface. Since the target must appear infinite in extent to the sensor, a tightly collimated electric field allows a smaller target to be used. In addition, guarded sensors are less sensitive to surface contaminants (such as water and oil) that alter the dielectric constant between the sensor and the target.

*ADE Microsense

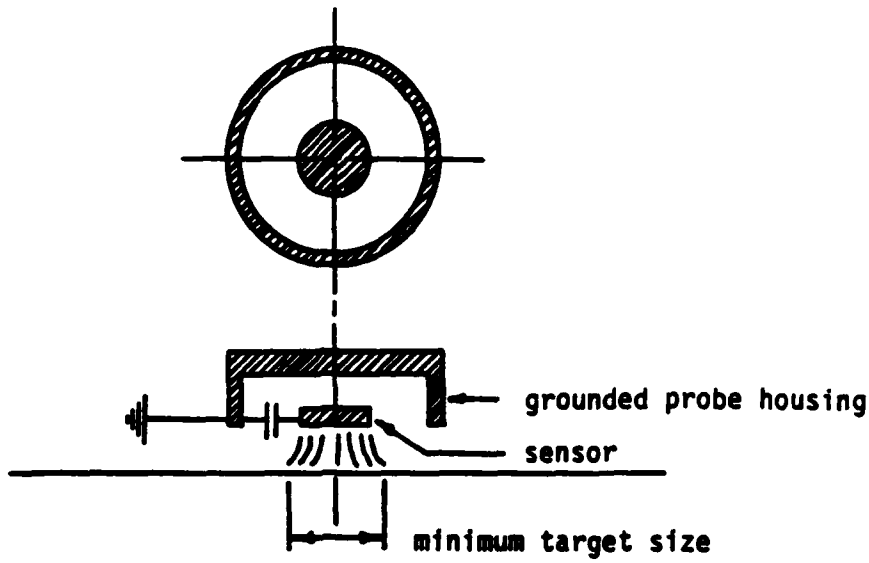

Figure 6. Unguarded Sensor

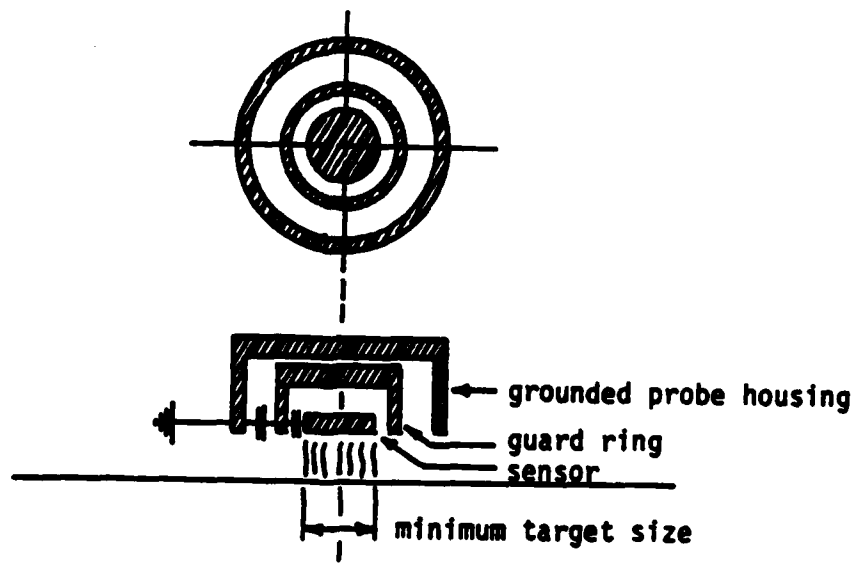

Figure 7. Guarded Sensor

Construction

Most of the following considerations effect static measurements primarily where long term drift in absolute displacment cannnot be tolerated. For most dynamic measurements, where only differential displacements are measured over a short time span, these considerations are less important. In any case, it is best to avoid the following:

1) heat from electric lights or other radiational sources
2) direct drafts and large variation in room temperature
3) excessive humidity
4) external vibration
5) Time varying stresses, vibration, large movement of the probe cable.

The sensing area of the probe should be positioned parallel to the target surface such that the probe-target distance is within the probe's standoff range. Ideally, the sensor should also be positioned at least a sensor diameter distance from the nearest edge of the sample surface.

For dynamic measurements where the prime interest is the acceleration output, care must be taken to minimize the mechanical coupling of vibration of the probes via their fixtures to the surface under investigation. A possible criteria for the maximum level of these vibrations is that any one net vibration amplitude as a function of frequency shall not exceed the acceleration output noise level.

An adequate ground path between the target and the gaging console must be provided. In the case of moving targets, a brush or slip-ring approach must be used. Bearings do not generally provide a satisfactory low noise ground connection.

When looking at the displacement, velocity, or acceleration outputs while monitoring a rotating target, a sync signal developed by the rotating shaft is often useful.

Performance

Capacitance probes are available in straight, right-angle, flexi-tip and lo-profile configurations to accommodate a variety of physical constraints. The size and shape of the probe are chosen to satisfy a specific application once accessibility, size, shape and roughness of the target surface and its range of motion have been considered.

Typical performance values for the ADE Microsense capacitance probes are given below.

Probe active diameter	.0.066 in.
Minimum distance from probe center to target edge for accurate measurements	.0.066 in.
Nominal standoff range	.0.003 in. to 0.005 in.
Linearity	.0.004 of full travel
Resolution	.0.5 microinch
Operating temperature range	.40 F to 130 F
Temperature stability	.4 microinches/degree F.
Frequency response (displacement)	.40 kHz. (3 dB down)
Analog output	.10 mv/microinch

The signal conditioner provides two parallel channels of non-contact displacement measurement utilizing any two of the many probe configurations available. Each of the two channels provide a low impedance (less than 1 ohm) linear d.c. voltage (+/- 10.0 VDC) proportional to the full calibrated range of the probe for the two displacement output, their algebraic addition, and subtraction. Peak reading operations such as +PEAK, -PEAK or TIR (Total Indicator Reading) can be performed in any one of the four displacement output modes. In addition, velocity and acceleration signal processing are performed and presented at analog output jacks.

Advantages and Disadvantages

Capacitance gages are well suited to precision displacement and thickness measurements of metallic and non-metallic materials. They can be used for vibration and displacement measurements in dynamic deformation testing. Their stability and linearity allow them to be used in the measurement of sub-microinch displacements. Solid state electronics give them portability and durability to function under manufacturing conditions. Signal response is such that process control or out-of-tolerance signals. Probe construction permits ease of set-up and calibration, extended versatility, and almost unlimited size capabilities.

Offsetting these advantages, capacitance gages in general are adversely affected by stray capacitances, temperature fluctuations, nonlinearities between displacement and output signal, and surface contaminants. Gaging equipment is designed mechanically and electrically to solve all but the latter of these problems. The requirement for electrical isolation is therefore the biggest disadvantage associated with capacitance gages.

4. Lever-Type Electronic Gage Head*

Construction and Theory of Operation

The Lever-type Gage head functions as a shaded-pole inductive pickup as shown in Figure 8. A flux producing winding is wrapped around

*Federal Products EHE-1048

the center leg of the core. The frequency of the input is 5000 Hz. the flux produced in this central leg is split into two parts in the outer sides of the laminated core.

Figure 8(a) shows the construction of this gage. The lever arm is mechanically connected to the shading loop. When the probe is at the zero position, the shading loop is centered and the voltage in each portion of the outer legs is equal and balanced. As the probe displaces, the shading loop moves to one side or the other of the center position and different voltages are induced in the two portions of the outer legs. The resulting output is the difference between the two induced voltages. The gage head output voltage is linearly proportional to the lever displacement.

The shading loop or coil in a shaded pole inductor is usually made of thin copper bands. A current is generated in the shading loop by the alternating current applied to the center coil. Figure 8(b) shows the vector diagram of the current (i), voltage (e), and the flux (Φ) in the center leg, shaded half, and unshaded half of the core. The subscript s denotes the shaded half and subscript u denotes the unshaded half. The current induced in the shading loop causes the current in the shaded portion to differ from the current in the unshaded portion. Similarly, the fluxes induced by these currents differ and generate voltages e_s and e_u such that a net voltage is produced in the output. This output voltage is linearly proportional to the loop displacement.

Description of the Involute Tip - The involute tip on the Lever-Type Gage Head permits measurement of motion without requiring the measurement arm to remain perpendicular to the axis of measurement. Angular deviations up to $\pm$ 20 degrees are automatically compensated by the curvature of the involute tip.

Lever-Type Gage Heads with ball tips require a correction factor to be multiplied by the reading to produce the true measurement. The correction factor compensates for the "cosine error" of the reading as illustrated in Figure 9. As the tip of the lever moves from position 1 to 2, the length of the lever would have to increase from r_1 to r_2 in order for the measurement to be correct. The ratios r_1/r_2 is the cosine of the swept angle, .

To automatically correct for cosine errors, the involute tip has a specific shape. Referring to Figure 9, the distance traveled by the center of a ball tip is

$$\delta read = r_1\theta.$$

We desire the true measurement to be

$$\delta true = r_1 \sin\theta.$$

The error is given by $\delta read - \delta true$, or

$$e = r_1(\theta - \sin\theta).$$

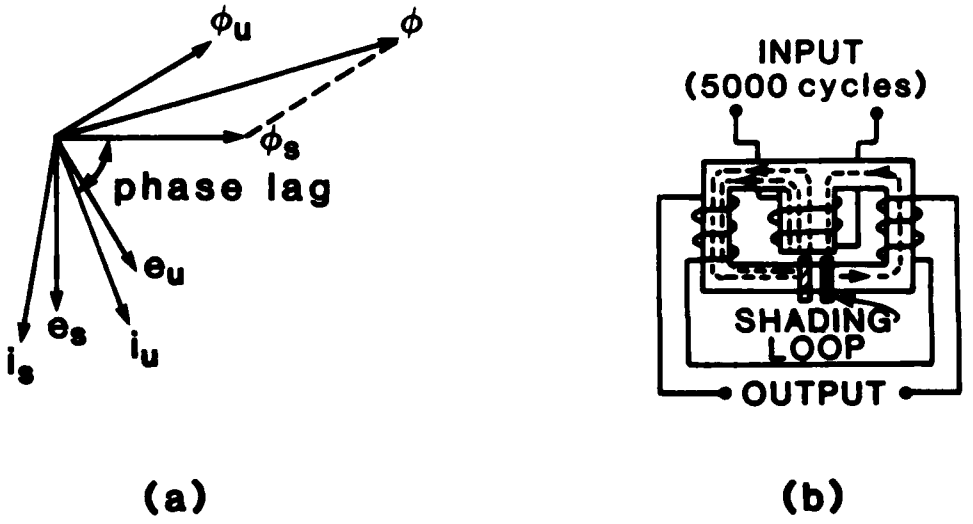

Figure 8. Vector diagram of shaded pole inductor and Federal Products Lever Type Gage Head electrical schematic

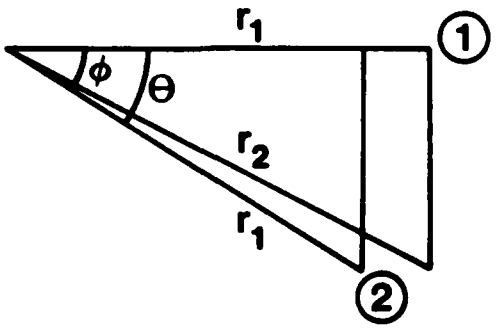

Figure 9. Illustration of cosine error

As discussed above, the length of the lever must increase from r_1 to r_2 in order for the measurement to be true. We can write the change in r as follows

$$\delta r = r_2 - r_1$$

$$\delta r = (r_1/\cos\phi) - r_1$$

$$\delta r = r_1\left(\frac{1}{\cos\phi} - 1\right)$$

To find the relation between ϕ and Θ ; write δtrue in terms of ϕ and Θ and equate the terms.

$$\delta\text{true} = r_1 \sin\Theta = r_1 \tan\Theta$$
$$\Theta = \sin^{-1}(\tan\phi)$$

The error term can be written as follows:

$$e = r_1(\sin^{-1}(\tan\phi) - \tan\phi).$$

Figure 10 plots the change in r versus the measurement error and is the required tip shape to correct for cosine error. A Scherr Tumico Optical Comparator was used to measure the tip geometry and the result is the same as shown in Figure 10.

Performance

Sensitivity and Range. Sensitivity is the ratio of the linear movement of the pointer on the instrument to the change in the measured variable. The amplifier has five ranges of operation and five sensitivities. The distance between graduations is 0.110 inches.

Accuracy. Accuracy is defined as the deviation from known input. The accuracy of the Lever-Type Gage Head system was verified three times. The reference standard was the Hewlett Packard Model 5528A Laser Measurement System Interferometer. Sweeps up and down were performed in order to verify hysteresis. Based on the measurement data the Lever-Type Gage Head system has a measurement accuracy of 10 percent and an instrument accuracy of 5 percent.

Discrimination. Discrimination is the ability of the system operator to discern the smallest measurement. The Lever-Type Gage Head System has a discrimination of 20 percent of the minimum graduation for each range. For example, the discrimination is 1 µin. on the ± 100 µin. scale.

Errors. The shading loop inductance method of operation is sensitive to temperature errors. As the temperature increases from 68 F. the resistances of the shading loop and core windings increase at different rates. The voltages do not change the same amount and error is introduced into the measurement.

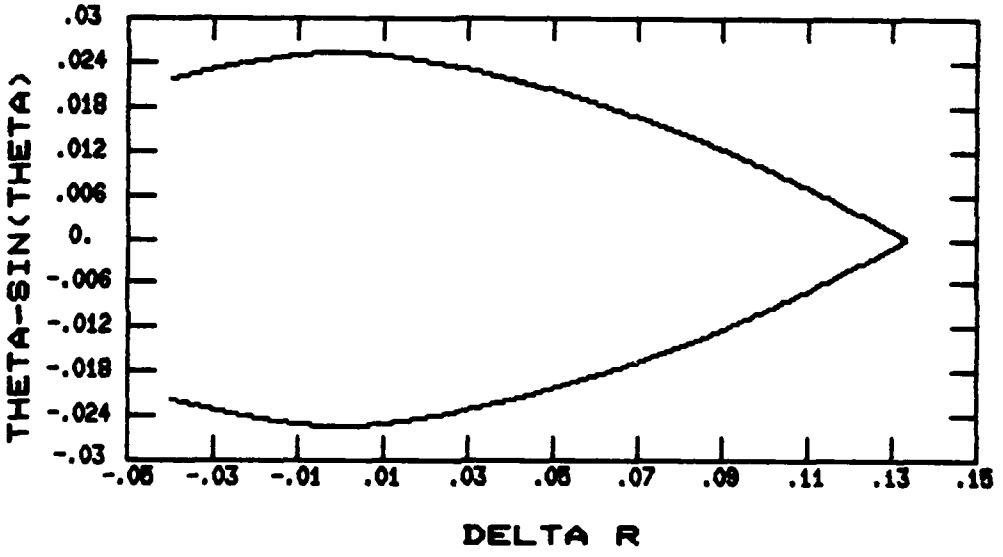

Figure 10. Involute tip profile

The gage head accuracy is a function of the involute tip length and shape. The involute tip dimensions are known values at 68 F. Measurements made at any other temperature will be in error because the dimensions will change due to thermal expansion or contraction. This error can be calculated. However, because the dimensions of the involute tip are small and the measurements are being made in a controlled environment at 70 F., the error is considered negligable.

Advantages and Disadvantages

A primary advantage of the Lever-Type Gage Head is the wide range of linear operation up to $\pm$ 0.010 inches. The range is greater than most conventional capacitance gages and is directly related to the shading loop principle of operation. Two additional features of the Lever-Type Gage Head are the ability to reverse direction of measurement and the ability to position the contact point anywhere in a 200 degree arc.

The disadvantages of this gaging system involve the limited bandwidth of the measurements and its non-averaging nature. Because of the lever mass and mechanical contact between the tip and the object to be measured, the lever-type gage head cannot measure displacements at frequencies greater than 300 Hz. In some instances, the point contact between the lever tip and the object can be a problem, especially when using this gage in a runout control system. Small irregularities in the reference surface (surface roughness) which are not really displacements can result in system response. However, changes in the control algorithm can also alleviate this problem.

5. Laser Interferometry System*

Theory of Operation

The principle of interferometric displacement measurement devices is that if two identical, coherent, monochromatic light beams are directed such that one beam travels a fixed length path and the other travels a variable length path, the combination of the two beams will produce an interference pattern that is directly related to the difference between the two path lengths. This principle was first demonstrated by A. A. Michelson in about 1890. In his apparatus and most that followed, one light beam is split in two by a half silvered mirror. One of the resulting beams is reflected off of a fixed mirror while the other is reflected off of a movable mirror. The two beams are then recombined, and the intensity of the resulting interference pattern on a specified detection surface was measured. Because the light exists as a coherent wave, the intensity of the interference pattern is a function of the phase difference between the two beams. This phase difference, in turn, is a function of path length variations between the beams and their optical wavelength. By counting the number of

*Hewlett Packard 5501 and 5528

sequentially light and dark interferences that occur during a translation of the movable mirror, the magnitude of that displacement can be determined to a resolution on the order of the wavelength of the light source. This type of interferometry system is called fringe counting, phase detecting, or Michaelson interferometry. It is helpful for gaining a conceptual understanding of interferometry, though it is rarely implemented in this simple form because of its two fundamental limitations: it cannot sense the direction of the motion, and its sensitivity is dependent on the amplitude stability of the component beams, which is strongly affected by the environmental characteristics of the optical path.

The Hewlett Packard Interferometry Systems (5501 and 5528) avoid these limitations through the use of a frequency detection scheme. The basic principle of both systems is that motion of the movable mirror will cause the reflected light to undergo a Doppler frequency shift that is linearly proportional to its instantaneous velocity. By integrating this velocity signal, the displacement of the movable mirror can be determined. The sensitivity of this system is ultimately limited by the degree to which the frequency of the incident beam can be held constant (four parts in one hundred million for this system). A schematic of the system is illustrated in Figure 11. At the heart of the system, the laser source generates a single beam composed of two slightly different frequencies, F1 and F2. The F2 beam is diverted from the F1 beam at the beam splitter and becomes the reference beam. The F1 beam passes through the beam splitter and is Doppler shifted by the movable retroreflector: the frequency of the reflected light is shifted from frequency F1 to frequency F1 + dF1 where F1 is the velocity of the movable retroreflector divided by the wavelength of the helium neon beam. Both reflected beams are recombined in the beam splitter and directed to a stationary photodetector. The frequency difference between the two beams is compared with the initial frequency difference to extract the Doppler frequency component dF1, which is in turn delivered Figure 1 to one of two possible electronics packages. Each of these is capable of converting the Doppler frequency signal into a velocity signal and of integrating this velocity signal to provide a displacement signal. The 5501 electronics are faster, hence more suited to computer data acquisition, while the 5528 electronics are more suited for display and calibration tasks.

Construction

The coherent light source is a Helium-Neon 1 milliwatt laser with a nominal wavelength of 638.2 nanometers, corresponding to a nominal frequency of 4.7 x 10**14 Hz. This laser source is Zeeman split meaning that the light emitted consists of two frequency components, F1 and F2, that are split about the nominal center frequency. The Zeeman effect dates back to 1955 when Forrester, Gudmunddsen, and Johnson* discovered that when atoms in a light beam are subjected to a magnetic field they undergo a split in stable energy levels. As a result, the emitted light contains two frequency components that differ in proportion to the magnitude of the applied field. For this laser, the two frequencies are split by 2 MHz. The lower frequency component F1 is left hand

*Photelectric Mixing of Incoherent Light, Physics Review, #99, p. 1691, 1955.

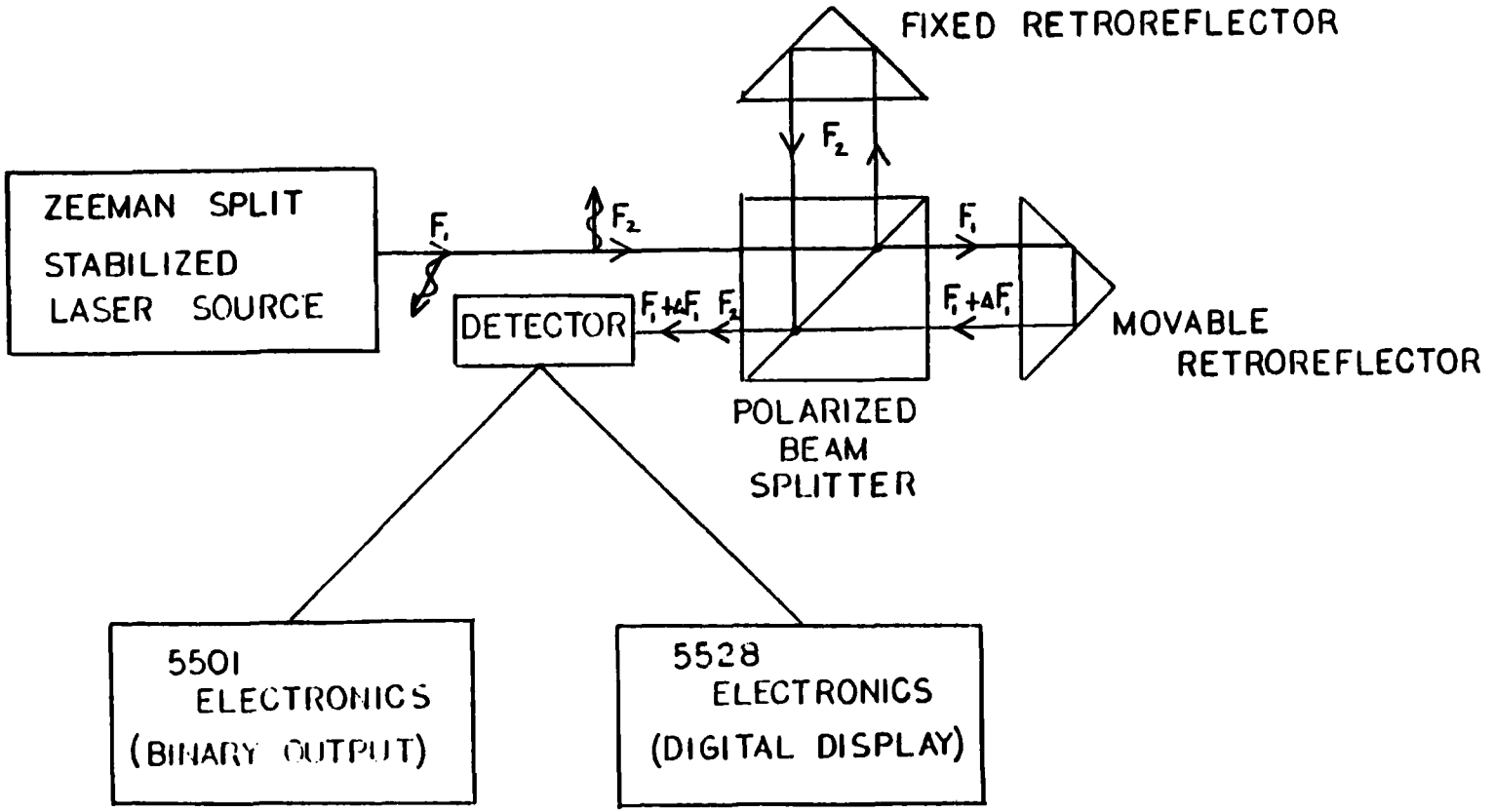

Figure 11. Schematic of Hewlett Packard interferometer

circularly polarized, while the higher frequency component F2 is right hand circularly polarized. A quarter wave plate converts these circular polarizations into linear, nearly orthogonal polarizations, while a subsequent half wave plate is factory tuned to further orthogonalize the linear components. At this point, the beam consists of a horizontally polarized component and a vertically polarized component at frequencies of F2 and F1 respectively. Next, the beam passes through a collimating telescope beam expander which produces a 1/4 inch wide parallel beam. Twenty percent of this beam is diverted to a frequency stabilization photodetector circuit which senses any drift in the lasing frequency and generates a compensation signal as feedback to both a PZT actuator (mounted at one end of the laser cavity) and a heater (encasing the laser cavity.) By controlling the length of the cavity, the PZT and the heater can stabilize the laser to approximately four parts in 100 Million.

The remaining eighty percent of the laser beam exits through the front of the laser head and enters a polarizing beam splitter (interferometer cube). The beam splitter transmits the vertically polarized component F1 and reflects the horizontally polarized component F2. Next, the F2 beam travels a fixed distance to a retroreflector (corner cube), that reflects it back into the beam splitter. Meanwhile the F1 beam travels to the movable retroreflector and is reflected with a Doppler frequency shift (dF1) that is proportional to the velocity of the retroreflector. This shifted beam recombines with the reference beam at the beam splitter. The combination of the fixed path length beam (frequency F2) and the variable path length beam (frequency F1 + dF1) leaves the beam splitter and is incident on a photodector which compares the difference frequency (F2 - (F1 + dF1)) with a reference frequency difference (F2-F1). This comparison manifests itself as a beat at the Doppler frequency dF1. The photodetector can respond to Doppler shifts caused by velocities of up to 12 inches per second, corresponding to a Doppler shift of approximately 500 kilohertz. The extracted Doppler frequency is transformed into a series of electronic pulses that can be counted to provide a velocity signal and integrated to provide a displacement signal.

The system optics are available in three possible configurations, as illustrated in Figure 12. The Linear Interferometer is the basic optical configuration, with the fixed retroreflector attached to the beam splitter. This system is intolerant of displacements of the movable retroreflector in the Y direction, such as would occur in measurements of the motion of the XY table. The Plane Mirror configuration avoids this problem by allowing the movable reflector to be a simple flat mirror. The Single Beam Interferometer utilizes quarter wave plates to permit collinear (overlapping) beam paths, resulting in a significant size reduction in the optics.

Performance

The sensitivity of the interferometry system is 1 microinch with the 5528 electronics and 0.6 microinches with the 5501 electronics. The major difference between the two electronics packages is speed; the 5528 can update its output at a rate of about 40 Hz., while the 5501 can transmit data to a computer at about 1.5 kHz.

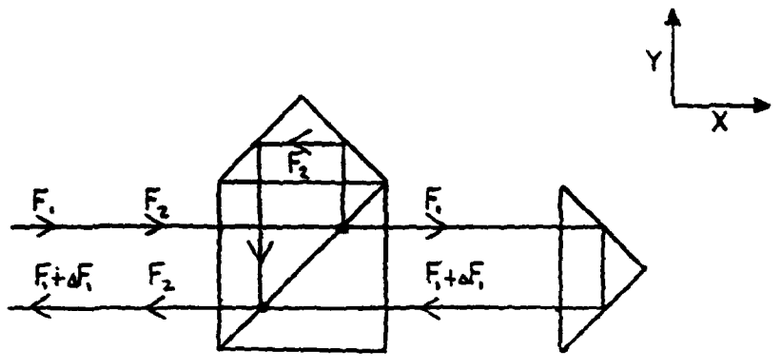

LINEAR INTERFEROMETER

- o INTOLERANT OF Y MOTION
- o RETROREFLECTOR OR INTERFEROMETER CAN MOVE

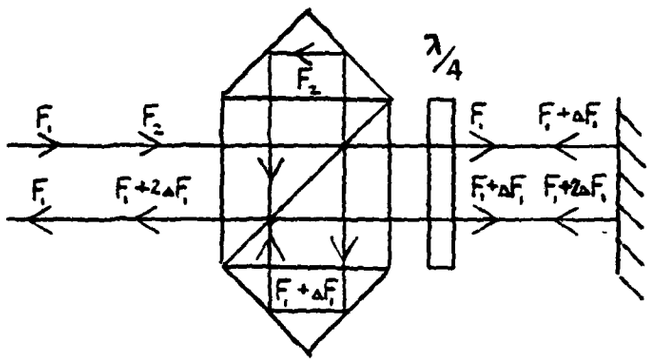

PLANE MIRROR INTERFEROMETER

- o TOLERANT OF Y MOTION
- o TWICE THE RESOLUTION OF THE LINEAR SYSTEM
- o USES THE QUARTER WAVE PLATE TO CHANGE BEAM POLARIZATION

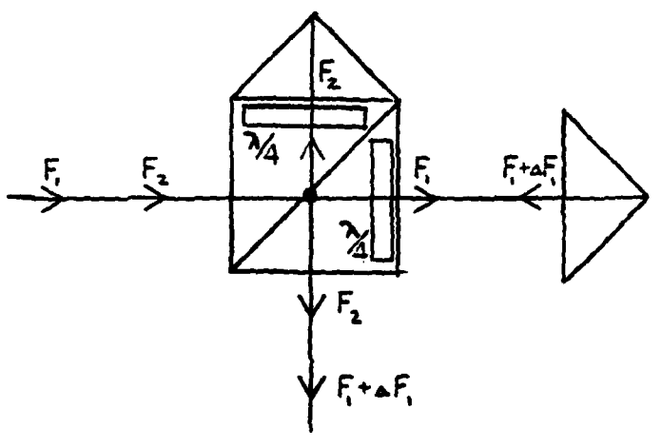

SINGLE BEAM INTERFEROMETER

- o COMPACT OPTICS
- o ALIGNMENT IS CRITICAL
- o INTERFEROMETER CUBE MUST REMAIN STATIONARY

Figure 12. Optical configurations available

There are five sources of error in the system. They are:

1) Cosine Error - due to skew in the translation path of the movable reflector
2) Laser Error - Frequency stability of the laser source, Photodetector limitations, electronic resolution
3) Temperature Error - changes the velocity of light (vol)
4) Pressure Error - changes the velocity of light
5) Humidity Error - changes the velocity of light.

The cosine error, described in Figure 13, is a systematic error that can be diminished through careful alignment of the system. The laser error is random, and an inherent component of this system. The final three errors affect the velocity of light in both a systematic and random fashion. These three errors can be compensated electronically at the beginning of a measurement by manually entering a VOL correction factor into the system electronics (using a VOL lookup table provided by H.P.). While this step will diminish the systematic portion of these errors, it will not decrease the errors due to environmental fluctuations during a given measurement. The magnitude in microinches per inch of travel due to all of the above errors is tabulated below.

Error	Microinches/inch
Cosine Error	S**2/8D see Figure 3
Temperature Error	1.0 / degree C
Pressure Error	1.0 / 0.1 inches Hs.
Humidity Error	1.0 30% change

Advantages and Disadvantage

Advantages:

1) 40 meter range
2) Linear output
3) Non-contacting
4) Traceable reference (Not a comparison gage)
5) Computer compatible digital output

Disadvantages:

1) Bulky
2) Expensive (approx. $25 k)
3) Requires a relatively constant temperature and pressure for accurate measurement
4) Requires the retroreflector to be mounted on the part to be measured for all but the plane mirror configuration, which requires a reflective surface on the part to be measured.

COSINE ERRORS

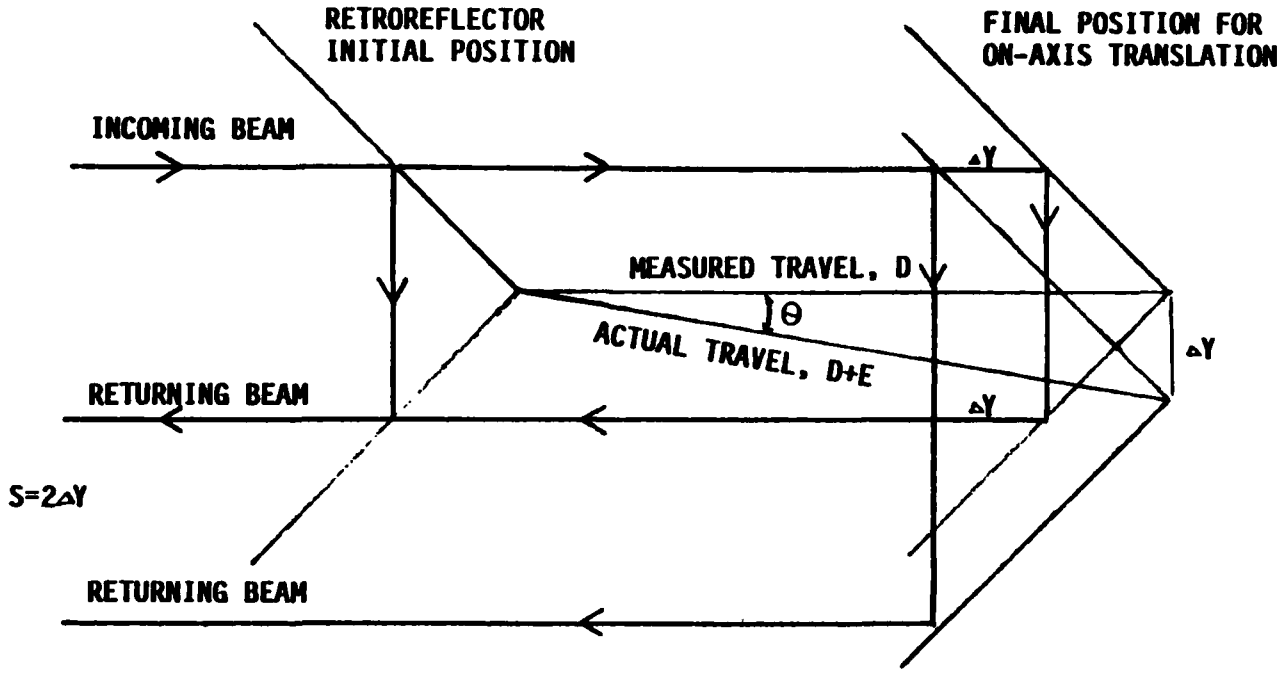

If the retroreflector translates along the axis of the incoming beam, the returning beam is not shifted vertically. The measured displacement is D, with no Cosine Error.

If the retroreflector translates along some line skewed with respect to the axis of the incoming beam, the measured displacement is still D, since the beam path length has not changed. The returning beam is shifted vertically by an amount S. The error in the measurement of the actual travel is a function of both the distance measured and the vertical displacement of the returning beam.

Figure 13. Cosine error in linear interferometer

THE FEASIBILITY OF USING MAGNETOSTRICTIVE TERFENOL AS A PRECISE ACTUATOR

By

Michael D. Bryant
Associate Professor
Mechanical and Aerospace Engineering Department

ABSTRACT

The work outlined in this section concerns feasibility of the use of magnetostrictive Terfenol as an actuator. A prototype device was built and tested to determine if magnetostrictive materials can be used as the basis for precise displacement and/or force actuators. Problems of heating in the excitation coil, magnetic bias, maximum bandwidth, and maximum practical device displacement are addressed.

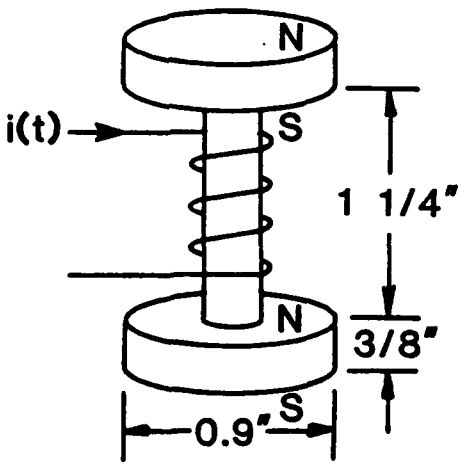

INTRODUCTION

Magnetostrictive materials exhibit strains when subjected to a properly oriented magnetic field. These strains occur when anisotropic magnetic domains present in the magnetostrictive material attempt to align with the local magnetic field. Anisotropies in the newly aligned domain geometries produce the magnetostrictive strains. Magnetostrictive materials also exhibit a reverse effect; i.e., strains in the material results in domain reorientation which produces a strain induced magnetic field.

Iron, cobalt, and nickel are three metals which demonstrate magnetostrictive properties. For these metals the maximum strain created is relatively small, being of the order of 1 part in 100,000. The Naval Ordance Laboratory (White Oak, MD) has recently developed mixtures of materials that include the lanthinide series of metals which display large magnetostrictive strains [1]; Terfenol, a mixture of iron, terbium, and dysprosium can achieve strains of the order of 1 part in 1000 [2]. Much larger displacements can be produced by application of a given magnetic field to Terfenol than to the common magnetostrictive materials.

Other important properties of Terfenol include a stiffness comparable to most metals (E = 2.5 - 3.5 x 10**4 MPa); a low tensile strength (28 MPa); a high compressive strength (700 MPa); and a moderate to high density (9.25 x 10**3 kg/m^3). In addition, the Curie temperature is about 400 C [3].

EXPERIMENTAL APPARATUS

To operate the Terfenol as a precision actuator, the magnetic field along its length is changed resulting in a change in length of the material. For a number of reasons (flexibility, linearity, etc.), it is desirable to induce a uniform magnetic field and then vary the field about this dc level. This will produce an increase and a decrease in length around some mean value. Preliminary experiments in which the DC magnetic field was produced by a current through a solenoid demonstrated device temperatures high enough to compromise performance. Thermal strains in the Terfenol and increased coil resistance seriously limited the resolution of the device and reduced the ratio of output displacement per unit of applied excitation (coil current or magnetic field).

To overcome these difficulties, the dc magnetic field was produced with a pair of permanent magnets and a solenoid driven by an ac source was used to induce the dynamic magnetic field. Figure 1 shows the geometry of the magnetostrictive device. A 1.25 inch long by 0.25 inch diameter rod of Terfenol is glued axially between two coin shaped permanent rare earth magnets each having 0.375 inch thickness by 0.900 inch diameter. The poles of the magnets are orientated to produce a constant (DC) magnetic bias within the Terfenol rod. This bias causes partial domain orientation (and concomitant DC displacements) in the

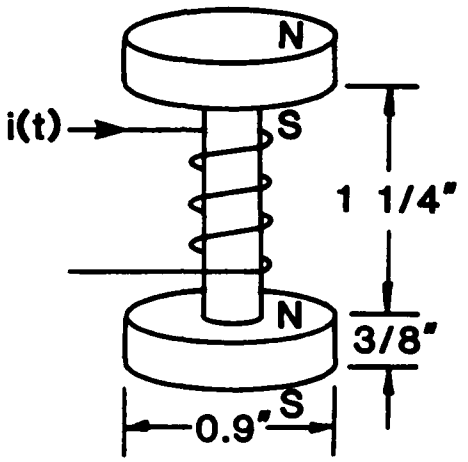

Figure 1. Device geometry featuring a Terfenol rod between two Samarium Cobalt permanent magnets

Terfenol material. The residual induction of each permanent magnet is about 8.2 kGauss.

Around the circumference of the Terfenol rod is wrapped 200 turns of number 18 gauge copper magnet wire. This coil is used to generate a time varying (AC) magnetic field which, when superposed upon the DC field, provides the magnetic excitation needed to cause magneto-elastic strains (and motions) in the Terfenol rod.

A Kepco Model BOP 15-20 (M) programmable power supply was used to excite the coil. This instrument has maximum ratings of plus or minus 20 amps and 15 volts with a 25 kHz. bandwidth. A wave form generator provided sinusoidal excitations to the power supply.

Motions of the Terfenol rod were measured using an ADE 3401 capacitance gauge. (This instrument is capable of microinch resolution and has a 40 kHz. bandwidth.) A small piece of aluminum was glued to the end surface of one of the permanent magnets and motions of the entire structure were measured via the capacitance gauge. The aluminum end cap was needed to separate the magnetizable capacitance gauge probe from the powerful field of the rare earth magnet. Output displacements were recorded and displayed on a digital oscilloscope and an FFT analyzer.

PROCEDURE AND RESULTS

A 10 Hertz sine wave was applied to the system described in the previous section to determine displacement characteristics. The input amplitude was varied from small to large while the displacement of the Terfenol rod was measured. Heating of the coil caused by the AC power dissipation was also monitored.

For small signal operation the displacement waveform as measured by the capacitance probe appeared to be sinusoidal with little harmonic distortion (less than about 5%). This linear behavior appears to be true as long as the output displacement remains smaller than about 0.002 inches. Also heating of the device was negligible for displacements smaller than about 0.0015 inches.

A steady state displacement of 0.0015 inches amplitude with stable coil temperatures was also observed. Under these conditions the device operated for several minutes without any sign of failure and was cool enough to touch. Attempts to increase the peak to peak displacement beyond this stable 0.0015 inch value usually led to device failure caused by over-heating of the coil (too hot to touch) or by dynamic fracture of the moderately brittle Terfenol. However, a maximum peak to peak displacement of about 0.003 inches was observed as the best case before device failure occurred. For this test a slight wave form distortion was detectable.

The system bandwidth was measured with an FFT analyzer and the upper 3 dB point of the system was found to exist at about 800 Hz. This

measurement may not be indicative of the achievable bandwidth of the prototype since the breakpoint of the power amplifier used was about 1000 Hz. (The amplifier used has a switch that can set the bandwidth to 1 kHz or 25 kHz; for the experiments conducted, the switch was set at the 1 kHz scale because the output at that frequency is more stable.) However, attempts to test the device at much higher frequencies resulted in dynamic fracture of the Terfenol probably due to inertial forces exceeding the tensile limits of the material.

DISCUSSION AND CONCLUSIONS

In light of the previously described study, use of Terfenol based actuators appears feasible if the following restrictions are observed:

1. For large strains at high frequencies, the device must be placed in compression to avoid dynamic fracture caused by inertial forces.

2. Linear operation with peak to peak displacement amplitudes of 0.001 inches are possible for 1 inch long devices. Larger displacements can be safely produced using longer rods.

3. Coil heating can be reduced using permanent magnets to provide a magnetic bias; the geometry of the device outlined above can produce displacements of 0.0015 inches before AC dissipation becomes significant.

4. Bandwidths exceeding 1 kHz may be possible if (1.) is observed.

REFERENCES

1. Clark, A. E and H. S. Belson, "Giant Room-Temperature Magnetostrictions in $TbFe^2$ and $DyFe^2$, Physical Review B, 5(1972), pp. 3642-3644.

2. Clark, A. E., M. L. Spano, and H. T. Savage, " Effects of STress on the Magnetostriction and Magnetization of Rare Earth-Re 1.95 Alloys," IEEE Trans. Mag., MAG-19(1983), pp. 1964-1966.

3. Clark, A. E., Presentation notes from 1985 Terfenol Workshop, Ames, Iowa.

ANALYSIS OF TRACTION FORCES IN A PRECISION TRACTION DRIVE

By

J. W. Kannel, *Research Scientist
Battelle Columbus Laboratories

and

T. A. Dow, Director
Professor
Mechanical and Aerospace Engineering Department

ABSTRACT

A theory to predict the tangential deflection in a traction drive has been developed. This theory can be used to calculate the elastic and non-recoverable deformation produced when moving a traction load through a distance. Traction and deflection parameters are derived and an approximate equation is presented which can be used to find the tangential deflection resulting from translation as well as rewind motions. An experimental apparatus has been built to corroborate the theoretical predictions of "wind up", and the results indicate good agreement with the theory.

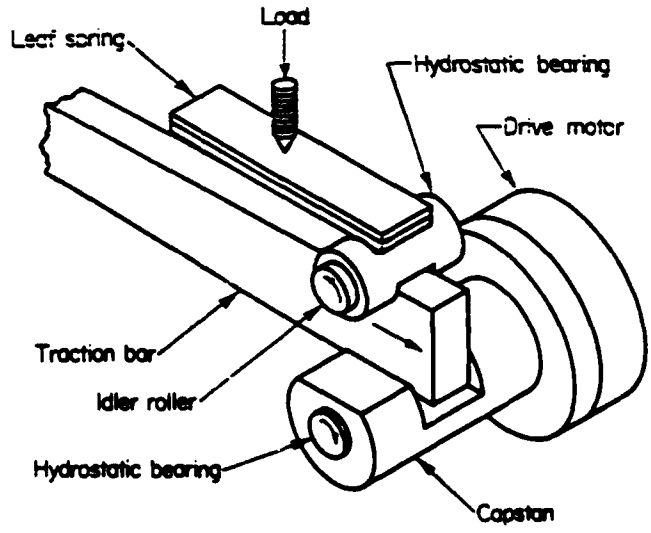

*Work conducted at Battelle - Columbus in partial fulfillment of the Ph.D degree in Mechanical Engineering at North Carolina State University.

INTRODUCTION

Two critical aspects of a precision machine are linear location of one part relative to another and smooth motion between limits. One method of achieving this result [1,2] is to use a traction drive on the slideway. Positioning accuracy below the microinch level is typically required. When accuracies of this level are involved, virtually all factors which affect motion must be considered in order to minimize errors in the system. One such factor is the shear deformation of the drive system, especially the elasticity of the traction interface. The elasticity is affected by many factors, including the Young's modulus of the traction components, surface layers on the rollers (such as solid film layers) and the roughness of the rollers and slideway.

The most extensive work reported on the analysis of the traction interface is by Kalker [3,4]. Kalker traces the traction interface between two extremes: the Cattaneo [5] problem and the Carter [6] problem. The Cattaneo problem occurs when a cylinder is rotated slightly, while in contact with a stationary surface. The Carter problem occurs when both the cylinder and the mating surface are moving but at slightly different speeds. Kalker's study traces the traction forces through the transients between the two extremes.

Bentall and Johnson [7] analyzed the slip between two dissimilar cylinders in rolling contact. This research allowed for tangential deflections due to microslip. Barber [8] conducted research similar to Kalker's, only he analyzed three-dimensional contacts of rollers under misalignment. Poritsky [9] derived basic equations for cylinders in contact and discussed the problem of rough surfaces. Krause and Senujma [10] did experimental studies with rollers which developed surface corrugations. The surface corrugations notably affected the traction behavior of the cylinders.

The work presented here is an extension of the Kalker and Poritsky work with allowances for surface layers. The surface layer algorithm is developed from the work of Sneddon [11], and Gupta and Walowit [12].

MODELING THE WIND-UP DEFLECTIONS

The research on the traction interface has yielded several interesting factors regarding stresses and deflection between cylindrical contacts. Surface finish analyses have shown that surface roughness plays a key role in the normal stresses and can alter shear stresses. The surface coating analyses have shown that very thin surface layers can make sizable reduction in the deleterious effects of roughness. Perhaps the most significant factor, however, is that the traction interface "winds up" elastically on the order of hundreds of microinches in a non-reversible manner.

The problem posed here is an attempt to summarize the traction studies into a usable algorithm for predicting "wind-up". The first

step in addressing this problem is to characterize the predictions in general formulation.

The approach used has been modeled after Kalker's work; that is, the traction (F_t) is scaled on the maximum possible traction and the tangential deflection (ϵ) is scaled on the maximum possible deflection. The traction parameter is

$$F_t/fW$$

where F_t is actual traction per inch of roller width, f is the friction coefficient, and W is the normal load per inch of width. The maximum tangential deflection (ϵ_f) for a Hertzian contact would be the deflection that would occur for full slip (i.e. a coefficient of friction type situation.) This deflection will be used to produce a non-dimensional deflection parameter. Using Poritsky's equation, the tangential deflection for a general point load is:

$$\epsilon = \frac{4(1-\nu^2)}{\pi E} P \ln|x/x_0| \tag{1}$$

where E is Young's modulus, ν is Poisson's ratio, P is the point load, x is the x location, and x_0 is the reference location. For a Hertzian contact

$$P = f\, p_h \sqrt{1 - x^2/b^2} \tag{2}$$

Also for a Hertzian contact

$$W = \frac{\pi b p_h}{2} \tag{3}$$

Combining equation (1-3) and integrating over the Hertzian contact, the maximum tangential deflection can be written as

$$\epsilon_f = \frac{8}{\pi^2} \frac{1-\nu^2}{E} fW \int_{-1}^{1} \ln\left|\bar{x}/\bar{x}_0\right| \sqrt{1-\bar{x}^2}\, dx \tag{4}$$

where $\bar{x} = x/b$

or for $\bar{x}_0 = 10$

$$\epsilon_f = 4.514\, fW \frac{1-\nu^2}{E} \tag{5}$$

$$\epsilon_f = 1.42 \times 10^{-7}\, fW \quad \text{inches (for steel).} \tag{6}$$

The predictions were put in the form ϵ/ϵ_f versus the traction parameter, F_t/fW.

Comparison of Deflections For Different Conditions

The computer program developed is based on the theory given in [13] and [14] and is known as ATCON (Analysis of Traction Contact). It was used to explore how different conditions affect "wind-up". The approach consisted of evaluating traction and deflections for a sequence of steps until three Hertzian contact widths (6 half widths) had been traversed. This number of half widths insured that the program had reached a steady state (Cattaneo's Problem). Following the three contact widths of traverse, the sequencing was reversed until the rollers were back in the starting position (minus the microslippage losses).

Figure 1 shows the non-dimensional deflection, $\varepsilon/\varepsilon_f$, plotted against the number of contact widths traversed, S. The shear stress distribution at different traverse distances are also illustrated. At point A, the driving cylinder has "wound-up" just to the point where the shear stresses are equivalent to the traction load, but no motion has taken place (Carter's Problem). This initial wind-up is 75 μin. for this case where the traction parameter is 0.57. The shear stress for this case shown in Figure 1(a). Shear stress is a minimum in the center of contact and grows toward the edges because each element must support a greater portion of the shear deformation outside the contact. This curve would follow the dotted line except for the limitation of the frictional force. When the required shear stress exceeds the normal pressure times the friction coefficient, slip will occur. This slip represents an unrecoverable loss. If the traction load is kept constant, a small increase in traction will cause movement of both rollers to occur; that is $S > 0$.

The curve for this case of $F_t/fW = .57$ is very linear for $S > 1$ or $S < 2$ (unwind); that is, under steady state conditions, the increase in microslippage with traverse is a constant. For low values of S or at points where the traverse is reversed, some non-linearities occur because the slippage rate is non-uniform. To better understand these non-linearities, it is helpful to compare the shear stress predictions which are also shown in Figure 1.

Figure 1(b) shows the shear stress after the cylinders have traversed one-half contact width (point b on the deflection curve). In advancing from Figure 1(a) to Figure 1(e), all of the shear stress regions limited by friction represent non-recoverable losses and must be made up by additional tangential deflections. Figure 1(c) shows a steady state condition at $S = 3$. Again there are non-recoverable losses, although here the loss rate will be constant. Figure 1(d) shows the shear stress curve at $S = 2.5$ on the rewind and Figure 1(e) shows the steady state rewind curve, illustrating that the rewind condition is just the mirror image of the forward traverse.

The influence of the traction parameter was explored using ATCON and the results are presented in Figure 2. Case 1 represents predictions for a cylinder with a half width of 0.01 inch, a friction coefficient of 0.3, and an initial "wind-up" of 75 μinch. For Case 2 the "wind-up" is reduced to 37.5 μinch which results in a reduction in the traction parameter to .29. In Case 3 the friction coefficient

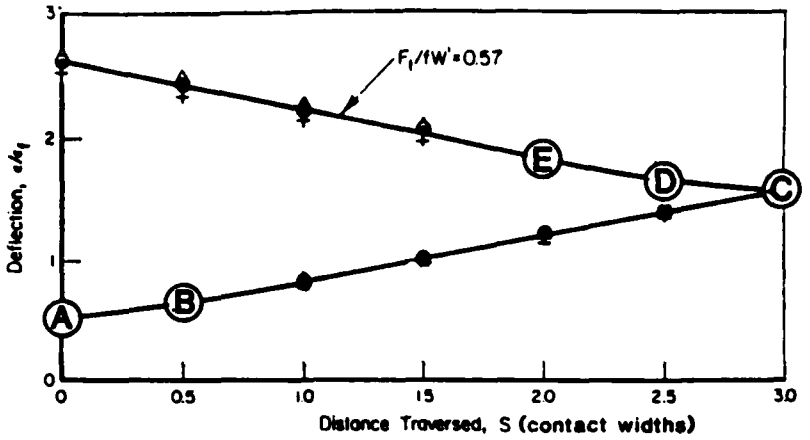

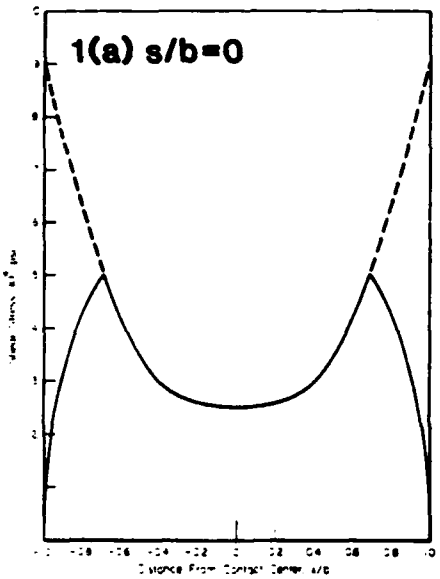

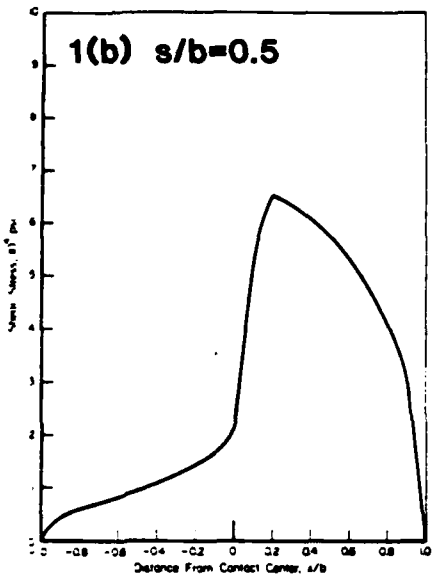

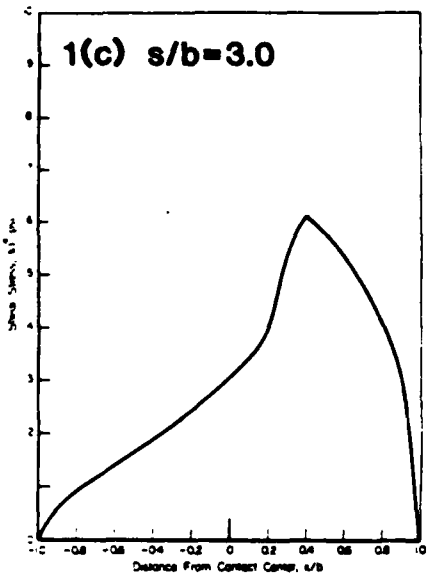

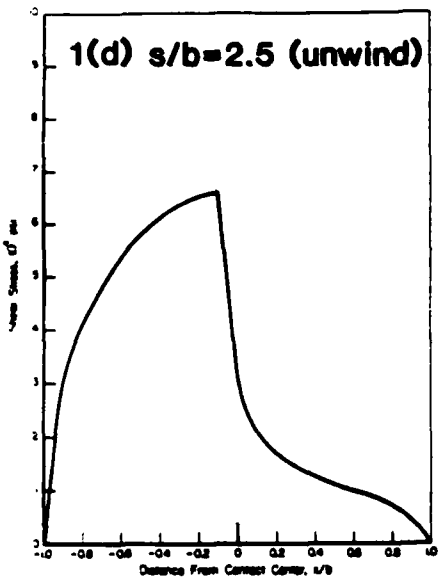

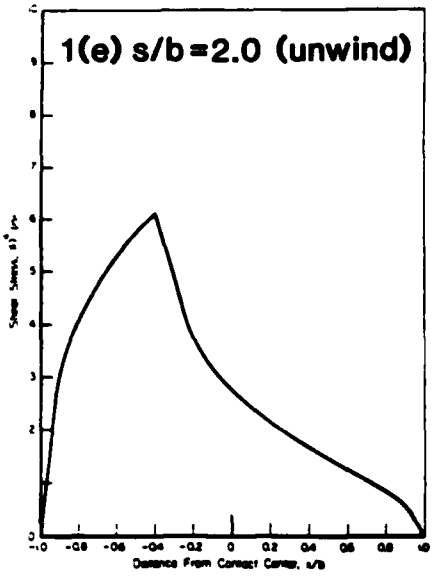

Figure 1. Tangential deflections and shear stress distribution across contact at different traverse positions

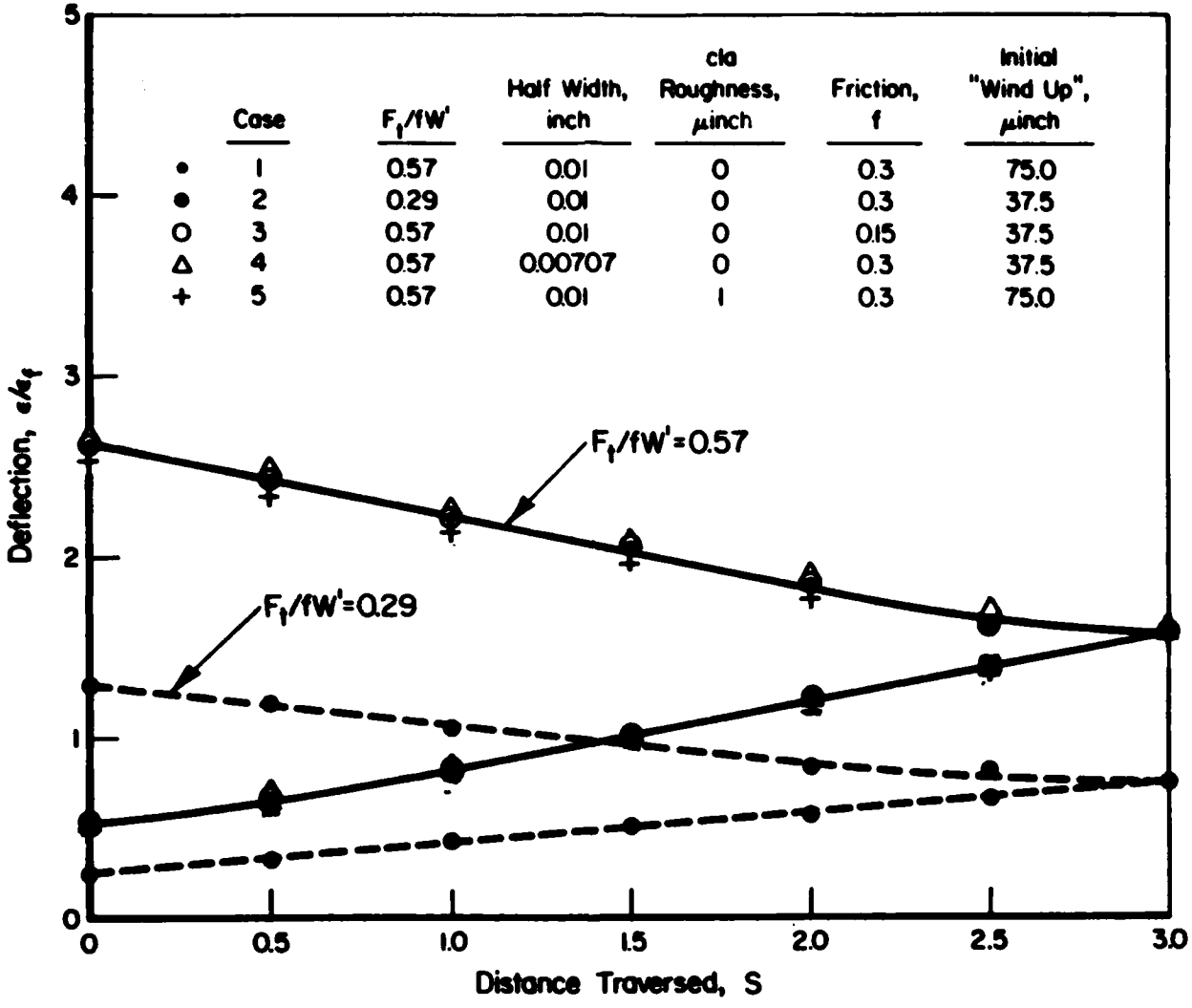

Figure 2. Comparison of scaled deflection parameters for different conditions

is increased and the half width is decreased so, again, the traction parameter is .57. Case 5 is the same as case 1 except for a small surface roughness factor.

As was anticipated from Kalker's work, the scaling parameters characterize the traction equations. Several combinations of values of b, f, and initial "wind-up" produced the same value of F_t/fW and essentially the same values of ϵ/ϵ_f for a given distance traversed. Further, even the predictions involving a small level of roughness (1 μinch cla) produced curves in reasonable agreement with the other results.

Tangential Deflections Due to Pressure Effects

One underlying assumption used in the analyses is that the effect of normal pressures on tangential deflections can be ignored in the traction analyses. Since this is a very convenient assumption commonly used, such as by Kalker, it is worthwhile to explore its validity. The deflections predicted are too large to be totally ignored without further evaluation.

To evaluate the role of pressure induced deflection, they were added to the shear deflections and used to compute shear stresses. As before, the rollers were allowed to traverse back and forth through three contact widths. The deflections produced by this traversing are shown in Figure 3. Pressure appears to have a major effect on the initial intercept but has little effect on subsequent non-recoverable losses. This is evident by the fact that the two curves are nearly parallel on the re-wind.

Figure 4 shows the deflection curve and typical shear stress distributions obtained at different points along it. Initially, the pressure effects introduce asymmetric deflections and shear stresses as shown in Figure 4(a). However, in a semi-infinite body these deflections extend indefinitely such that after the load is applied, the bodies are in a fixed state of tangential deflections. As the points on the two cylinders move into mesh the "wind-up" deflections are simply superimposed on the pressure deflections. At steady-state, the pressure effects have been "rolled out". During unwind, the problem simply digresses to the problem where pressure deflections were ignored.

In general, based on the assumptions presented here, the pressure deflections can be ignored. Further treatment of the subject would require rewriting the stress equations to couple shear and normal stresses. Such analysis seems to be not only difficult but also unnecessary based on the arguments given here.

Modeling the "Wind-Up" Deflection

When the traction parameter is reduced to .29, the non-linearities appear to be less pronounced. Therefore good modeling of the interface can be achieved by limiting the traction parameter. A series of ATCON runs were made to further explore this conclusion. For these cases, the

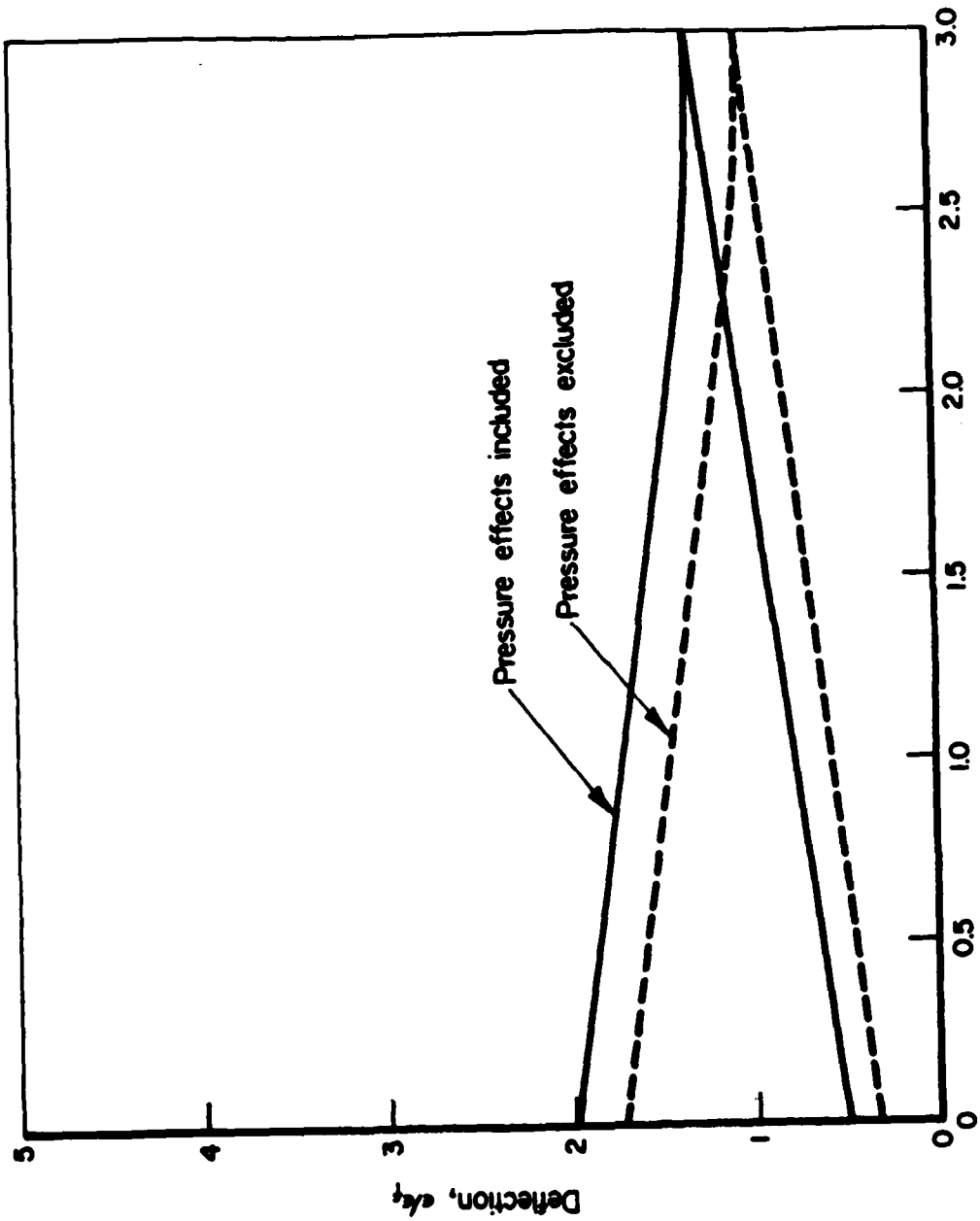

Figure 3. Effect of tangential deflection from normal pressure on non-elastic losses $F_t/fW' = .4$

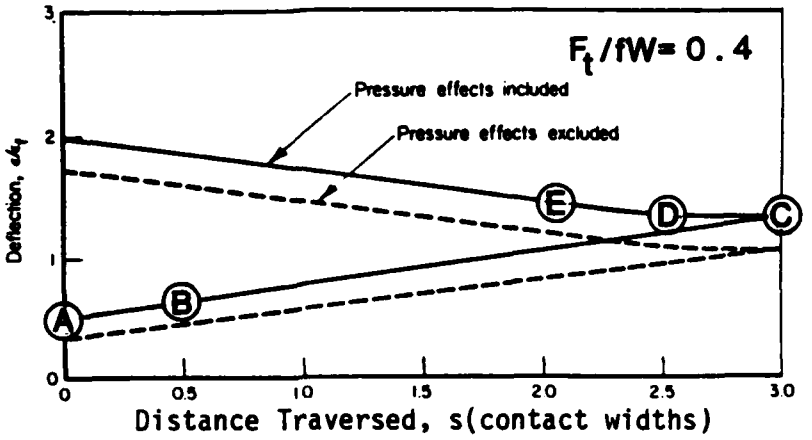

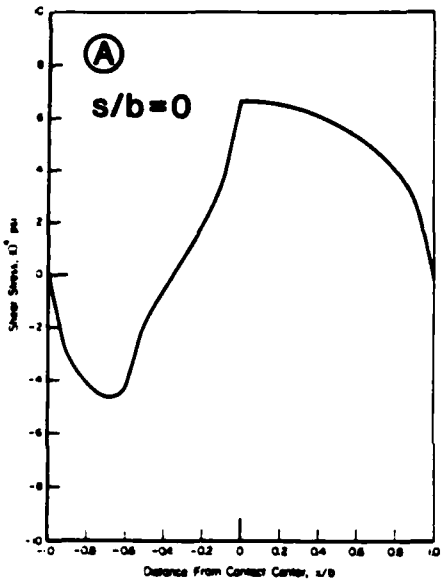

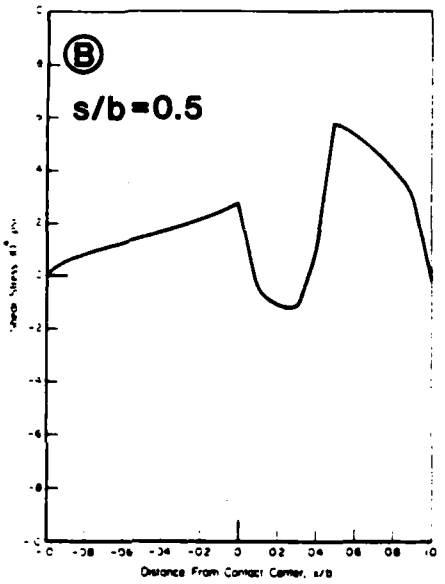

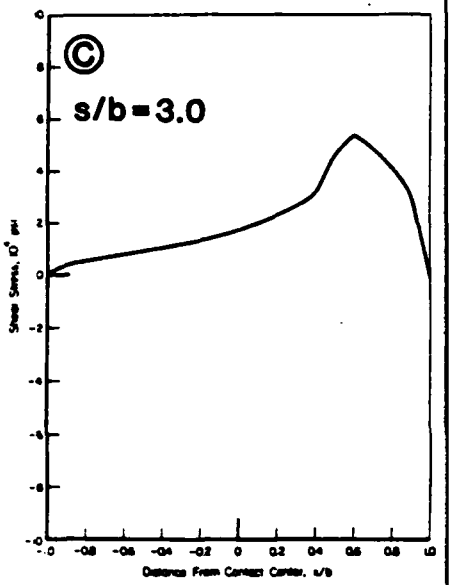

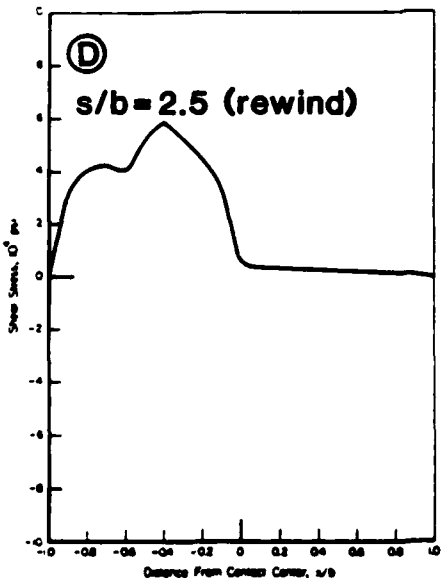

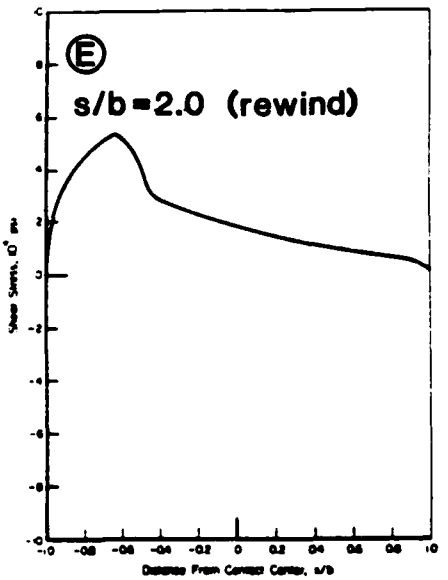

Figure 4. Comparison of shear stress distributions including pressure effects for different traverse-rewind positions

initial "wind-up" was adjusted (by trial and error) to yield the even values of the traction parameter, (F_t/fW = .2, .4, .6 and .8) given in Figure 5. Straight lines were drawn between the initial point and the point where S = 3.

It is obvious from Figure 5 that the larger the values of the traction parameter, the greater is the slippage loss $\varepsilon/\varepsilon_f$. For example, if F_t/fW = .8, a total slippage loss of 4.26 occurs when the interface is moved out and back three contact widths. For example, if the traction load was 50 lb on a 1 inch wide roller, the slippage loss would be 38 μinch. Conversely, if the value of F_t/fW = .2, the slippage loss is .78, which represents only 7 μinch for this example loading. Since the smaller the loss, the more accurate would be the control, it is important to minimize the traction parameter. This is accomplished by making the normal load significantly higher than the traction load to be moved.

To further evaluate the effect of the traction parameters, the intercept (S = 0) values of $\varepsilon/\varepsilon_f$ are shown as a function of F_t/fW in Figure 6. The values of this intercept clearly increase linearly with tractions, F_t, which in itself suggests that F_t be held to a minimum. Perhaps even more significant is the manner the slope of the curves of Figure 5 increases with F_t. To show this effect, the steady state slopes (i.e. the slope where S > 1 with S increasing or S < 2 with S decreasing) are also plotted as a function of F_t/fW in Figure 6. At low values of the traction parameter, the slope increases linearly with F_t/fW. Further, at larger values of the traction parameter (F_t/fW>4) the slope increases monotonically. As F_t/fW approaches 1, it would be expected that the slope would approach infinity.

In any real translation mechanism, the traction load would be somewhat variable. Therefore, as the mechanism moves, any nonlinearities in the slippage could become a problem, and any prediction of the loss impossible. To minimize this problem, it is suggested that the value of the traction parameter be kept as small as possible, such as F_t/fW = .2. For very small values of F_t/fW, the loss could be approximated by

$$\varepsilon/\varepsilon_f = m(S/b - .5N_R) + (\varepsilon/\varepsilon_f)\text{intercept} \tag{7}$$

where N_R is the number of motion reversals.

A reasonable fit for the slope of the data in Figure 5 is:

$$m = .10417\ F_t/fW + .0417(F_t/fW)^2 + .6125(F_t/fW)^3 \tag{8}$$

and intercept

$$(\varepsilon/\varepsilon_f)i = .875\ F_t/fW \tag{9}$$

Prediction of $\varepsilon/\varepsilon_f$ after S = 6 with two reversals (N_R = 2) using equation 7 are given in Table 1, along with predictions using ATCON. It is apparent that the approximation is most valid for small values of F_t/fW, both in terms of absolute losses and in terms of relative

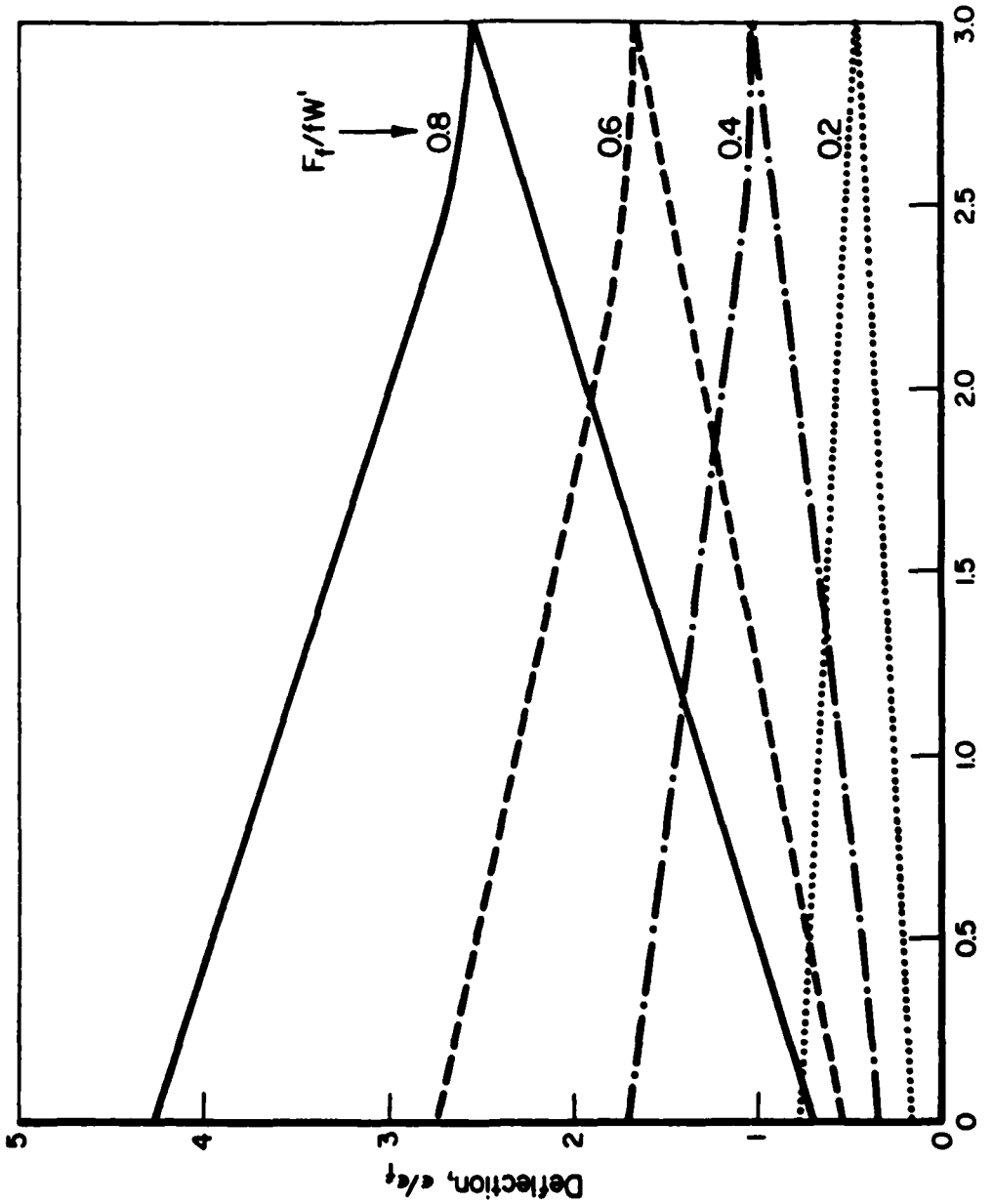

Figure 5. Effect of F_f/fW' on "Wind-Up" Losses

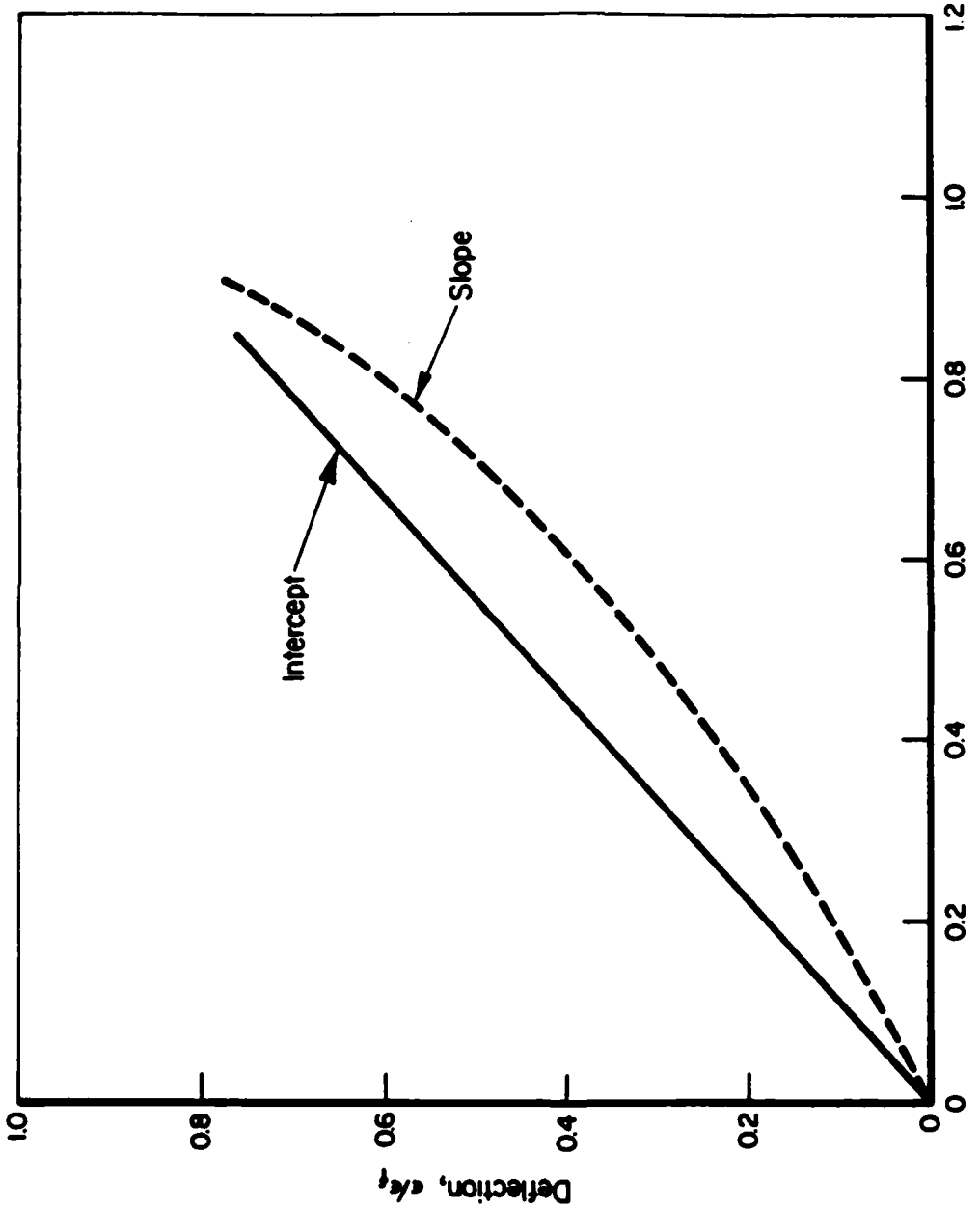

Figure 6. Effect of F_t/fW' on the slope and intercept of a loss function

losses, and that the most reasonable approximation can be obtained when $F_t/fW < .2$.

TABLE 1

F_t/fW	ATCON	Equation (7)	Error
.2	.78	.795	1.9%
.4	1.72	1.64	6.1%
.6	2.74	2.565	6.4%
.8	4.26	3.59	15.7%

Effect of Surface Coating

Soft surface coatings represent a good method to reduce contact and shear stresses for rough surfaces [13]. It would also be expected that coated cylinders would produce more consistent shear deflections by dampening asperity stresses. However, when the surface roughness is less than one microinch, the deflection patterns are quite similar to the patterns for mathematically smooth surfaces. Coatings, then, need only be used for extremely rough surfaces. Although use of the coatings produce smoother shear stress distributions between rough surfaces, there is a penalty.

Figure 7 shows the inelastic deflection loss curve for a coated and non-coated steel roller. If the coating is 100 μinch thick with a modulus of 290,000 psi, there is a marked expansion of the loss curve. If, however, a thinner (h = 10 μinch) coating of the same material is used, the loss curve is nearly identical to the curve for uncoated steel. As discussed in [13], a 10 μinch layer provides some reduction of the pressure spikes due to asperity loading. Also shown in Figure 7 is the effect of using a 100 μinch coating of a material with a higher modulus of elasticity (E = 2,900,000 psi). The effect of using this material in a 100 μinch coating is nearly identical to using a 10 μinch coating of the lower modulus material.

In general then, coatings on traction devices can be used without seriously altering the amount of slippage loss during translation of the drive. The level of protection and also the losses due to the coating is directly proportional to the coating thickness and inversely proportional to the modulus. The best compromise appears to be to use a very thin soft coating such as molybdenum disulfide or a moderately thick, harder coating such as zinc.

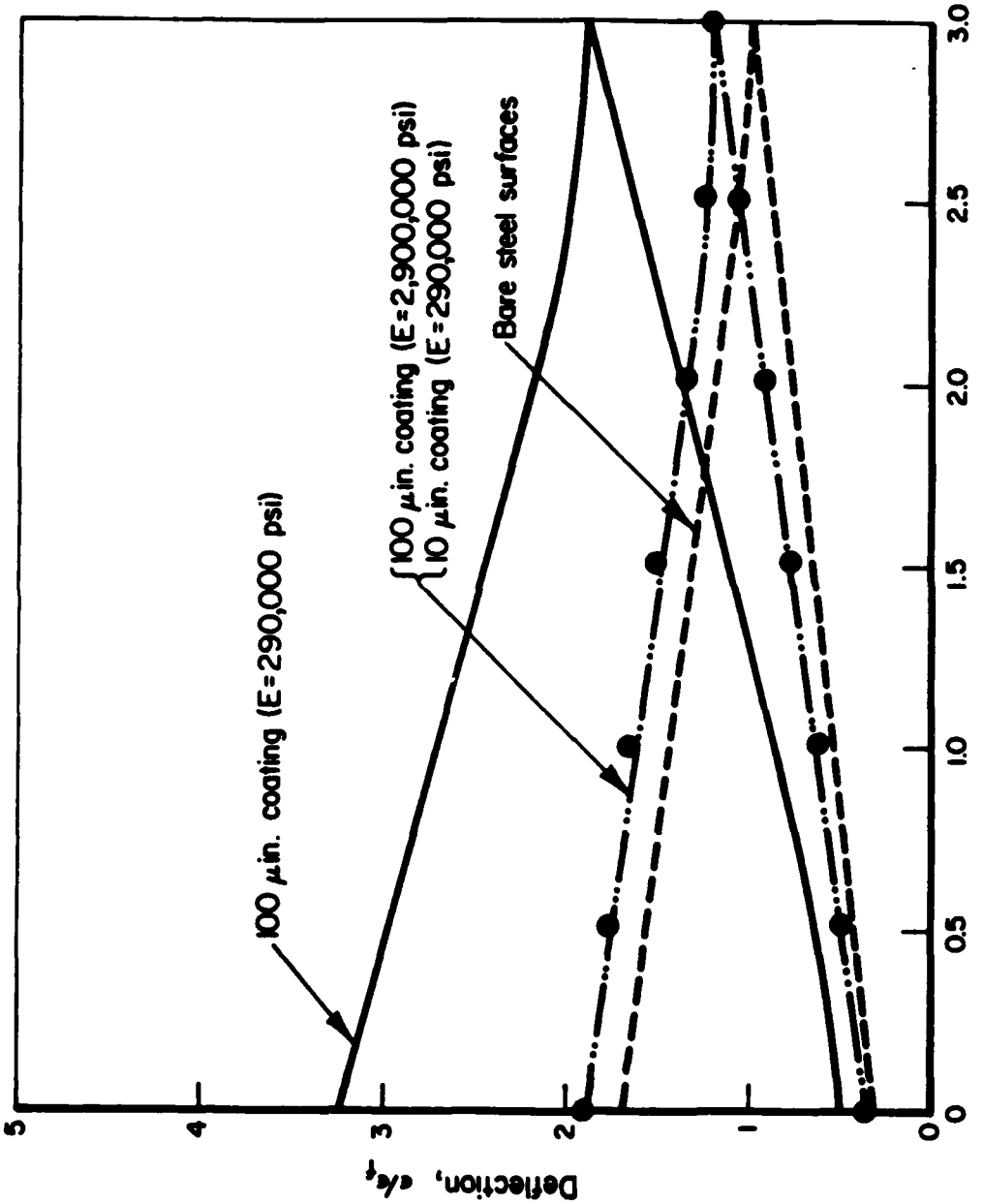

Figure 7. Effect of surface coating on inelastic "Wind-Up" ($F_t/fW' = .4$)

Effect of Surface Finish

Surface finish has been shown to affect the shear stress distribution between cylinders and therefore would be expected to alter the traction force and the inelastic losses. To explore the role of surface finish, a series of ATCON computer runs were made for steel-steel surfaces with various surface roughnesses; 0, 1, 3, 6 and 12 inch (cla). For each roughness the initial deflection was adjusted to produce a value of the traction parameter (F_t/fW) of .4. The cylinders were allowed to traverse three contact widths and return to the initial position.

Figure 8 shows the results of the surface finish evaluation. If the roughness is less than 3 μinch, roughness does not alter the traction behavior. Since a roughness of 3 μinch does considerably alter the pressure distribution, this insensitivity of traction to a roughness of this level is somewhat surprising. The explanation seems to be related to the fact that with a 3 μinch roughness the cylinders are essentially in complete contact. With the cylinders in complete contact, the surfaces will move as a continuum with very little localized slip.

At higher roughness levels some localized slippage will occur and the deflection predictions, considering rough surfaces, will deviate from the prediction considering smooth surfaces. When a roughness of 12 μinch is used in the computations, the predicted deflections are significantly different than the predictions considering smooth surfaces. It is interesting that a finish of 6 μinch only slightly alters the predicted deflection.

As discussed previously, the surface coatings can be used to neutralize the stress variations associated with surface roughness. Figure 9 shows predicted deflections where surface coatings as well as roughness is considered. For a 100 μinch surface layer with a modulus of 2.9 million psi, the increased deflection associated with a 6 μinch roughness is smaller than the increase associated with that roughness on bare steel surfaces as shown in Figure 8. At a roughness of 12 μinch the increased deflection is the same as with bare surface. Therefore, for certain roughness levels and coating parameters, the roughness dominates the traction, independent of the surface coating.

When the surface is coated with 100 inch of a softer film (E = .29million psi), the effect of surface roughness up to 6 μinch is negligible and even a 12 μinch roughness does not cause a large increase in deflection. Of course, the presence of a surface layer does increase the total deflection.

EXPERIMENTAL EVALUATION

Apparatus

The theory developed has been based on elasticity theory and can be assumed to be valid within the underlying assumptions. The earlier

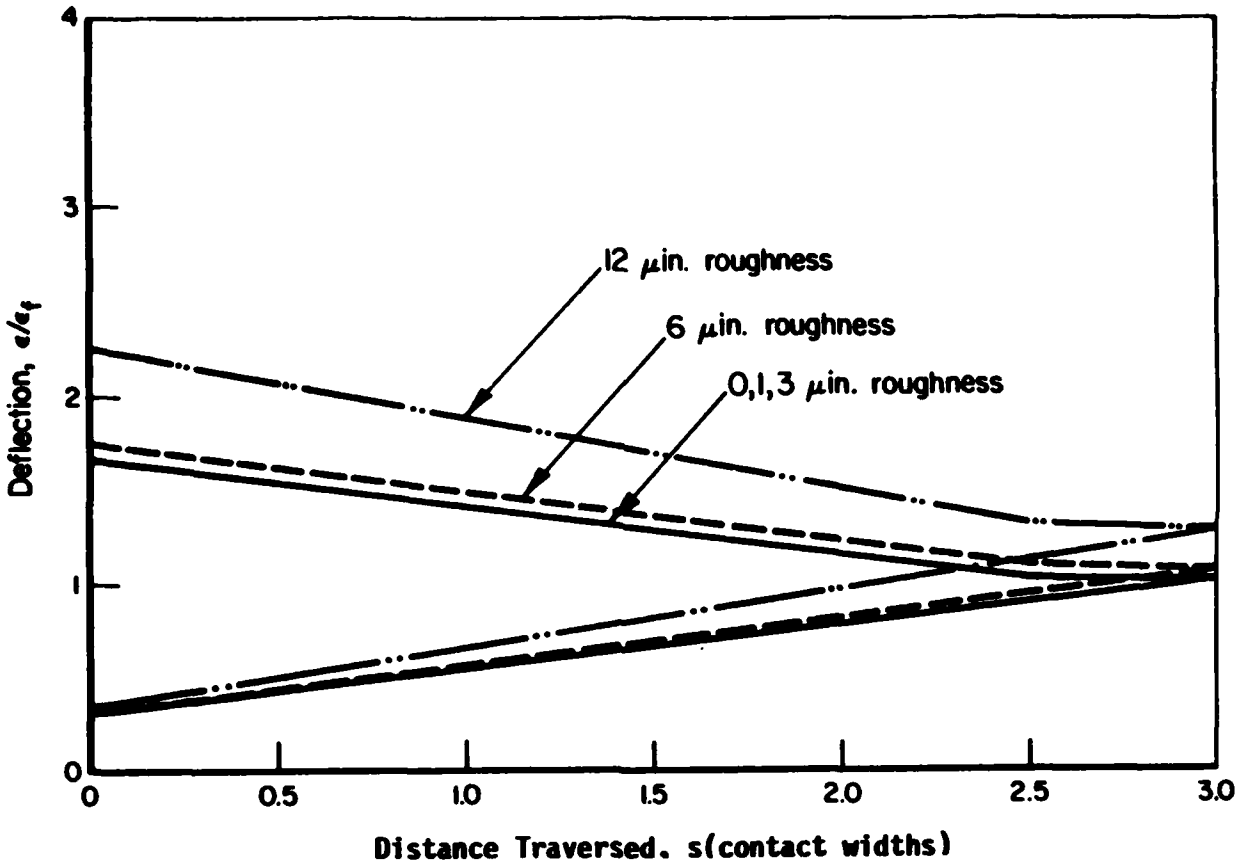

Figure 8. Effect of surface roughness on inelastic "Wind-Up" for steel cylinders

$F_t/fW' = .4$

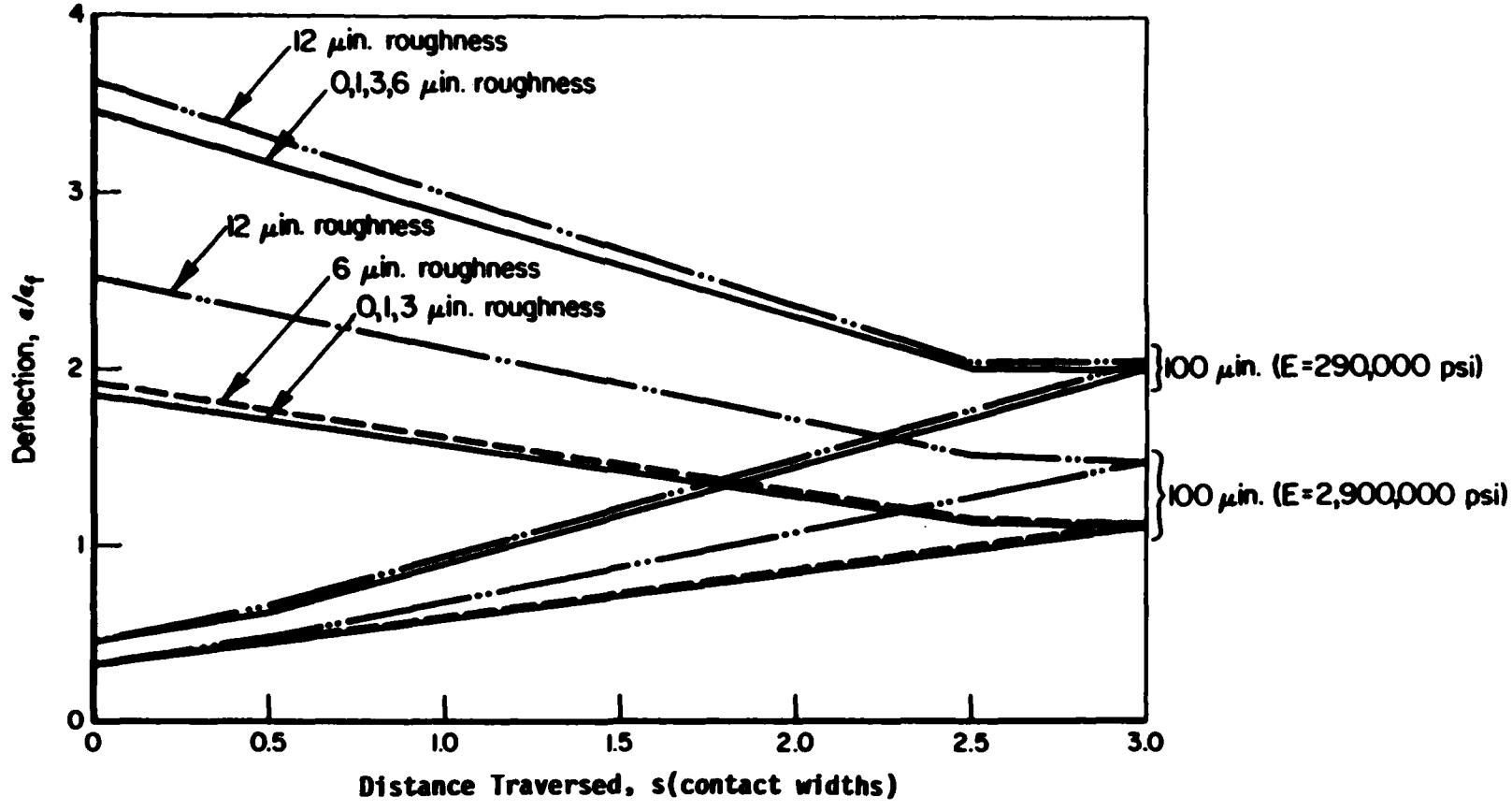

Figure 9. Effect of surface roughness on inelastic "Wind-Up" for coated cylinders

$F_t/fW' = .4$

sections have modeled the "wind-up" of the cylindrical interface relative to some point ten half-widths from the center of contact. The purpose of the experiment has been to corroborate the total "wind-up" of the interface. A drawing of the experimental apparatus is shown in Figure 10.

One cylinder (1.42 inch diameter) is loaded against a fixed cylinder (1.42 inch diameter), as in the "Carter" problem. Both cylinders are .25 inch wide but for some experiments the driving cylinder contained a 5.5 inch radius transverse crown to minimize alignment problems. The fixed cylinder is anchored by a plate with a cylindrical groove bolted to the support block. The driving cylinder is mounted in tight fitting bearings, 3/8 inches in diameter.

The fixed cylinder is mounted to a flexible plate which in turn is attached to a stiff crystal load cell. The cylinders are loaded by means of a loading screw arrangement. When the screw is turned, a load cell is wedged between the fixed cylinder and the spring plate. The load cell reads the loading on the fixed cylinder. Loads up to 1,000 lbs. are possible with this arrangement. In the experiment, the driving cylinder is rotated by a torsion load applied through a flexible arm. This load creates a "wind-up" of the interface between the two cylinders. The "wind-up" loading is detected by a crystal load cell. The motion of the interface is detected by eddy-current proximity probes with resolution in the micro inch range. One probe detects the rotation of the driving cylinder while the second probe detects the combined vertical movement of the two cylinders. The "wind-up" of the interface is rotation as referenced to the surface of the cylinder minus the translation.

Results of Experiments

Three types of experiments were conducted:

* uncoated cylinder on cylinder
* uncoated crowned roller on cylinder
* coated crowned roller on cylinder

It would be expected that the use of a crowned cylinder would not materially alter the "wind-up" deflection. Theoretically, "wind-up" is a function of the total tractive load and involves the entire width of the cylinder. However, it was important to experimentally substantiate these hypotheses. A crowned roller was used to minimize edge loading and coating scuffing.

The sequence for the experiments involved loading the cylinders radially with the loading nuts to of 500 lbs. (2,000 lb./in.). A series of torsional loadings and unloadings were required to obtain reproducible readings on the crystal load cell. The upper limit traction was fixed at 160 lbs./in. to reduce the possibility of gross slip at the interface. Note, the traction parameter was less than 0.27 for all conditions. This is consistent with "good" design practice for traction devices, as discussed earlier. In recording the data, the probe

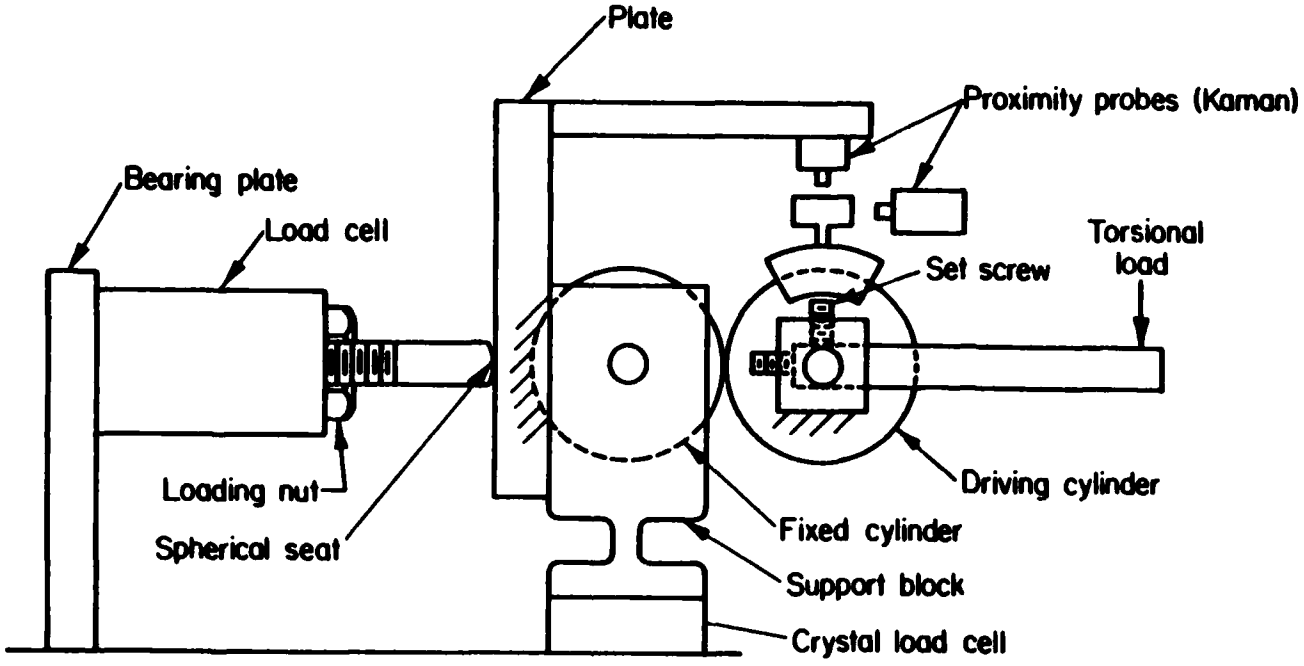

Figure 10. Concept for experimental evaluation

readings for zero traction were first recorded. Next torsional load was applied by a micrometer on a flexible beam until the required load was sensed by the crystal load cell. At the required load, the output from both probes was recorded. These outputs were analyzed in terms of contact zone tangential deflection.

The data recorded in the experiments are presented in Table II for each of the three sets of conditions. Also shown in Table II are theoretical predictions. In general, the agreement between theory and experiment is quite good. Actually, the best sequence was obtained in a test with a crowned roller against a flat cylinder with no coating. For this test, the agreement is very good and tends to confirm the theoretical predictions. When a coated cylinder was used, the measured deflections increased about 30 - 50% which is also consistent with the calculated values.

It should be noted that the primary purpose of the research has been to develop an analytical model of the traction interface. The objective of the experimental studies has been to substantiate the theory. Only a limited number of experiments were needed for this substantiation. However, more emperical research needs to be done to develop and understand precision traction drives. It is hoped that the research presented here can form the impetus for further work in this very important field of study.

TABLE II

Results of Shear-Deflection Experiments

Experimental Condition	Traction	Probe Output (μin.)		"Wind-Up" (μin.)	
	lb/in.	Horizontal	Vertical	Experimental	Theoretical
Cylinder on Cylinder (No Coating)	40	53	45.5	7.5	5.07
	80	105.5	89	16.5	10.1
	120	157.5	138	19.5	15.2
	160	211	188	23	20.3
Crowned Roller on Cylinder (No Coating)	40	50	45.5	4.5	5.07
	80	103	92	11	10.1
	120	156	140.5	15.5	15.2
	160	211	188.5	22.5	20.3
Crowned Roller on Cylinder (100 μinch MoS_2 Coating)	40	54	45	9	6.7
	80	107	87.5	19.5	13.3
	120	161	136	25	20
	160	213	180.5	32.5	27

REFERENCES

1. Bryan, J. B., "Design and Construction of an Ultraprecison 84 Inch Diamond Turning Machine," Precision Engineering, Vol. 1, No. 1, 1979, pp. 13-17.

2. Barkman, W. E., "Machine and Tool Drive System," Precision Engineering, Vol. 2, No. 3, 1980, pp. 141-146.

3. Kalker, J. J., "Transient Rolling Contact Phenomena," Trans. ASLE, Vol. 14, 1971, pp. 177-184.

4. Kaler, J. J., "Rolling With Slip and Spin in the Presence of Dry Friction," Wear, 9, 1966, pp. 20-38.

5. Cattaneo, C., "Ul Cantatto di du Corpi Elastici: Destribuzione Locale Degli Sfoizi," Red. Acad. Lincei, Ser. 6, Vol. 27, 19838, pp. 342-348, 434-436, 474-478.

6. Carter, F. W., "On the Action of a Locomotive Driving Wheel," Proc. Royal Soc., A 112, 1926, pp. 151-157.

7. Bentall, R. H. and K. L. Johnson, "Slip in the Rolling Contact of Two Dissimilar Elastic Rollers," J. Mech. Eng. Sci., Vol. 9, 1967, pp. 389-404.

8. Barber, J. R., "The Rolling Contact of Misaligned Elastic Cylinders," J. Mech. Eng. Sci., (I. Mech. E.) Vol. 22, No. 3, 1980, pp. 125-128.

9. Poritsky, H., "Stress and Deflections of Cylindrical Bodies in Contact with Application to Contact Gears and Locomotive Wheels," Trans. ASME, J. App. Mech., 1950, pp. 191-201.

10. Krause, H. and T. Senuma, "Investigation of the Influence Dynamic Forces on the Tribological Behavior of Bodies in Rolling/Sliding Contact With Particular Regard to Surface Corrugations," Trans. ASME, J. of Lub. Tech., 1981.

11. Sneddon, I. N., Fourier Transforms, McGraw-Hill Book Company, 1951.

12. Gupta, P. K. and J. A. Walowit, "Contact Stresses Between a Cylinder and a Layered Elastic Solid," Trans. ASME, J. of Lub. Tech., April 1974, pp. 250-257.

13. Kannel, J. W. and T. A. Dow, "Evaluation of Contact Stresses Between Rough-Elastic and Layered Cylinders," presented at Leeds-Lyon Tribology Symposium, Lyon, France; Aug. 1985.

14. Kannel, J. W. and T. A. Dow, "Analysis of Traction Forces in a Precision Traction Drive" ASME Paper 85-TRIB-45 to be published in the ASME Journal of Tribology in 1986.

15. Kannel, J. W. "Development of an Analytical Model for Traction between Cylinders" Ph.D. Thesis, N. C. State Univ., December 1985, Appendix A.

LASER INTERFEROMETRY

By

Dan Luttrell
Graduate Student
Precision Engineering Laboratory

And

Thomas A. Dow
Professor
Mechanical and Aerospace Engineering Department

ABSTRACT

Commercially manufactured laser interferometry systems are available with the capability of measuring linear displacement in the microinch range. However, these systems tend to be rather expensive and do not offer a means of rapidly transferring data such that the interferometer can be effectively used as a position sensor in real-time microposition control systems. To remedy this situation, modifications are currently being made to an existing low-cost laser interferometer that was built in the Precision Engineering Laboratory. Proposed improvements will facilitate set-up of the instrument for different experiments and enable the system to better interface with a microprocessor. Changes should also enable the interferometer to measure objects moving at rates up to 24 in./sec. with a resolution of approximately 3μin. and, by orienting the digital electronics section toward microprocessor operation, a micropositioning control system with this instrument as a position sensor could operate at a maximum sampling rate of approximately 300 kHz.

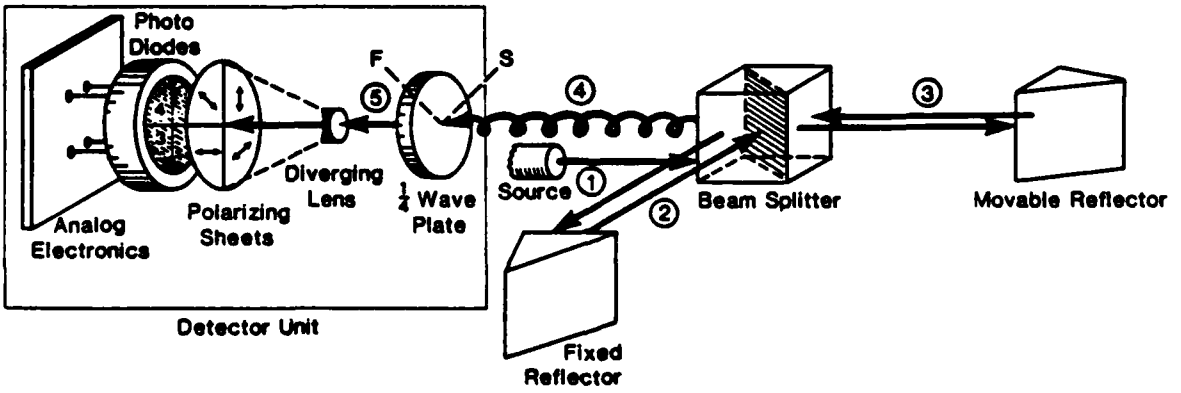

INTRODUCTION

A low cost laser interferometer for measuring linear displacement was previously built and tested in the Precision Engineering Laboratory and described in the first two Annual Reports. This interferometer was based on a concept developed at the National Bureau of Standards [1] and incorporated high speed digital components for necessary signal processing. Further development of this system is currently underway with several objectives that are motivated by other ongoing and proposed projects in the Laboratory.

Improvements to be made include mounting the laser source, interferometer optics, detector unit, electronics, and required power supplies in one unit. This will make the system easier to set-up and reduce alignment problems encountered with the original system. Redesign of the electronics has been made so the system will produce information that can be readily utilized by a microprocessor. This will enable the interferometer to operate as a position sensor in a high speed real-time micropositioning control system.

The basic interferometer operation, which does not differ significantly from that described in previous annual reports, is summarized below. The proposed modifications are then described along with anticipated results. Future plans for the interferometery system are also discussed.

INTERFEROMETER SYSTEM DESCRIPTION

Operation of the interferometer is based on a Michelson-type interferometer using a linearly polarized HeNe laser as the light source (see Figure 1). The laser's polarization is oriented 45^{o} from horizontal so that the polarizing beam-splitter divides the laser beam into a horizontal and vertical component of equal magnitude. The vertical component is returned to the beam-splitter along a fixed path through a fixed retroreflector mounted on the side of the beam-splitter. This vertical beam serves as the reference beam. The horizontal component is returned to the beam-splitter by the moveable retroreflector whose position is being measured. These two components recombine in the beam-splitter and the resulting beam consists of two orthogonally polarized components each of which contain information about the length of one arm of the interferometer. The combined beam then enters the detector unit.

Since the length of each arm is different, the horizontal component will be phase shifted relative to the fixed vertical component. When the combined beam is examined one does not see the two individual waves but the result of superpositioning the two components. Depending on the amount of phase shift present, the resultant beam exhibits different states of polarization. When the two components are precisely in phase or 180^{o} out of phase, the resultant is linearly polarized with the plane of polarization oriented 45^{o} from the plane of the components. When the two components are 90^{o} or 270^{o} out of phase, the resultant is circularly polarized. When the two individual waves are neither precisely in phase

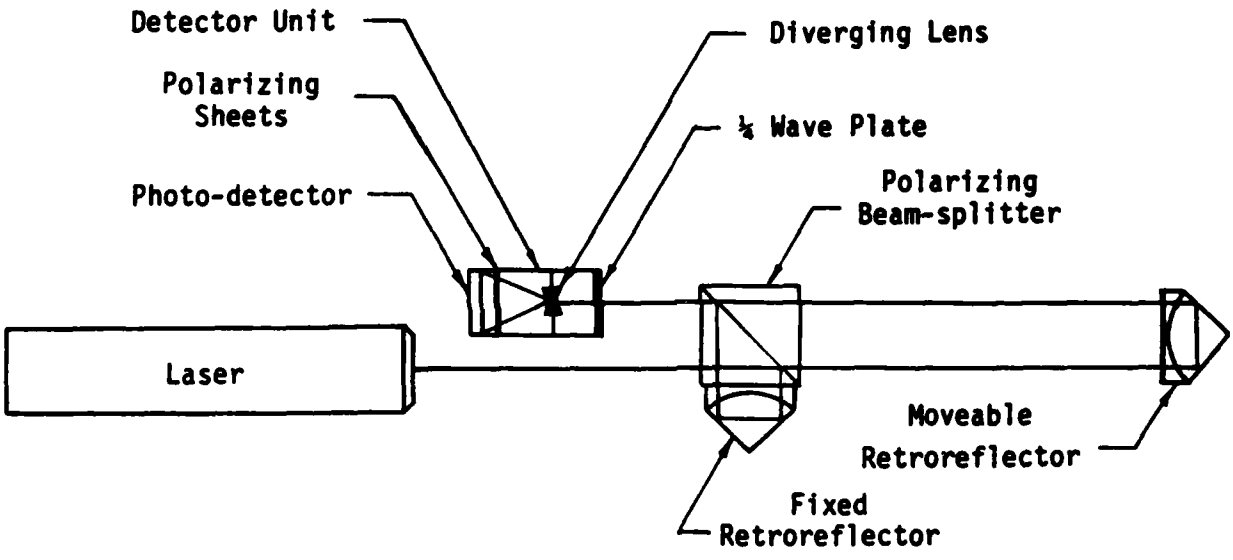

Figure 1. Interferometer operation

nor out of phase by 90°, 180°, or 270°, polarization of the resultant is a combination of linear and circular polarization; i. e. elliptical polarization. Figure 2 illustrates graphically the several types of polarized resultants.

The first component of the detector unit is a 1/4 wave plate. This plate has its optical axis oriented such that a linearly polarized beam which is 45° from the horizontal passes through the plate unchanged and a circularly polarized beam is converted to a linearly polarized beam. The combined beam can have four possible states of linear polarization depending on the phase shift between the two components. The four possible states of polarization are oriented 45° relative to each other as shown in Figure 3. After the 1/4 wave plate this resultant beam is expanded by a diverging lens so that it impinges on a quad photo-detector. Each of the four quadrants on the photo-detector has a sheet of polarizing material mounted in front of it. The polarized directions of the sheets are oriented 45° relative to each other to match the four possible states of linear polarization of the impinging beam. The result of this arrangement is a device that detects a phase shift between the two components of the beam entering the detector unit.

As the phase angle between the two individual waves changes, the state of polarization appears to rotate as shown in Figure 3. The direction of rotation depends on whether the measured arm of the interferometer is getting longer or shorter. The distance traveled by the horizontal component in the measured arm of the interferometer is twice the distance the moving retroreflector travels. Therefore, a phase shift of 90°, or 1/4 of a wave length, corresponds to the moving retroreflector traveling half that distance or 1/8 of a wave length. When the moving retroreflector translates a distance equal to 1/8 of a wave, the state of polarization rotates from one state to the next, the direction of rotation being determined by the direction of movement. Since the wave length of HeNe laser is approximately 632.9 nm, the resolution of this interferometer is about 3μin.

Signals generated by the photo-detector when the state of polarization changes are translated by the electronics to relative position information. The digital portion of the interferometer counts the number of polarization changes as seen by the photodetectors and also determines the direction of movement. It is in this section of the instrument that modifications are being made which will enable the interferometer to measure objects moving a higher rates and better interface with a microprocessor.

Proposed Modifications

The first planned modification of this system is to mount all components of the interferometer, except the moving retroreflector, in one unit. The laser source, optics, detector unit, electronics, and power supplies will all be mounted on a common platform (see Figure 4). This is to make the instrument easier to set-up as well as reduce the amount of time required for alignment each time it is relocated. Once

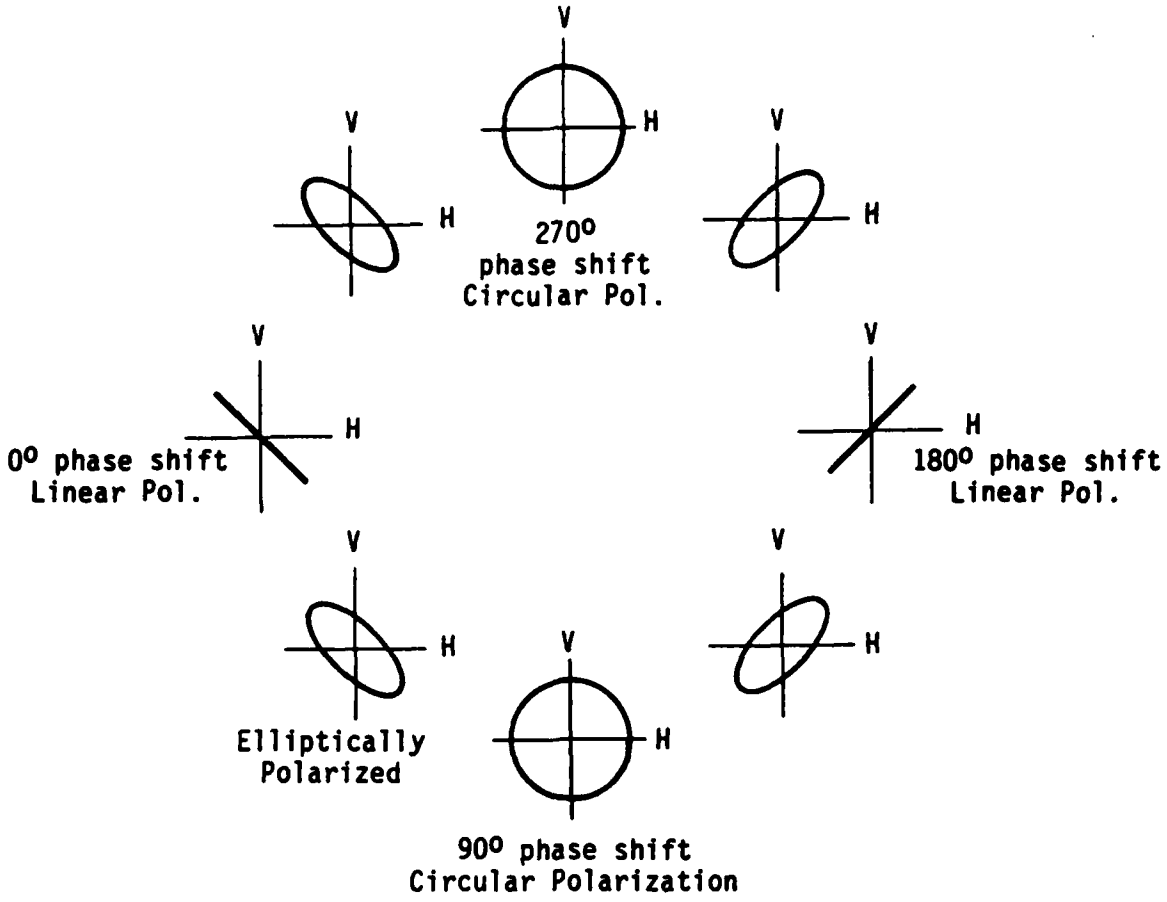

Figure 2. States of polarization

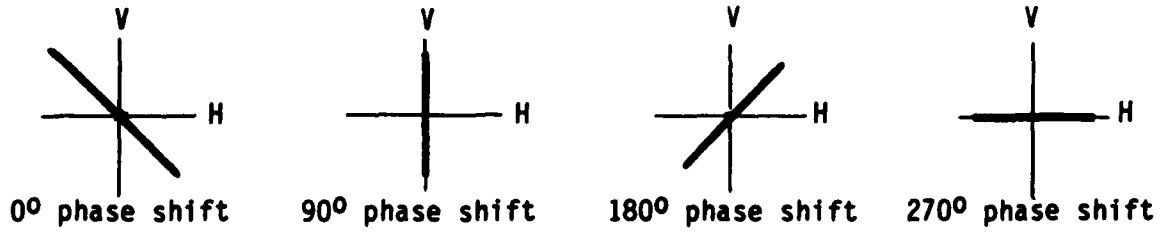

Figure 3. State of polarization after ¼ wave plate

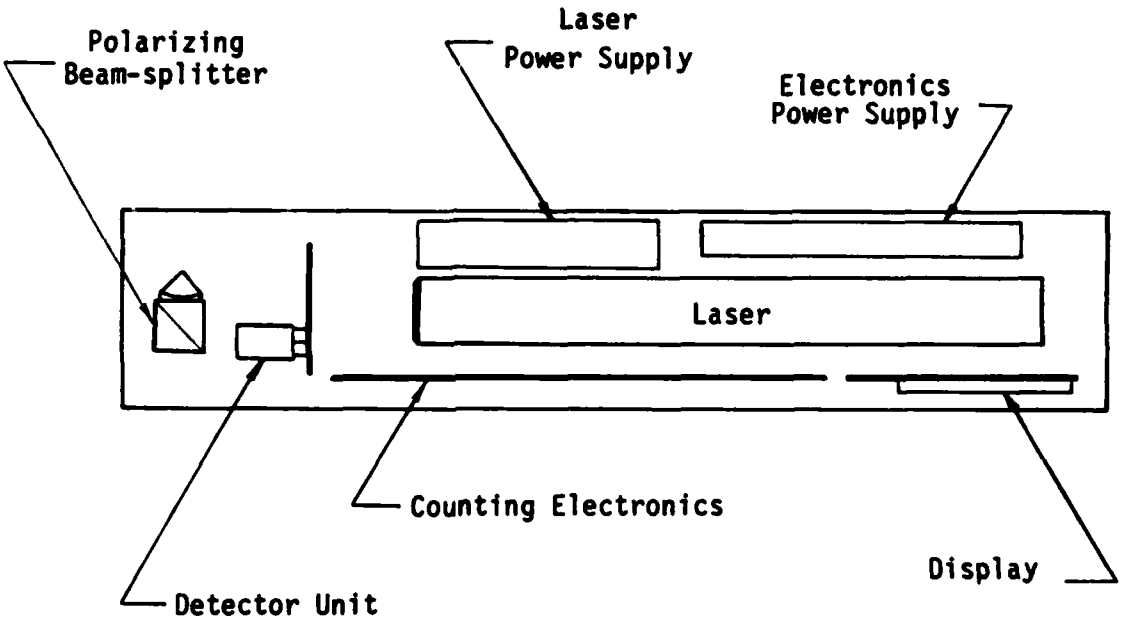

Figure 4. Proposed Interferometer Layout

the laser, interferometer cube, and detector unit have been aligned relative to each other, the only alignment required during set-up will be the overall unit with respect to the moving retroreflector. Alignment was one of the major problems encountered with the original mechanical design.

Another improvement planned for this system will enable the instrument to measure objects moving at a higher rate. The speed of the original system was limited by the device that counted signals from the detector unit and drove the display. The counting electronics will be made independent of the display device. Since the counting electronics can operate at much higher speeds than the photodetector can generate signals, the photodetector will become the limiting device. Slew rates as high as 24 in./sec. can be obtained with these changes. The numerical display is also being changed to a liquid crystal type. This is being done because these device operate at a fraction of the power required by LED's. This reduces the size of the power supply required which is an important consideration when integrating all components into one package.

A separate counting circuit has been designed to generate position information that can be readily accessed by a microprocessor. The position information will be available in a parallel binary form which can be read by microprocessors using a minimum number of instructions. For example, one proposed project at the laboratory would use a signal processing chip that can read and store 16 bits of information in 400 nsec. If the time required to produce a second order control signal is 3.0 μsec. then a control system with this interferometer as a position sensor could operate at a maximum sampling rate of about 300 kHz.

Discussion

The reason for designing a special counting electronics section to interface with a computer is to integrate the interferometer into a real-time micropositioning control system. The interface has been designed to operate with a 16 bit microprocessor that will handle whatever digital control algorithm needed for a given control task. The objective here is to reduce the amount of time required for the control computer to gather position information in a form that can be readily used. In this process, better methods of interfacing measurement sensors with the computers that perform the control calculations will be developed.

Once these improvements are made, this instrument will serve as a basis for further development work in non-contact position sensors in the Precision Engineering Laboratory. There are other methods available to detect the phase shift described earlier which offer the possibility of better resolution with the same high slew rate possible with the present detector [2]. More interesting and perhaps more useful would be the development of position or angular displacement sensors that use fiber optic cables. It has been shown that optical fiber sensors offer

approaches to metrology that have many advantages over other techniques [3]. This instrument could serve as a useful tool in the development of such a sensor.

REFERENCES

1. Dorsey, A., R. J. Hocken, and M. Horowitz, "A low Cost Laser Interferometer System for Machine Tool Applications," Precision Engineering, Vol. 5, 1983, pp. 29-31.

2. Smythe, R. and R. Moore, "Instantaneous Phase Measuring Interferometry," Optical Engineering, Vol. 23, 1984, pp. 361-364.

3. Johnson, M., "Fiber Displacement Sensors for Metrology and Control," Optical Engineering, Vol. 24, 1985, pp. 961-965.

SECTION 2. REAL-TIME CONTROL

DEVELOPMENT OF HIGH-SPEED MICROINCH POSITIONING LINEAR STAGE

By

James B. Gleeson*
Graduate Student
Precision Engineering Laboratory

And

Charles C. LeVay
Research Engineer
Precision Engineering Laboratory

And

Thomas A. Dow
Professor
Mechanical & Aerospace Engineering Department

ABSTRACT

Static and dynamic response tests have been conducted using a linear stage with a two-tiered actuation system: a stepper-motor driven lead screw for large displacements and a piezoelectric actuator for fine adjustment and control of dynamic errors. The position feedback to the control system is via a laser interferometer which operates with both actuation systems. Real-time control algorithms have been implemented using a DEC PDP-11/23 computer as the controller. The results of the experiments indicate the system can position the stage at up to 10 in./sec. translation speed to an accuracy of ±1 laser count (± 6 microinches). Whereas the piezoelectric actuator has been shown to reduce the dynamic overshoot of the stage it cannot completely eliminate the need for a setting time to produce microinch positioning accuracy.

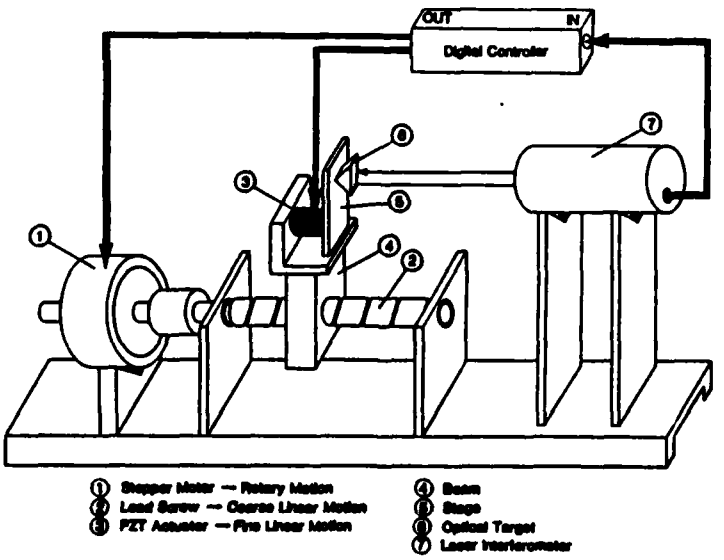

*Currently employed at Battelle's Columbus Laboratories, Columbus, Ohio

INTRODUCTION

One problem in precision engineering is that of obtaining fast, accurate, linear translation of a stage or slideway. Typically, trade-offs must be made between the speed and the precision of the linear motion.

To study the problems and limitations of a linear translation stage, the Precision Engineering Laboratory has designed and built a two level actuation system incorporating a stepper motor driven ball screw which horizontally translates a stage. Mounted on the stage is a piezoelectrically driven cantilever beam. The linear motion of this system is regulated by a microprocessor based control algorithm which takes its input from a linear interferometer (Figure 1).

The microinch positioning stage was designed to produce fast, precise single-axis translation. The basic approach toward achieving precision is to correct a lead screw drive by utilizing real-time control feedback. A piezoelectric transducer (PZT) mounted on the stage displaces a beam in a direction parallel to the axis of the lead screw. The position of the beam is the controlled variable, and is measured with a laser interferometer. The output of the interferometer provides both a feedback signal and a measure of the accuracy of the controlled motion.

The objective outlined for this experiment is to obtain linear translation over a range of 12 inches, with a tolerance of $\pm$ 6 microinches, with no overshoot. Additionally, it is desired to achieve a maximum velocity of 10 in./sec. for this translation.

MECHANICAL STAGE DESIGN FEATURES

To attain system repeatability on the order of microinches it was necessary to minimize sources of mechanical errors; e.g. roll, pitch, and yaw (which create Abbe offset errors), stiction, thermal stability, and shaft or screw misalignment. Specific construction features were used to control these variables.

* The steel base sections were ground parallel before and after assembly
* the rail and ball screw supports were pinned and then simultaneously machined and ground to control parallel misalignments
* linear bearing rails were specified with less than .0005 in./ft. straightness and sized for a maximum deflection 160 µin.
* self aligning linear bearings with adjustable preload were used to reduce stick/slip and stage skewing.
* a "zero backlash" single preloaded ballnut was used
* a duplex thrust bearing arrangement achieved zero ball screw axial play
* a flexured steel coupling allows limited shaft and angular misalignments with zero backlash

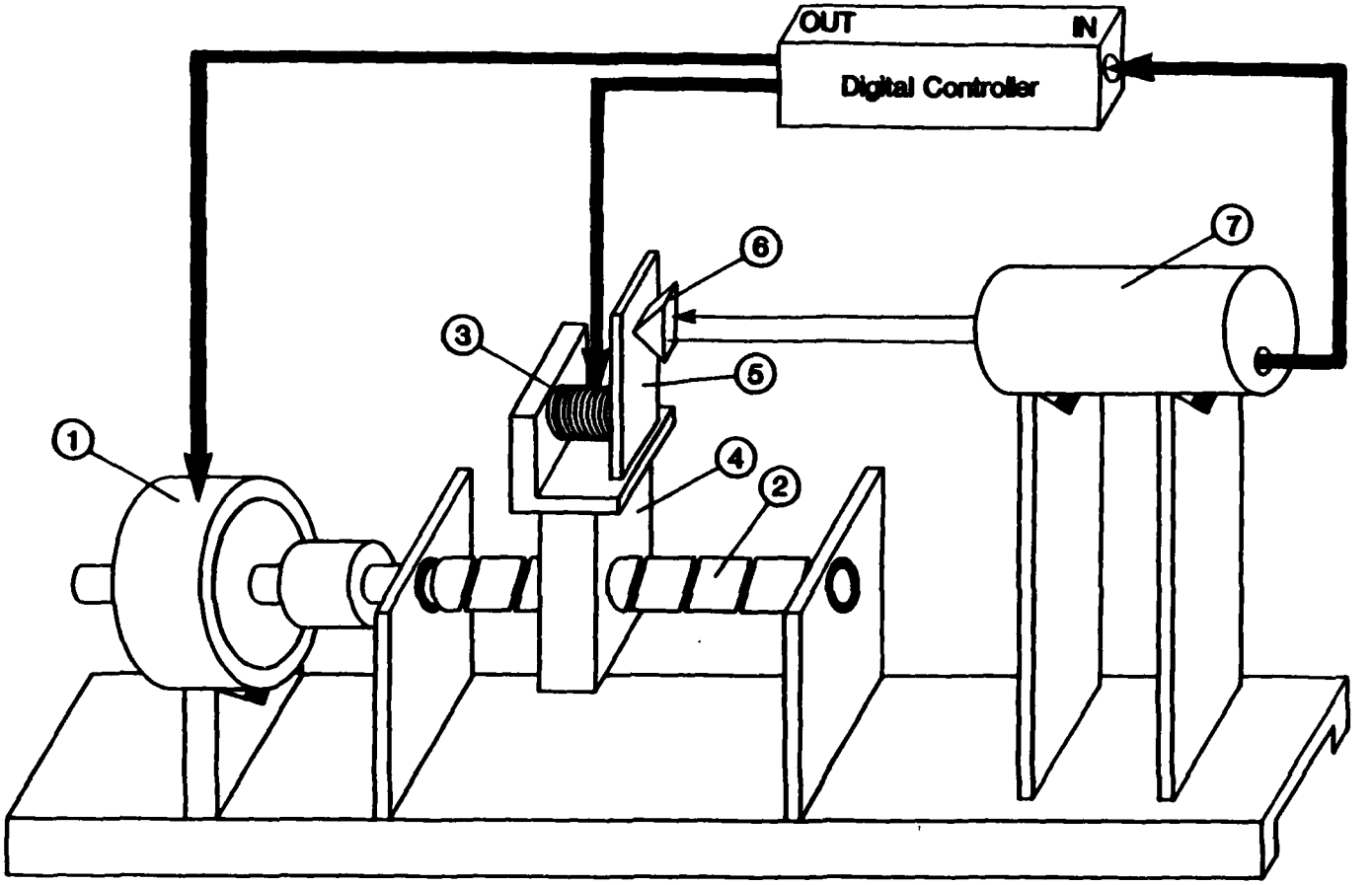

① Stepper Motor → Rotary Motion
② Lead Screw → Coarse Linear Motion
③ PZT Actuator → Fine Linear Motion
④ Beam
⑤ Stage
⑥ Optical Target
⑦ Laser Interferometer

Figure 1 Microinch positioning stage schematic

* an extruded aluminum heat sink and a mylar shim limit heat transfer from the stepper motor to the stage base

Selection of the ball screw involved matching the stepper motor angular resolution (steps/rev.) and the screw pitch (thread/in.) to obtain a coarse motion resolution within the 200 μin. range of the PZT actuator and the ability to slew the stage table at 10 in./sec. These constraints also limited the acceptable lead accuracy and shaft critical speed. A .551 in. (14 mm) ball screw with a .315 in. (8 mm) lead, 90% efficiency, 13.8 in. (350 mm) stroke, and calculated critical speed of 5000 RPM was chosen. The published accuracy specifications for the screw are:

* mean travel deviation	.0010 in./ft.
* maximum width of variation	.0008 in./ft.
* wobble error	.003 in./rev.

These ball screw inaccuracies dominate the system's mechanical errors, e.g. the wobble error is an order of magnitude greater than the backlash. The design concept accounts for these travel deviations by utilizing closed loop control of both actuators, but the magnitude of the maximum deviation must be known to implement an efficient control scheme.

The systematic travel deviation of the precision translation stage was calibrated using an Hewett Packard 5501A laser interferometer as a standard reference. The assembled stage was moved unidirectionally, quasistatically, and at intervals of 4 full steps (1/50 revolution). This procedure maintained the maximum repeatability of the stepper motor and limited the resultant errors to combined ball screw inaccuracies and Abbe offset errors. Figure 2 is a plot of the lead screw calibration data. The travel length is the reference laser interferometer output and the lead deviation is calculated as the theoretical displacement minus the actual reference position. Referring to Figure 2, the screw calibration curve indicates a maximum lead deviation of 0.002 inch with a superimposed once per revolution deviation (wobble error) of 100 microinches.

SYSTEM RESPONSE

The first test of the precision translation stage involved the stage response to open loop stepper motor actuation. The stepper motor controller was programmed to operate in its highest resolution mode, 25600 steps per revolution, which produced via the ball screw a 12.3 μinch/step translation of the stage. An eddy current probe, mounted on the vibration isolation table near the front of the beam, was used to measure the relative motion of the stage. Figure 3(a) is the stage response to a single step (of the stepping motor). The maximum displacement of the stage was 12.4 μin. and the 220 Hz. oscillation stabilized at a net 7 μin. displacement, and error of 5 in. This position error is due primarily to elastic windup of the ball contacts in the ball nut and the linear bearings. Figure 3(b) is the stage

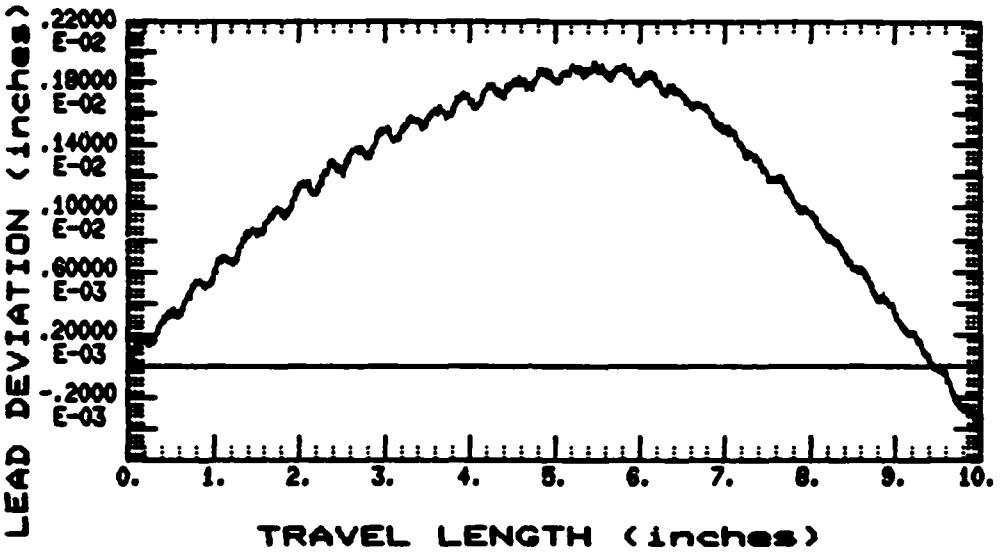

Figure 2 Ball Screw Calibration
(*Deviation = Theoretical Displacement - Actual Position)

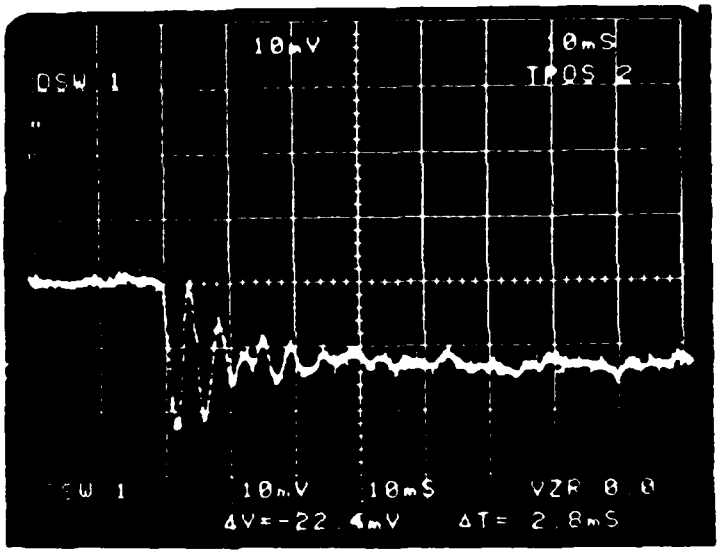

Figure 3(a). Single Step Response of Stage
vertical scale: 10 mV = 5.3 µin.

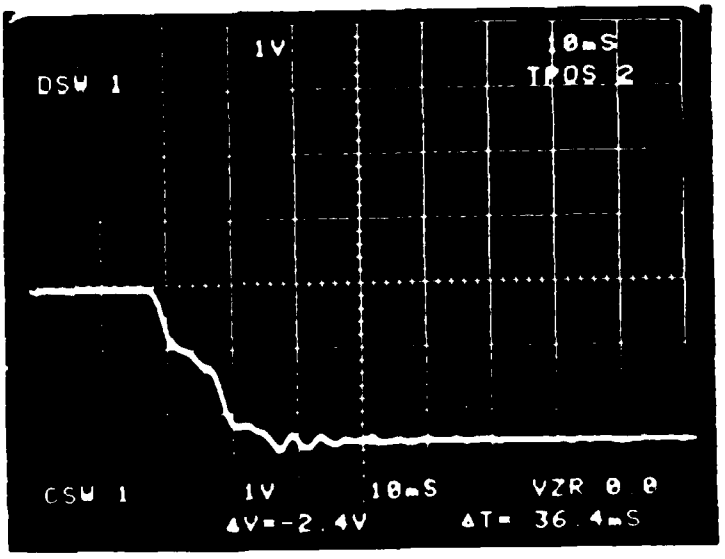

Figure 3(b). 100 Step Response of Stage
vertical scale: 1 V = 533 µin.

Figure 3. Open loop response of the stepper motor driven lead screw

response to a 100 step input, which theoretically should command a 1230 μinch displacement. The end of this motion has a response similar to the single step test and finally stabilized at a displacement of 1280 μinch. The 50 μin. position error is primarily due to the lead screw wobble error, and to a lesser degree the ball nut loading.

The frequency response of the assembled precision translation stage was experimentally determined. An accelerometer was mounted on the stage and on the beam. This information identified several low frequency responses (below 650 Hz.) associated with the stepper motor/ball screw drive system and high frequency responses (above 3 kHz.) related to the stage supports and th PZT actuator assembly (beam). The frequency and amplitude of the displacement response can be seen in the step response traces (Figure 3). In all cases, an oscillatory displacement at approximately 200 Hz. is dominant, and some lower amplitude and frequency beats were also observed. A goal of this study was to use feedback and electromechanical compensation to offset these oscillations that are, in effect, dynamic position errors. Because the PZT actuator is not excited by these low frequency inputs, then it should be possible to effectively nullified these dynamic position errors using an opposing motion of the PZT.

Steady State Response

The accuracy of the precision translation stage is limited by the resolution of the laser interferometer. The HP 5501A can be used in two modes: A high speed mode, which has a maximum velocity of 12 in./sec. and a resolution of 6 μin. (6 μin. = 1/4 HeNe wavelength = 1 laser count), and an extended resolution mode where the maximum velocity and the resolution are reduced by a factor of 10. The feedback is always a multiple of laser counts -- in contrast the desired position is rarely an even multiple of laser counts. It follows then that the position error (DELTA = desired position - feedback position) will always include some fractional laser count inaccuracy. Hence the desired position can be achieved only within a 6 μin. range at high speed or 0.6 μin. at low speed.

In addition to the feedback resolution, the control cycle time and the maximum PZT/amplifier response are important considerations in the development of the PZT control loop. To achieve adequate computer through-put, the PZT control loop must be very efficient; i.e. minimize the number of computations, especially IF statements and intrinsic functions.

Proportional, bang-bang and integral control of the PZT loop have been implemented. With proportional control, corrective action is taken which is proportional to the feedback error. Proportional control of the PZT loop cycled at 880 Hz. and therefore had marginal potential for dynamic compensation. In contrast the simpler program for bang-bang control cycled at 1800 Hz. and was more effective. Bang-bang control is an approach which involves the strategic switching of maximum corrective actions. For this system the maximum corrective action is limited by

the combined PZT/amplifier response, which was approximately 10 μin. per step. The integral controller cycled at 6000 Hz. The high-speed was mainly due to the fact that this algorithm was implemented in machine language. Each control approach, has merits which are demonstrated by their affect on steady state position.

The steady state position describes the position of the beam after a move and allowing the dynamic oscillations to equilibrate. Figure 4(a) is an example of the steady state position envelope using proportional control. The top trace is the computer D/A output (unfiltered) to control the PZT/amplifier. One important characteristic of proportional control is that a sustained disturbance to the system will produce a steady state error. The fractional laser count inaccuracy in the position error (DELTA) is equivalent to a continuous input disturbance and the resulting steady state error produces an oscillation about the target position. The bottom trace is the steady state motion of the beam which mimics the output control signal (top trace). The envelope establishes the range of the beam position, which is less than 7 μin., which is approximately 1 laser counter.

Figure 4(b) is an example of steady state position using bang-bang control. The top trace is the computer D/A output which is low-pass filtered at 2 kHz and input to the PZT/amplifier. Again the bottom trace is the steady state motion of the beam which mimics the output control signal. For this case the range of beam motion is 17 μin. The increase in motion, as compared to the proportional steady state response, is primarily due to a phase lag in the PZT actuation. Comparison of the maximum points of the output signal (top trace) and the beam position (bottom trace) produces a difference of 1.5 control steps.

The integral controller was implemented for the high resolution laser output (1 count = 0.6 μin.) to determine the best steady state performance. A comparison of the end of travel positioning using this system with the PZT and the stepper motor above is shown in Figure 5. The desired position and the position achieved using the motor/PZT are within 1 microinch whereas the motor only is about 13 microinches from the desired position.

The system response to low frequency loading was examined by slowly applying a one pound load to the stage and measuring the effectiveness of the PZT position correction scheme. Figure 6 pictures the beam displacement during the quasistatic loading. In the top trace with no PZT control, the beam had a maximum deflection of 110 μin. The bottom trace represents similar loading of the beam with proportional control of the PZT. Here the maximum change in position was 8 μin. This correction of positional errors resulting from external loading is an important attribute of the precision translation stage.

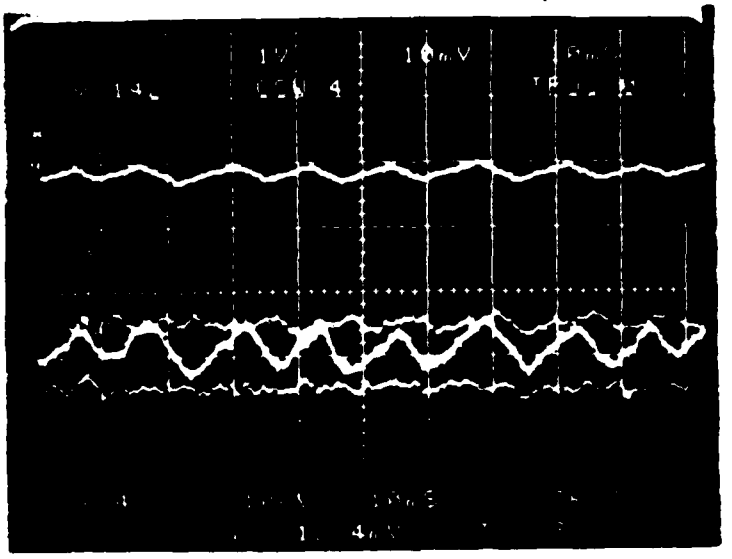

4(a). Steady State Position - Proportional Control
(top) computer D/A output
(bottom) beam position; 10 mV = 5.3 µin.

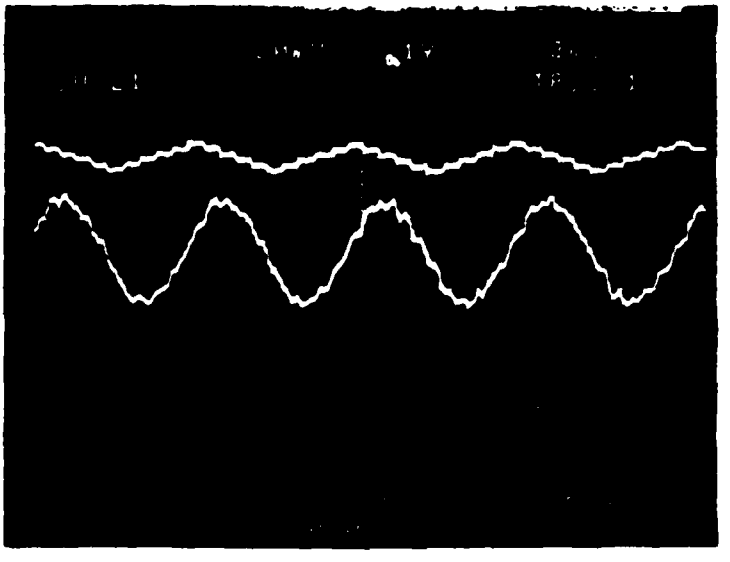

4(b). Steady State Position - Bang-Bang Control
(top) computer D/A output
(bottom) beam position; 20 mV = 10.6 µin.

Figure 4. Stead-state positioning using laser interferometer in high-speed mode

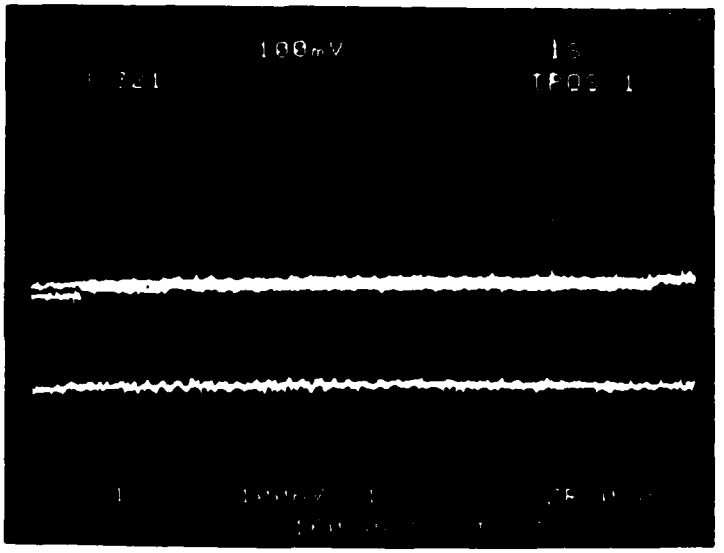

Figure 5. Steady-state positioning of stage using laser interferometer in high resolution mode

Center - Desired position
Center - PZT/motor controlled position
Lower - Positioning with motor only

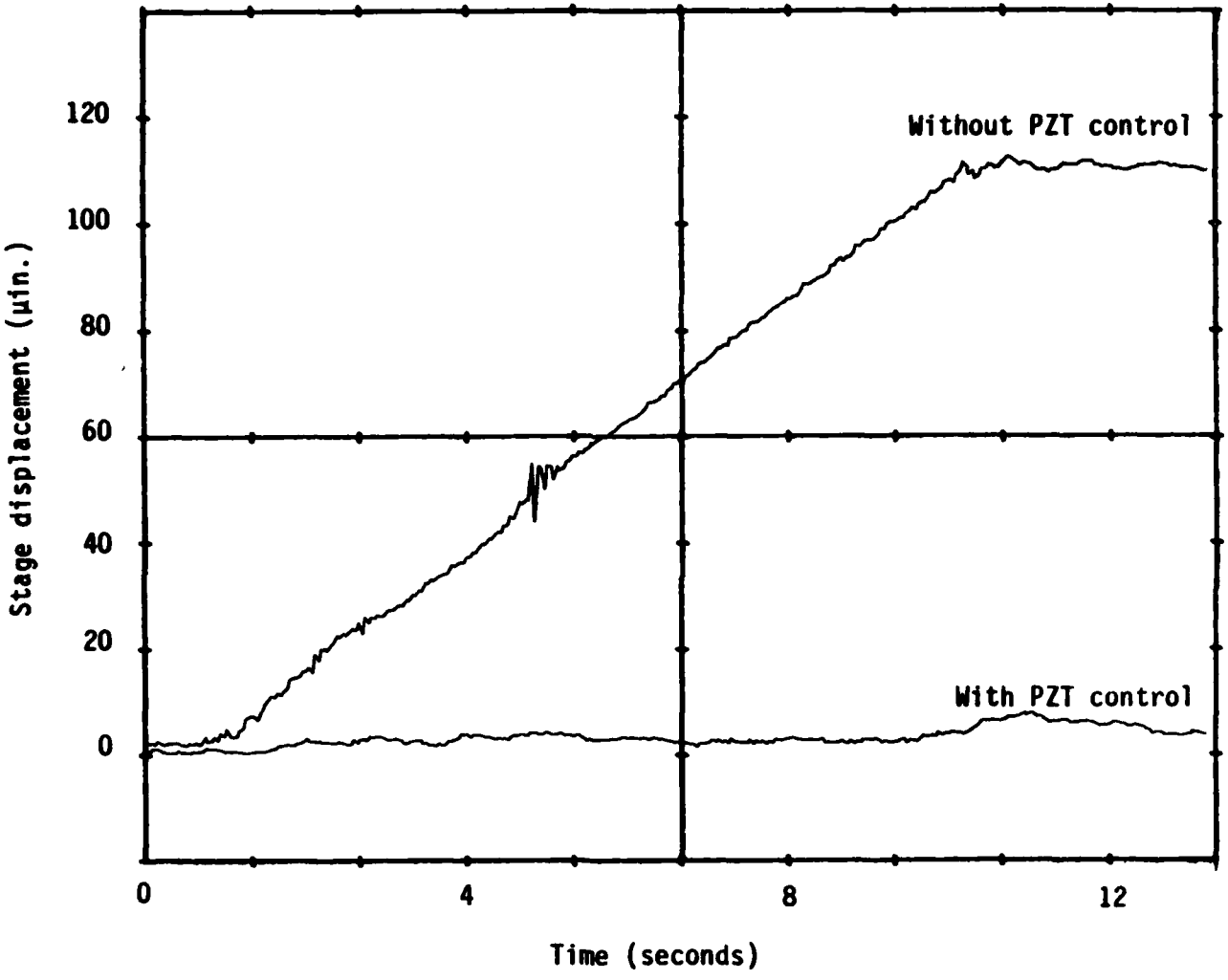

Figure 6. Quasistatic loading of beam

Dynamic Characteristics

Typical lead screw applications require a compromise between speed and accuracy. Translation speed is directly related to the lead (inches/rev.) of the screw whereas the position resolution is inversely proportional to the lead. High speed translation introduces an exponential increase in inertial effects resulting in larger overshoot and settling time. An objective of the precision translation stage was to combine both high speed and high accuracy -- by utilizing real-time control feedback to the PZT.

The "end of motion" profiles describe the response of the beam whose position is what ultimately is to be controlled by the system. To establish the stopping response characteristics and the extent of PZT compensation three cases of end of move response were examined:

1. open loop - no feedback
2. control around stepper motor only
3. control with stepper motor and PZT

In the first case the stage is moved to a position defined by the theoretical travel of the screw. The actual stage position will be a superposition of the lead deviation and the open loop end of move response. Hence the stopping characteristics consist of an absolute position error, overshoot and dynamic system response. Figure 7 demonstrates the open-loop dynamic stopping response. The response shown is at the end of a 9.5 inch move. After many trials the end of move dynamics was found to fall into one of these very repeatable cases. The marked difference in amplitude response is attributed to a change in the stepper motor holding torque. The equivalent spring rate of the motor is a function of the holding torque, therefore both characteristics vary significantly with the fractional rotor position (microstep) between stator poles. The worst case of overshoot is 64 μin. A characteristic 200 Hz. oscillatory response was always observed with a natural decay in amplitude.

In Figure 8 the stage is moved to the desired position using interferometric feedback to the stepper motor. The motor is controlled in its highest microstep mode which translates into a minimum step size of 12.3 μin. The controlling program (for stepper motor only actuation) had a short delay to allow dampening of the dynamic oscillations before allowing position correction. This can be seen in the middle of the trace where 50 msec. after the end of the "previous" move the stepper motor indexes 3 or 4 microsteps to the correct position. The maximum overshoot for the case 2 tests was 48 μin. and the respective higher amplitude oscillations result from the higher velocity "previous move." The response oscillations were similar to that of Figure 7.

PZT correction is added to the control scheme in Figure 9. The oscillatory behavior of the stage is superimposed on the PZT correction which moves the beam in response to the laser feedback. The PZT is operated in a bang-bang control scheme, cycling at 1.8 kHz. and can displace the PZT 3 μin. per cycle. Note that after 20 msec. the

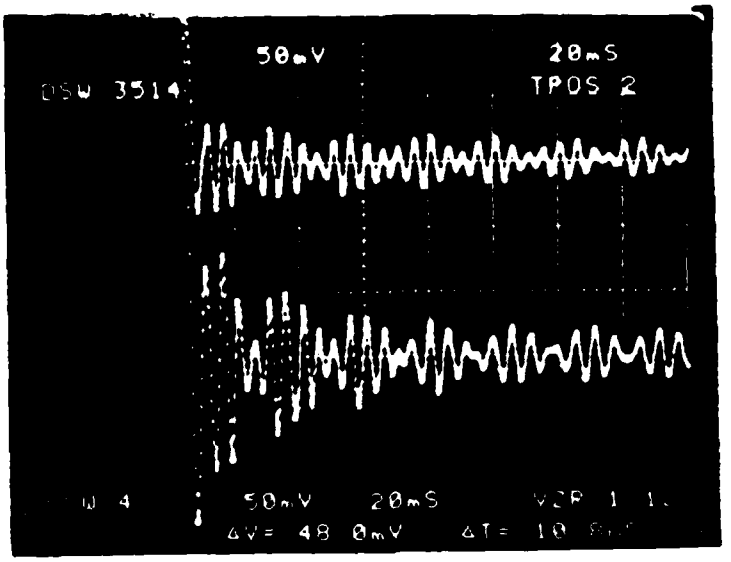

Figure 7. Case 1 Stopping Response
open loop - no feedback
vertical scale: 50 mV = 27 μin.

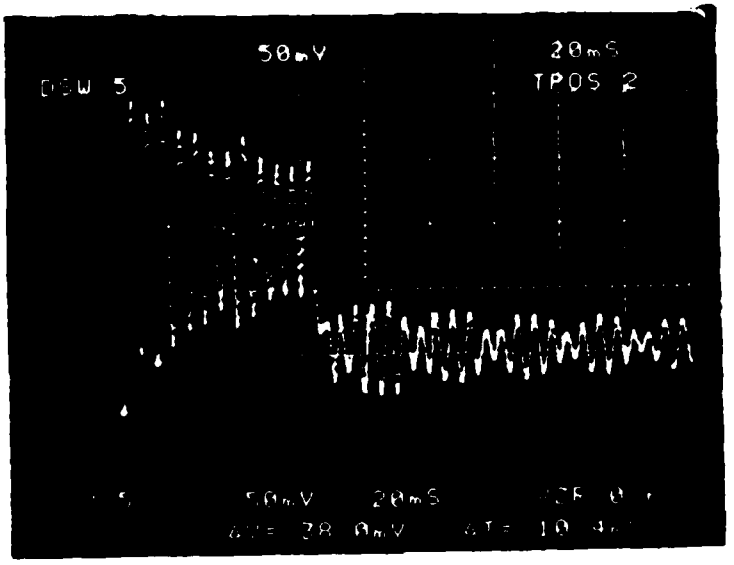

Figure 8. Case 2 Stopping Response
control around stepper motor only
vertical scale: 50 mV = 27 μin.

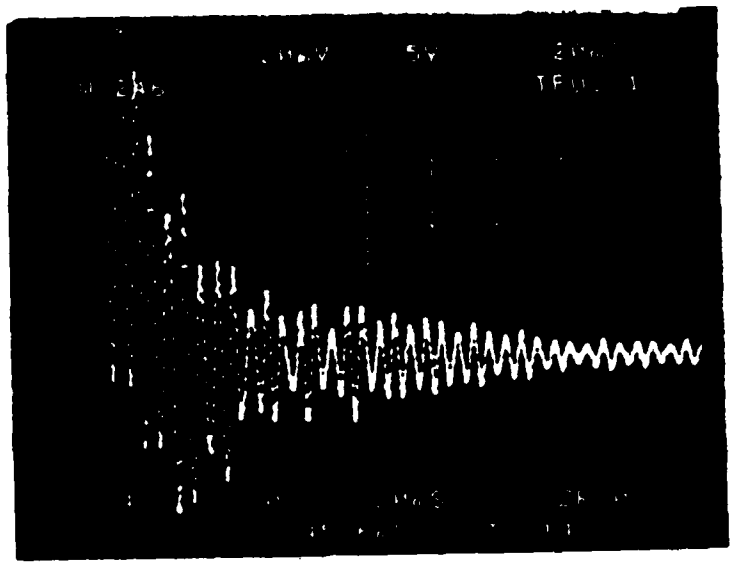

Figure 9. Case 3 Stopping Response control with stepper motor and PZT vertical scale: 20 mV = 10.6 µin.

oscillatory motion has increased in amplitude and then gradually decays. This exaggeration of the stopping response, as a result of PZT actuation, is partially due to a phase lag in the PZT/amplifier system. PZT actuation did however achieve greater control of absolute position and the maximum overshoot was reduced to 24 μin.

A PID controller (proportional-integral-derivative) is being designed and implemented on the stage. This controller should alleviate some of the problems of dynamic control discussed in this section.

CONCLUSION

The purpose of this study was to utilize electro-mechanical actuation and laser interferometric feedback to enhance the accuracy and precision of a lead screw stage. The precision translation stage was designed to produce rapid, precise, single axis translation. A two level actuation system consists of a piezoelectrically driven bean which is mounted on a lead screw propelled table. The precision translation stage experiments produced the following results:

* a controlled maximum translation velocity of 10 in/sec.
* an established steady state position accuracy of $\pm$ 6 μin.
* demonstrated position correction of disturbances from low frequency external loading, a 36 μin. increase over the uncompensated position accuracy
* a 63% reduction of the dynamic overshoot

These conclusions are consistent with the targeted goals. The goal of no overshoot is bounded by the steady state position error of $\pm$6 μin. The dynamic overshoot was 24 μin., which is a significant reduction from the open loop characteristics. Phase lag effects were identified as the primary limitation of improved compensation of the dynamic stopping motion including overshoot.

SIMULATION OF MECHANICAL MOTION CONTROL

By

Charles C. LeVay
Research Engineer
Precision Engineering Laboratory

And

Clarence J. Maday
Associate Professor
Mechanical and Aerospace Engineering Department

ABSTRACT

To study the effect of different control algorithms on motion control of mechanical systems, a simulation routine was developed to theoretically evaluate their performance. This routine included a model of the mechanical system, including the actuation system, and the details of the digital control scheme. The results indicate that the simulation does represent the dynamics of the controlled system and can be used to optimize the design of the control algorithm.

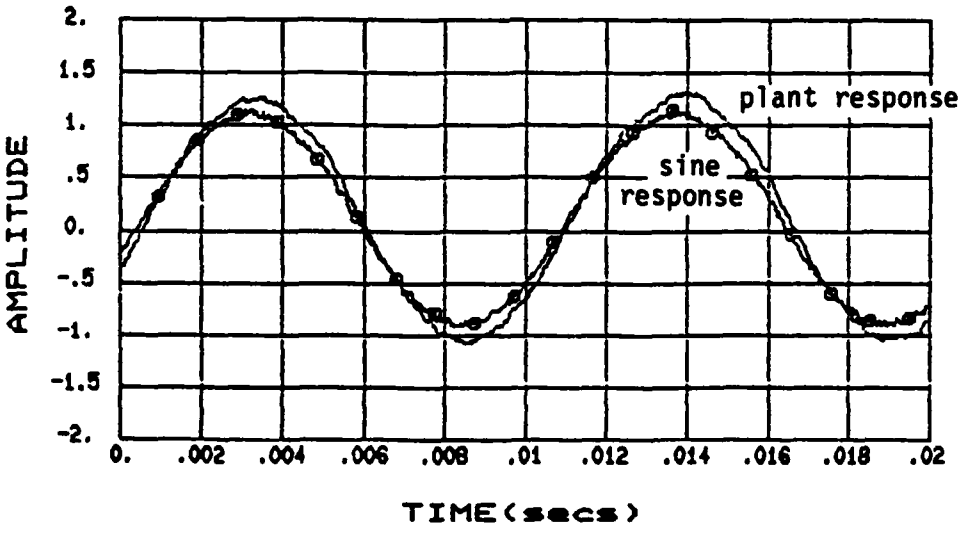

INTRODUCTION

Previous experiments to study piezoelectric actuator and eddy current proximity probes have been performed on a specially designed cantilever beam test fixture.(First Annual Report, pg. 90) A simple integral control algorithm was implemented on the PZT/Beam system to demonstrate the effective use of PZT's for precision position control of mechanical system. The goals of the current effort is to: 1) develop a linear model of the PZT/Beam system, 2) create a computer simulation of the dynamic response of the system, and 3) simulate a simple integral control algorithm. The computer simulation will be used for evaluation of new control design techniques aimed at improving the error tracking performance of mechanical systems.

EXPERIMENTAL APPARATUS

The test fixture, Figure 1, is an aluminum cantilever beam. The actuator is a Burleigh PZ-40 piezoelectric crystal (PZT) with a range of approximately 250 in. for a voltage range of 0-1000 V. from the Burleigh PZ-70 high voltage amplifier. The transducer is a Bently Nevada Microprox eddy current probe which senses the horizontal position of the beam. The control algorithm was implemented on a MINC PDP-11 computer which contained both A/D and D/A converters for sampling and feedback. A Hewlett-Packard 3311A function generator was used to produce step and sine input functions. Figure 2 illustrates the components of the experimental procedure.

System Modeling

Transfer function measurements were made on the PZT/Beam system using a sine sweep input. The measurements were recorded on a Wavetek 660 B Spectrum Analyzer. A Bode plot (Figure 3) was generated from the recorded data. The magnitude of the transfer function, expressed in decibles, is given in the upper portion of Figure 3 and the phase, expressed in degrees, is given in the lower portion. A graphical technique was used to make a first approximation of poles and zeros. It was determined that the PZT/Beam system had at least six poles and no zeros. The recorded data was then downloaded to a VAX 11/750 for statistical analysis. Using a random optimization routine on the recorded data with first approximations of pole location as an initial guess, a transfer function was derived to be:

$$\frac{W_a^2}{s^2 + 2\,{}_aW_a s + W_a^2} \quad \frac{W_b^2}{s^2 + 2\,{}_bW_b s + W_b^2} \quad \frac{W_c^2}{s^2 + 2\,{}_cW_c s + W_c^2} \qquad (1)$$

where W_a, W_b, W_c are frequencies 2283, 4000, and 5575 Hz respectively. The constants ${}_a$, ${}_b$, ${}_c$ are 0.017, .86, and 1.0. Generating a Bode plot from equation (1), Figure 4, and comparing it with the experimental

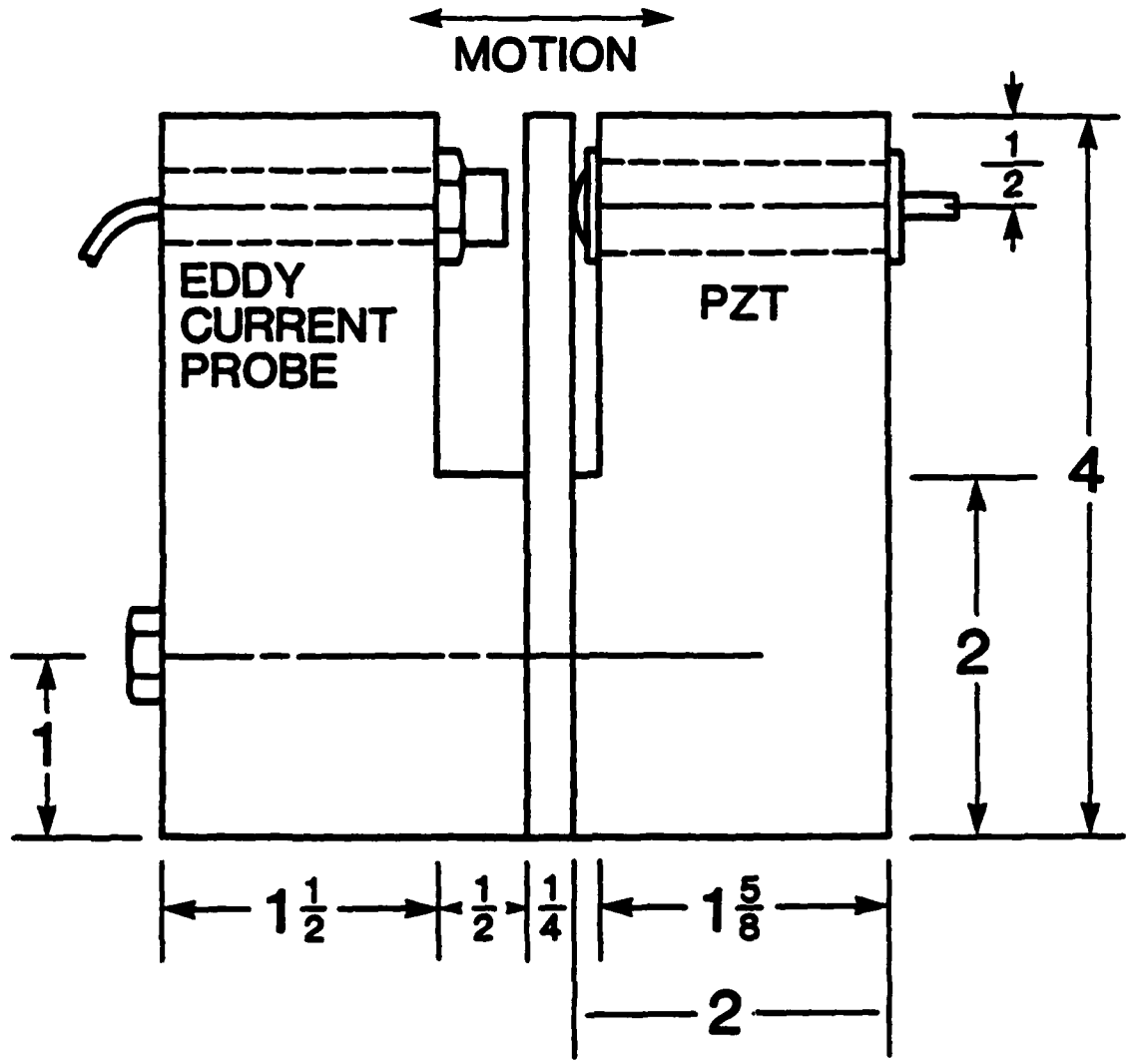

Figure 1. Vertical beam PZT test apparatus (side view)

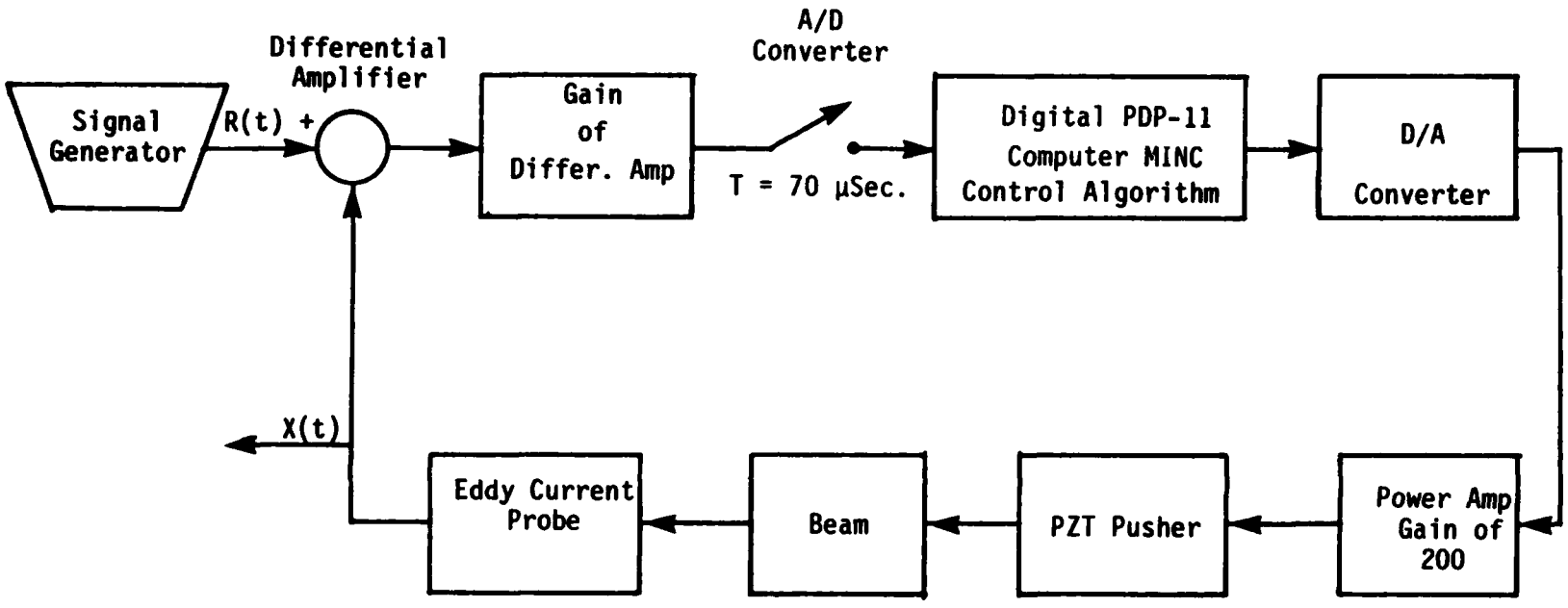

Figure 2. Experimental configuration

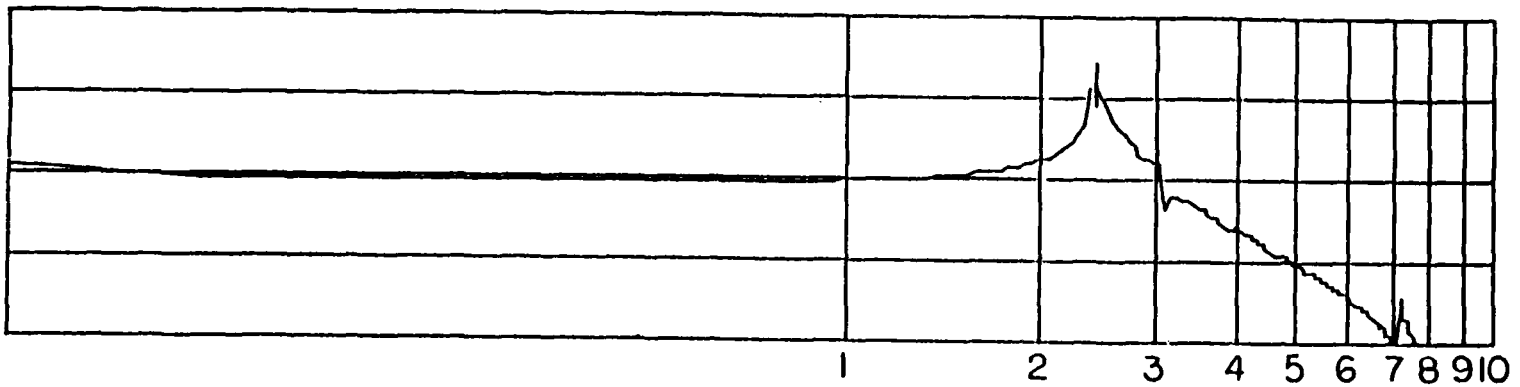

XFR FN MAG : 24.7dB 2.45 KHZ N: NONE P: 50HZ

SPAN: 0.000000HZ-10.0000KHZ FS: 41.00dB 20dB/

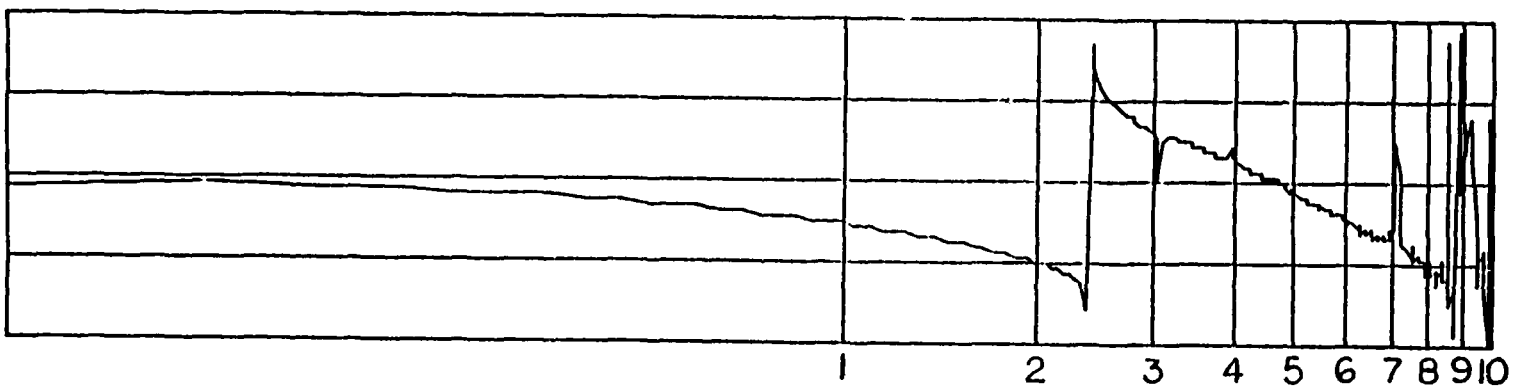

XFR FN PHASE : 131.8° 2.45 KHZ N: NONE P: 50HZ

SPAN: 0.000000HZ-10.0000KHZ FS: ±180° 90°/

Figure 3. Bode plot of PZT/Beam system

AD-A166 884 PRECISION ENGINEERING - SRO 154(U) NORTH CAROLINA STATE 2/4
UNIV AT RALEIGH PRECISION ENGINEERING LAB
T A DOW ET AL. JAN 86 N00014-83-K-0064

UNCLASSIFIED F/G 13/8 NL

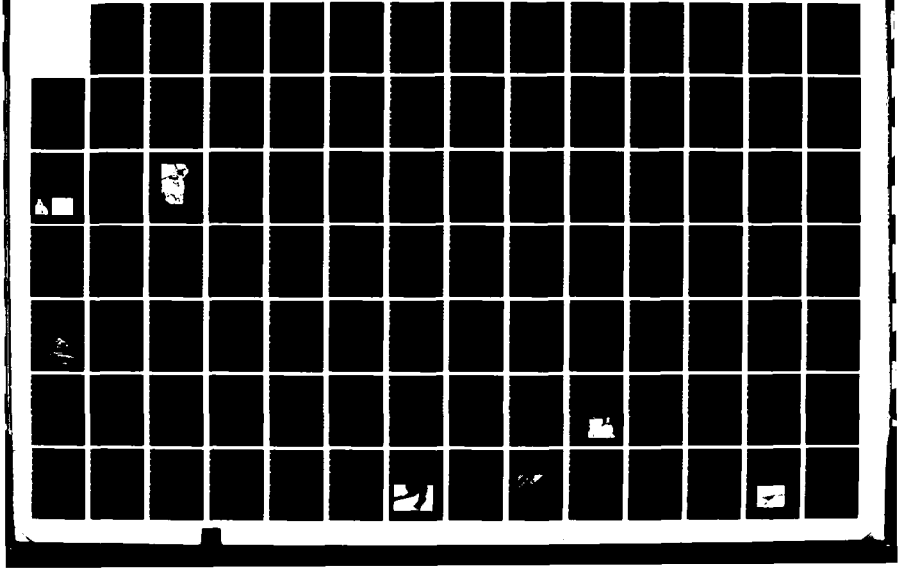

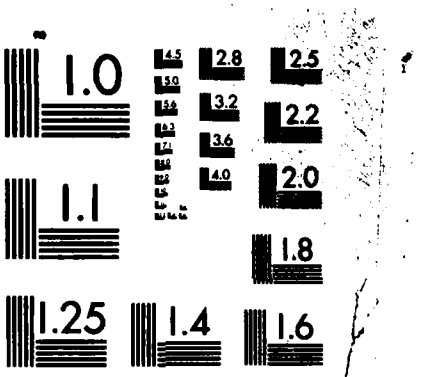

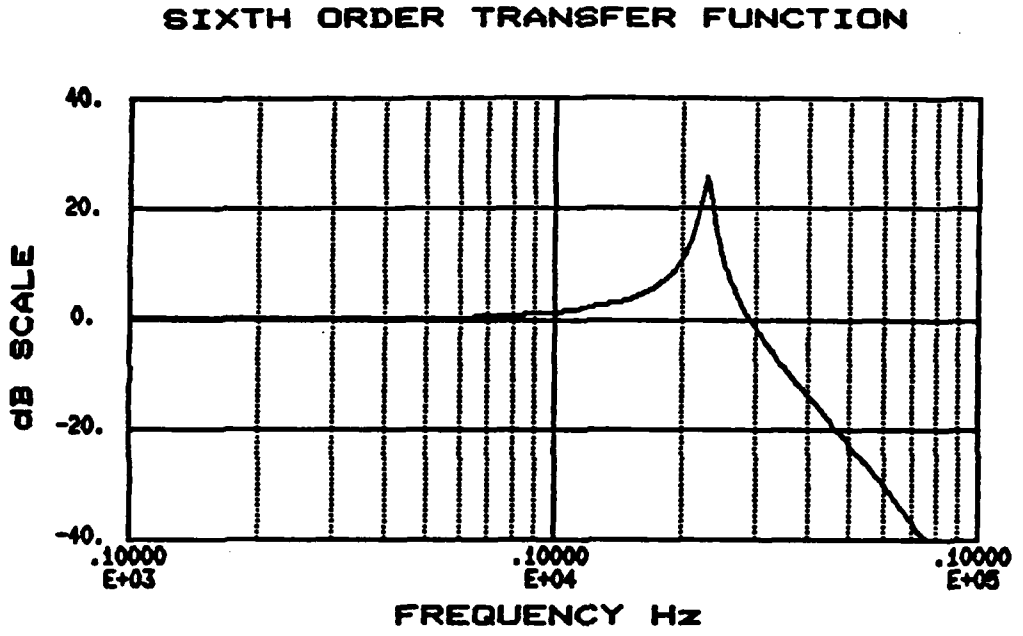

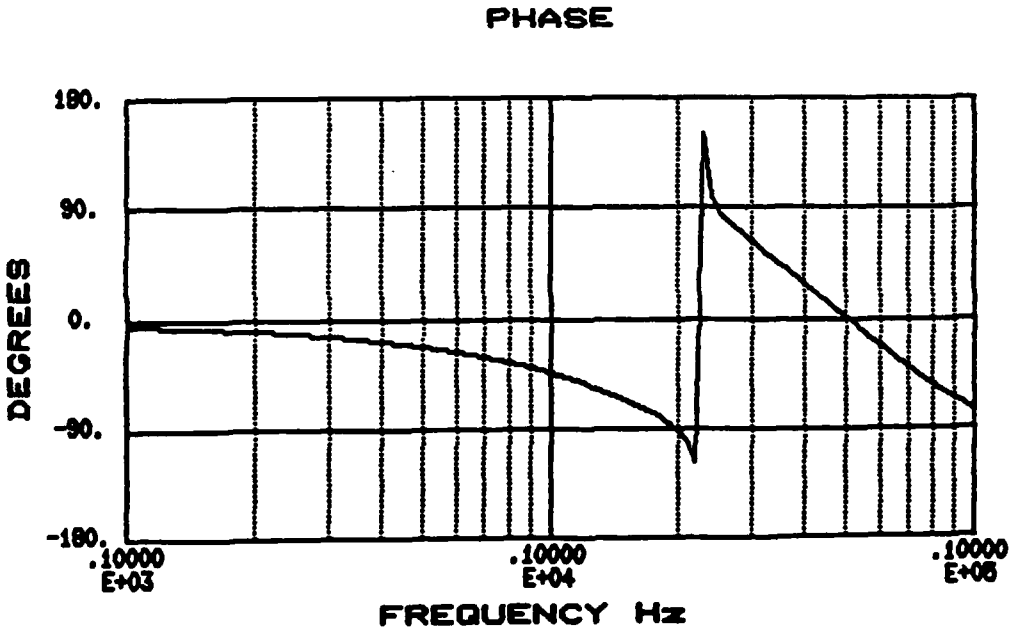

Figure 4. Bode plot of sixth order model

case, Figure 3, indicates that equation (1) is a good approximation of the PZT/Beam transfer function.

Simulation of System Dynamics

A simulation of the dynamic response of the system model was produced for comparison to experimental dynamic responses to step and sine forcing functions. In practice, solving for the time response for a system is often cumbersome. Therefore, it is necessary to use a numerical technique for calculating time response without having to solve a complicated differential equation. The numerical technique used is the Euler approximation method. This method is a simple way to approximate a set of linear first order equations with a set of discrete difference equations. These discrete difference equations may be recursively solved on a computer using a simple algorithm.

To use the Euler approximation, the system must be describe as a linear set of first order differential equations in state-vector notation.

$$\frac{dx(t)}{dt} = Ax(t) + Bu(t) \tag{2}$$

$$y(t) = Cx(t)$$

Where x(t) is an (n x 1) state-vector, A is an (n x n) state-matrix, u(t) is a scalar input, B is an (n x 1) input vector, C is an (1 x n) output vector, and y(t) is the scalar output. Substituting (3) the discrete Euler approximation for the derivative into (2)

$$\frac{dx(t)}{dt} = \frac{x(k+1) - x(k)}{t} \tag{3}$$

yields

$$\frac{x(k+1) - x(k)}{t} = Ax(k) + Bu(k) \tag{4}$$

$$y(k) = Cx(k)$$

rearranging (4)

$$x(k+1) = [I + tA]x(k) + Bu(k) \tag{5}$$

$$y(k) = Cx(k)$$

where I is the (n x n) identity matrix.

Equation (5) can be expanded into a set of n difference equations of the form:

$$x_1(k+1) = a_{11}x_1(k) + a_{12}x_2(k) + \ldots + a_{1n}x_n(k) + b_1u(k)$$

$$x_2(k+1) = a_{21}x_1(k) + a_{22}x_2k) + \ldots + a_{2n}x_n(k) + b_2u(k) \qquad (6)$$

$$x_n(k+1) = a_{n1}x_1(k) + a_{n2}x_2(k) + \ldots + a_{nn}x_n(k) + b_nu(k)$$

An algorithm was developed to recursively solve the difference equations calculated for the PZT/Beam system. Implementing this algorithm on a digital computer yields the discrete approximation of the time response of the continuous sixth order system described by Equation (1). The algorithm was coded in Fortran, and the results were produced on a VAX 11/750. Figure 5 shows the experimental step response of the PZT/Beam system measured with a Tektronix 7854 oscilloscope and the simulated step response of the sixth order model. The simulated step response accurately predicts initial overshoot, oscillation and damping. Similarly, Figure 6 and Figure 7 show examples of experimental and simulated sine response for a 100 Hz. and 500 Hz. sine wave, respectively. The simulation accurately predicted amplitude and phase characteristics of the PZT/Beam. This demonstrates that the sixth order model and the simulation algorithm accurately approximates the PZT/Beam system dynamics. Therefore, this algorithm was also used in the control simulation to produce the plant dynamics necessary for the closed-loop control system.

CONTROL SIMULATION

Although, the PZT/Beam system dynamics have been simulated, models must be developed for the differential amplifier, the A/D and D/A converters. The differential amplifier produces the difference voltage, or error signal, between the reference signal and the output signal of the eddy current probe. This is modeled by:

$$E = Ref - x \qquad (7)$$

where E = floating point number corresponding to error voltage signal
Ref = floating point number corresponding to reference voltage signal
x = floating point number corresponding to the displacement voltage from the eddy current probe

The A/D converter is modeled by:

$$IER = INT (E * a) \qquad (8)$$

where E = the error signal from (7)

$$a = \text{constant} = \frac{(2^N)}{\text{voltage range}}$$

N = resolution (# of bits) of A/D converter

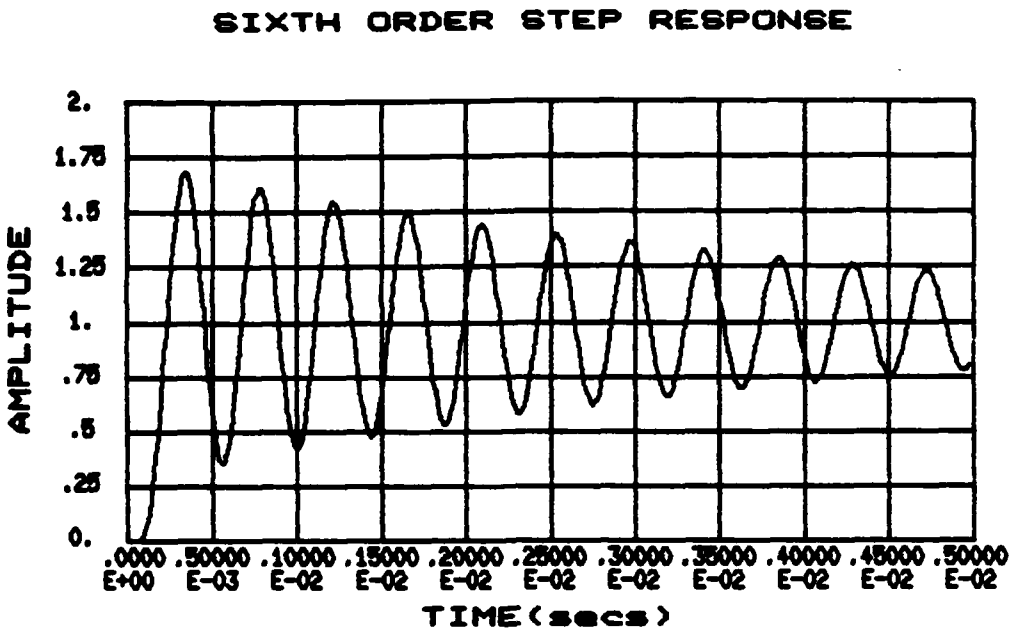

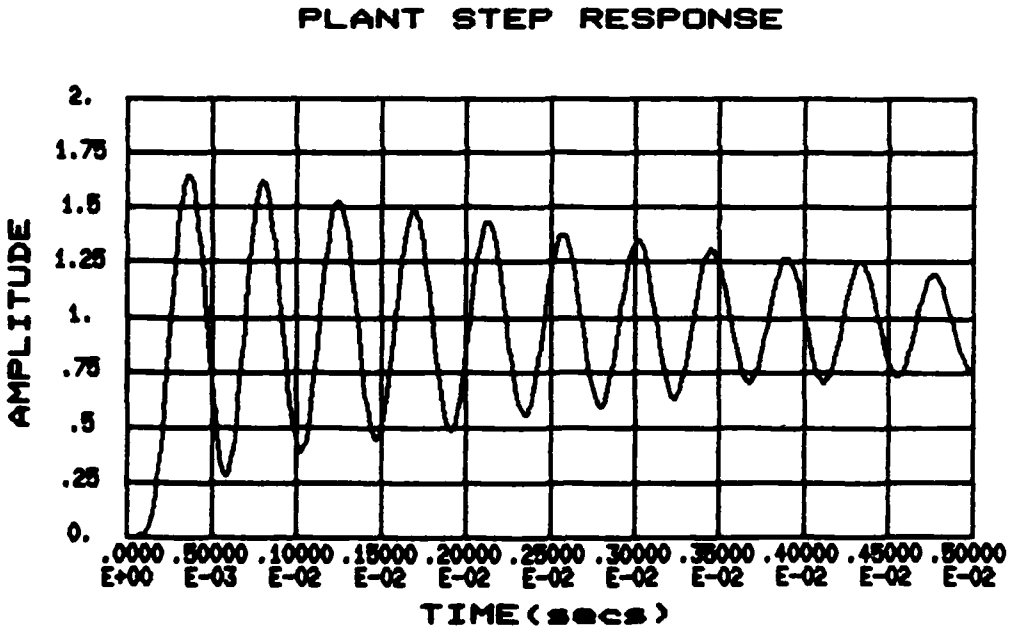

Figure 5. Comparison of analytical model of sixth order system to actual system response for a step input

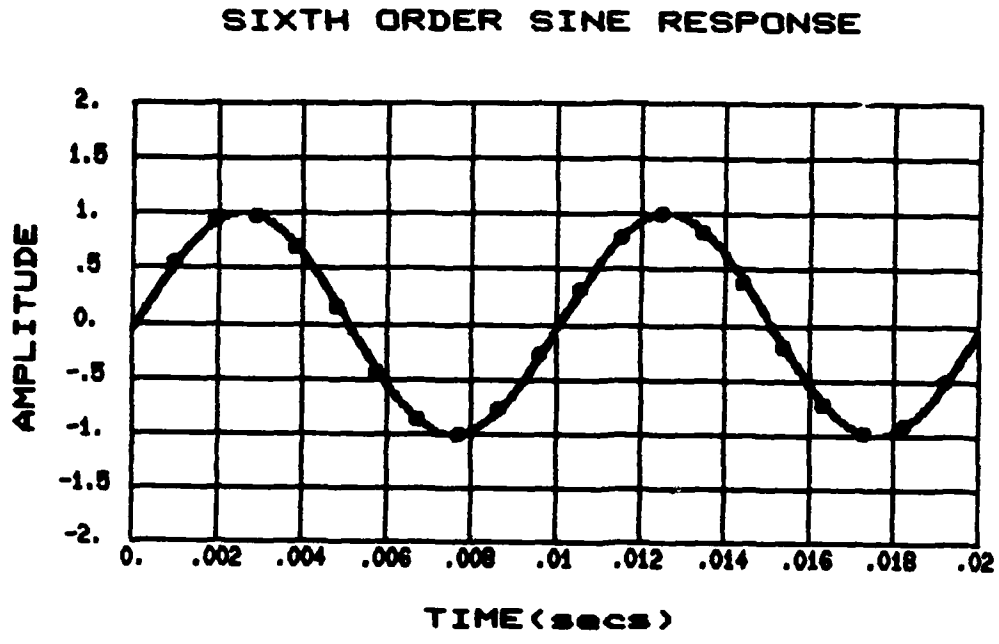

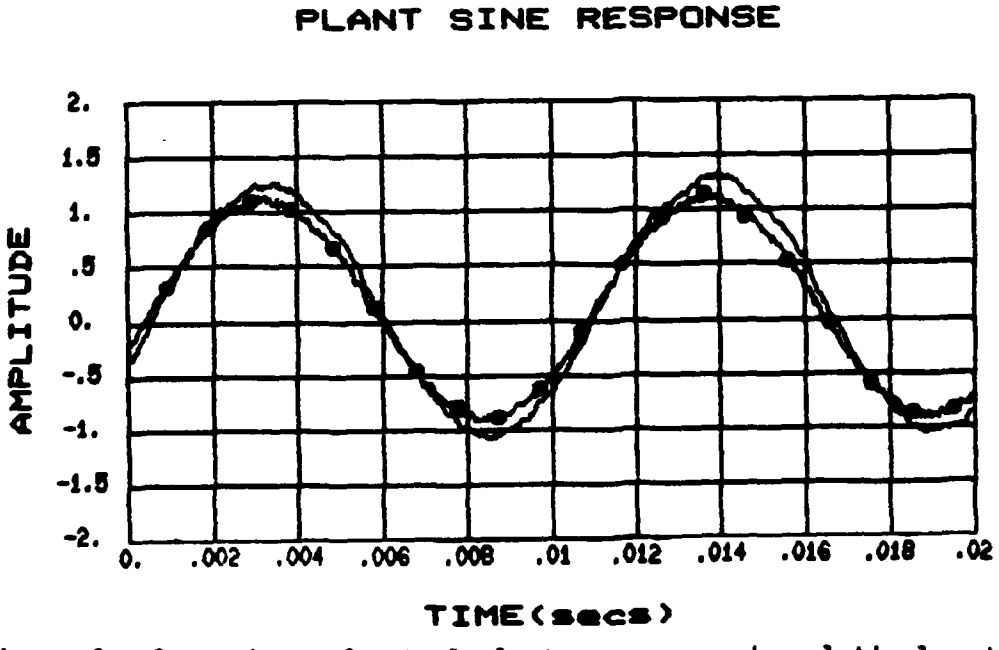

Figure 6. Comparison of actual plant response and analytical model to 100 Hz. sine wave input

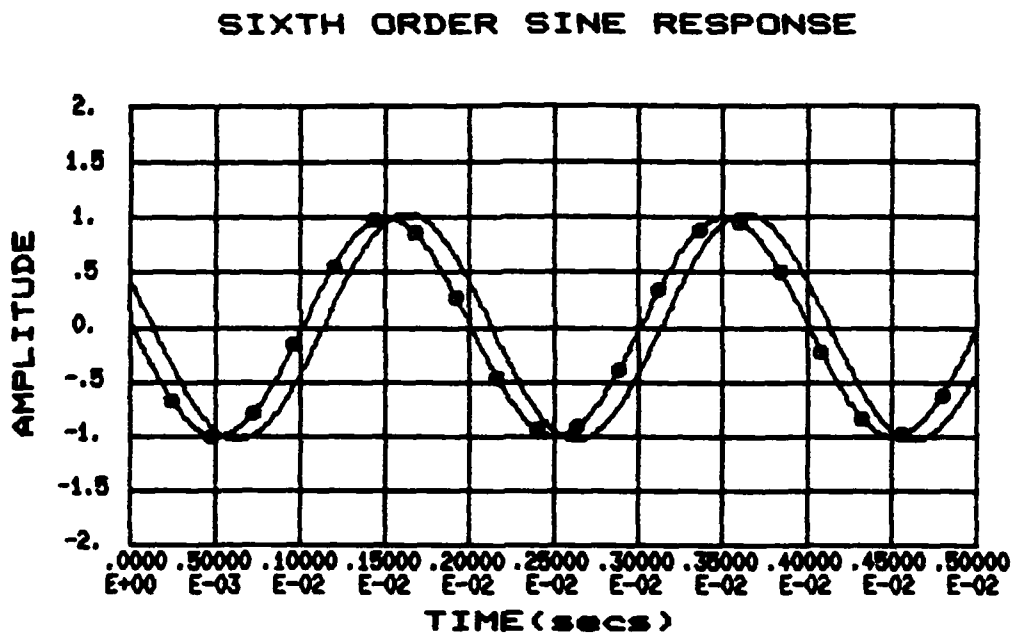

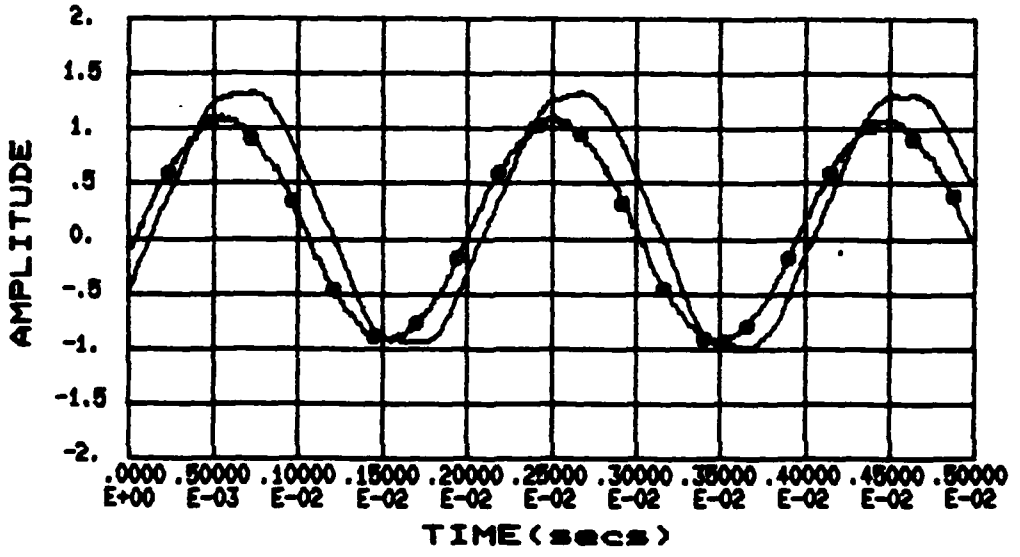

Figure 7. Comparison of actual plant response model to 500 Hz sine wave input

INT = Fortran function to convert floating point numbers to integer number
IER = integer number corresponding to floating point error voltage signal

The D/A converter is modeled by:

$$EO = Float\ (IEO * b) \tag{9}$$

IEO = the integer number representing the output signal calculated by the control algorithm

$$b = \text{constant} = \frac{\text{(voltage range)}}{2^N}$$

N = resolution of D/A (# of bits)
Float = Fortran function integer to floating point conversion
EO = Floating point output voltage

The integer control algorithm for the experiment is implemented on a PDP-11 computer. The algorithm is coded in Macro-11 assembly language using integer arithmetic for fast efficient processing. The control algorithm is an Eulerian integrator. The algorithm is:

$$IEO_t = IEO_{t-dt} + K*IER_t \tag{10}$$

where IEO_t = New output
IEO_{t-dt} = Previous output
K = gain of integrator
IER_t = Present error signal

The control algorithm used in the control simulation is Equation (10), however, for simplicity, the algorithm was coded in Fortran using integer arithmetic.

Timing is an important factor in the control simulation. The cycle time defined as the time from A/D conversion, calculation of control output to D/A conversion is measured at 70 microseconds. Note that as a sample is taken immediately after the controller outputs a correction to the D/A, the plant has not had time to respond to the latest correction. Therefore, when a sample is taken, it sees th effects of the output of the previous control cycle. This implies a one cycle delay in the system. This delay is accomplished by calculating the beam position, x, based on the previous output EO. From the Euler Approximation, time is incremented in small discrete time intervals dt. Therefore, by choosing dt to be 1000 times smaller than the cycle time T, then 1000 iterations of the difference equations must be calculated to generate x for each sampling interval. It is important to note that dt must be chosen to be sufficiently small with respect to the highest frequency of oscillation for an accurate solution. One drawback of choosing dt to be small is that a considerable number of calculations are required. This may lead to a less accurate solution due to the inherent computational error of the computer. Therefore, some experimentation with dt is necessary. The order of calculation is shown in Figure 8. The flow diagram shows that the error signal, A/D conversion, control output, and D/A conversion are

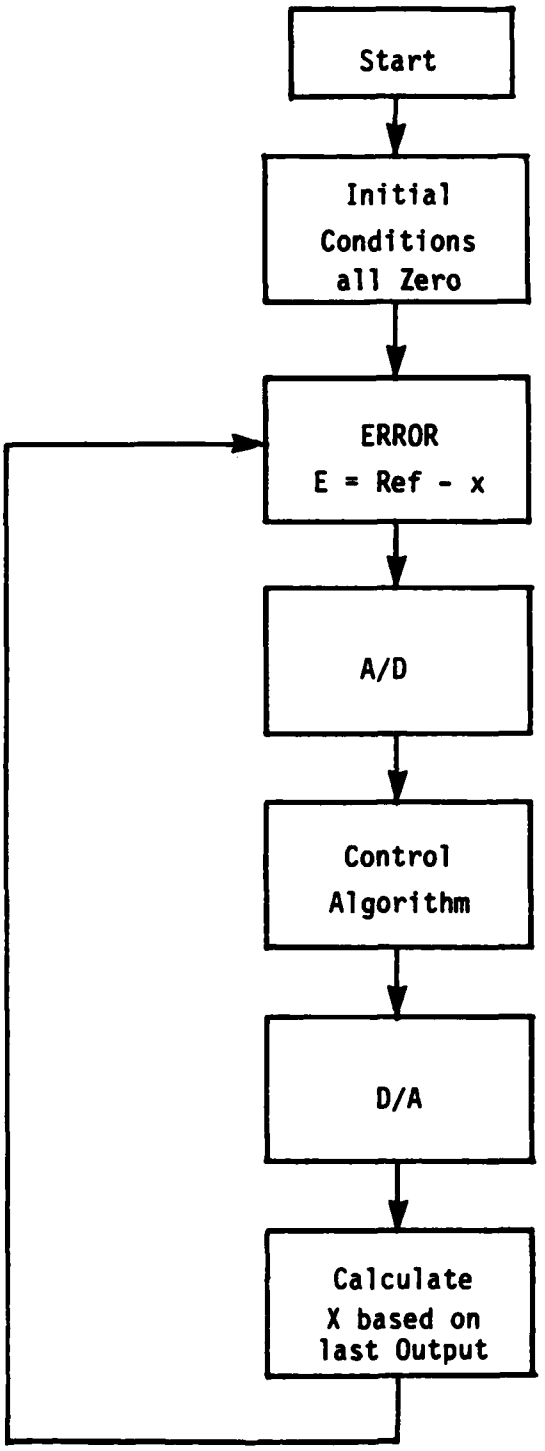

Figure 8. Flow Diagram of Simulation Program

calculated sequentially, then 1000 iterations of the plant difference equations are calculated, using the previous control output as the input forcing function. This process is repeated until the selected time frame is finished.

Figures 9 through 12 compare the simulated output response of the beam to a sine wave disturbance at 100 Hz. The upper graph illustrates the results of the simulation and the lower graph is the experimental results. The curve with the circles depicts the input function to the system and the other curve is the response of the beam using the integral control scheme described. Figure 9 shows the comparison for a integral gain of unity. for this case the amplitude is reduced and a considerable phase lag exists. Figures 10, 11, and 12 illustrates the improvement in system response when the gain is increased to 2, 4, and 8 respectively. At a gain of 8 (Figure 12), the amplitude and phase of the beam response closely match that desired. As the frequency is increased, the system does not follow the input as well as at lower frequencies as indicated in Figure 13 -- at 500 Hz with a gain of 8. However, the simulation program does accurately predict the performance of the control system.

CONCLUSIONS

The Euler approximation method is a quick and accurate way to produce the dynamic response of a mathematical system model. With the addition of a sampler model and a controller, an accurate control simulation can be produced. This procedure has been used as a tool to test new control algorithms and control design techniques. With a control simulation, plant and control parameters can easily be manipulated to better understand design constraints and achieve improved control performance.

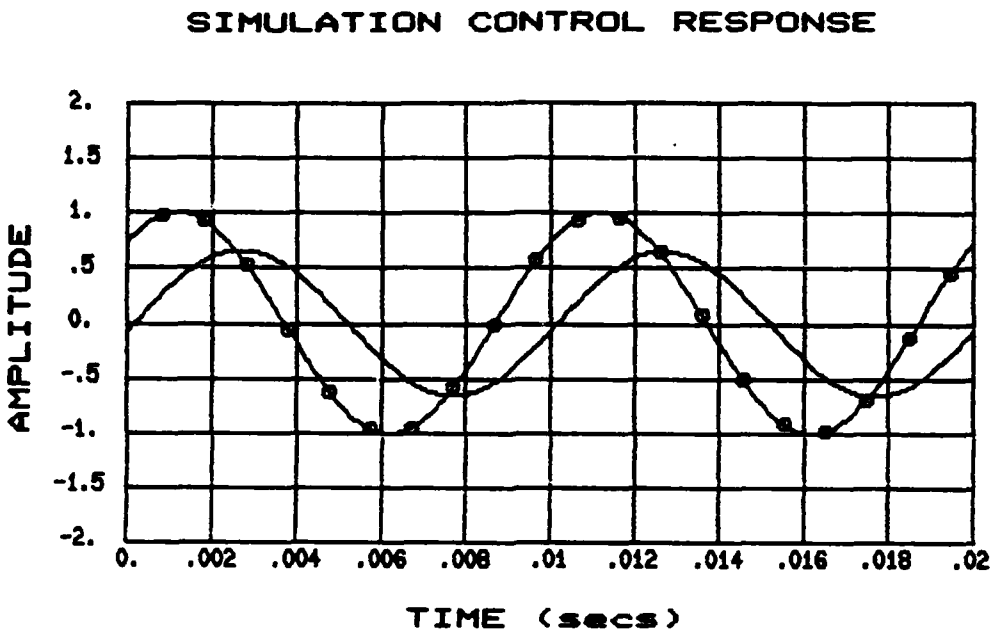

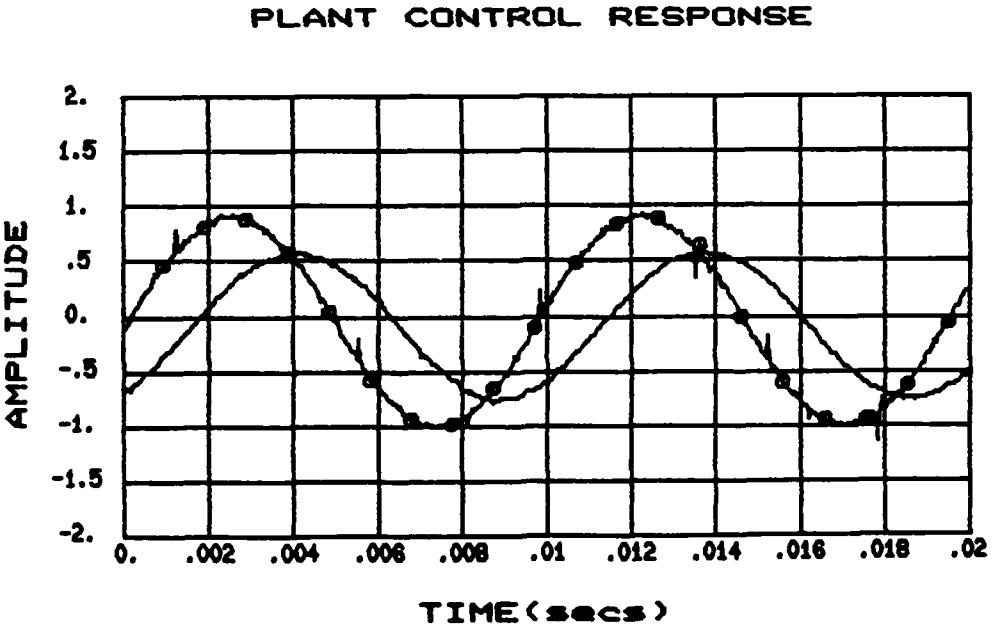

Figure 9. Controlled response of simulated and actual system to 100 Hz sine wave input (Gain = 1)

SIMULATION CONTROL RESPONSE

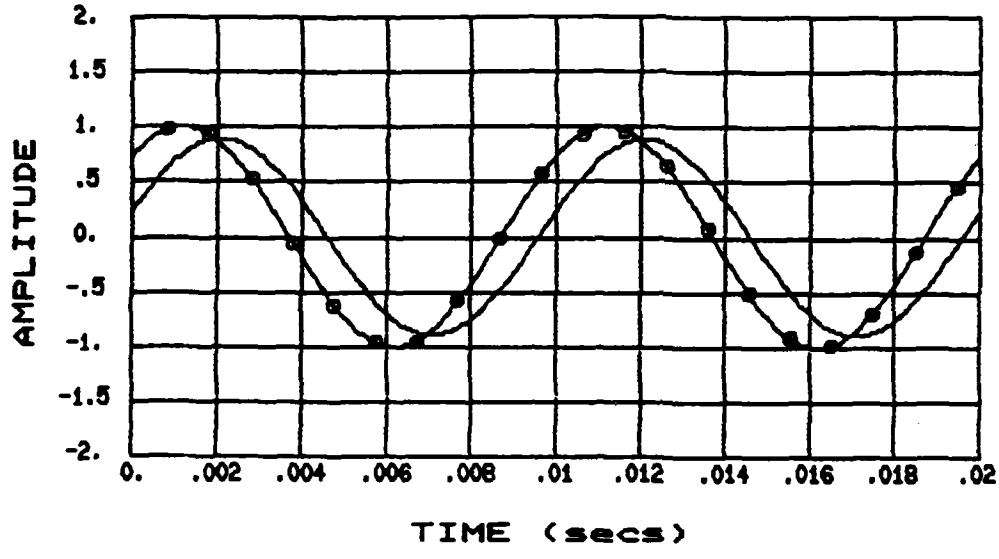

PLANT CONTROL RESPONSE

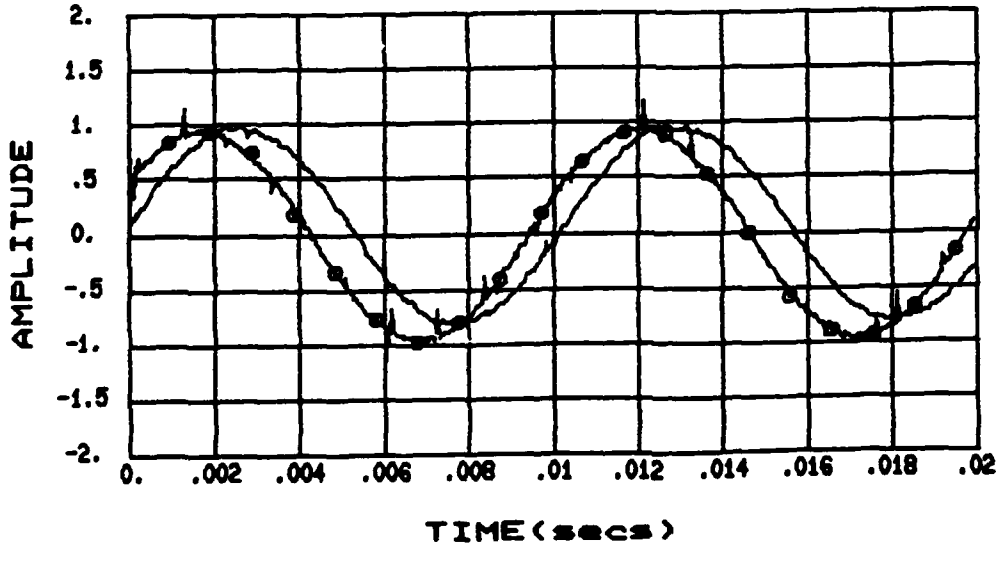

Figure 10

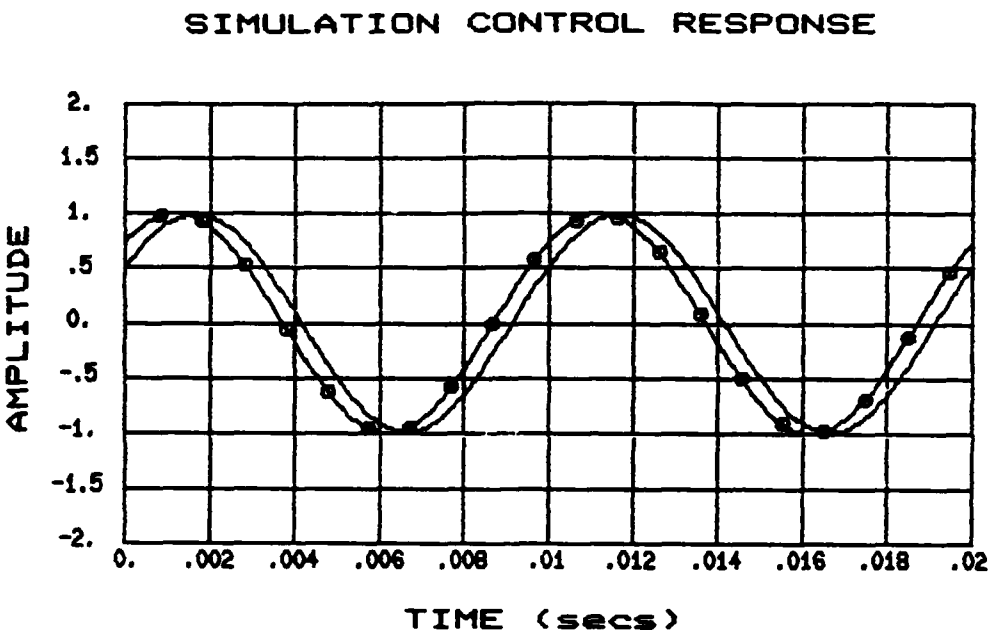
SIMULATION CONTROL RESPONSE
AMPLITUDE
2.
1.5
1.
.5
0.
-.5
-1.
-1.5
-2.
0.
.002
.004
.006
.008
.01
.012
.014
.016
.018
.02
TIME (secs)

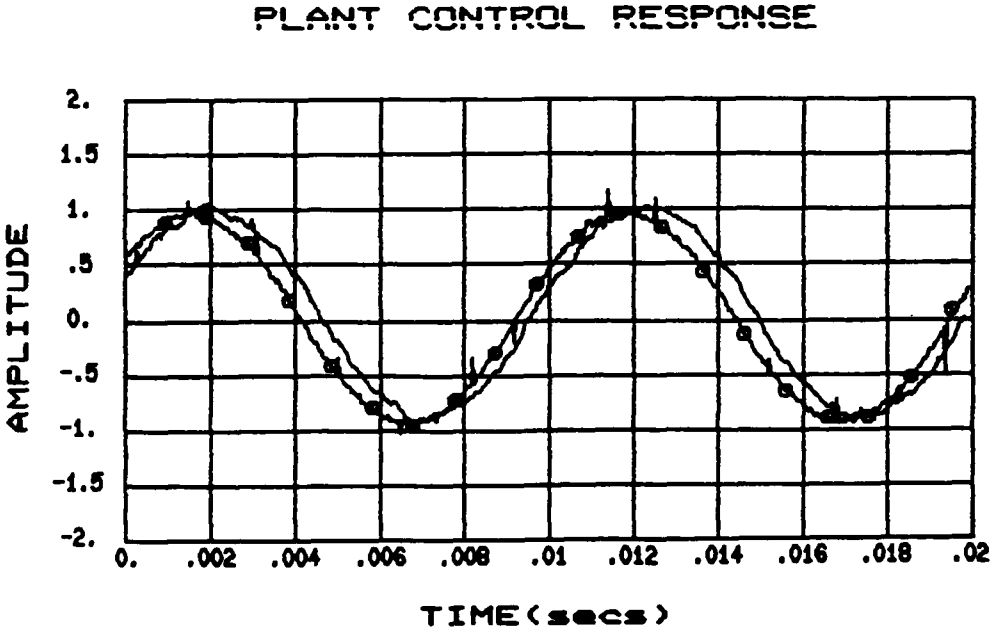
PLANT CONTROL RESPONSE
AMPLITUDE
2.
1.5
1.
.5
0.
-.5
-1.
-1.5
-2.
0.
.002
.004
.006
.008
.01
.012
.014
.016
.018
.02
TIME(secs)

Figure 11

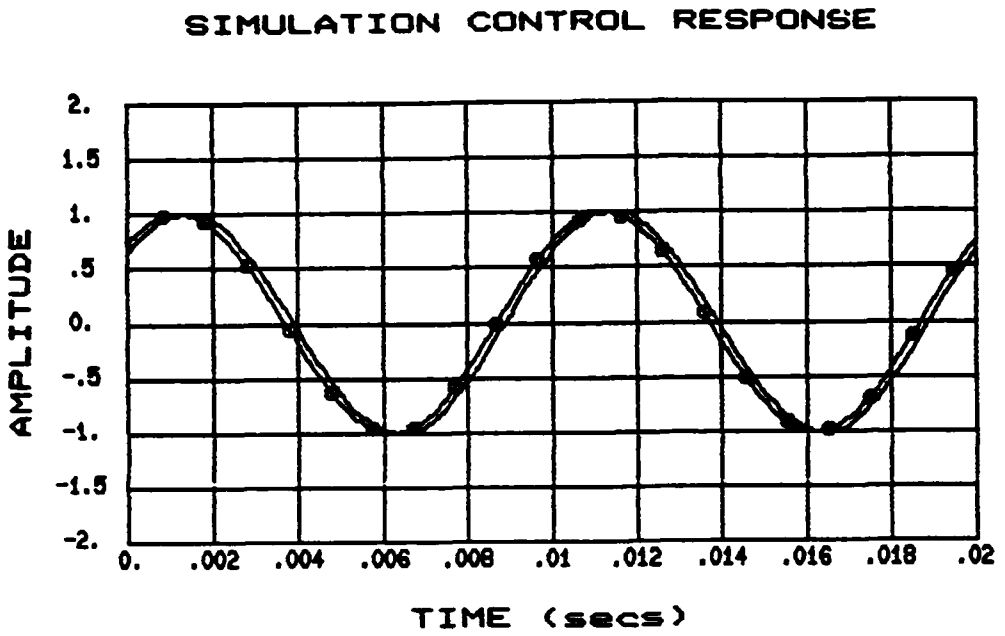
SIMULATION CONTROL RESPONSE
AMPLITUDE
2.
1.5
1.
.5
0.
-.5
-1.
-1.5
-2.
0.
.002
.004
.006
.008
.01
.012
.014
.016
.018
.02
TIME (secs)

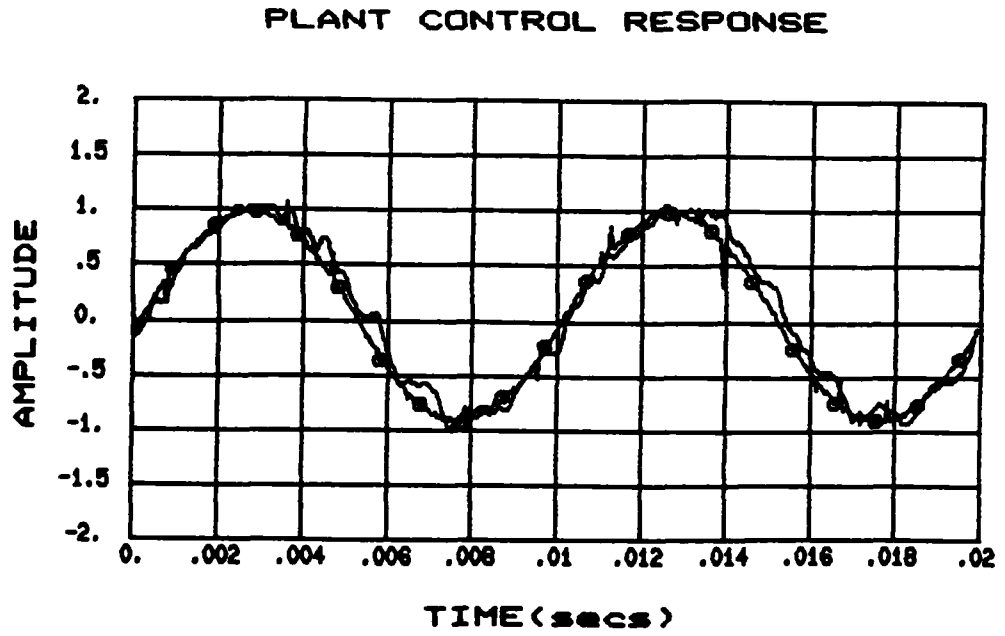
PLANT CONTROL RESPONSE
AMPLITUDE
2.
1.5
1.
.5
0.
-.5
-1.
-1.5
-2.
0.
.002
.004
.006
.008
.01
.012
.014
.016
.018
.02
TIME(secs)

Figure 12

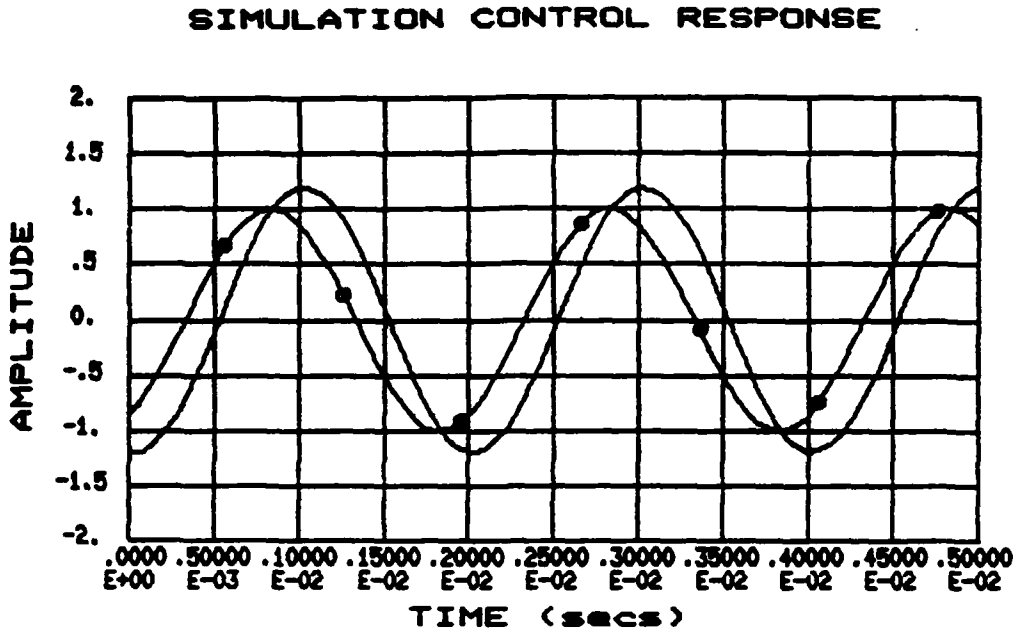

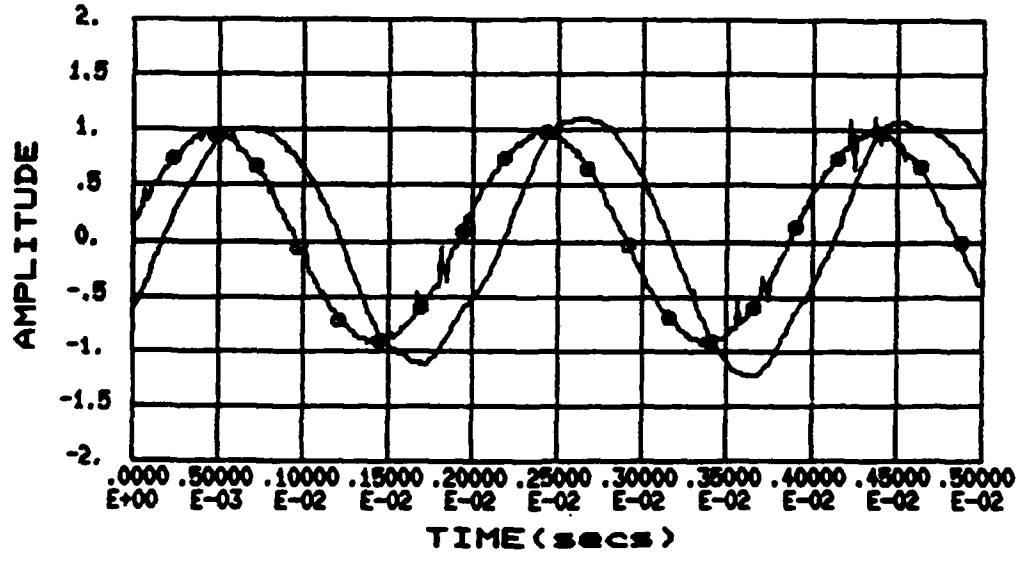

Figure 13. Controlled response of simulated and actual system to 500 Hz sine wave input (Gain = 8)

REFERENCES

1. Beale, G. O. and S. E. Bentley, "Parameter Estimation Using Microprocessors and Adaptive Random Search Optimization," IEEE Trans. on Industrial Electronics, Vol. IE-31, No. 1, February 1984, p. 85-89.

2. Bently, S. E. and G. O. Beale, "Identification and Improved Control of GTAW Voltages Utilizing Digital Series Compensation," Proc. 19th IEEE Conf. on Decision and Control, December 1980, p. 1050-1057.

CONTROL OF PZT ACTUATED BEAM

By

Mark Landy
Graduate Student
Precision Engineering Laboratory

And

Clarence J. Maday
Associate Professor
Mechanical & Aerospace Engineering

ABSTRACT

Determination of the characteristics of piezoelectric transducers (PZT's) is essential in the development of controllers for PZT actuated mechanical systems. Of greater importance in the design of these controllers is which characteristics can and can not be neglected. To study this problem, an analog controller was designed and built to control the position of a PZT actuated cantilever beam. The investigation showed that a system incorporating a PZT could be modeled linearly and be successfully controlled.

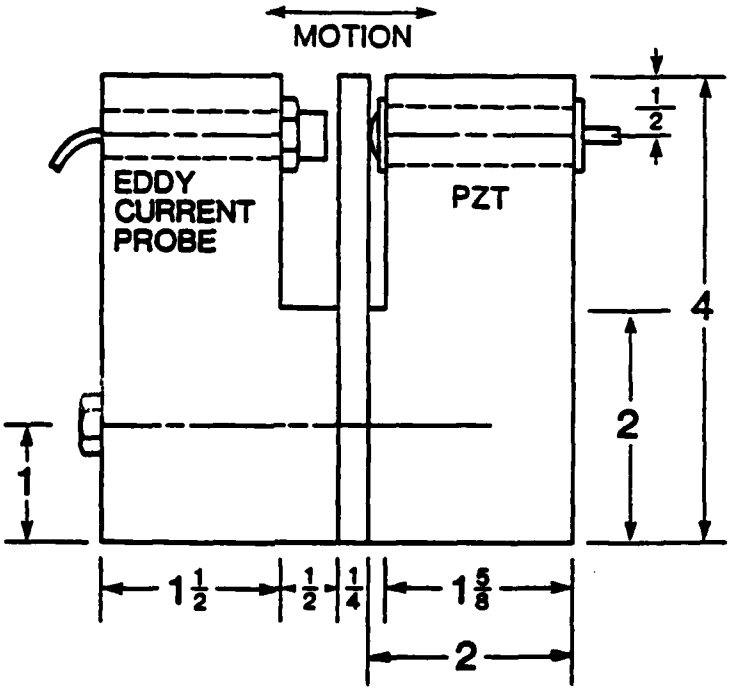

INTRODUCTION

Active feedback control of cutting tools in precision machining processes has the ability to precisely position cutting tools while compensating for tool chatter and machine vibration and flexure. Current trends have been to use piezoelectric actuators (PZT's) to position cutting tools because of their ability to precisely move small distances. PZT's however are fairly complex in nature, exhibiting hysteresis and nonlinearity. Nonlinearity considerably increases the complexity of a controller and its design. It is important to determine what effect the PZT's hysteresis and nonlinearity have on the performance of a controlled system that incorporates a PZT.

In this investigation the position of a aluminum cantilever beam has been controlled by a cylindrical PZT (Burleigh PZ-40) driven by a variable gain high voltage amplifier (Burleigh PZ-70). The position of the beam was measured with an eddy current proximity probe. A specific concern of this investigation was to determine whether or not the PZT/beam assembly, which is nonlinear, could be modeled as a linear system and whether or not a controller based on this linear model would perform as desired. The goal was for the system to have zero steady state error to a step input or constant disturbance and for the system to have a dead-beat (no overshoot) response to a step input.

The investigation consisted of four stages; system modeling, controller design, circuit design and simulation, and controller testing.

SYSTEM MODELING

The amplifier/PZT/beam system model was determined with the use of a spectrum analyzer and an adaptive random optimization routine. A Wavetek 660B FFT analyzer was used to obtain experimental Bode plot data of the system from 0 to 10 kHz. This data file was transferred to a VAX 11/750 computer where an adaptive random optimization routine was used to determine the best system model.

The optimization routine used, written in Fortran, is a slight modification of the algorithm described in reference [1]. The routine is supplied with initial parameter guesses and perturbation ranges. Also supplied to the optimization routine is a callable subroutine which uses the parameters, determined by the optimization routine, to determine the sum of the squared differences between the experimental phase and magnitude and those of the system model. The sum of the squared differences for a set of parameters is called its error. The error subroutine requires a basic model in which to try the parameters supplied by the main routine. A fourth order model with no zeros was used because the experimental Bode plot showed almost 360 degrees of phase lag at 10 kHz (there are 90 degrees of phase for each order if there are no zeros). The optimization routine initially determines the error associated with the parameters supplied. The parameters are then randomly perturbed to some value within the specified range. The range is always centered about the best set of parameters tested. After each perturbation the

error is again calculated and compared to the error for the best to date set of parameters. If the new set of parameters has a smaller error then the best to date error then the new set becomes the best to date and is stored along with its error. At prespecified intervals the size of the range for each parameter is optimized separately in order to speed convergence. The optimization routine ends if any of three prespecified criteria are met; the number of iteration has exceeded a limit, the number of consecutive failures has exceeded a limit, or the error of the best to date set of parameters is less the a specified amount. This optimization routine was chosen because it converges to the global minima, whereas many deterministic optimization routines have a tendency to converge to local minima.

The Bode plots of the model and the experimental data are shown in Figure 1. The experimental data is the solid line and the optimized model is the dotted line. The best combination of parameters for the fourth order model showed that there was one set of complex poles and one set of critically damped poles. It is suspected that the complex set of poles is due to the mass/spring/damper effect of the mechanical system and that the remaining set is due to the electrical/mechanical effect of the PZT and high voltage amplifier.

CONTROLLER DESIGN

Two criteria were specified for the controlled system; (1) the controlled system should have zero steady state error to a step input or constant disturbance, (2) the controlled system should have a dead beat response to a step input. The first criteria required the inclusion of an integrator in the forward portion of the controller. The second criteria was met by designing the controller so that all of the poles of the controlled system were on the real axis in the s plane. The lack of complex poles insures that there are no oscillations. Complete control of the placement of the poles for the controlled system was made possible by having four orders of feedback. The feedbacks were proportional to the position of the beam and the first three derivatives of the position. The derivative signals could have been produced by differentiation of the signal from the eddy current probe. This method would have produced unacceptable signal to noise ratios for the second and third derivatives. The alternative approach taken was to use a state observer to estimate the unmeasured states, the first three derivatives in this case. The states to be estimated did not necessarily have to be the derivatives of the position signal from the eddy current probe but were chosen as such to simplify the construction of the controller.

The state observer estimates the states of the system based on the control signal going to the system to be controlled and the measured signal coming from the system. The observer recreates the states through a series of integrations instead of differentiations so a minimum amount of noise is produced. The observer compares the estimated states to the measured states, in this case only the position, and partially compensates for modelling errors by using feedback of the error signal. The rate at which the observer compensates for modelling errors can be

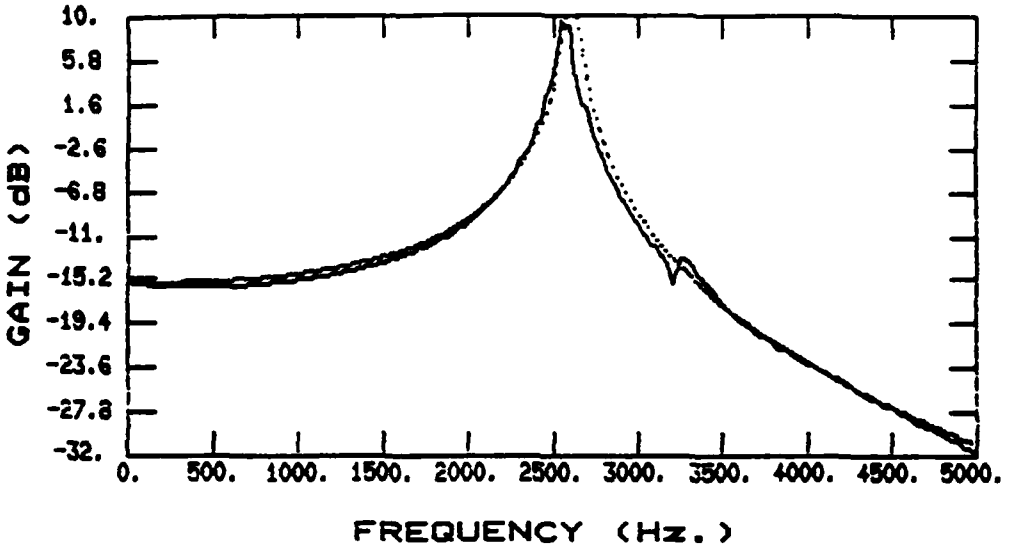

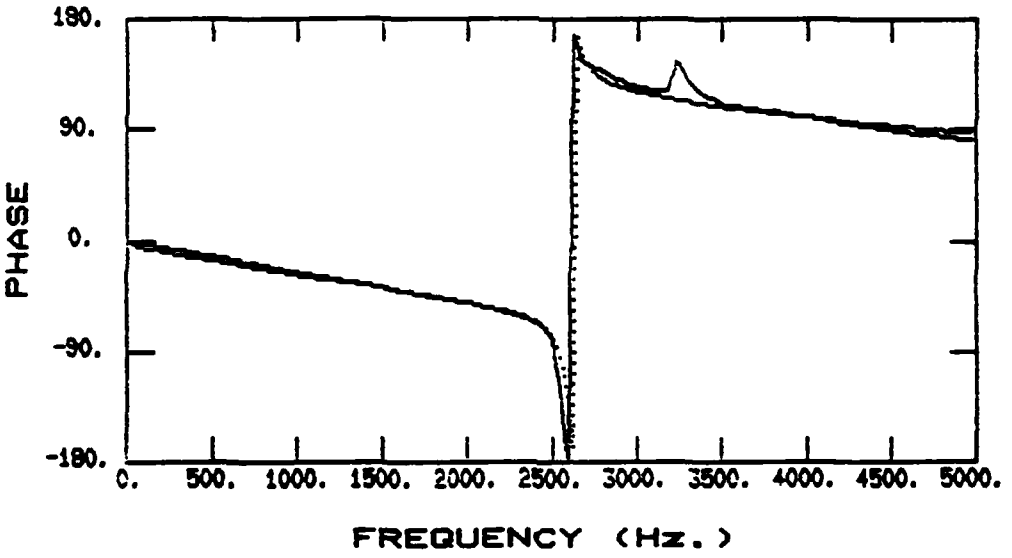

Figure 1. Experimentally obtained Bode plot of Amplifier/Pzt/ Beam system (solid), and Bode plot of system model (dotted)

controlled by varying the gains of the feedback of the state estimation error. A block diagram of the controlled system is shown in Figure 2.

CIRCUIT DESIGN AND SIMULATION

The controller was built as an analog circuit, mainly composed of operational amplifiers. An analog controller was chosen over a digital controller for this initial investigation because of its high speed. Before the circuit was built a computer program was written to simulate the control circuit and the amplifier/PZT/beam assembly. The simulation, written in Fortran, used a Euler approximation for the integrators. The simulation was used to determine the voltage levels at key places in the circuit and voltage slew rate at the output of the high voltage amplifier. These voltages are important because the output of the op-amps are limited to $\pm$ 12 volts and the slew rate of the high voltage amplifier driving the PZT is limited to 7.4 x 10**5 volts per second. Using this simulation, the individual gains of the op-amps were manipulated to achieve the best compromise between voltage levels and gains while keeping the overall feedback gains at there required values. The simulation, which calculated the necessary feedback gains for a specific pole placement, was used to determine what pole placement would produce the fastest response while staying within the limitations of the circuitry and amplifier. The simulation included a random amount, within a certain limit, of offset error and gain error for each amplifier and integrator in the circuit along with signal noise. Based on the results of the simulation the poles of the controlled system and the poles of the observer were set at -27000. The pole placement of the observer determines the rate at which the observer compensates for estimation errors. Figure 3 shows a block diagram of the controller circuit.

RESULTS

After constructing and debugging the controller a Bode plot of the controlled system was acquired and compared to the Bode plot of the uncontrolled system. These plots are shown in Figure 4. As can be seen the controlled system no longer has an increase in magnitude at 2600 Hz. The controlled system has a one to one amplitude ratio at low frequencies where as the uncontrolled system has a ratio of about one to seven. The -3 dB point for the controlled system is at approximately 1660 Hz.

When given a step input or step disturbance the controlled system had zero steady state error. The uncontrolled system, when driven with a step input, overshot its steady state value 70% and took approximately 12 milliseconds to damp out. The controlled system showed no overshoot and reached steady state in 0.4 milliseconds when given a step input. This shows that the controlled system reaches steady state 30 times faster than the uncontrolled system. Figure 5 shows the uncontrolled and controlled system responses for 500 Hz. square wave reference signals. For the uncontrolled system, resonant behavior at the natural frequency of the beam (2600 Hz) dominates the motion. The controlled

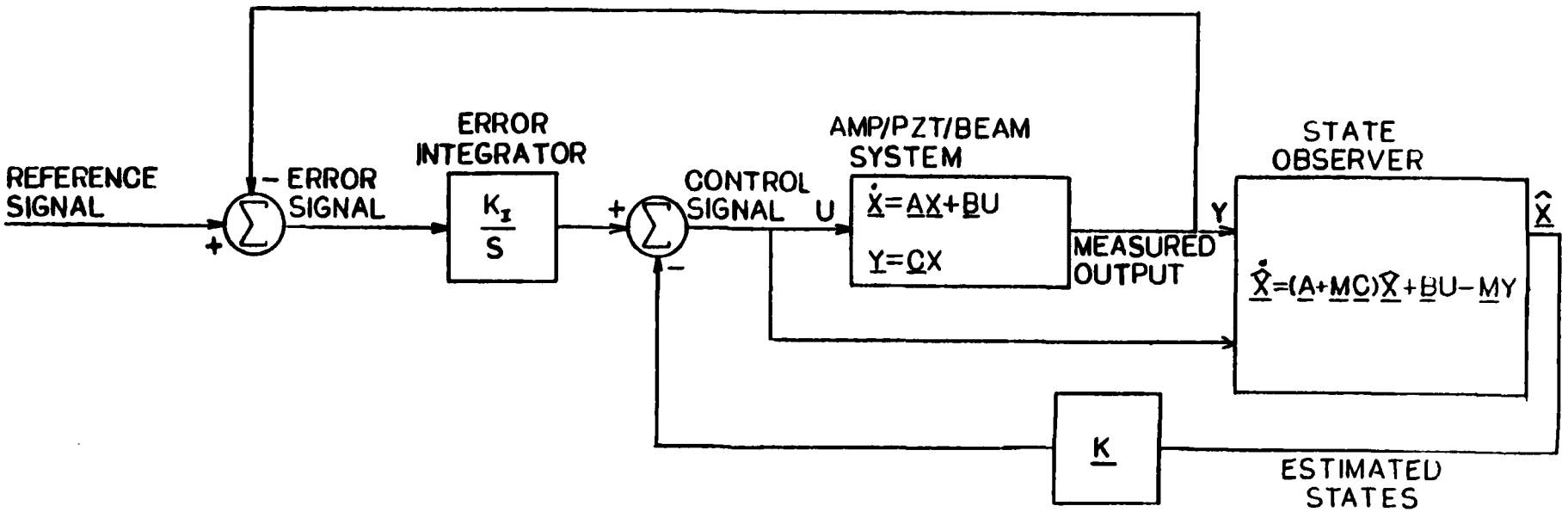

Figure 2, Block diagram of controlled system

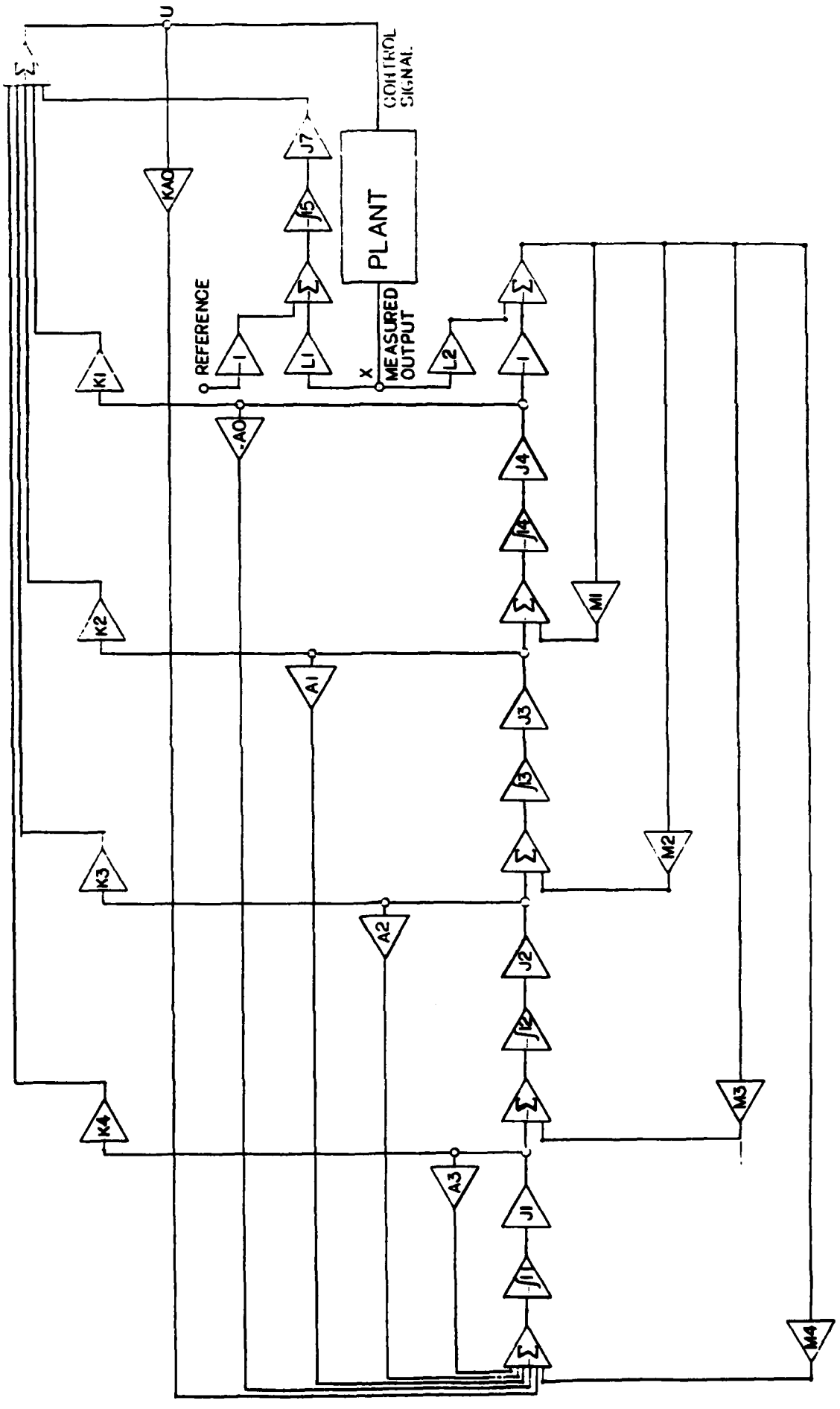

Figure 3. Block diagram of controller circuit

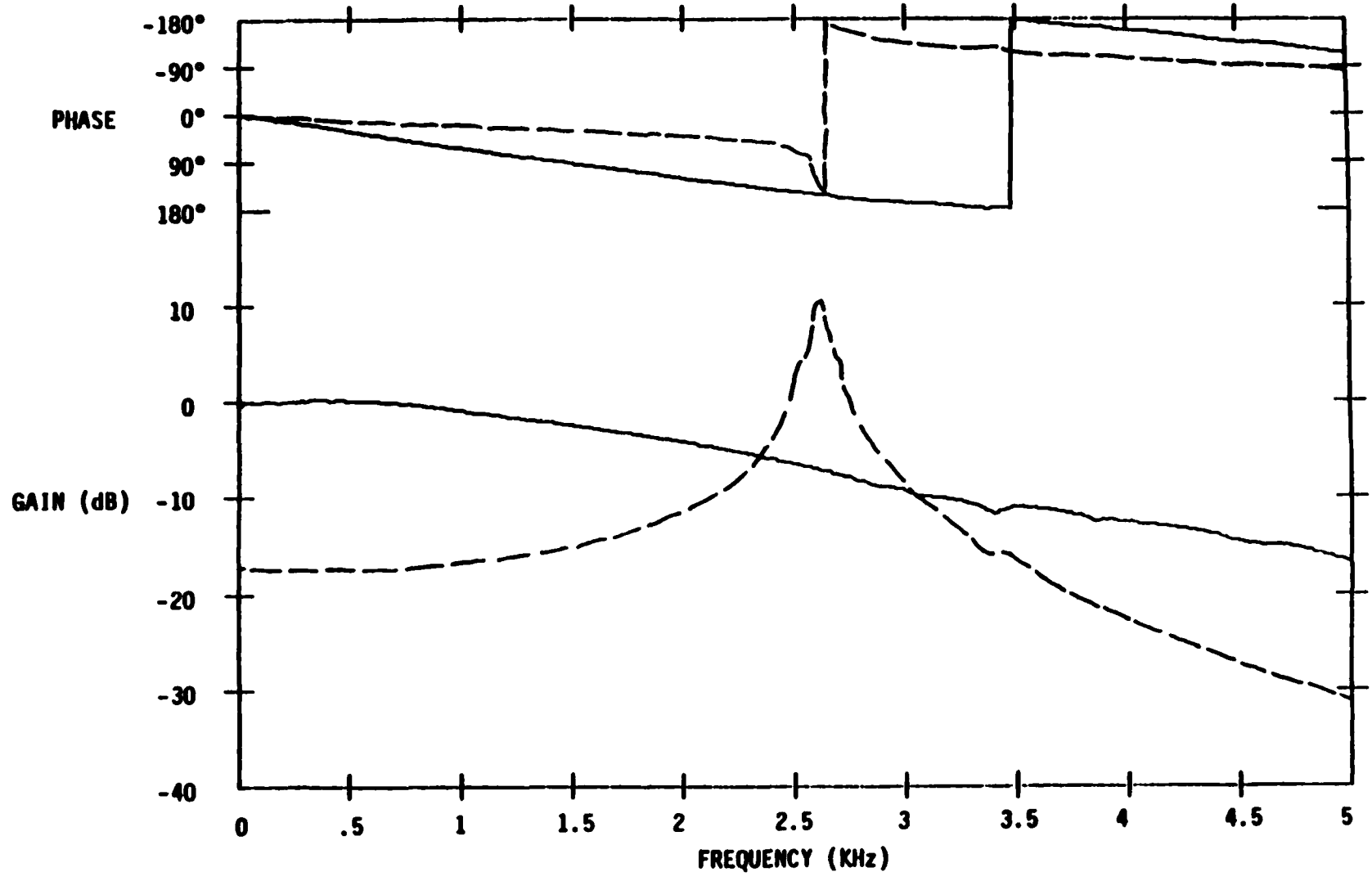

Figure 4. Bode plots of uncontrolled (dashed) and controlled (solid) systems

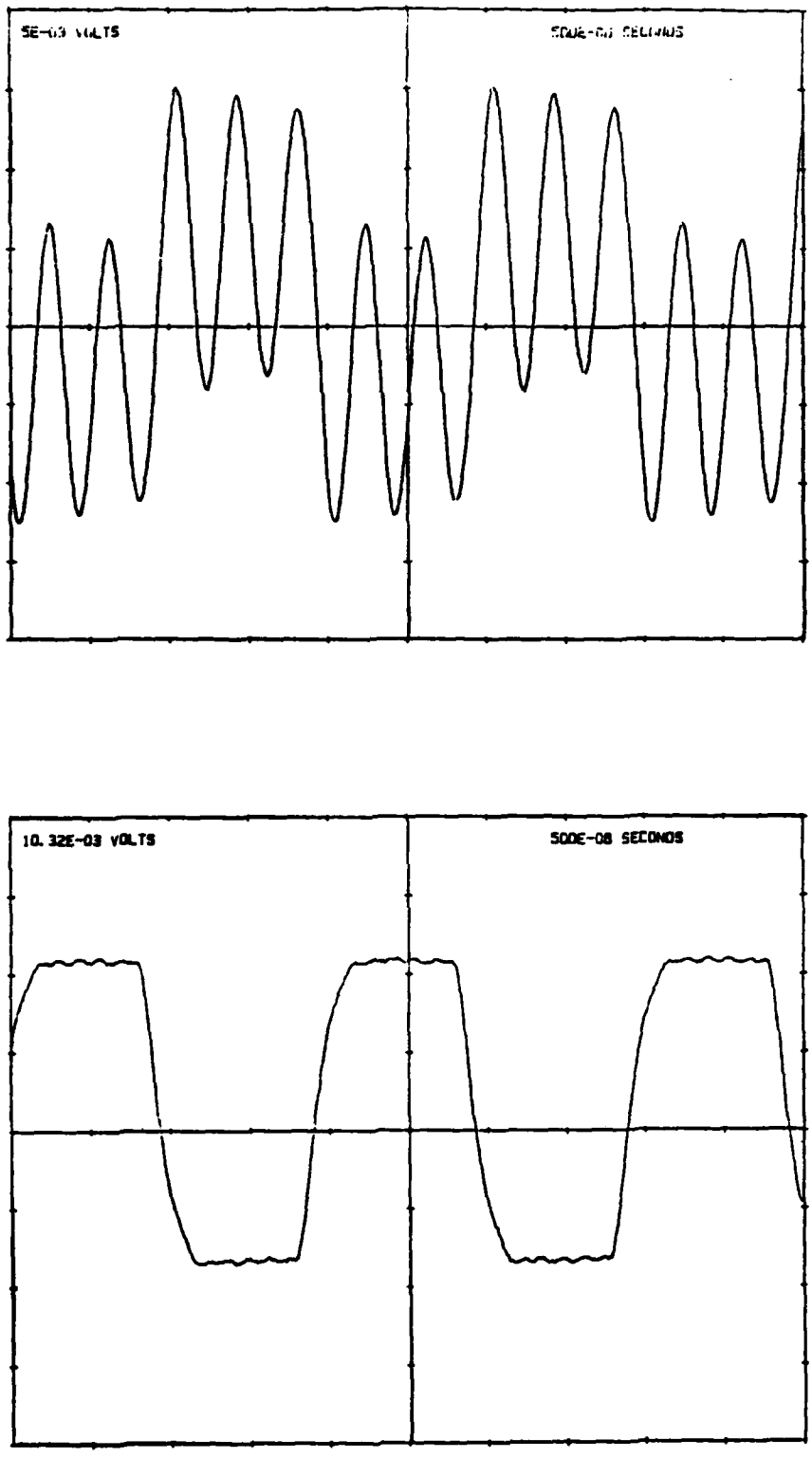

Figure 5. System response to a 500 Hz. square wave for uncontrollled (top) and controlled (bottom) systems

response of the beam mirrors the square wave input while exhibiting the rise time behavior described above. This behavior is achieved by modifying the control signal to the PZT with the analog controller.

CONCLUSIONS

Past annual reports have described the hysteresis and nonlinearity of typical PZT actuators. It has been shown that a mechanical system incorporating a PZT can be modeled, using Bode plot information, as a linear system. This approach greatly simplifies the design of the controller.

The results of this investigation indicate that such an approach, coupled with the use of a state observer, can result in a control system which allows rapid response to a step input but eliminates the oscillatory behavior inherent in the mechanical system.

REFERENCES

1. Masri, S. F., G. A. Bekey, and F. B. Safford, "A Global Optimization Algorithm Using Adaptive Random Search," Applied Mathematics and Computation, Vol. 7, 1980, pp. 353-375.

2. Fortman, T. E. and Konrad L. Hitz, An Introduction to Linear Control Systems, Control and Systems Theory Series Vol. 5, Marcel Dekker Inc. New York, 1977.

REAL-TIME FEEDBACK SYSTEMS FOR CONTROL OF POSITION IN PRECISION ENGINEERING

By

Thomas G. Bifano
Graduate Student
Precision Engineering Laboratory

And

Thomas A. Dow
Professor
Mechanical and Aerospace Engineering Department

ABSTRACT

Attaining accurate, smooth motion control with microinch precision and millisecond response time demands a careful review of the interaction between the measurement sensor, the control algorithm, and the actuation device. In these applications, the use of sensors and actuators at the current limits of precision measurement and controlled movement challenge the implementation of standard control theory. In this paper, these difficulties are presented in terms of the real-time control of the radial runout of a ball bearing spindle. Additionally, the development of several working real-time control strategies are introduced. These algorithms are part of an attempt to address the problems of real-time precision control in a general way; to identify both specific problems and plausible solutions common to all precision actuation of structures. The algorithms developed are robust and widely applicable; they incorporate a balance between control speed and algorithm versatility. The concept of direction sensitive feedback represents the culmination of this control philosophy, and its relative merits and deficiencies are discussed.

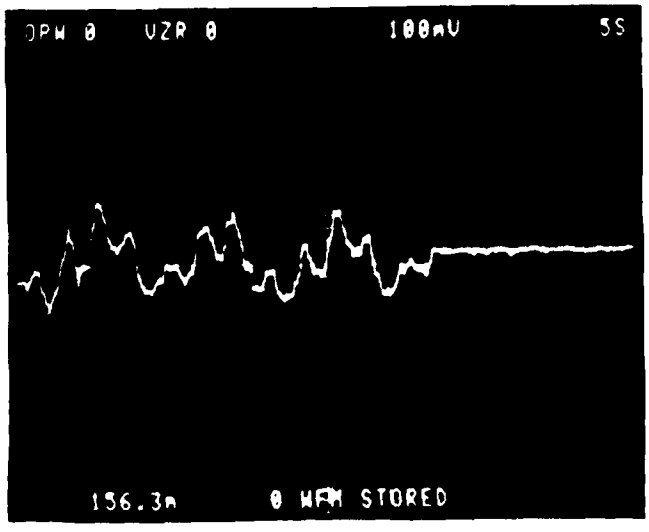

INTRODUCTION

The use of real-time feedback to control the accuracy of precision machines has been impeded by both the complex dynamics of the electro-mechanical structures and by the unavailability of practical control systems that could provide robust performance and relative economy of implementation. However, future industrial demands for precision parts will dictate active error compensation to supplement open loop machine control.

The task of accurately positioning a structure to microinch tolerances in real-time presents a challenging area of application for automatic control. To combine sensors and actuators operating at their limits of speed and resolution into a workable error correction scheme necessitates innovative development of practical control techniques. This paper documents the development of a real-time feedback control scheme for reducing radial runout errors in a ball bearing spindle. Through this specific example, some general guidelines for the use of high-speed, real-time position controllers of position will be introduced. Additionally, the benefits of active error correction will be demonstrated, and two practical control strategies will be compared.

Common to all real-time control systems are three distinct subsystems: a measurement sensor, a control algorithm (implemented either in software on a digital computer, or in hardware on a dedicated circuit), and an output transducer. In the specific case of a system controlling the linear position of a structure in real-time, a displacement measuring gauge is the sensor and a linear actuator is the output transducer. Typically, the control algorithm for such a system is tailored to the characteristics of both the sensor and the actuator, and to the dynamics, (e.g. linearity, natural frequency, stiffness, damping, etc.) of the structure being controlled.

The design process for a control system begins with the selection of a sensor and an actuator suited to the speed and resolution desired from the controller. This is followed by an analysis of the open loop characteristics of the structure that is to be controlled. These open loop characteristics help to qualitatively identify the linearity and number of degrees of freedom (order) of the structure, information which is used in the development of the control algorithms.

THE PHYSICAL SYSTEM

For this study, the control system is used to reduce the radial runout of a ball bearing spindle [1]. At the heart of the spindle is a steel shaft supported by a pair of ABEC 9, 12 mm bore ball bearings. The bearings are press fit into a steel housing that is attached by a cantilever springs to a spindle support housing, as illustrated in Figure 1. The spindle support housing is in turn rigidly affixed to a vibration isolated table. The cantilevers are designed to allow motion in one horizontal direction (x), but are extremely stiff in a perpendicular horizontal direction (y). An aluminum plate is mounted on the

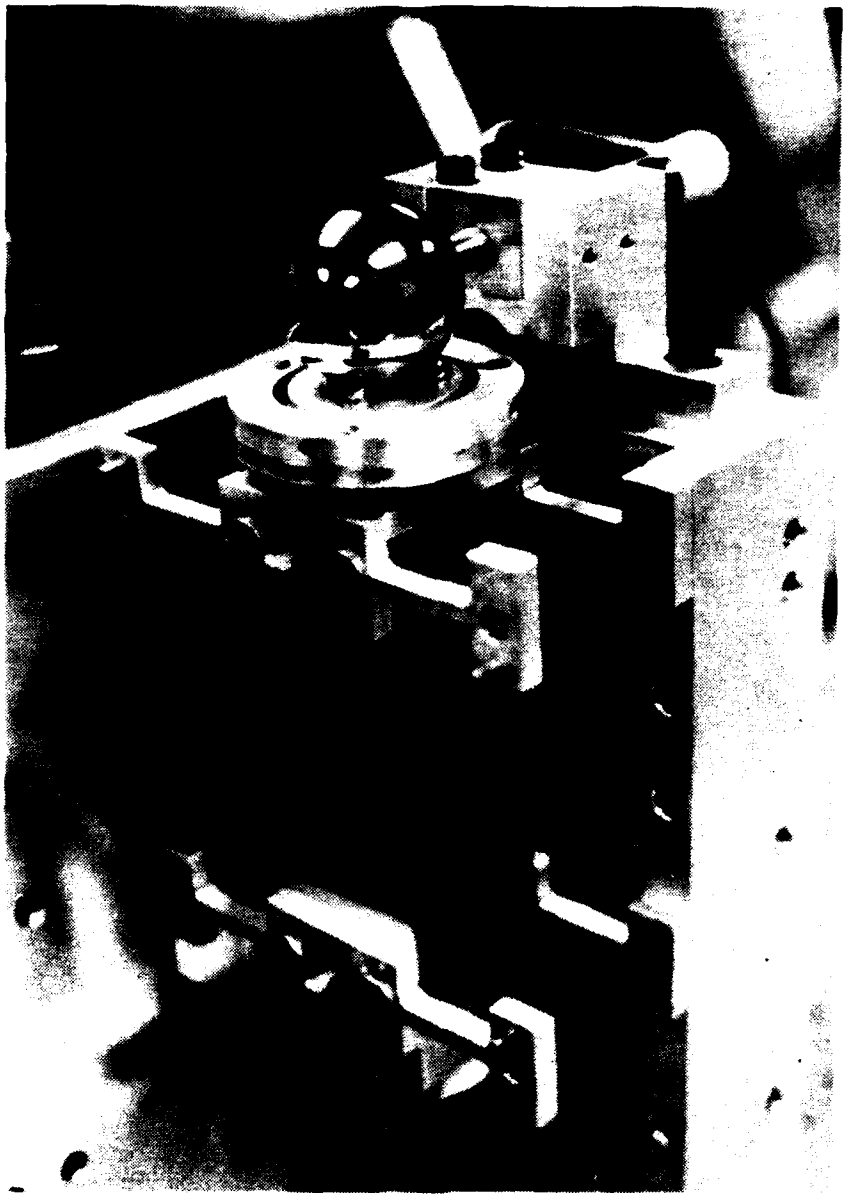

Figure 1. Experimental spindle apparatus

tapered end of the spindle shaft, and forms the spindle face. The plate and shaft are belt driven by a DC servo-motor. A 500 pulse/revolution incremental encoder, also belt driven, is used in conjunction with a once-per-revolution magnetic pick-up to trigger data collection.

On top of the spindle face is a 1 1/2" diameter master ball (5 microinch sphericity) that rests on a three point support. The master ball is the reference for the control system and all efforts to control the position of the spindle are referenced to it's surface. Because the spindle is to be corrected in real-time, as it rotates, a sensor/actuator pair exhibiting fast response is required. In addition, reasonable error correction of the nominal 100 μin. open loop radial runout of the spindle demands sensor and actuator resolution of 1 μin. or better.

The sensor used for measuring the remount error is a capacitance gage. This gage has a resolution of 0.1 μin. with frequency response of 40 kHz. and a 0.06 in. diameter spacially averaging probe tip. The first gage used with this spindle was an eddy current gage; however, it had significantly less resolution. In addition, because it is sensitive to target material composition, the eddy current gage added about 10 μin. of uncertainty to measurements of ball motion. The system actuator is a Piezoelectric Transducer (PZT) capable of smooth motion over increments as small as 1 μin. and frequencies up to 5 kHz with a usable displacement range of nearly 400 μin. With this sensor/actuator pair, the dynamics of the open-loop performance of the spindle system can be analyzed and an appropriate control scheme developed.

The open-loop frequency response of the system is illustrated in Figure 2. This transfer function represents the combined dynamics of actuator/structure/sensor. The transfer function shows 360° of phase shift in 0 - 500 Hz. The output/input amplitude of the transfer function is characteristic of a complex high order system with multiple poles and zeros. Further analysis of this system reveals two significant nonlinearities: hysteresis in the PZT actuator motion and a nonlinear input/output actuation characteristic. These effects are illustrated in Figure 3. A curve of dc input signal to the PZT actuator vs. output motion of the structure over the entire actuation rage. The upper curve represents positive motion (loading), while the lower curve represents negative motion (unloading). The separation between the loading and unloading curves is a nonlinearity known as the PZT's hysteresis. The overall curvature of the input vs. output represents a second nonlinearity.

Clearly, developing a reasonable control scheme for this system must incorporate either extensive, complex system modelling, significant simplification and approximation, or a compromise between the two.

THE CONTROL SCHEME

As a first approximation, a zero order system model can be assumed. That is, the response of the structure will be considered instantaneous and of constant gain. Such an assumption will not be valid at high

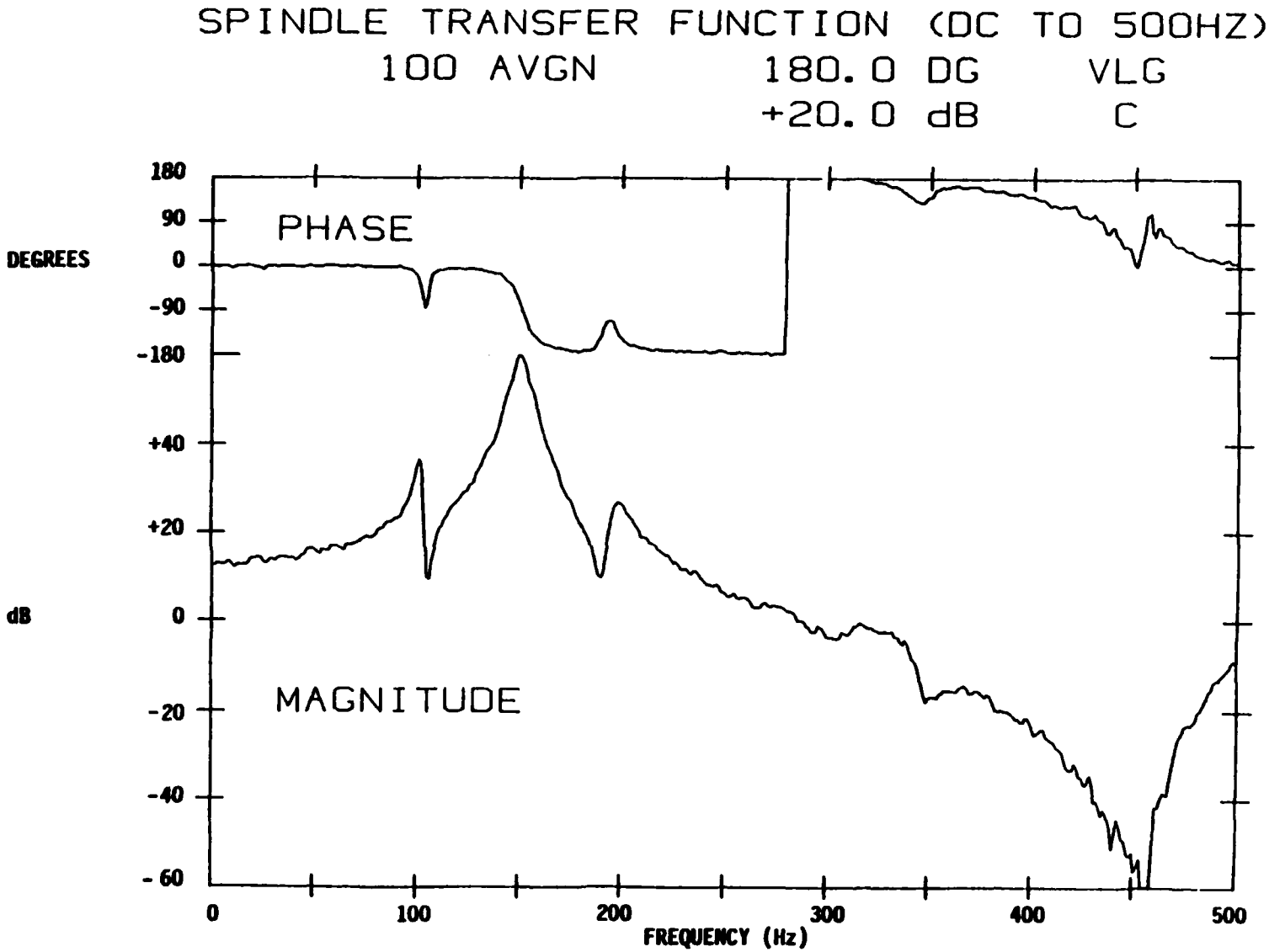

Figure 2. Open loop frequency response of spindle system

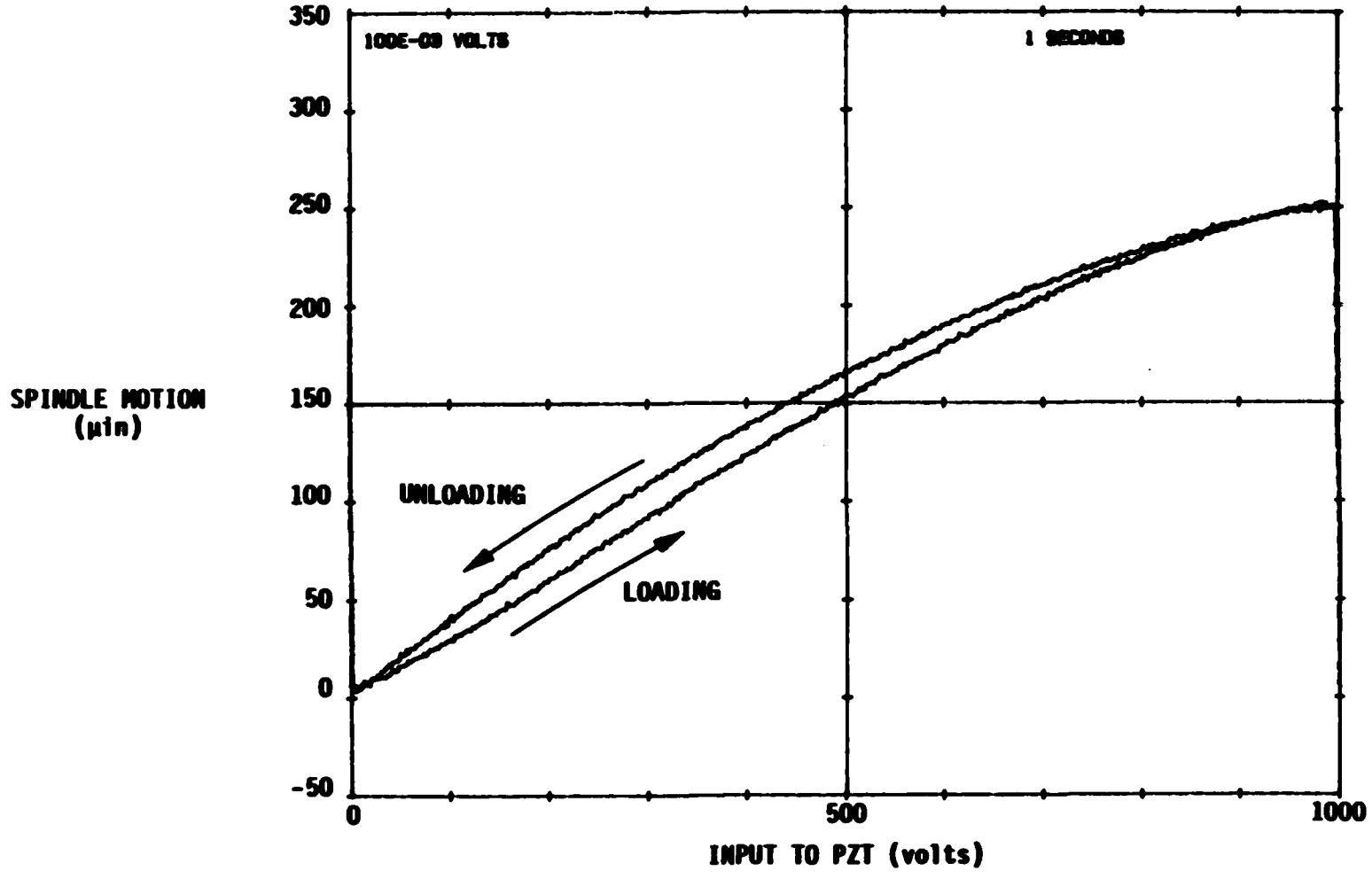

Figure 3. Non-linear characteristics of the PZT actuator

speeds of actuation, where the phase shift and attention shown in the transfer function become dominant. In fact, even at low speeds the lumped nonlinear input/output characteristic that was demonstrated in Figure 3 will stretch the constant gain assumption. At low/moderate speeds and in a closed feedback loop, however, these simplifications should prove adequate for the development of a satisfactory real time control algorithm.

The most elementary control algorithm from classical automatic control theory is proportional control, where the actuation input signal is proportional to the measured error. The drawback of this type of control algorithm used by itself is that it allows the existence of a steady state error. Such an error is intolerable for a position control scheme. This leads to a consideration of the next level of sophistication in a control algorithm: integral control. With this scheme, the error signal is multiplied by a gain and added to the current actuator input signal to form a new actuator input signal. In essence, the actuator input signal is then the integral sum of all of the past measured errors. With integral compensation, no steady state error can exist since any error, however small, will generate corrective feedback.

In discrete form the integral controller can be represented as

$$G_n = K \cdot E_n + G_o \qquad (1)$$

where G_n is the new actuator input signal, K is a constant gain, E_n is the current measured error, and G_o is the current actuator input signal. Such an algorithm is easily implemented on a digital computer, supplemented by an appropriate A/D converter to interpret the sensor output and D/A converter to supply the necessary analog compensation signal to the actuator. This was the first algorithm to be tested successfully as a real-time controller of the spindle runout [1]. The control system schematic is illustrated in Figure 4. This discrete control loop was implemented on a PDP 11 mini-computer with a 500 μs loop cycle time. This control system reduced the 100 μin. P-P open loop spindle radial runout by an order of magnitude to less than 10 μin. P-P at rotational speeds of up to 6 RPM.

An analysis of the operation of this control system uncovered several significant facts concerning its effectiveness. The first of these is that the system dynamics are significant; i.e. the zero order model is insufficient for control of motion at frequencies of motion above 150 Hz (the lowest frequency of vibration for this system). This difficulty is compounded by the fact that the D/A signal changes in discrete step functions. Since the frequency spectrum of a step contains energy at all frequencies, all of the natural vibrational frequencies of the system are excited to some extent by each output step. This effect is illustrated by the step response function of the spindle system presented in Figure 5. Two solutions to this problem have been tested. The first solution involves a two-step actuation scheme, in which the PZT is actuated with a primary step to achieve a desired displacement and then a secondary actuation step is used to effectively cancel the oscillations set up by the primary step [2]. This hybridized

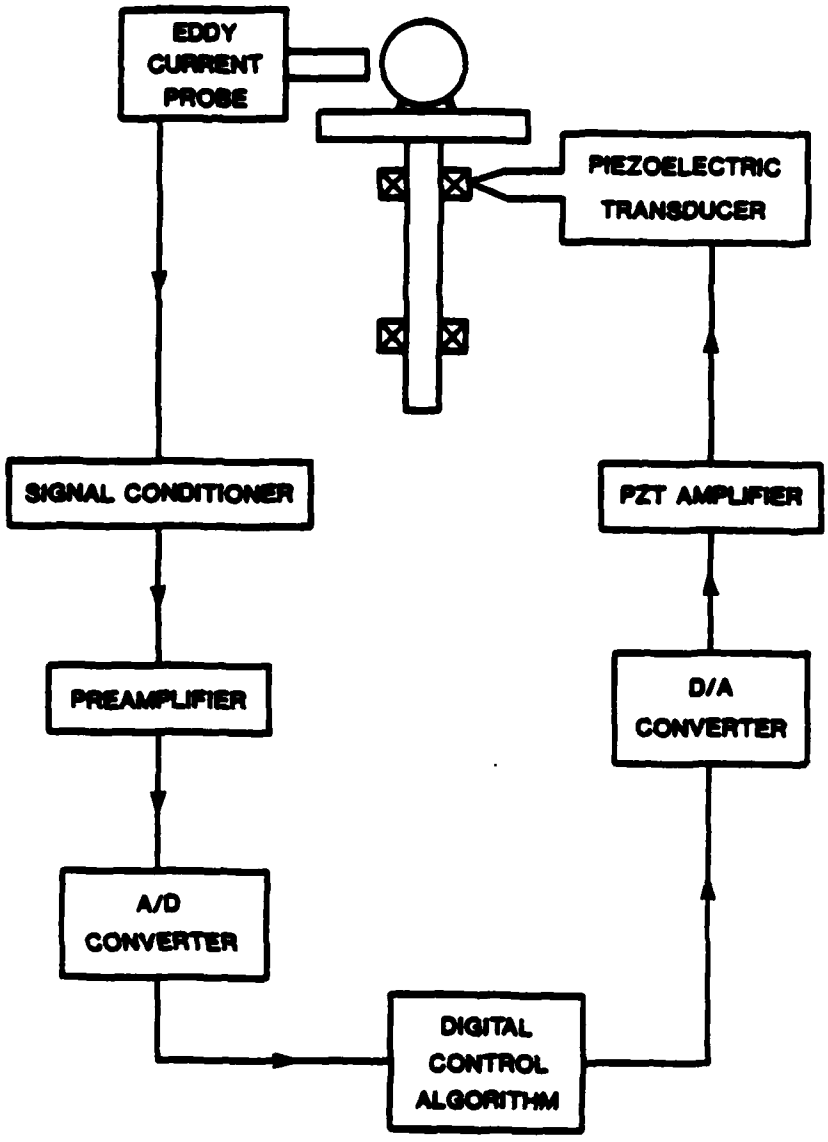

Figure 4. Schematic of feedback signal path

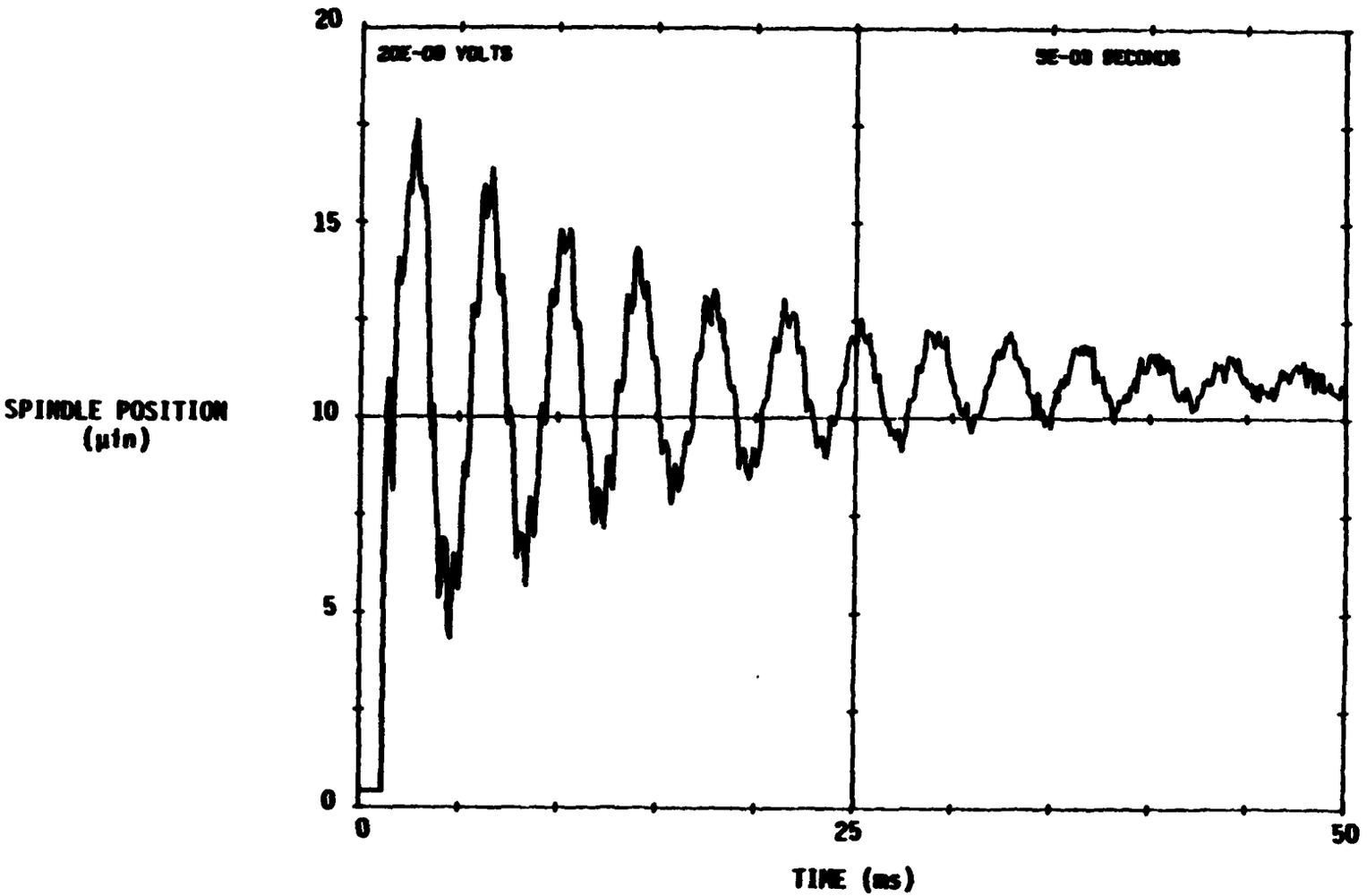

Figure 5. Step response of the uncontrollable spindle

method of actuation is well suited to a second order system, but it can only reduce oscillations at one frequency; the higher harmonics of structural vibration are unaffected.

A second option, more viable in this case, is to add damping to the PZT actuator. This is accomplished electrically with an in-line resistor as described by Burton [3]. The tradeoff here is between a sluggish system response and an effective elimination of actuator introduced vibration. An appropriate compromise considerably improves the overall step response of the PZT actuator.

A second discovery concerning the effectiveness of the control scheme was that the speed of the correction -- even with the introduction of "sluggish" PZT response -- was so fast that the average error measured per control cycle was on the order of 1 - 2 μin. That is this compensation scheme generally calls for a magnitude error correction that is comparable to the motion resolution of the PZT. Clearly, this small compensation signal is indicative of an effective control scheme; if the error ever gets larger than a few microinches per control cycle there will be a corresponding increase in the overall closed loop radial runout. The question, then, is why go to the trouble of measuring the magnitude of the error if it is always going to be approximately the same value? In other words, since the error must be small for the algorithm to reduce the radial runout, a measurement of the sign or direction of the error coupled with a small incremental correction provides an adequate control signal. At each sampling interval, the controller utilizes the directional error information to move the actuator one incremental "step" in the opposite direction. A step is a displacement which is small compared to the total range of the actuator. By continually incrementing or decrementing the actuator position in this stepwise manner, the displacement errors in the system are compensated. Clearly, the performance of such a system will depend directly upon the rate at which these incremental corrections are made. Ideally, this sampling rate should be high enough to keep the error within a tolerance equivalent to two incremental steps. That is, the controller will sense a small positive error and send a correcting step to the actuator, whose motion will create a slightly negative displacement error, returning the actuator to its original position. The two variables in the system are step size and sampling rate. While the former sets the sensitivity of the system, the latter determines its stability and robustness.

This direction sensing technique is ideally suited for differential measurement sensor. If a rigid structure is positioned between two similar transducers operated indifferentially, the sign of the difference signal is all that is required to determine the direction of the displacement error.

The advantages of a direction sensitive control scheme are significant. First, the requirements of the runout sensor are dramatically reduced. All that is required is a null detecting or differential gage. Thus, the linearity and absolute accuracy of the gage are irrelevant, presuming sufficient resolution and range. A second advantage is the reduced computational complexity of this system. The algorithm is

simple and direct; the PDP-II mini-computer used in the previously described integral controller could be replaced by several discrete electronic chips. Additionally, the A/D converter is eliminated from the control loop. This latter point is of considerable importance where shorter cycle times are necessary -- the A/D converter is often the bottleneck in control loop speed.

Mathematically, the algorithm is:

$$G_n = K \frac{E_n}{|E_n|} + G_o$$

or

$$G_n = \pm K + G_o$$

where G_n is the new actuator input, $E/|E|$ represents the sign of the error, K is the smallest incremental step size and G_o is the old actuator input.

This algorithm, incorporated into the radial runout control loop, is illustrated in Figure 6. The controller circuit is made from standard components, as there is no need for unusually refined analog or digital signal manipulation. An 8-bit digital to analog converter provides incremental signals to the PZT amplifier corresponding to discrete steps of 1 μin., with a maximum range of ± 128 μin. The clock rate and step size can be adjusted to suit the particular control application: A 1 μin. step at 150 Hz proved optimal for the radial runout control of the spindle. The 150 Hz clock rate is fast enough to control the spindle runout at speeds of up to 10 RPM, but slow enough to avoid the difficulty associated with forcing the spindle at its natural frequency. Clearly the controller described by Figure 6 will continue to either increment or decrement the PZT by 1 step per cycle even when there is no error to correct. This difficulty can be either ignored--resulting in a steady state sawtooth back and forth motion--or eliminated by incorporating a "dead zone" with no corrective action. The dead zone is treated extensively in the field of "relay" control, and can improve the performance of the system if the ± 1 microinch dither is a problem. For this particular application, the added controller complexity was not warranted.

The performance of this control system was comparable to that of the more complicated integral control, reducing the radial runout from 100 μin. to less than 10 μin. P-P at rotational rates of up to 10 RPM. Figure 7 illustrates the dramatic effect of this controller in a linear oscilloscope trace of runout vs. spindle rotational position.

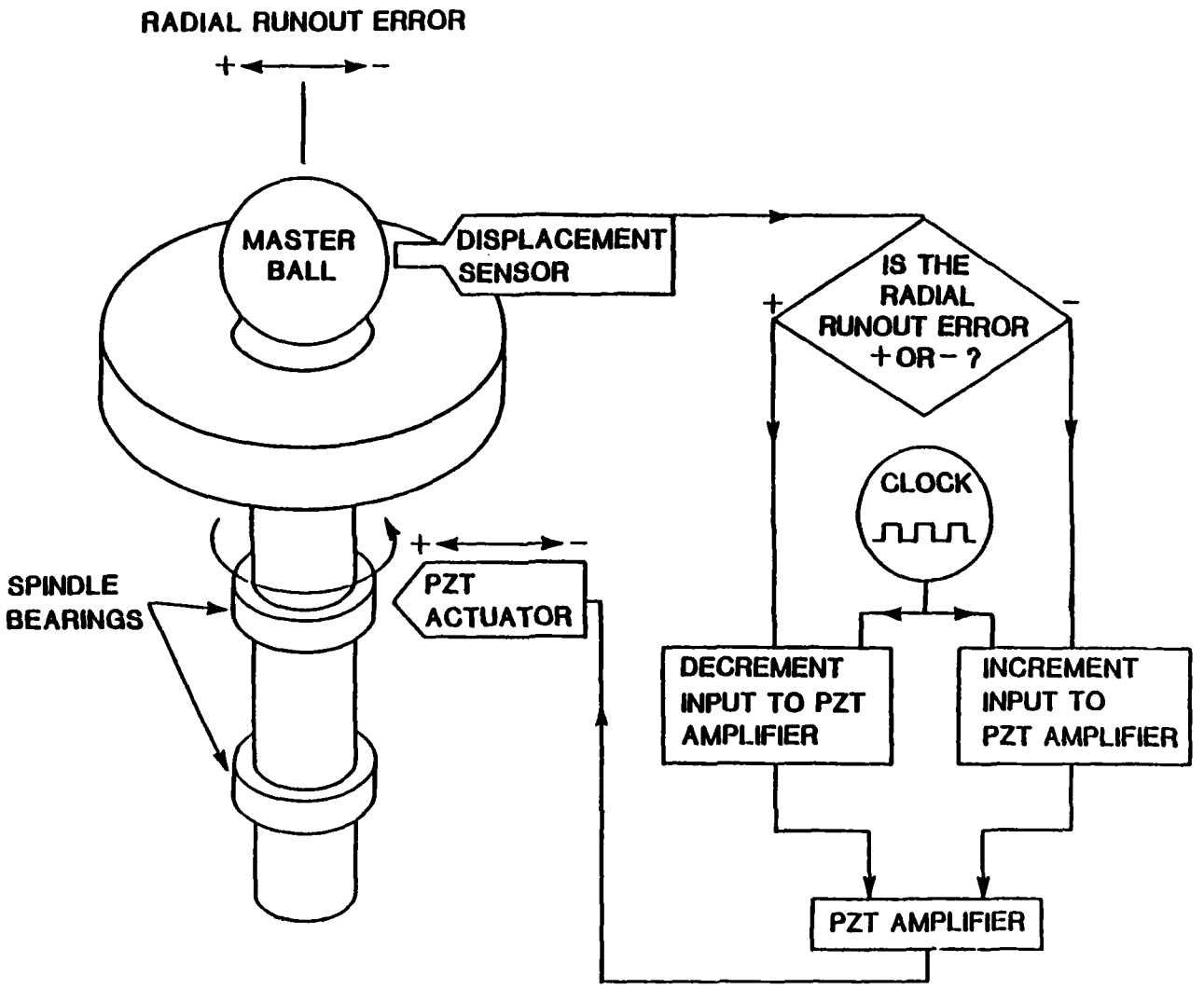

Figure 6. Schematic of the control system for radial runout correction

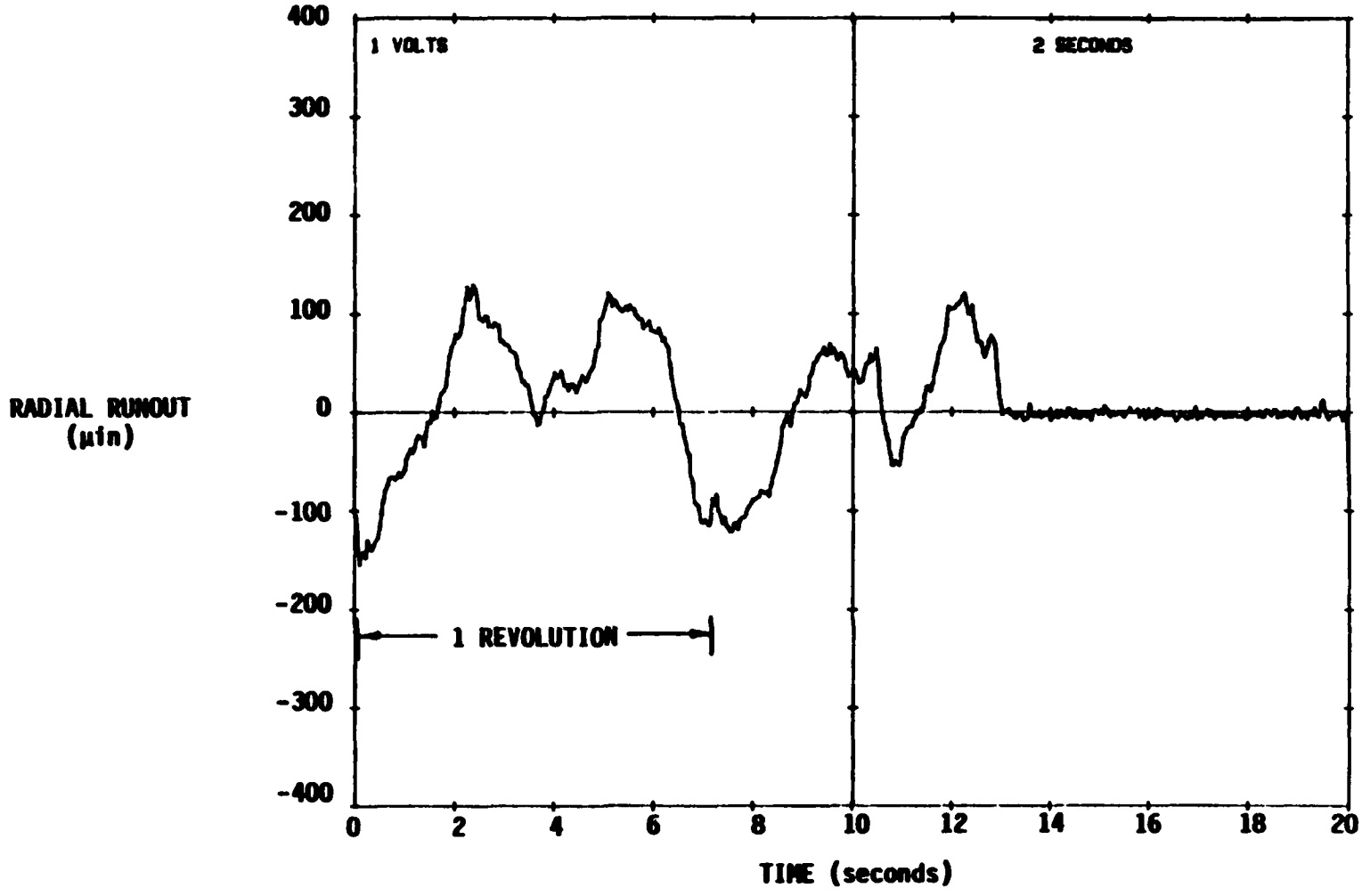

Figure 7. Runout correction using direction-sensitive controller

CONCLUSION

The development process for two real-time feedback systems for controlling position on a precision engineering apparatus has been presented.

The design process includes the selection of appropriate sensors and actuators along with carefully simplified modelling of the structure to be controlled. A straightforward integral controller has been presented, along with some methods for improving the response of this control strategy by the incorporation of added damping in the actuation loop. The results of this integral control study paved the way for a novel direction sensitive control system which greatly simplifies the complexity of both the sensor and the control algorithm, without sacrificing robustness or time response.

Although these results are presented for a specific control problem, the design process is similar for many positioning problems in precision engineering. Additionally, the algorithms (most notably the direction sensitive controller) are largely independent of the specific structure being controlled. Versatility of application is designed into the algorithms, which rely on straightforward error compensation and direct, simple implementation.

REFERENCES

1. Bifano, T. G. and T. A. Dow, "Real-Time Control of Spindle Runout," Optical Engineering, September/October 1985, p.

2. Bifano, T. G. and T. A. Dow, Second Annual Report on Precision Engineering, North Carolina State University, January 1985, p.

3. Burton, R. A., First Annual Report on Precision Engineering - SRO154, North Carolina State University at Raleigh, January 1984, p. 20

REAL-TIME CONTROL OF SPINDLE RUNOUT

By

Christopher M. Cagle
Graduate Student
Precision Engineering Laboratory

And

Thomas A. Dow
Professor
Mechanical and Aerospace Engineering Department

ABSTRACT

An effort has been made to control in real-time the runout of a ball bearing spindle. Position of a master ball mounted to the spindle is measured by a capacitance gage displacement transducer. A dedicated mini-computer is used to control the position of the spindle by supplying a time varying voltage signal to a piezoelectric transducer (PZT). A parameter-optimized proportional-integral-derivative (PID) controller is used to supply the proper signal to the PZT. Results indicate that a stable controller can be realized which greatly reduces the runout of the spindle. At 30 rpm a reduction of spindle runout from 100 μin. to 5 μin. is typical.

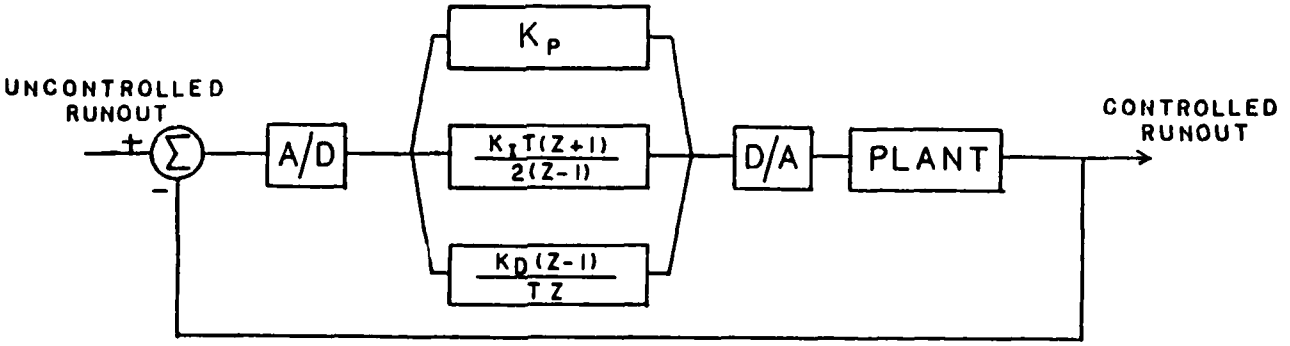

INTRODUCTION

One of the most important aspects of precision machining is the accuracy of a rotating spindle. Various types of bearings have been used to produce the required high stiffness and runout in the microinch range. Precision ball bearings are, at best, at the upper limit of allowable accuracy for ultra-precision applications, and are subject to wear. Well designed air and fluid bearings have high stiffness, very low runout, and do not wear, but tend to be very expensive. Efforts have been made to improve the runout of air and fluid bearings by varying the supply pressure as a function of position to correct runout [1,2,3]. These efforts have promise at low speeds but may have stability problems at higher speeds. The study described in this paper represents an extension of previous work done in the Precision Engineering Laboratory toward real-time control of runout in a ball-bearing spindle.

The runout in a ball bearing is of two types, systematic and random. Systematic errors are due to inaccuracies in inner and outer races, and in the balls. Random error is caused by impurities within the bearing, internal vibrations, and external disturbances. Due to the complexity of systematic runout, the error is treated as purely random. The existing test structure was redesigned to minimize unwanted vibration. A digital proportional-integral-derivative (PID) controller is utilized because it is both easy to implement on a computer and has a fast cycle time. The PID controller uses position feedback to make a first order approximation of velocity to produce a quick step response with little overshoot. To optimize the controller, three variables must be chosen which will produce a satisfactory response. This is done using a combination of frequency domain and time domain analyses. Frequency analysis is used to generate a transfer function for the system. With the transfer function, a state variable model is created which will show in the time domain the response to any input with any controller. This model is used to generate the three constants for the PID controller.

APPARATUS

The test apparatus consists of a ball bearing spindle attached to an outer housing by means of eight cantilever springs. The previous apparatus (see 1st Annual Report pg. 95) was plagued by excessive vibration at the reference ball largely due to the size of the spindle shaft and the large mass attached at the end of the shaft well away from the support points (Figure 1). A redesign was made which minimized this vibration without a total rebuild of the structure. The spindle diameter was made larger, the overhanging mass was greatly reduced, and the distance from the support to the mass was made as short as possible. The result was an increase of the natural frequency from 120 Hz. to 270 Hz. with a corresponding decrease in amplitude of vibration. The present design utilizes a pair of 15 mm (.6693 in.) bore ABEC-7 angular contact preloaded ball bearings. These bearings exhibit no measurable free play with light preloading. The cantilever support springs are unchanged from the previous design. A dynamic finite element analysis

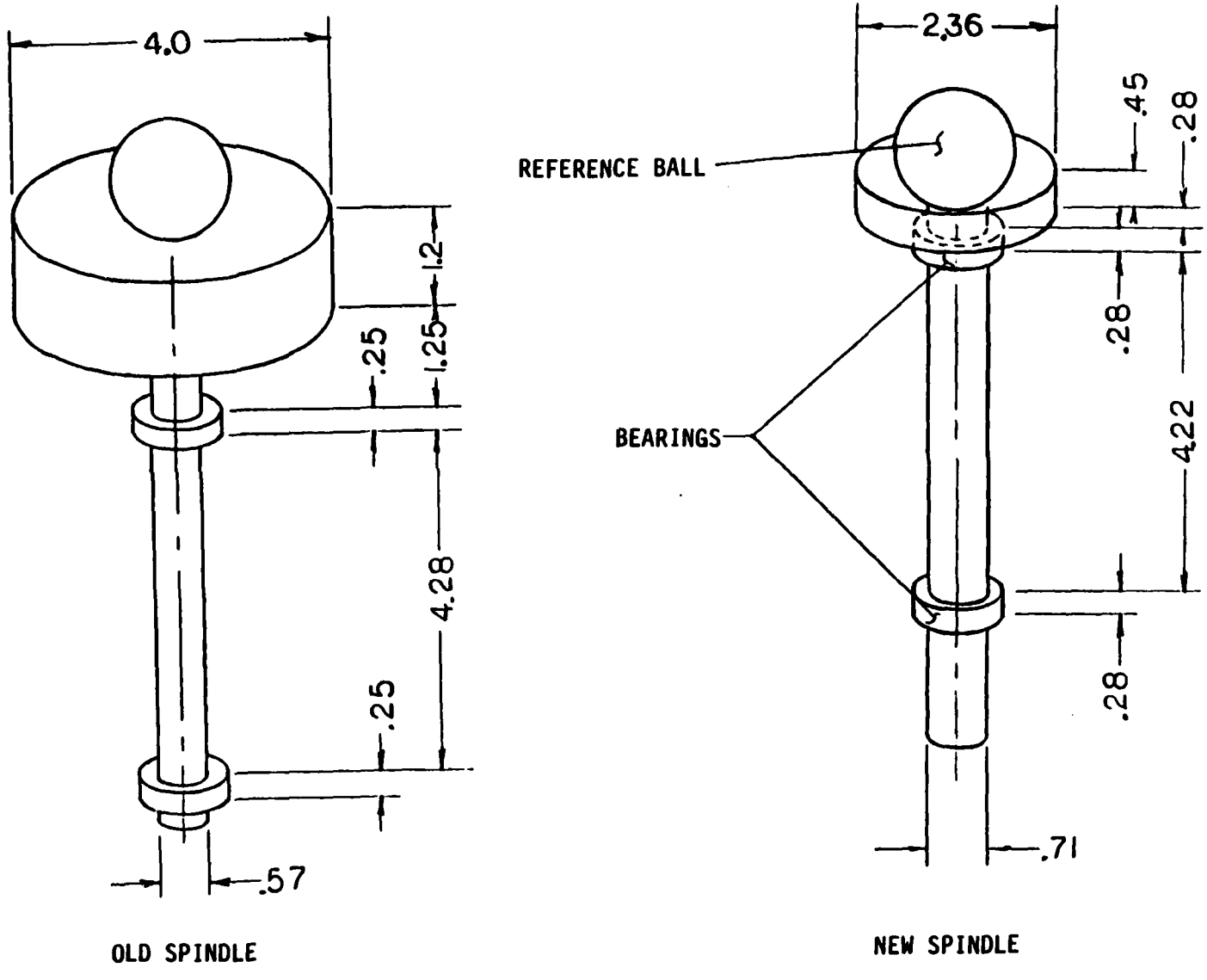

Figure 1. Dimensions in inches

(using SAP IV) was performed on the spindle-bearing-cantilever assembly to determine the mode shapes of the vibration. This analysis was used to redesign the structure to minimize vibration. The finite element analysis predicted a natural frequency of about 310 Hz. while the measured vibration is at about 270 Hz. The displacement is measured by a capacitance displacement transducer. This device has a sensitivity of about .5 μ in. as observed in the laboratory. Motion actuation is by a Physics International piezoelectric transducer of the stacked disc type located at the upper bearing. This device has a range of about 250-300 μ in. The control algorithm is implemented on a DEC PDP/11 based data aquisition computer.

CONTROL SYSTEM

A PID controller was chosen for three reasons: 1) it produces a quick step response, 2) it is easy to implement on a computer, and 3) it has a reasonable cycle time. While the control algorithm itself is easy to program, there are three variables, or gains, in the controller which must be determined in order for the controller to perform well. The determination of these gains require modelling of the structure and the controller to simulate the dynamic response of the assembly.

Derivation of Controller

In the z-domain the digital PID controller can be described by the system transfer function G_c: [4]

$$G_c(z) = K_p + \frac{K_i T(z+1)}{2(z-1)} + \frac{K_d\,(z-1)}{Tz}$$

where:

K_p = proportional constant
K_i = integral constant
K_d = derivative (velocity) constant

Expanding this equation yields;

$$G_c(z) = \frac{C(z)}{R(z)} = \frac{(2K_pT + K_iT^2 + 2K_d)\,z^2 + (K_iT^2 - 2K_pT - 4K_d)\,z + K_d}{2Tz^2 - 2Tz}$$

If the following substitutions are made:

$$K_1 = (2K_pT + K_iT^2 + 2K_d)/(2T)$$

$$K_2 = (K_iT^2 - 2K_pT - 4K_d)/(2T)$$

$$K_3 = 2\,K_d/(2T)$$

Then;

$$\frac{C(z)}{R(z)} = \frac{K_1z^2 + K_2z + K_3}{z^2 - z} = \frac{K_1 + K_2z^{-1} + K_3z^{-2}}{1 - z^{-1}}$$

This can be easily converted to a difference equation,

$$C(n) = C(n-1) + K_1R(n) + K_2R(n-1) + K_3R(n-2) \qquad (1)$$

where

C = Output
R = Input
T = Sample period
K's are constants
n represents time step i.e. (n = current time step)
(n-1 = previous step)

Equation (1) is all that is needed to be implemented on the computer. This derivation shows that the only information needed is the current displacement error plus the two previous displacements.

Modeling of System

To model the system, an open loop transfer function of the spindle assembly (plant) is obtained as follows. A sinusoidal signal is input to the spindle assembly through the PZT actuator and varied throughout the desired frequency range. The transfer function is obtained from a two-channel frequency analyzer by comparing the input sinusoidal signal to the output of the capacitance gage mounted at the reference ball. From this experimental data, a mathematical transfer function is obtained. First an estimation of the transfer function is made using graphical techniques [5]. Then, a least squares minimization program is used to obtain a best fit between the mathematical and experimental transfer functions. The minimization program used was a direct search method of Powell [6,7]. From the transfer function, a state variable model was obtained [8]. From this, a computer program using Runge-Kutta to solve the resulting system of first order differential equations produces difference equations which describe the time response of the system with any input and any controller [9]. Now the time response of the system can be studied with different combinations of the three gains to determine the optimum performance.

Implementation and Results

From experimental data, it was determined that a second order transfer function adequately describes the current structural configuration at frequencies up to about 450 Hz. The amplitudes of any vibrations above this were measured to be less than that of the fundamental frequency (270 Hz.) by a factor of ten or more and could be neglected. Figure 2 shows the experimental and mathematical transfer functions up to 500 Hz. These demonstrate good agreement in amplitude and phase. Figure 3 shows a typical simulation for values of the PID controller optimized to produce a good step response. Figure 4 shows an uncontrolled actual step response and a step response using an optimized controller. Comparison of Figures 3 and 4 exhibit good agreement between simulation and actual response indicating that the model used is adequate. The PID controller produces zero steady state error with good step response. However, for the rotating spindle, there is no steady state. Therefore the controller will always be responding to transient input and will not have zero error. Attempts to improve the transient response by increasing the gains lead to stability problems. On the PDP/11, integer arithmetic is performed much faster than real arithmetic. For the control sequence, real arithmetic takes about four times longer than integer math. If the three gains can only have integer values, then resolution is limited. As the gains are increased the margin of stability decreases. This limited resolution and narrow stability margin prevent a stable controller with increased gains. The integer-valued controller used has a cycle time of 350 microseconds in FORTRAN on the PDP/11.

An oscilloscope trace showing transition from uncontrolled to controlled rotation demonstrates a dramatic reduction in runout, Figure 5. At 60 rpm., a reduction from 100 μin. runout to about 7 μin. is typical. Figure 6 shows the relation between rotational frequency and runout. The controlled runout increases as frequency increases. This error has two major causes. At low rotational speed, the major error is due to the spindle vibrating at its natural frequency. This vibration is caused by the integer roundoff of the controller, by slight oscillation inherent in a fast controller, and by sharp transients in the uncontrolled runout signal. At high rotational speed this vibration is overwhelmed by phase lag due the inability of the PID controller to produce zero steady state error for any input other than a step.

The PID controller exhibited some ability to counteract transients due to external sources. With a sharp impulse input, there was an estimated reduction of 25% in the amplitude of the controlled spindle over the amplitude of the uncontrolled spindle. The period of vibration was significantly reduced with the controlled spindle having a period about half that of the uncontrolled spindle. However, a steady (or low frequency) disturbance produced no measurable displacement in the spindle. That is, the spindle has infinite stiffness with respect to low frequency disturbances.

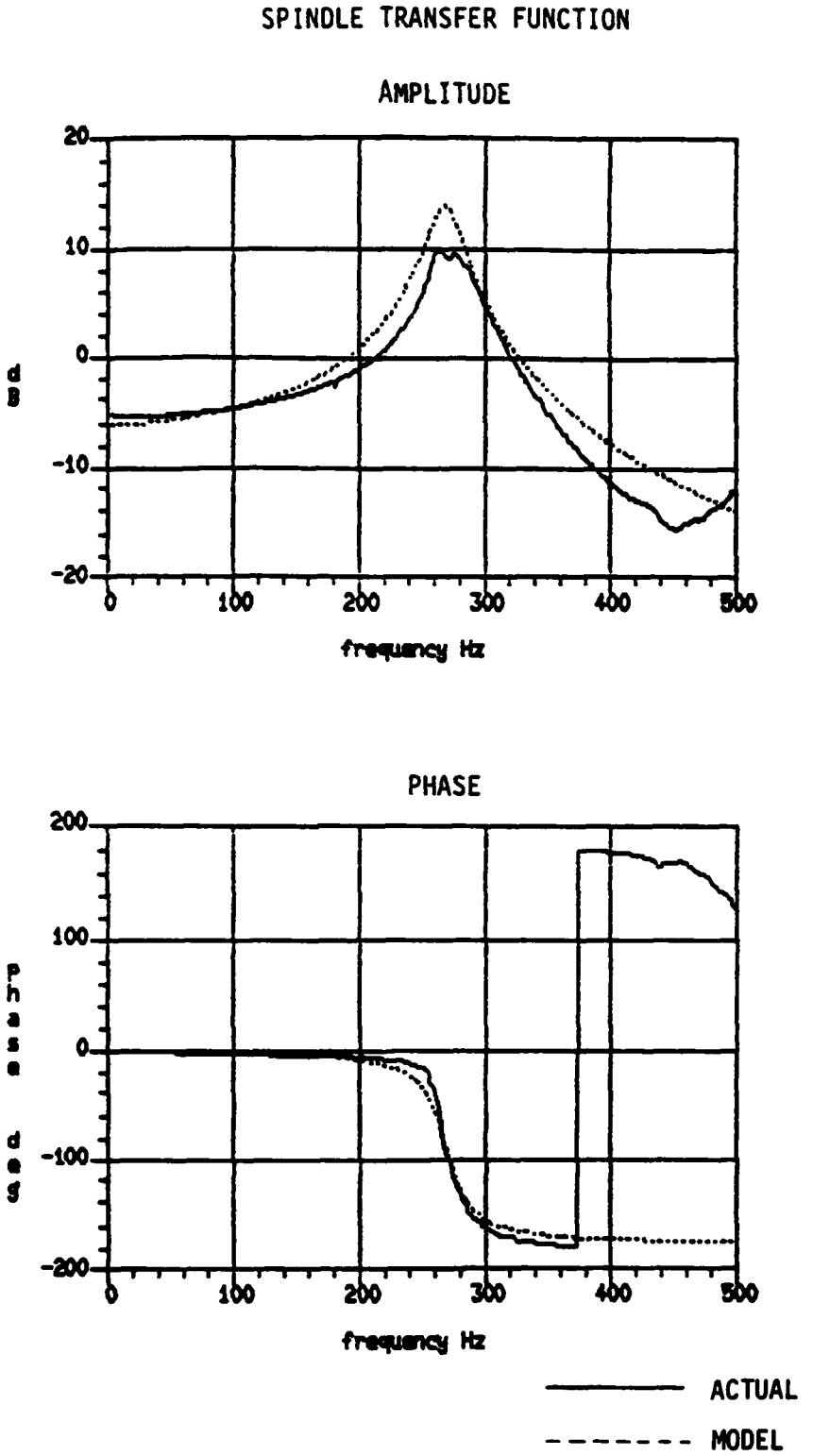
SPINDLE TRANSFER FUNCTION
AMPLITUDE
20
10
0
-10
-20
dB
0
100
200
300
400
500
frequency Hz
PHASE
200
100
0
-100
-200
degrees phase
0
100
200
300
400
500
frequency Hz
ACTUAL
MODEL

Figure 2.

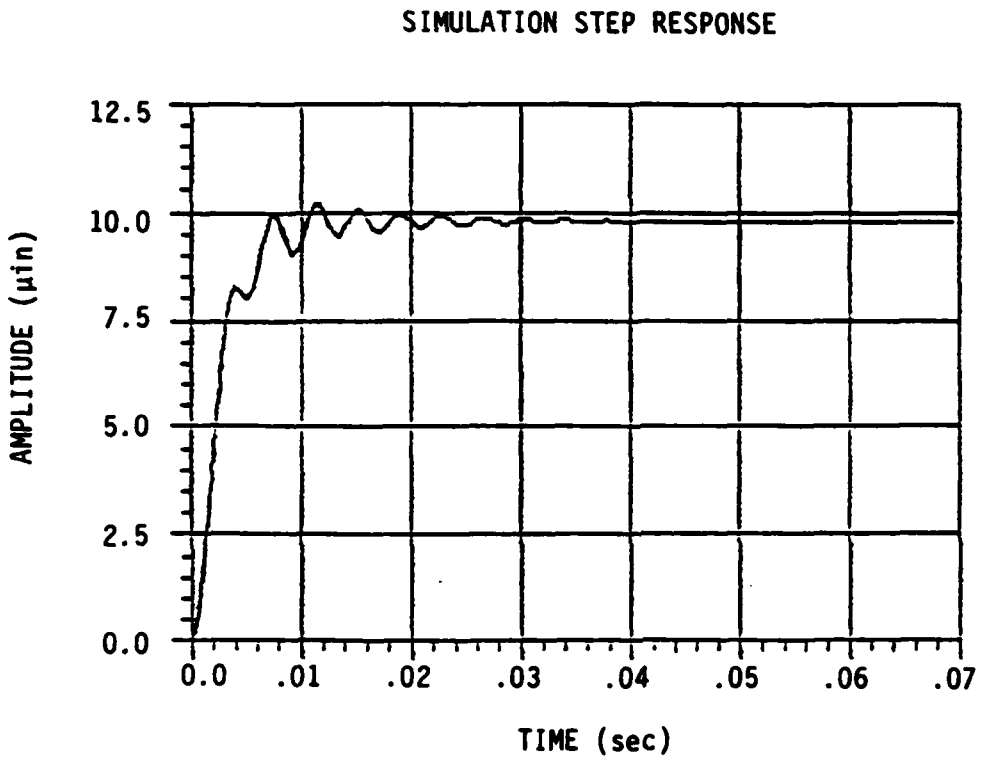
SIMULATION STEP RESPONSE
12.5
10.0
7.5
5.0
2.5
0.0
AMPLITUDE (μin)
0.0
.01
.02
.03
.04
.05
.06
.07
TIME (sec)

Figure 3.

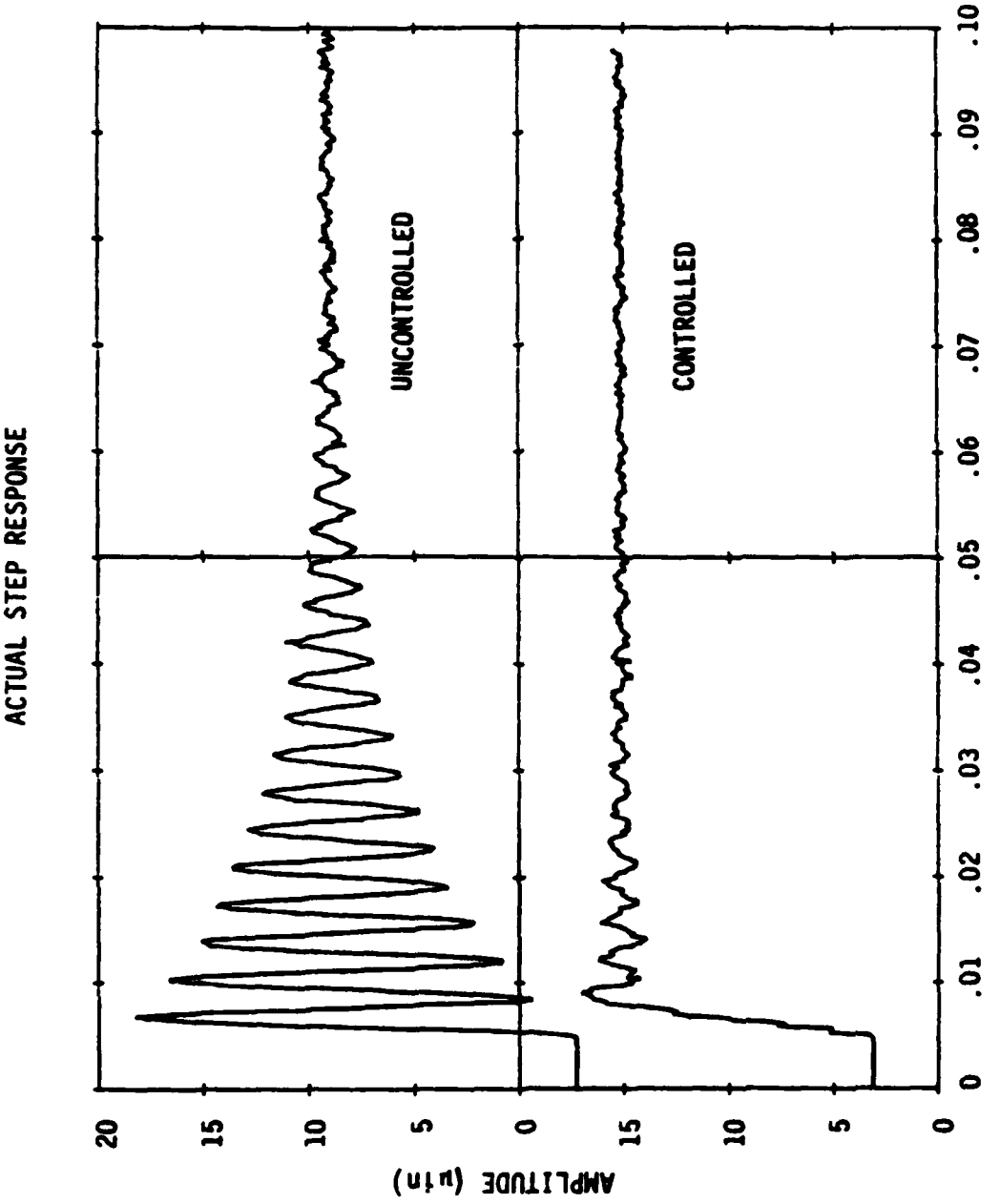
ACTUAL STEP RESPONSE
UNCONTROLLED
CONTROLLED
AMPLITUDE (μin)
TIME (SEC)
20
15
10
5
0
15
10
5
0
0
.01
.02
.03
.04
.05
.06
.07
.08
.09
.10

Figure 4.

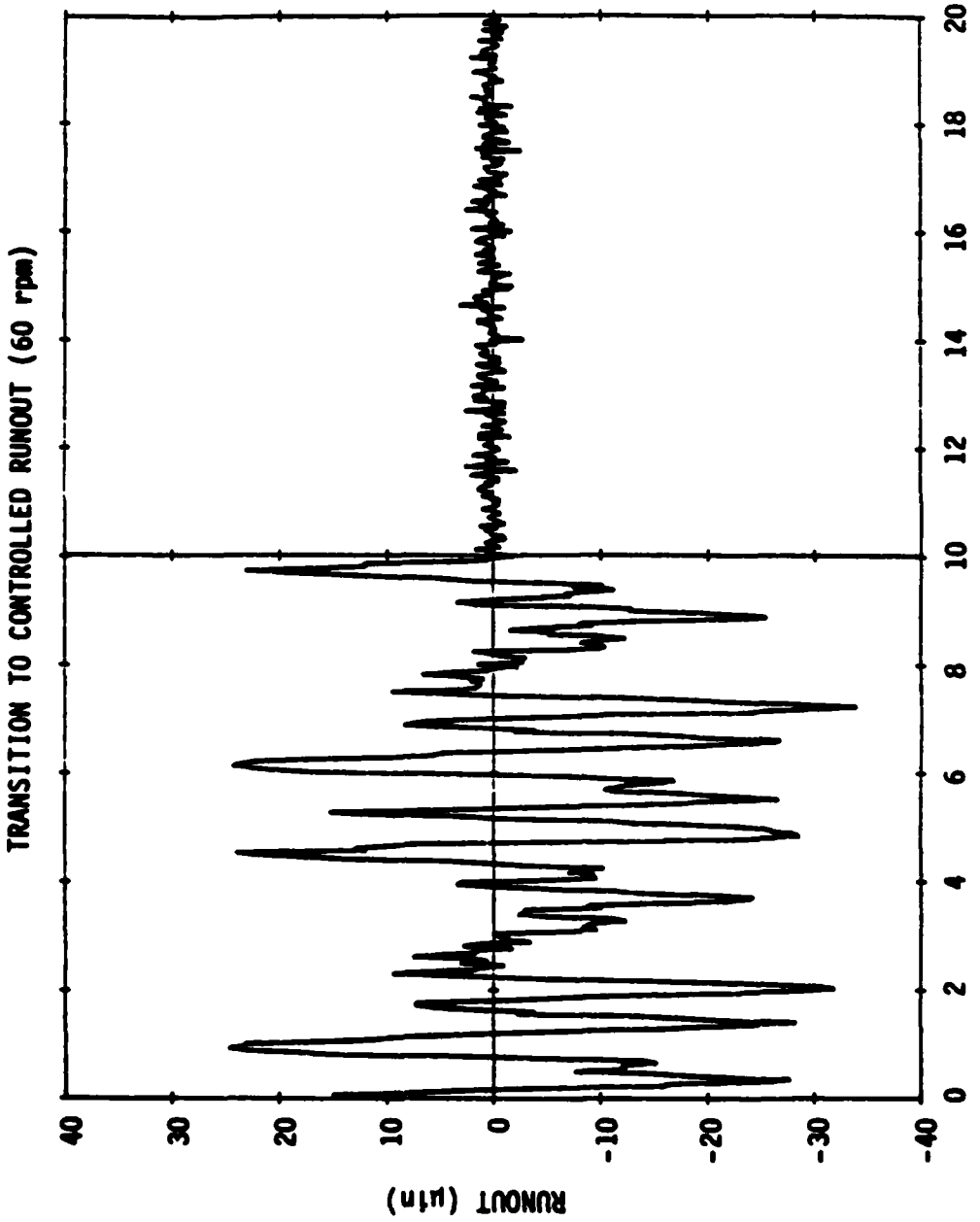
TRANSITION TO CONTROLLED RUNOUT (60 rpm)
RUNOUT (μin)
40
30
20
10
0
-10
-20
-30
-40
0
2
4
6
8
10
12
14
16
18
20
TIME (sec)

Figure 5.

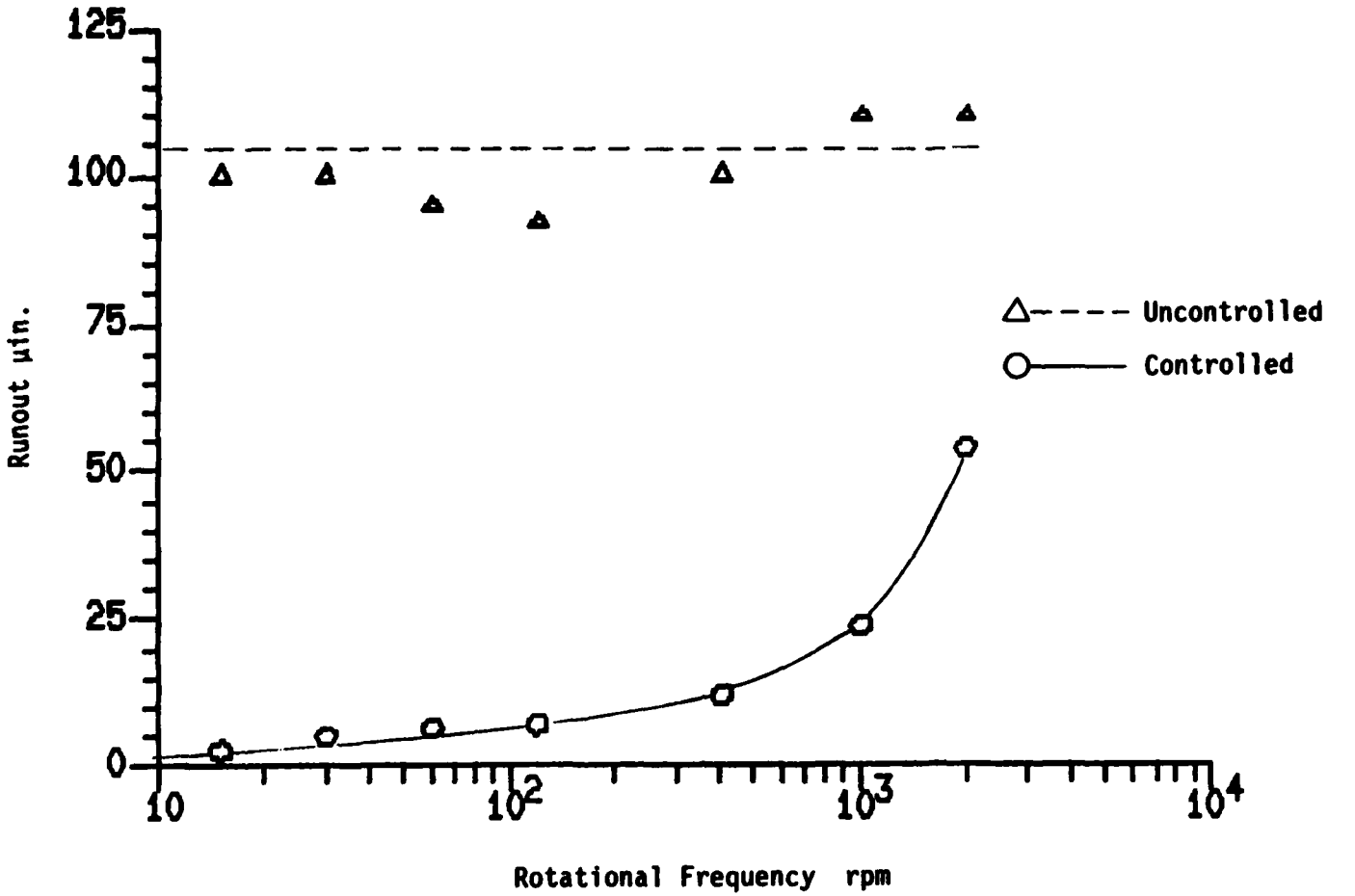

Figure 6. Runout vs. frequency for spindle assembly

CONCLUSIONS

The PID controller was compared to an integral controller for the same physical system . The parameter-optimized PID controller decreased the runout by a factor of about two compared to a slightly faster integral controller. The redesigned apparatus performs much better than the original due to an improved control system and reduction of extraneous vibration. The increased natural frequency of the spindle decreased the response time of the system enabling better tracking of a transient error signal. Within the limits of the piezoelectric transducer the corrected spindle exhibits infinite stiffness to low frequency external forces. The active control also provides correction for wear and thermal growth since all changes are treated as random errors.

REFERENCES

1. Pande, S. S. and S. Somasundaram, "Analysis of Aerostatic Journal Bearings with Positioning Sensing Restrictor", Wear, Vol. 70, No. 2, Aug. 1981, pp. 141-154.

2. Kanai, A. and M. Miyashita, "Nanometer Positioning Characteristics of Closed Loop Differential Hydro-or Aerostatic Actuator," Annals of the CIRP, Vol. 32, No. 1, 1983.

3. 回転振れ補正機構を持つ高精密回転軸系の開発(第3報)
   ―開発した高精密回転テーブルと回転振れ補正―
   東芝・生研 ○野村武彦　　都立大 金井 彰　　宮下政和

4. Kuo, Benjamin C., Digital Control Systems, Holt, Rinehart & Winston, New York, 1980.

5. Hale, Francis J., Introduction to Control System Analysis and Design, Prentice-Hall, New Jersey, 1973.

6. Rao, S. S., Optimization Theory and Applications, 2nd ed., John Wiley & Sons, New York, 1984.

7. Powell, M. J. D., "An Efficient Method for Finding the Minimum of a Function of Several Variables Without Calculating Derivatives," Computer Journal, Vol. 7, 155, 1964.

8. Kuo, Benjamin C., Automatic Control Systems, Prentice-Hall, New Jersey, 1982, pp. 62-87.

9. Maday, C. J., First Annual Report on Precision Engineering, North Carolina State University, Raleigh, 1983, p. 61.

ACTIVE CONTROL USING POWER FLOW TECHNIQUES

By

Richard F. Keltie
Associate Professor
Mechanical and Aerospace Engineering Department

ABSTRACT

The structure of a machine tool has a profound effect on the characteristics of the finished workpiece. The desire for high precision parts with microinch tolerances on both the shape and surface finish has created new demands on machine tool structures. Past solutions have involved increased stiffness of the assembly to reduce the relative motion between tool and workpiece. For future needs, this solution may not be sufficient.

The concept of active structural control based on structural power flow considerations is described. Control of vibratory energy is a more basic approach than that involving kinematic variables such as displacement. In addition, it is possible to address more complicated structures, and higher frequencies, using this technique. Initial studies have been directed towards the formulation of structural power flow concepts and the experimental techniques whereby the measurements may be performed. A baseline experimental investigation is described, along with results obtained from a numerical simulation.

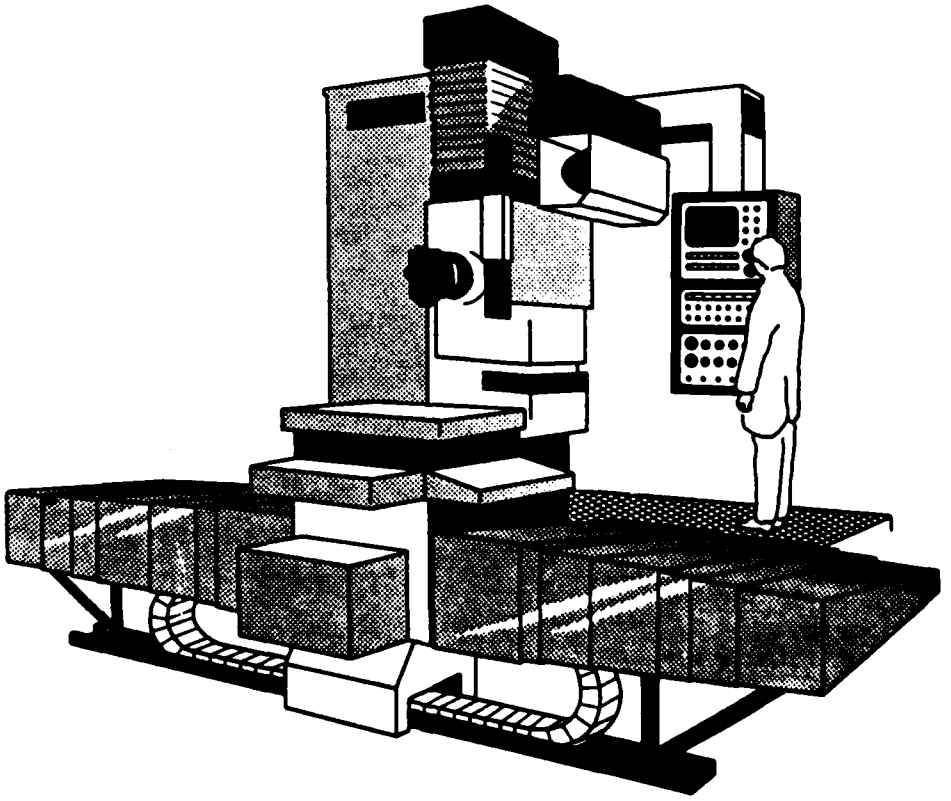

INTRODUCTION

Precision machining of mechanical components to fine tolerance, together with requirements on surface finish characteristics, have placed new demands on the ability to minimize the dynamic relative motion arising in machine tool structures between the tool and the workpiece. Reduction of this motion is one of the most readily identifiable approaches for increasing machined part precision, and is manifested in modern machine tools by very high local stiffness values. This high stiffness assures that even though the disturbing forces remain unchanged, the subsequent local deformation will be reduced. A parallel, and more fundamental, approach to this problem of motion reduction is to reduce the forces responsible for the motion.

The control of disturbing forces may be sought either at their source, reducing the magnitude of the generated forces, or along the many transmission paths whereby dynamic disturbances propagate to the tool/workpiece location. It is the problem of energy propagation in complex built-up structures that represents both the greatest challenge as well as the greatest potential for achieving control and reduction through machine design. When the precise mechanism controlling energy flow, wave interactions, and structural scattering and dispersion are well understood, it will be possible to design structural components and interfaces to block the transmission of unwanted vibratory motions, including both wideband and narrowband disturbances.

Active control of structural components typically focuses attention on one of the kinematic variables in the system, either displacement, velocity or acceleration. Implementation techniques usually begin with a modal description of the system, which is essentially an N-degree-of-freedom discrete model, meaning that the structure is divided into discrete mass and spring elements. Within the limitations of this formulation, a set of externally applied control forces are generated to achieve the desired structural motion. Owing to the basic nature of this approach, it is generally limited to fairly low frequency due to the inability to accurately describe the boundary conditions and response of complicated structures at higher frequency. Practical, factors such as modal overlap, boundary dissipation and boundary condition uncertainties, complicate the modeling process. In addition, the attachment of the control actuators often alters the dynamic character of the original system, thereby adding another uncertainty to the discrete model.

As the complexity of the system and the frequency range of interest increase, the modal model approach becomes less useful for structural characterization. This is especially true for systems possessing either large inherent damping due to material properties or significant external damping. For these situations, it is more appropriate to develop a wave-type model of the structure [1,2]. This methodology allows a much more complete description of the system's dynamics and the interaction between the structure's various components. Within such a framework, it is possible to focus attention on a more fundamental parameter than displacement, namely the distribution of actual vibratory power in the structure. From a control viewpoint, it is certainly true that any response variable will be minimized if the one can minimize the struc-

tural energy reaching that location. Thus the ability to describe, measure and control (either actively or passively) structural power flow represents a viable means for ultimately implementing effective control at any frequency in structures of arbitrary complexity. Since power flow descriptions in complicated structures are largely unknown at this time, the initial task in this research effort involved formulation of experimental power flow mesurements. Given this capability, it will be possible to investigate the control of structural power flow using active real-time techniques.

POWER FLOW FORMULATION

One of the most important types of wave motion in engineering structures is that of transverse flexural motion, as occurs in beamlike and platelike components. The one-dimensional equation of motion is given by:

$$D \frac{\partial^4 y(x,t)}{\partial x^4} + m \frac{\partial^2 y(x,t)}{\partial t^2} = f(x,t) \tag{1}$$

where

D is the flexural rigidity,
y(x,t) is the transverse displacement,
m is the mass per unit length,
f(x,t) is the applied force distribution,

In such a system, power is transmitted via two mechanisms: one arising from the shear force through the thickness and the other arising from the bending moment. It can be shown [3] that the analytical expression for the total structural intensity vector J_x (power flow per unit area) in such a structure is given by:

$$J_x = D \left\{ \frac{\partial^3 y}{\partial x^3} \frac{\partial y}{\partial t} - \frac{\partial^2 y}{\partial x^2} \frac{\partial^2 y}{\partial x \, \partial t} \right\} \tag{2}$$

In equation (2) the first term represents the power flow due to the shear force and the second that due to the bending moment. The nature of the terms in this equation show the physical quantities that must be measured to monitor power flow: 1) second and third order spatial gradients of the displacement; 2) transverse velocity; and 3) rotational velocity. All quantities must be measured at the same location on the structure. This represents a formidable experimental task, since only transverse motion may be simply measured with transducers such as accelerometers. It is possible however to make approximate measurements of these quantities by employing finite difference approximations.

Consider the problem of estimating the power flow at the point x_0 shown in Figure 1, and suppose that the transverse displacement is measured at the four locations x_1, x_2, x_3 and x_4. Let the corresponding displacements be given by y_1, y_2, y_3 and y_4. If h is the distance between these measurement points, then the approximate form corresponding to equation (2) is given by [3]:

$$J_x = \frac{D}{h^3} \left\{ \frac{\partial y_3}{\partial t} (y_1 - 2y_2 + y_3) - \frac{\partial y_2}{\partial t} (y_2 - 2y_3 + y_4) \right\} \qquad (3)$$

Thus it is possible to obtain the desired information employing only displacement and velocity measurements, but an array of four transducers is required. This will allow the measurement of the instantaneous power flow at a point, and the orientation of the array will provide the sense of direction associated with the intensity vector J_x.

Since we are dealing with a time-varying quantity, it is usually of greater importance to measure the time-averaged value. It may be shown that the expression for the time-averaged intensity vector, $\langle J_x \rangle$ is given by:

$$\langle J_x \rangle = \frac{D}{h^3} \left\langle \frac{\partial y_2}{\partial t} (4y_3 - y_4) - \frac{\partial y_1}{\partial t} y_3 \right\rangle \qquad (4)$$

Equation (4) represents the basic result for obtaining estimates for the one dimensional power flow in a structure due to flexural motion. In such a problem there are two distinct types of motion [4]: 1) true wave motion corresponding to propagating flexural waves, responsible for transferring energy over large distances; and 2) the so-called near field component that does not propagate but rather is found only near applied forces, structural boundaries, or other locations where the structural impedance changes. Although this latter component contributes to the total energy density locally, it is generally not of importance in the free-field of the structure (that is, remote from forces, boundaries, etc.). When this component may be safely neglected, it is possible to obtain a further simplification for equation (4). For the case of harmonic motion in space and time (single frequency component ω), the simplified time-averaged intensity vector expression is given by:

$$\langle J_x \rangle = \frac{2\sqrt{Dm}}{h\,\omega} \left\langle \frac{\partial^2 y_2}{\partial t^2} \frac{\partial y_3}{\partial t} \right\rangle \qquad (5)$$

Thus, in the free-field, the structural power flow may be measured by an array of only two transducers, one measuring transverse acceleration, and one measuring transverse velocity. A laboratory experiment was

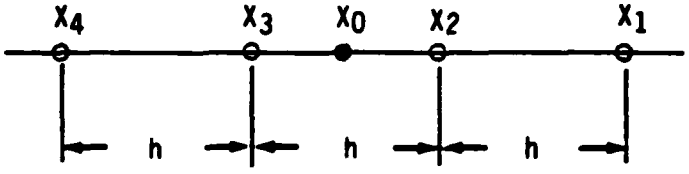

Figure 1. Finite difference grid for structural intensity vector approximation

designed in order to implement this measurement. A numerical simulation and a description of the experimental procedure are described in the following sections.

Theoretical Investigation of Power Flow

In order to evaluate the results anticipated from the experimental study, the theoretical power flow in a simply-supported beam was calculated. A steel beam was used for this simulation, measuring 1.5 inches wide, 0.5 inches thick, and 144 inches long. The power flow was calculated using equation (2), for two different values of the structural loss factor, which is a measure of the damping in the structure. A single excitation frequency was used, 314 Hz., and the location of the force was taken to be the center of the beam. The results calculated for a loss factor of 0.01 are shown in Figure 2, and the results for a loss factor 0.1 in Figure 3. Comparing these results, it is seen that the power flow increases nearly linearly with increasing loss factor. This is to be expected, for in such a model, the only means of dissipating energy is found in the internal structural hysteresis. Since the structural intensity is a measure of the power actually flowing down the beam, then there will be a larger power flow when there is increased dissipation.

In addition, the vector nature of the structural intensity can be seen from Figures 2 and 3. The sole source of power in the beam occurs at the external force, located at $x/L = 0.5$. The power in the beam itself must flow symmetrically from this point toward the beam endpoints. Thus, for a constant accelerometer array orientation, measurements would show positive power flow on one half of the beam and negative power flow on the other half. This behavior is shown in the simulation results. Except for algebraic sign, the intensity pattern should be symmetric as well. It is interesting to note the prediction of zero structural intensity at the driving point. Since the intensity is a vector quantity, the right-going intensity and the left-going intensity should precisely cancel at the force location, as observed. This of course does not mean that the power delivered by the force is zero. In fact, the delivered power is given by the time-averaged product of the external force and the velocity at the driving point. This quantity was not calculated in the simulation, but may be shown to be exactly equal to the power dissipated in the beam due to the presence of damping.

Experimental Investigation of Power Flow

Figure 4 shows the experimental arrangement used to develop the structural power flow measurement technique. The apparatus consisted of a steel beam (same dimensions as that used in the simulation) suspended by two wires. The beam was driven by an electrodynamic vibration exciter at its midpoint. An array of two accelerometers (Rion Type PV-36) was attached to the beam. The accelerometer outputs were passed

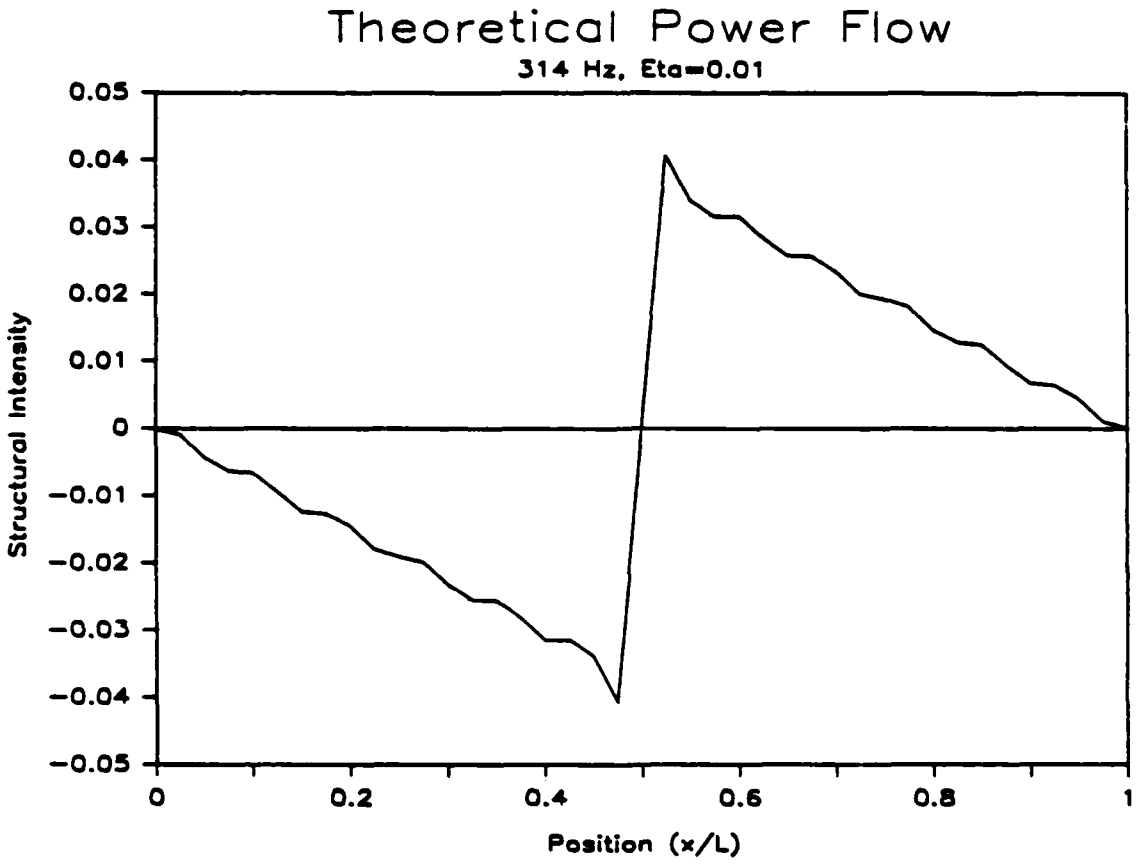

Figure 2. Theoretical power flow for loss factor equal to 0.01

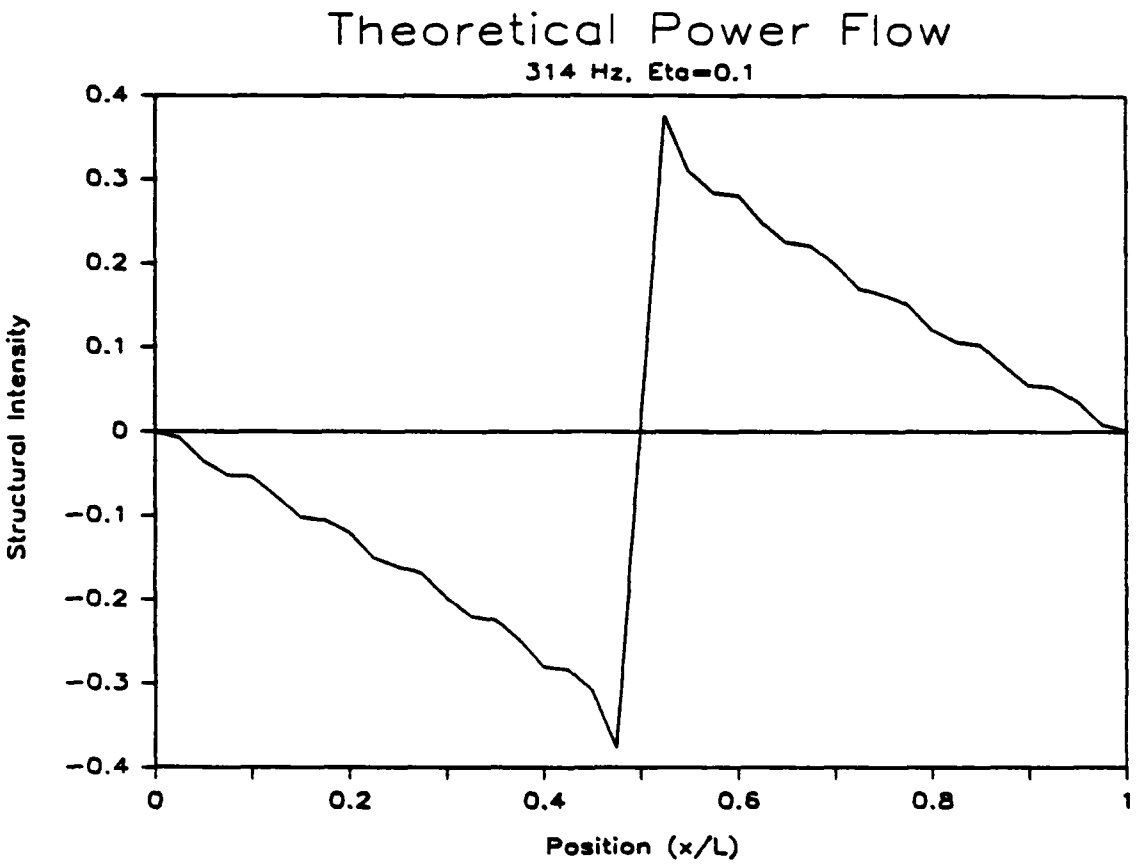

Figure 3. Theoretical power flow for loss factor equal to 0.1

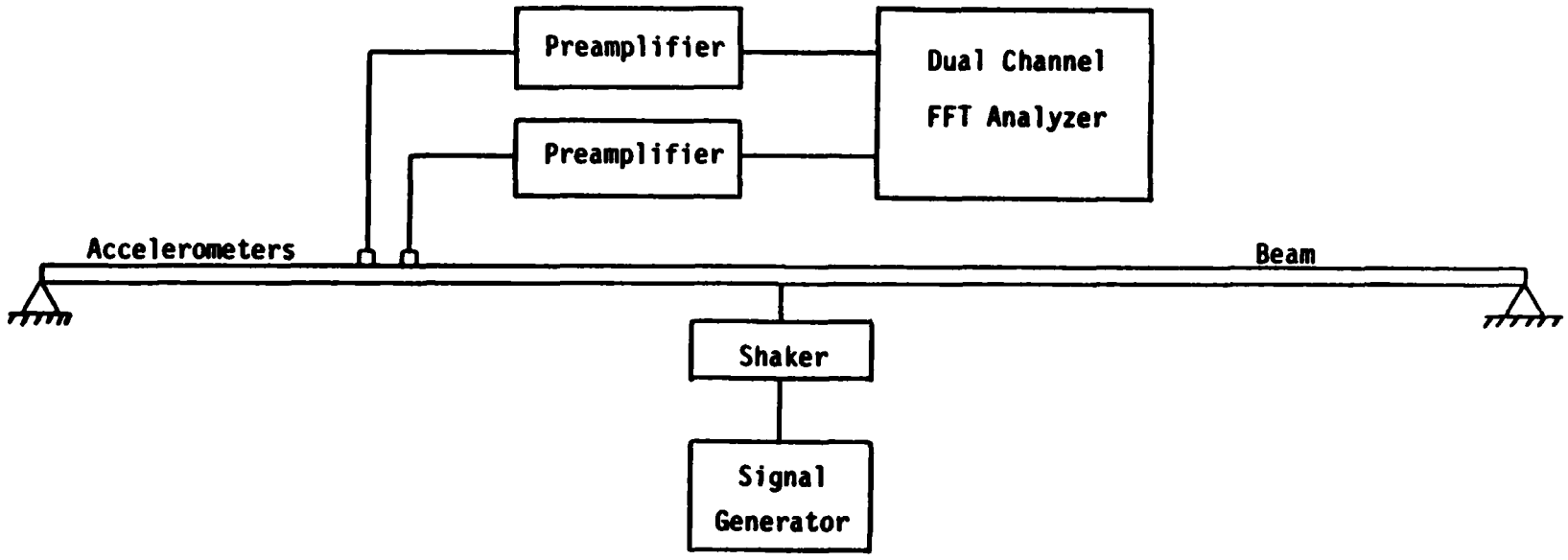

Figure 4. Experimental apparatus for structural power flow measurement

through preamplifiers (GenRad Type P-42) into a dual-channel FFT analyzer (Nicolet Type 660-B). The analyzer was then programmed to perform the necessary signal processing in order to implement the frequency domain counterpart of equation (5). This equation is given by [5]:

$$\langle J_x \rangle = \frac{\sqrt{(Dm)}}{\pi h} \int_0^{\infty} \frac{\mathrm{Im}[G(\ddot{y}_2,\ddot{y}_3)]}{\omega^2} \, d \qquad (6)$$

where Im[ ]denotes 'the imaginary part of', and $G(\ddot{y}_2,\ddot{y}_3)$ is the cross-spectrum between the acceleration signals at positions x_2 and x_3.

One of the most important steps in any such multichannel measurement is the phase-matching that must be performed between the analysis channels. In the present case, this is being accomplished through phase calibration using wideband excitation of the accelerometer array. The associated phase characteristics are stored in the FFT analyzer for use during the data processing. Although initial steps have been completed toward performing this analysis, no confident results have been obtained thus far.

REFERENCES

1. Lyon, R. H., Statistical Energy Analysis of Dynamical Systems: Theory and Applications, MIT Press, 1975.

2. White, R. G. and J.G. Walker, Noise and Vibration, Ellis Horwood Limited, 1982.

3. Pavic, G., "Measurement of Structure Borne Wave Intensity, Part 1: Formulation of the Methods," J. Sound and Vibration, Vol. 49, No. 2, 1976, pp. 221-230.

4. Junger, M. C. and D. Feit, Sound, Structures, and Their Interaction, MIT Press, 1972.

5. Verheij, J. W., "Cross Spectral Density Methods for Measuring Structure Borne Power Flow on Beams and Pipes," J. Sound and Vibration, Vol. 70, No. 1, 1980, pp. 133-139.

SECTION 3. PRECISION FABRICATION

TECHNOLOGY OF PRECISION FABRICATION

By

Thomas G. Bifano
Graduate Student
Precision Engineering Laboratory

And

Thomas A. Dow
Professor
Department of Mechanical and Aerospace Engineering

ABSTRACT

From the twenty five year old technology of single point diamond turning to the recently developed technology of atomic bit machining, the field of precision fabrication is driven forward by the ever increasing demands on component tolerances required by both industry and government. A difficulty associated with applying this research is that it is not always clear which of the many frontiers in precision fabrication holds the most promise for the production of a specific component. The purpose of this paper is to categorize the various precision machining processes and to evaluate the current capabilities of each. This evaluation includes a process description, the performance characteristics (including contour accuracy and surface finish achievable), and the application areas for each technology in terms of the components that can be produced. The discussion is mainly limited to the material removal processes; namely, single point diamond turning, precision grinding, polishing, and energy beam machining.

INTRODUCTION

Precision Engineering can be broadly divided into three interrelated research fields: measurement, control, and fabrication, with dimensional tolerances that challenge the limits of current technology. Ultimately, the thrust of precision engineering research lies in the fabrication of components demanding extreme dimensional accuracy. This is not a singular task, nor one that is easily defined. Dimensional accuracy might refer to control of overall size, contour shape, surface roughness, thickness, or a combination these. Moreover, the exact specification of dimensional tolerances is elusive: for example, the numerical specification of surface finish depends quite literally on the way it is to be measured. Some measurement systems produce a single surface finish value (usually Ra or rms roughness) while others calculate statistical quantities based on a profile of the surface [1,2]. Even if a common definition of surface finish could be determined it might not be readily measured since the resolution limits of displacement sensing are being approached. The range of components currently fabricated under the umbrella of precision engineering is quite diverse, spanning the fields of mechanical devices, electronics, and optics. Although there are many similarities between the methods of precision fabrication of components in these three categories, there are also significant differences. This paper is an attempt to classify the various types of precision fabrication technology in terms of both the function of the parts produced and the production process utilized in their manufacture.

Most current precision fabrication research is directed toward five distinct areas of manufacturing:

* Aspheric optic production
* Memory disks production
* VLSI and microelectronic component production and placement
* Tool forming and sharpening
* Bearing production

These five manufacturing areas call for distinctly different types of dimensional control and ultimate finish, as summarized in Table 1. The production of these components is discussed vis a vis fabrication processes in the following section.

Table 1

Mfg. area	Range of part size (inch)	Dimensional tolerance < μin.
Aspheric optics prod.	0.1 -> 100	Contour (form) in 3-D < 10 μin.
Memory disk prod.	1 - 10	Flatness tolerance < 100 μin.

Table 1 (continued)

Mfg. area	Range of part size (inch)	Dimensional tolerance < μin.
VLSI	.0001 - .1	Thickness, width tolerance <100 μin.
Tool fabrication	.001 - .1	Edge sharpness & contour tolerance
Bearings	.1 -> 10	Roundness, flatness <100 μin.

There are three ways to produce a new surface. They are: material removal, material deposition, and material deformation. At the accuracy levels currently required in precision engineering (dimensional control to < 10 in.), these categories can be further subdivided according to the following outline.

Material Removal

TURNING
* Single point diamond turning (SPDT)

GRINDING
* Precision grinding

POLISHING
* Abrasive polishing
* Mechanical-chemical polishing
* Electrochemical polishing

ENERGY BEAM MACHINING
* Energy beam vaporization
* Diffusion or dissolution
* Ion sputtering
* Vacuum evaporation

Material Deposition

* Chemical plating
* Electrochemical plating
* Vapor deposition

* Sintering
* Sputtering deposition

Material Deformation

* Hydropolishing
* Surface tension
* Burnishing
* Fine lapping

PRECISION FABRICATION PROCESSES

What follows is a brief description of the most widely researched of these technologies, material removal. This is not to diminish the importance of deformation and material deposition as precision fabrication processes. Indeed, these areas represent a research area ripe with opportunity for precision engineering at atomic levels. The following sections review material removal processes, capabilities, limitations, and applications currently at the forefront of precision engineering.

Single Point Diamond Turning (SPDT)

Process Description

In SPDT, the workpiece is cut with a monocrystalline diamond tool, which shears material away by virtue of its exceptionally sharp edge. The hardness of diamond allows sharpening to dimensions approaching that of its interatomic spacing: in the range of 0.3 to 0.5 nm [3]. (This sharpening process is in fact another precision engineering fabrication research area.) Additionally, the longevity of the tool's sharp edge is enhanced by the diamond's hardness. SPDT machines are usually configured as either flycutters or lathes. In both cases there are either two or three degrees of freedom (one rotation plus one or two translations), allowing the production of flat or contoured parts, respectively. Because of the high accuracies required by SPDT, the rotation and translations are usually accomplished via hydrostatic bearings, and attention must be paid to machine stiffness, spindle and slide accuracy, vibration, and temperature. As with all of the processes discussed in this review, these variables must either be eliminated, controlled or compensated for in the production of parts with microinch accuracies.

Performance

Consider as an example the case of an SPDT machine in which the workpiece is rotated on a hydrostatic spindle, while the diamond tool is free to translate radially and axially with respect to the spindle axis. Clearly, by simultaneously controlling all three of these motions, nearly any continuous contour can be cut by the single point tool on the workpiece face. In fact, the hardness of the diamond permits a single pass of the tool to produce a surface which exactly replicates the

leading edge of the tool. With the use of radius tools, surface finishes of nearly 10 angstroms RMS are currently being produced [3]. With the help of the machine's overall stiffness and controlability, contour accuracies over the entire part of 1.1 μin. rms can be produced on parts as large as 60 inches in diameter [4,5]. This combination of contour accuracy, ultra smooth finish, and versatility on part shapes and sizes attainable make SPDT technology a foundation of precision engineering fabrication research.

Applications

Currently, single crystal diamond tools are used to cut only certain metals: i.e. FCC structures characteristic of copper, aluminum, and electroless nickel. These tools are not effective for cutting BCC metals such as steel [3,6,7]. Brittle materials such as glass and silicon have been cut with only marginal success in SPDT, and usually require a post polish for spectral finishes.

Both the optical and mechanical applications of SPDT are currently expanding. Aspheric optics have been a mainstay for SPDT for more than 20 years, beginning with the work of J. Bryan at Lawrence Livermore National Laboratory and V. Ford of Polaroid in the 1960's. Before the arrival this technology, there was no feasible method for producing aspheric components. Today these parts are being used in laser optics, telescopes, advanced communications systems, photographic equipment, and contact lenses. Unfortunately, the current state-of-the-art of SPDT is limited to production of optics of longer wavelengths (infared). Some post polishing is required for visible and shorter wavelengths. SPDT is also used to machine master molds for plastic lenses. Using injection molded optics replicated from an aspheric mold, one plastic lens can replace a compound multiple lens system. A second, rapidly expanding application for SPDT is producing multifaceted mirrors for laser printers and bar code readers. Diamond turning excels in this application because it can leave extremely sharp edges between mirror facets.

There are also applications for SPDT in the production of flat, smooth surfaces, most notably, computer hard disks. About half of the world's computer memory hard disks are currently produced with SPDT machines. (The other half are ground.) Research in this manufacturing area is focussed on decreasing the surface roughness of the flat substrate, whereupon the magnetic read head can fly closer to the disk, allowing increased areal storage density.

Grinding

Process Description

In precision surface finish grinding, fine abrasive grains (carborunum, alundum or diamond) are bound to a wheel on an precision spindle. This rotating wheel is then used as a cutting tool on a stiff, 2 axis grinding machine. For effective grinding, the wheel peripheral

speed must be at least 1200 in./sec [8]. Lower peripheral speeds increase the normal component of the grinding force, necessitating higher grinding pressure and causing deflections that reduce the overall grinding accuracy. For a .010" wheel diameter, as is used in the production of miniature ball bearings, this surface speed necessitates a spindle speed of 200,000 rpm [9], while a more typical 1.4" diameter wheel used in external precision grinding requires only 1600 rpm.

Grinding removes material through the action of many arbitrarily positioned abrasive grains in the wheel. Like SPDT, grinding can produce chips without melting or burnishing the workpiece surface [10]. The abrasive grains wear rapidly because they are subject to high pressure. Theoretically grinding is a higher stress process than SPDT. This is because the small depth of cut in grinding precludes the use of dislocation motion as a failure mechanism. (Since there are statistically few dislocations less than 40 μin. from the workpiece surface). Thus, the failure mechanism is a breaking of stable crystal bonds -- a high stress phenomenon. These high stresses result in a continual cycle of wheel wear and grain fracture, producing randomly oriented new cutting surfaces. Under this type of mechanical deformation, peaks and valleys in the material will be randomly distributed. Thus, for a specular finish, grinding must be often followed by polishing.

Applications

Unlike SPDT, grinding is used for precision machining all types of metals and ceramics. It is particularly useful in the contouring of brittle materials such as optical glass and tungsten carbide, and silicon carbide. Often, this machining is performed on the same machine used for single point diamond turning [8]. Grinding can also be used to achieve shapes that are unobtainable with traditional SPDT machines; such as narrow hole boring and finishing.

Another widespread use of grinding is in the fabrication of hard memory disks, where the lack of a spectral finish can be tolerated. Peaks, and their potential for causing a crash of the read head must be minimized.

Performance

A recent benchmark test for precision grinding of brittle materials resulted in flatness of 6 μin./in. and a surface roughness of 20 angstrom P-V. on a silicon carbide workpiece [11].

Polishing

Process Description

Several very important polishing techniques have been recently developed for precision fabrication. These are particularly applicable

to the production of flat, damage free surfaces on brittle workpieces. All ultraprecision polishing falls into the category known as "atomic bit machining," because the chip thickness approaches the dimensions of a single workpiece atom [12]. Polishing requires a pressurized suspension of abrasive particles (.4 -> 4 μin.) flowing between a flat (or spherical) reference surface and the workpiece surface. The abrasive action can be enhanced by chemical reactions in progressive mechanical-chemical polishing, where a chemical removal process smooths the discontinuous scratches made by mechanical abrasion. Work is currently underway at Lawrence Livermore National Laboratory and China Lake Naval Weapons Center in attempting to understand the kinetics, chemistry, and thermodynamics of surfaces in order to prescribe sound theoretical approaches to improving the process and products of polishing [13].

Performance

In PMAC (Progressive Mechanical & Chemical) polishing, a new technology [14], surfaces with 200 μin./in. flatness and 0.8 μin. Ra surface finish have been produced on 2" diameter semiconductor wafers. These results were obtained with a colloidal suspension of silicon in an alkaline solution against a polyurethane polisher. Other laboratories, using elastic emission machining selective chemical mechanical polishing and hydrodynamic polishing have typically achieved surfaces with 4 μin. flatness and 100 angstrom surface finish on brittle substrates [12]. On metals (electroless nickel) surface finishes of 10 angstrom rms. have been reported. With the exception of electroless nickel, however, soft metals are much more difficult to polish than glasses and brittle materials. Uneven material removal at grain boundaries, polishing rate dependence upon crystal orientations, and inclusion pull-out are three of the more important causes of these difficulties.

Applications

Atomic bit machining techniques are by definition very low removal rate processes. As such, they are used either for final processing of nearly acceptable precision fabricated surfaces (i.e. improving the spectral reflectivity of ground optical components) or for removing thin layers of brittle materials (semiconductors). The combination of mechanical/chemical polishing with masking techniques is finding an expanding utility in the formation of large scale integration electronic circuits (LSI). In these applications, the two most important characteristics of polishing that are exploited are its finely controllable removal rate and the avoidance of subsurface damage, both of which are essential for microelectronics fabrication.

Energy Beam Methods

Process Description

In energy beam processing the machining energy for material removal is supplied directly onto the atoms of the workpiece by an energy beam -- a directed flux of microscopic particles. This flow of particles presents a concentrated kinetic, electric, chemical or thermal bombardment of the workpiece via electrons, photons, ions, or other particulate streams. This type of processing can be carried out at the atomic level, and controlled removal of single atoms is possible. Although there are many forms of energy beam processing, the most important from a precision fabrication standpoint are: electron beam, laser beam, and ion beam processing [12].

Performance and Applications

The selection of energy beam methods is usually based upon their sharply focused material removal characteristics, though the choice of a particular energy beam method must be linked to the characteristics required of the finished workpiece surface and subsurface. This is because energy beams tend to penetrate the surface and cause some subsurface damage. Table 2 presents the current status of energy beam usage in precision engineering.

Table 2. Energy Beam Fabrication Methods*

Method	Application	Comments
Electron Beam Machining	* drilling small holes * penetration welding and microwelding	Due to high penetration and subsurface bubble formation, this is not a useful surface material removal technique.
Electron Beam Lithography	* radiant exposure for mask prototyping	Fine electron beam can produce pattern accuracies of 1 μin.
Laser Beam Machining	* drilling small holes * trimming semiconductor wafers * optically promoted	Pulsed YAG laser 40 μin. wavelength. Subsurface melting precludes fine surface machining.
Laser Beam Lithography	* radiant exposure for mask prototyping	Excimer laser λ= 10 - 20 μin. Not as precise as electron beam.
Ion Beam Sputtering	* aspherizing spherical lenses (duoplasmatron)	Process knocks out target atoms by incident high

Table 2. Energy Beam Fabrication Methods* (cont.)

Method	Application	Comments
Ion Beam Sputtering (continued)		
	* finish machining block gages (high frequency * mask prototyping (~10 μin. accuracy) * sharpening diamond tools and knives (edge radius ≤ 0.4 μin.)	energy ions 10 - 30 KeV argon ions typical

Ion beam machining is complimented by ion beam sputter deposition, forming new layers on a substrate by consolidating atoms which have been knocked loose via sputtering. Ion beam sputtering generates neither heat nor strain damage in the substrate, but some of the ions substitutionally displace the resident workpiece lattice atoms. As a machining process, sputtering has a resolution of 0.4 μin., comparable to electron beam machining and significantly better than laser beam machining.

CONCLUSIONS

While material removal processes represent only one of three possible surface alteration techniques (the other two being material addition and deformation), currently the most significant, when they are viewed in terms of precision fabrication technology. The material removal research field is driven by the distinct and unique qualities required of precision optical, mechanical, and microelectronic components. In pursuing optimal properties for these diverse end products, a wide range of "extreme" machining technologies have evolved, and can be loosely grouped into four categories defined by the specific material removal method: single point diamond turning, precision grinding, polishing, and energy beam removal. Together with the ever-changing demands of precision manufacturing, these techniques form a basis upon which the evolution of future processes will be built.

REFERENCES

1. Bennett, J. M., "Comparison of Techniques for Measuring the Roughness of Optical Surfaces," Optical Engineering, Vol. 24, No. 3., May 1985, p. 380.

2. Church, E. L., T. V. Vorburger, and J. C. Wyant, "Direct Comparison of Mechanical and Optical Measurements of the Finish of Precision Machined Optical Surfaces," Optical Engineering, Vol. 24, No. 3, May 1985, p. 388.

3. Krauskopf, B., "Diamond Turning: Reflecting Demands for Precision," Manufacturing Engineering, May 1984, (includes 26 refs. on diamond turning).

4. Donaldson, R. R., and S. R. Patterson, "Design and Construction of a Large, Vertical-Axis Diamond Turning Machine," Lawrence Livermore National Laboratory, Doc. UCRL-89738 DE83 017629, August 1983.

5. Atkinson, D. P. and W. T. Estler, "Results of Accuracy Testing and Initial Operating Experience of The Large Optics Diamond Turning Machine at Lawrence Livermore National Laboratory," 1985 Precision Engineering Conference at North Carolina State University, November 1985.

6. Arnold, J. B. and P. J. Steger, "Diamond Turning on Advanced Machine Tool Prototypes," SME Document # MR74-943, 1974.

7. Casstevens, J. M. and C. E. Daugherty, "Diamond Turning Optical Surfaces on Electroless Nickel," Union Carbide Document V/DA-7758, August 1978.

8. Chaloux, L. "Diamond Grinding of Optical Surfaces on Brittle Materials," 1985 Precision Engineering Conference at North Carolina State University, November 1985.

9. Ota, M., "Design and Applications of Ultrahigh Speed Internal Grinding Head," 1985 Precision Engineering Conference at North Carolina State University, November 1985.

10. Shaw, M. C., "Surface Melting in Grinding Operations," Annals of CIRP, Vol. 33, No. 1, 1984.

11. Yoshioka, J., F. Hashimoto, M. Miyaghita, A. Kanai, T. Abo, K. K. Daito, and M. Daito, "Ultraprecision Grinding Technology for Brittle Materials - Application to Surface and Centerless Grinding Processes," 1985 Precision Engineering Conference at North Carolina State University, November 1985.

12. Taniguchi, N. "Current Status in, and Future Trends of, Ultraprecision Machining and Ultrafine Materials Processing," Annuals of the CIRP, Vol. 32, No. 2, 1983.

REFERENCES (continued)

13. Brown, N., "Polishing Research," 1985 Precision Engineering Conference at North Carolina State University, November 1985.

14. Kasai, T., "Application of PMAC Polishing to Si Wafers," 1985 Precision Engineering Conference at North Carolina State University, November 1985.

PAUL PARALLEL AXIS ULTRAPRECISION LATHE

By

Peter J. Falter
Graduate Student
Precision Engineering Laboratory

And

Thomas A. Dow
Professor
Mechanical and Aerospace Engineering Department

ABSTRACT

A small single axis diamond turning machine has been designed and built by the Precision Engineering Laboratory at North Carolina State University. This machine has been used to produce parts with a surface finish of 0.15 μin. (4 nm) rms and a total figure error of less than 2 μin. (50 nm) over 2 inches. This paper outlines the design of the apparatus and discusses some of the results of the cutting experiments performed.

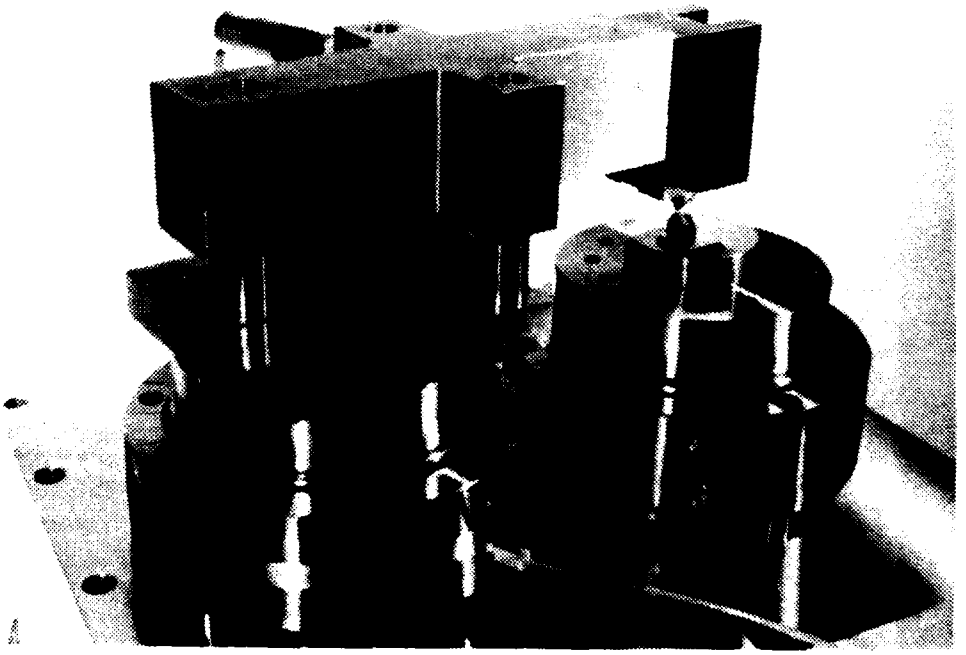

Design Goals

Precision engineering involves metrology, control, and fabrication of devices with tolerances in the microinch range. To implement new ideas, a precision fabrication process was necessary to serve as a test bed to evaluate the concepts developed in the program. Diamond turning is an example of such a fabrication process and was selected as the first one for study.

Commercially available diamond turning machines were too expensive to be considered so a small, laboratory-scale machine was designed and constructed. The design goals were: high stiffness, low error motion, low to moderate cost, and the flexibility to be adapted for different experimental objectives. All of these objectives were achieved in the Parallel Axis Ultraprecision Lathe -- PAUL.

Construction

The layout of the apparatus is shown in Figure 1. The major components of the lathe are a pair of vertical axis air bearings, one which supports the workpiece and is driven by an integral motor. The second bearing supports the cutting tool and provides the geometric constraint for its motion. A dc motor driven lead screw moves the tool across the workpiece.

A pair of 4 inch vertical axis air bearings (Professional Instruments Model #4R) form the heart of the machine. These are mounted to a 2 inch thick steel plate at three points. Spacers (0.25 in. thick) are used between the air bearings and the base to allow the axes of the spindles to be aligned. The stiffness of these bearings for axial and angular motions are given in Table 1.

TABLE 1

Location	Direction	Stiffness
tool tip	z	80,000 lbf/in
tool tip	y	300,000 lbf/in
tool tip	x	70,000 lbf/in
spindle	z	2,000,000 lbf/in
spindle	x or y rotation	4,000,000 in-lbf/rad

The workpiece is attached to one spindle which is directly driven by an integral brushless dc motor (Inland model #BM3217). The motor is attached to the air bearing with a Kelvin Coupling to allow accurate repositioning if disassembly is required. The motor can deliver up to 560 oz.-in.(4 N-m) of torque and is capable of driving the spindle at speeds up to 3000 rpm. Speed control of the motor is achieved using a

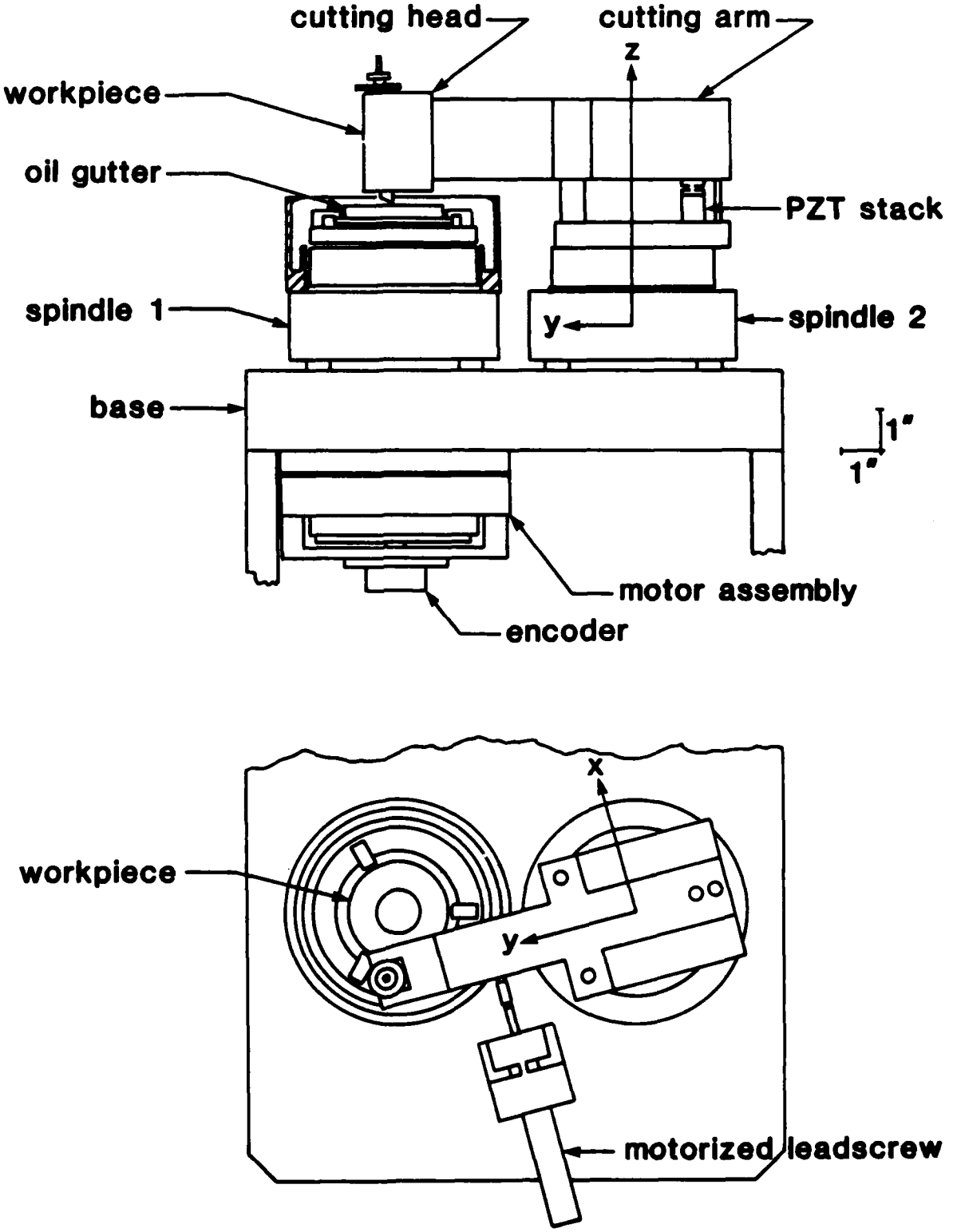

Figure 1. General views of PAUL

programmable digital controller (Inland model #BSA) and a 1024 line optical encoder for feedback.

The specimens are mounted directly to the air bearing spindle via clamping at three points. The three mounting faces have been turned in this lathe after assembly to assure thin flatness.

The cutting arm is mounted to the spindle by three columns, which act as flexures and permit some adjustment of the vertical position of the arm. The rear column is a preloaded piezoelectric stack which can be used to Statically or dynamically change the tool height by 350 μin. (9 μm). The preliminary tool height is set with a differential screw mechanism in the tool holder, which is part of the cutting head assembly. This structure mounts to the end of the cutting arm and may be easily removed and replaced by another fixture. This flexibility allows several cutting heads each designed for a different tasks to be interchanged.

The cutting arm is advanced across the workpiece surface using a small dc motor driven lead-screw (Oriel Corp. Motormike with controller). The lead-screw barrel has a ball end which was originally loaded against the side of the cutting arm with a dead weight load of 200 gm. However, figure errors were noted on the machined surface at a period equivalent to the lead-screw motion. This difficulty was greatly reduced by introducing a coupling between the ball end on the lead-screw and a ball mounted to the cutting arm.

The overall static stiffness of the system measured at the toop tip is 80,000 lbf/in. (14×10^6 N/m) in a direction normal to the workpiece. Table 1 shows the stiffness at the tool in different directions. The largest component of the vertical compliance of the tool is the tilting of the air bearing which supports the cutting arm about a horizontal axis. This motion also accounts for the lowest natural frequency (300 Hz) measured for the tool arm assembly. The entire apparatus is supported on a Newport Corporation vibration isolated table to reduce the effects of floor motion on the cutting process.

Alignment

The most difficult and critical alignment on the PAUL machine is parallelism of the vertical spindle axes. A two step procedure was used to adjust these axes to within 1-2 microinches of parallel. The first step was to replace the workpiece with an optical flat and to measure the shape of that flat with an indicator mounted in the cutting arm. An LVDT was used to make this measurement and it was swept across the surface of the flat.

The spindle was then rotated 180^0 and the measurement was repeated to remove the effect of non-parallelism between the faces of the flat. (A 3 inch optical flat with 1 arc second parallelism is 15 μin. thicker at one point on the edge than at the opposite point, therefore this wedge is a significant source of error if no compensation is made.)

Preferentially tightening three the mounting screws on each spindle non-uniformly compressed the spacers and allowed the spindle axes to be aligned.

The final accuracy of this initial alignment was sufficient to produce a finished part flat to about 5 microinches. Further correction of the spindle axes was made by observing the shape of cut parts with the Talysurf and adjusting the load in the spindle mounting screws until a flatness better than 2 microinches was achieved. Correction beyond this point was not possible because of the error motions inherent in the spindles.

Specimens

The specimens turned on the lathe are disks 2.5 inches (64 mm) in diameter and 0.5 inches (13 mm) thick, as shown in Figure 2. The parts are supported and clamped at three evenly spaced points along the outside edge. This method of part support does not cause warping problems with workpieces of this geometry.

Tools

The tools used are polished single crystal diamond tools from J. Robert Moore Co. Tool radii of 0.030 and 0.125 inches (0.76 and 3.2 mm) have been used with rake angles of -1 degrees and clearance angles of 6 to 10 degrees.

Lubrication

Several lubricants have been used during cutting, including ethanol, kerosene, Dialla, and WD-40. The usual lubricant is Dialla which is sprayed onto the workpiece and collected with the chips in a gutter surrounding the main spindle. Lubrication significantly improves the quality of the finished surface, although it makes part cleaning more difficult.

Cutting Tests

Cuts have been made on a variety of materials. These include: OFHC copper, 2024 aluminum, electroless nickel, free machining brass, nylon, and acetate. Of the metals turned so far the brass yields the most consistent results. The copper has a tendency to be badly galled by chips which are not removed and subsequently pass beneath the tool. This galling is not as much of a problem on the brass and nickel specimens. It is hoped that the addition of a chip suction device and an improved oil spray system will aid in the removal of the chips and will eliminate the cause of the galling.

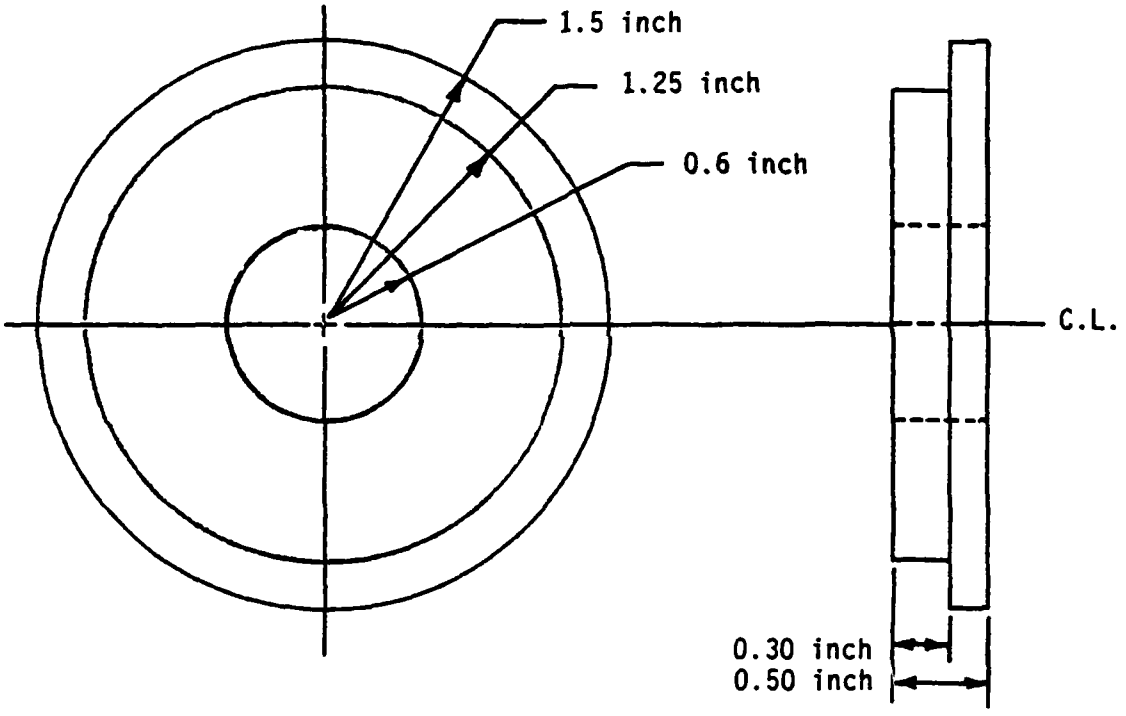

Figure 2. Typical specimen

The best surface finishes have been produced on the copper, nickel, and brass specimens. A roughness of 0.15 microinches (4 nm) rms was measured for an OFHC specimen sent to Lawrence Livermore Laboratories for testing on a WYCO interferometer. This result was confirmed on a Talystep profilometer at the National Bureau of Standards. The surface finish of this part seems to be typical of the surface quality which may be produced on this lathe. A chart of the theoretical surface finish produced by a radiused tool with a constant feed is shown in Figure 3. The actual surface roughness Ra, will be higher since vibration, stress relief in grains, material imperfections, diamond edge quality, and other phenomena diminish surface quality.

Flat Specimens

The copper specimen examined by LLNL and NBS had a figure error of approximately 4.5 microinches (110 nm). The axes of the spindles were later readjusted to produce parts which are flat to within 2 microinches (50 nm) peak to peak.

Sine Wave Surface Profile

The ability to produce a flat specimen is a measure of the adjustment of the spindles and the ability to drive the tool without influencing the spindle accuracy. The accuracy achieved indicates the capability of the PAUL design. However, the aim of this research effort is to control the tool position as a function of both the radial position of the tool (as measured from the cent of the workpiece) and the rotational position of the workpiece. Such a system can produce spherical, aspherical, and non-axisymmetric specimens.

As the initial experiment, a sine wave surface was generated on a brass substrate. This surface was produced by driving the piezoelectric actuator, which supports the back of the cutting arm, with a sine wave. Provided the feed rate of the tool was constant, a uniform sine wave should be produced on the surface.

A Talysurf trace of a sine wave surface generated on a brass substrate is shown in Figure 4. This surface was cut in a single pass with an average depth of cut of approximately 80 microinches. The spatial period of the sine wave produced was 0.106 μinches (270 μm) with an amplitude of 60 μin. (1.5 μm) peak to peak. The specimen was cut with a tool radius of 0.030 inches (0.76 mm) and and a feed rate of 240 μin. per revolution. A power spectrum was made of the profile (Figure 5) which shows the surface to contain a single frequency. The small side lobes which are symmetrically spaced about the peak frequency resulted from the windowing of the data in the Fourier transform operation.

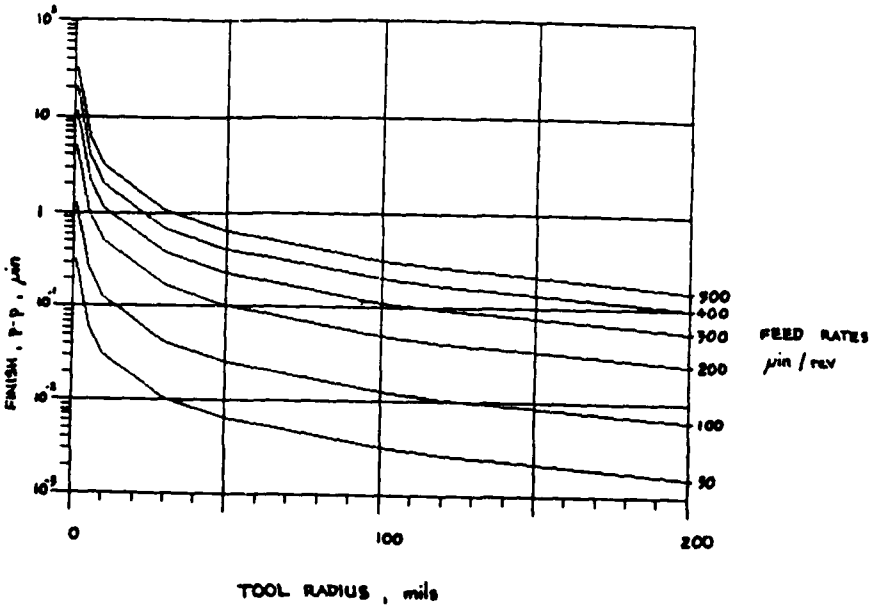

Figure 3. Theoretical finish of a diamond turned specimen as a function of tool radius and feed rate

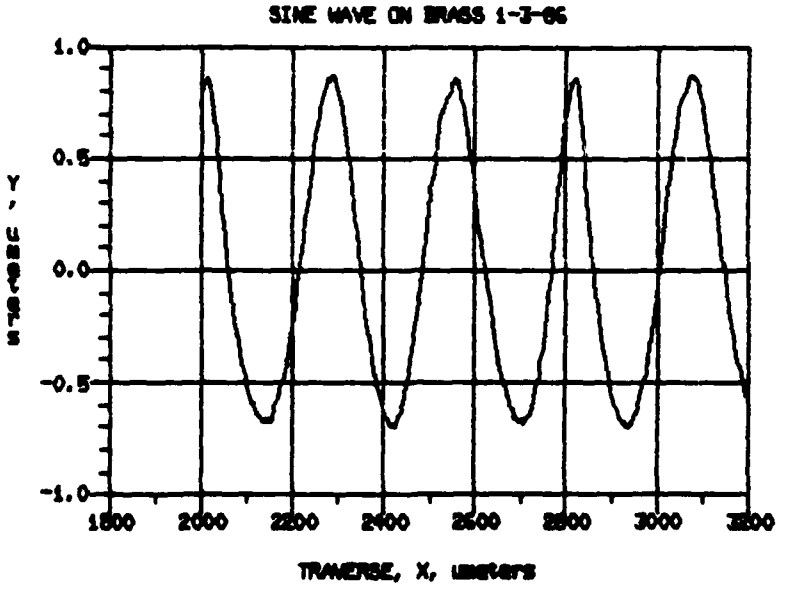

Figure 4. Trace of a sine wave

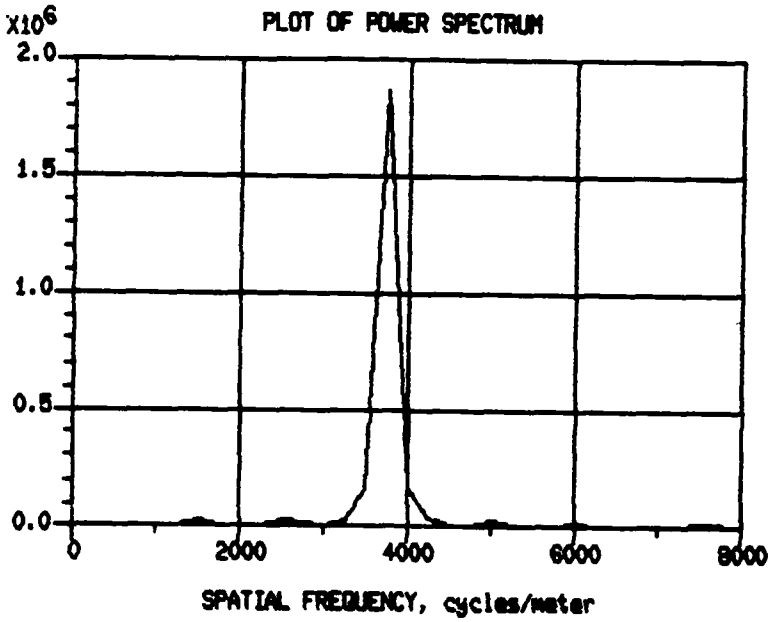

Figure 5. Power spectrum of the sine wave surface

CONCLUSIONS

The major performance objectives have been met by the current design of the PAUL. The machine is stiff and accurate enough to produce flats of very good quality both in figure and finish. The lathe is also versatile, being easily altered to perform cutting force studies [1] and allowing the videotaping of the cutting process. Future modification of PAUL will allow control of the tool position as a function of both feed and workpiece rotation. The major tasks involved with this project will be the development of a stable metrology frame, the design and construction of an improved tool height actuator, and the development of a control scheme. The proposed enhancement of PAUL's capabilities will be completed by the end of 1986 and to publish papers pertaining to the project as work progresses.

REFERENCES

1. Carroll, J. T. and T. A. Dow, "Tool Force Measurement Experiment," Third Annual Report on Precision Engineering - SRO 154, North Carolina State University at Raleigh, 1986, p. 197

GEOMETRY OF DIAMOND TOOL

By

Peter Blake
Graduate Student
Precision Engineering Laboratory

And

Ronald O. Scattergood
Professor
Materials Engineering Department

ABSTRACT

A preliminary evaluation of techniques to measure the edge radius of a diamond cutting tool has been undertaken. The edge radius, reported to be less than 100 angstroms, plays an important role in the machining process. Changes in this radius will affect the tool forces, residual stress, and finish of a diamond turned surface.

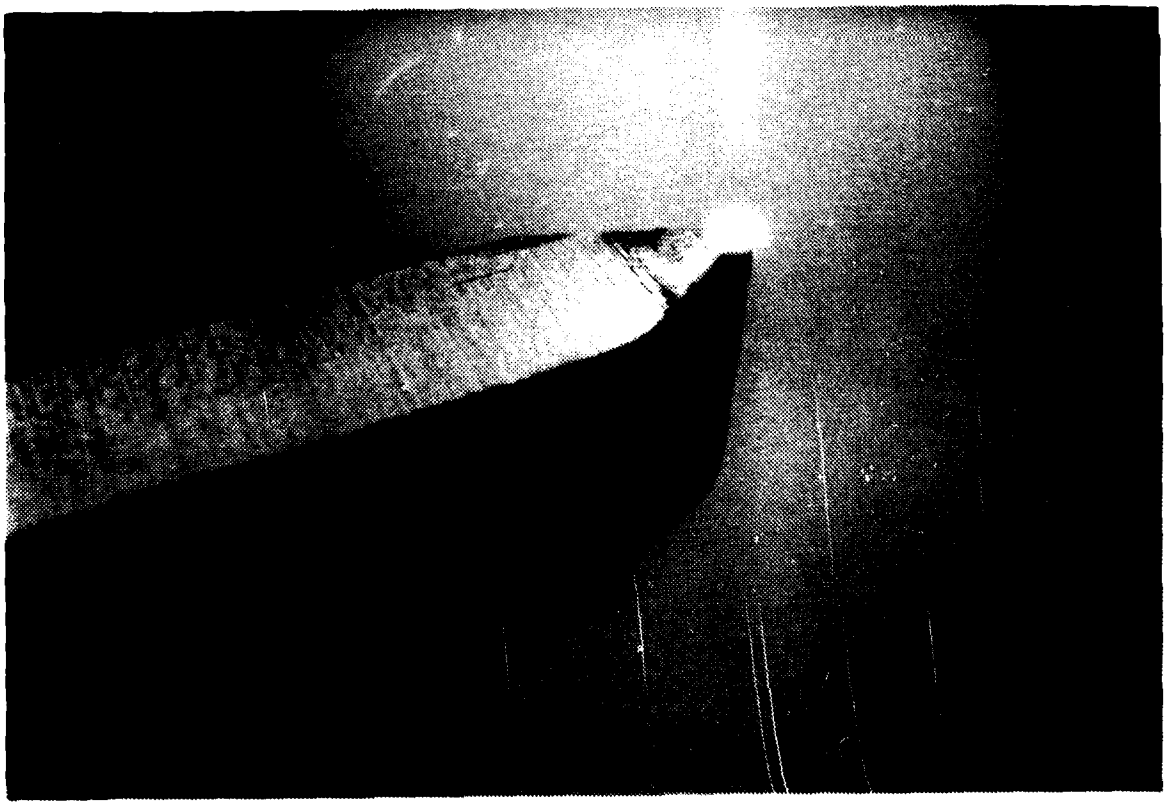

INTRODUCTION

The need for a quantitative method of evaluating the edge radius of a diamond tool is driven by two goals of the research program. The first involves the study of stresses and deformations during the turning process. The theoretical models, described in following sections, require input of edge radius (sharpness of the tool) to study the stresses at a critical region -- that adjacent to the cutting edge. This is the region where the chip separates from the substrate, and where new surface is formed. The second area of interest involves comparing the experimental cutting performance and surface finish achievable on a variety of substrate materials. Because of the importance of the stresses in the region of the cutting edge, comparative evaluations of cutting performance demand a characterization of the tool edge -- both at the microscopic as well as the macroscopic level. For these reasons, an effort was begun to develop an edge characterization procedure which would have the necessary resolution yet be sufficiently simple to implement that it could be done on a routine basis.

Evaluation of Techniques

Scanning electron microscopy (SEM) reveals the three-dimensional surface topography of a sample and is non-destructive; so it is the natural first choice of the research program. The SEM instruments that are immediately available to the laboratory offer the ability to take micrographs of 20,000x magnification and return the tool immediately to the lathe. It is thus possible to monitor the effects of cutting on the tool and the effects of tool wear on the cutting process.

The limitation of standard SEM techniques in this application is resolution. Ikawa and Shimada [1], reasoning on the basis of surface energy considerations and transmission electron micrographs (TEM) of cracks in diamond plates, have estimated the minimum achievable tool edge radius to be between 2 nm and 10 nm. Under the best contrast conditions, SEM resolutions can be brought to 3-5 nm; but these conditions are not obtained with the diamond edge. First of all, it is difficult to get surface detail from a sharp edge (edge effect). Secondly, the diamond is non-conductive, so that the 15-25 KV electron beam usually used for metal or metal-coated samples will charge the sample; and the sample will then repel the beam. Coating the diamond with gold (in order to conduct away the excess charge) may partially obscure the surface details of interest.

Both of these problems are answered by using a low acceleration voltage. For each non-conductive material, there is a narrow range of low voltages for which sample charging does not occur. For diamond, this voltage is close to 1 KV. The electron optical systems of most SEM's are not designed for the lower voltages; but an operator, experimenting with the settings on an instrument that can deliver a high beam current density, can achieve good resolution at low accelerating voltage. Figure 1 shows an example -- an uncoated diamond tool edge at 20,000x under an accelerating voltage of 3 KV.

Figure 1. Diamond tool edge

The micrograph of Figure 1 was taken on a JEOL 840 SEM. The Microelectronics Center of North Carolina (MCNC), in nearby Research Triangle Park has such an instrument. This Center is jointly owned by the Triangle Universities (North Carolina State University, University of North Carolina, and Duke University) and the State of North Carolina. Negotiations have recently been completed to obtain access to the microscope.

If a higher resolution than that obtainable from the MCNC SEM is needed, other procedures can be tried. This laboratory (through Dr. Philip Russel, Materials Engineering Department, North Carolina State University) has access to a Hitachi SEM at Hitachi Offices in California and in Japan. This instrument is equipped with a field emission electron gun, which give extremely high brightness in a small beam, and could allow 100-200 angstrom resolution at a magnification of 40,000x. This is not standard and could take a skilled operator several days of experimentation. To attain the 20 angstrom resolution necessary to measure the edge radius, an experienced graduate student should expect to spend six months developing a technique. The Hitachi will accept samples somewhat smaller than our tools, so much of the tool shank must be cut off.

Another useful instrument is the Hitachi H-800 scanning transmission electron microscope (STEM) available on the North Carolina State University Campus. In its SEM mode, and after considerable manipulation and experimentation it could offer a magnification of 40,000x. Its drawback is that it requires a sample no thicker than one micron; it is thus a destructive technique.

Another possibly useful instrument is the scanning tunnelling microscope, which is, in essence, a profilometer with a laterial resolution of < .1 angstrom [2]. Such an instrument is as yet unavailable at North Carolina State University; but plans are being made for the construction of one soon in the near future.

Transmission electron microscope (TEM) replication techniques have been tried for measuring tool wear [3] and absolute tool edge radius [4]. They take advantage of the fine resolution attainable with TEM (< 10 angstrom). But the techniques are manually very difficult, sensitive, and time consuming. For edge radius measurement, only Villalobos's method of measuring an indentation of the tool [4] is applicable; and there is no guarantee that systematic errors are not present in this procedure.

CONCLUSION

It is clearly recognized that tool edge characterization could be an important part of the research program in single-point diamond machining. The logical succession of characterization techniques used for this purpose should start with the simplest, high resolution non-destructive technique. As has been discussed, non-charging SEM techniques in a state-of-the-art instrument fulfill these requirements.

This procedure will be used for tool edge characterization during the initial research studies. If the results prove inadequate, than techniques based on TEM or scanning tunnelling microscopy will be adopted.

REFERENCES

1. Ikawa, N. and Shimada, S. "Cutting Tool for Ultraprecision Machining," Proc. 3rd Int. Conf. on Production Eng., Kyoto, July 1977, Japan Society of Precision Engineering.

2. Binnig, G., H. Rohrer, "The Scanning Tunnelling Microscope," Sci. Amer., Vol. 253, No. 2, 1985, p. 50.

3. Decker, D. L., H. H. Hurt, J. H. Dancy, and C. W. Fountain, "Preselection of diamond single-point Tools," Production Aspects of Single Point Machine Optics, SPIE Proceedings, Vol. 508, 1984, p. 126.

4. Villalobos, H. F. M., Process of Determining Dimensions and Properties of Cutting Edges of Molecular Dimensions, Patent #3,447,366, Patented June 3, 1969.

CHIP TOPOGRAPHY

By

Peter N. Blake
Graduate Student
Precision Engineering Laboratory

And

Ronald O. Scattergood
Professor
Materials Engineering Department

ABSTRACT

The nature of diamond turning has been studied via detailed analysis of chips produced in a laboratory-scale diamond turning machine. The characteristics of these chips, produced for lubricated and unlubricated conditions, are discussed in this section. While detailed conclusions cannot be reached at this stage of the research, the chip geometry indicates that the material flow is non-uniform and made up of lamella whose spacing seems to be related to the chip thickness.

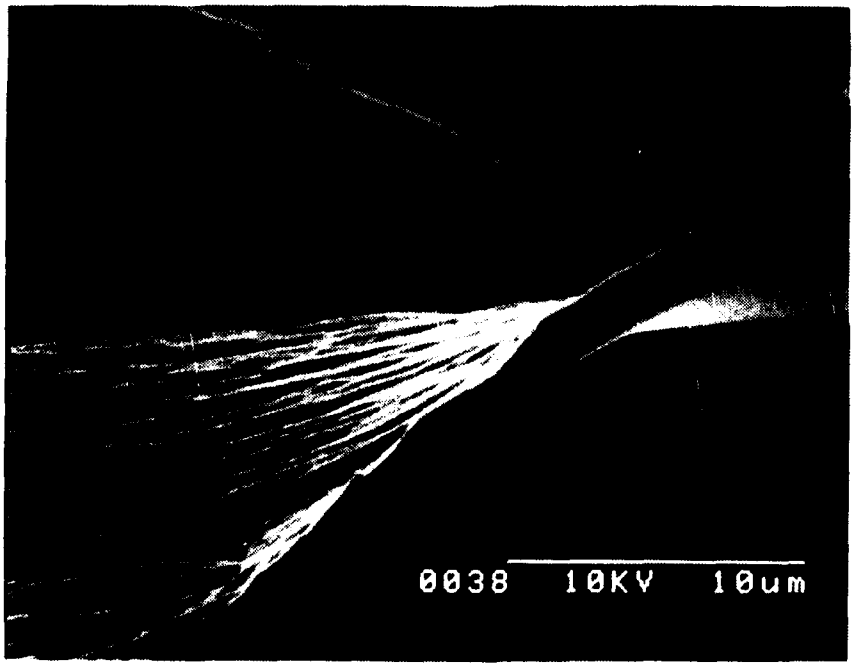

INTRODUCTION

A major emphasis of the research effort during the past year was to understand and model the chip formation process in precision micro-maching of metals. One source of clues about the deformation process lies in the machining chips. Consequently, an effort was undertaken to study chips produced in the PAUL machine for different machining conditions and depths of cut. All of the chips shown here were machined with a single crystal diamond tool from OFHC copper samples with a depth of cut varing from 20 μin. to 300 μin.

BACKGROUND

The PAUL machine, described previously, consists of a vertical axis spindle rotating the workpiece and a second spindle which allows the tool to sweep across the face of the workpiece. A cross-sectional view of the apparatus through the center is illustrated in Figure 1. The tool can be adjusted vertically to cotnrol the depth of cut and driven horizontally at different feed rates. Increasing either of these parameters will increase the volume of material removed per revolution of the workpiece.

The geometry of the cutting process is illustrated in a vertical section, Figure 2, tangent to the feed lines. The material within the region enclosed by the undeformed chip thickness (t) will be separated from the workpiece and become the chip. The resulting chip thickness can be different from t depending upon the details of the shear process in the plastically deforming material. Thus, the dimensions of the chip and its structure should give some insight into the deformation process which will be useful for the theoretical model development.

The idealized shear plane theories of cutting assume that the shear occurs locally in the chip and the angle of this plane would account for the relationship between the actual chip thickness and the undeformed thickness, t. However, previous evidence seems to indicate that the deformation process is not uniform but rather like a shear band that occurs periodically with time. Evidence of such periodic shearing has been noted in large scale machining and attributed to fracture followed by rewelding [1], adiabatic heating and dislocation mechanisms [2,3], or an unstable bifurcation of the strain state [4].

A photomicrograph of a typical chip produced in this study is shown in Figure 3. This view is interesting because both sides of the chip appear at once: the smooth side which was against the rake face of the diamond tool and a striated side which was the free surface. The shiny appearance on the rake face side is generally attributed to secondary shear due to the friction along the rake face. The striations, which are perpendicular to the chip flow (possibly along the shear plane in Figure 2) indicate that the chip has a lamellar structure made up of blocks of material. Because this particular chip has torn along one of the lamellae, it may indicate a change in properties along the edges of these regions.

AD-A166 084 PRECISION ENGINEERING - SRO 154(U) NORTH CAROLINA STATE 3/4
UNIV AT RALEIGH PRECISION ENGINEERING LAB
T A DOW ET AL JAN 86 N00014-83-K-0064

UNCLASSIFIED F/G 13/8 NL

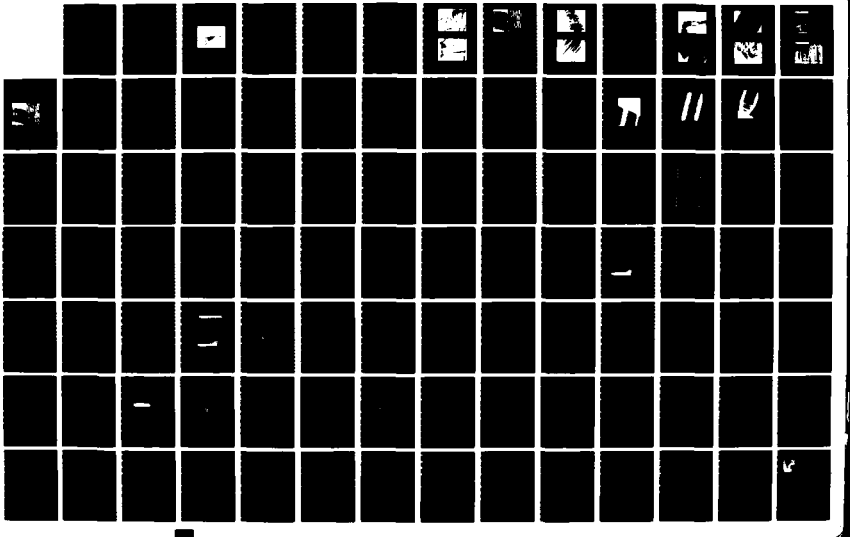

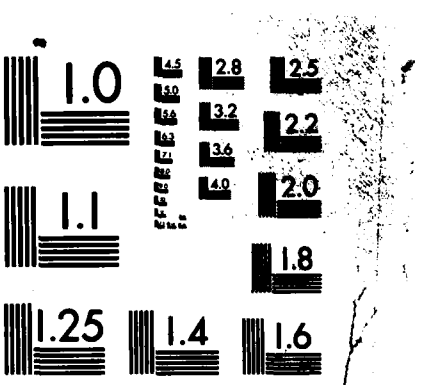

MICROCOPY RESOLUTION TEST CHART
NATIONAL BUREAU OF STANDARDS-1963-A

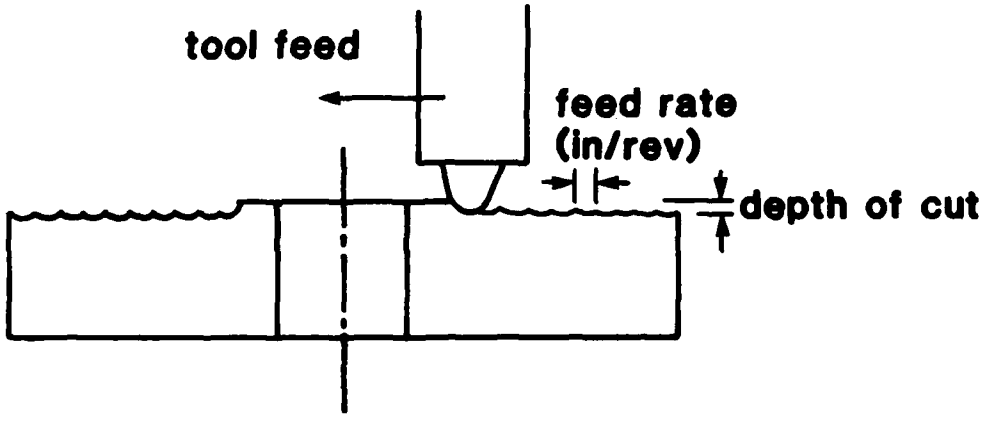

Figure 1. Facing operation on PAUL

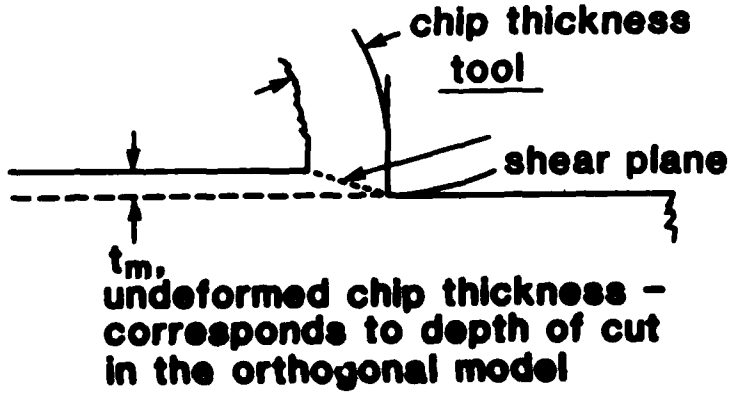

Figure 2. Ch[illegible]ormation process

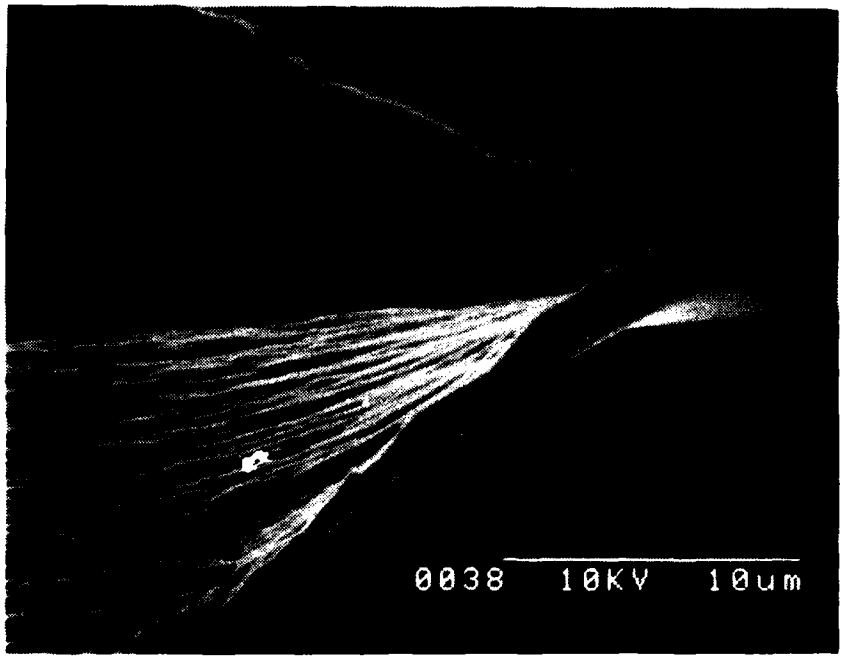

Figure 3. A torn machining chip reveals both sides (4000x)

The present study is aimed at determing the details of chips to build an empirical understanding of the flow process and the parameters which influence the shape and structure of chips produced in diamond turning. Parameters of interest include cutting speed, geometry of cut, and lubrication condition.

PROCEDURE

Samples of OFHC copper were machined on the laboratory's research lathe with a diamond tool (nose radius .030 in., rake angle 0 degree). The samples were premachined to a smooth mirror finish (Ra < 10 nm) and test cuts were made. Two different chip geometries were produced and the resulting chips are described. The first series involved a constant feed rate at a constant depth of cut. This procedure is called a facing cut. The second series involved moving the tool to a fixed depth of cut and cutting a groove in the workpiece without feeding the tool. This procedure is called a plunge cut.

The first series of chips were produced by facing, in which the tool, is moved at a constant feed rate and a constant depth of cut towards the center of the workpiece. A typical finish cut in the facing of metal optics may involve a depth of cut of 80 microinches and a feed rate of 210 microinches/revolution. The cross-section of the undeformed chip geometry of such a cut is shown to scale in Figure 4. This view is along a direction perpendicular to the cutting path and shows that the depth of cut (t) varies slowly across the width of the chip. A formula for the chip thickness can be developed from the geometry of the cutting process which involves the tool nose radius (R), the feed rate per revolution (f) and the depth of cut (d). The chip thickness is the following function of width (x):

$$t \cong \frac{f}{R}\, x \quad \text{where } 0 < x \leq R \cos^{-1}\left(1 - \frac{d}{R}\right) + \frac{f}{2}$$

The chip geometry produced in such a facing cut is similar but not identical to the orthogonal model utilized in the analysis described later in this report. For the orthogonal model, the chip is flat and the undeformed chip thickness is constant across the width of the cut.

The second series of cuts produces quite a different chip geometry, namely the undeformed cross section of the chip was the same as the tool. In this case the chip depth (d) as a function of width (x) can be written as,

$$d = \frac{x^2}{2R}$$

where

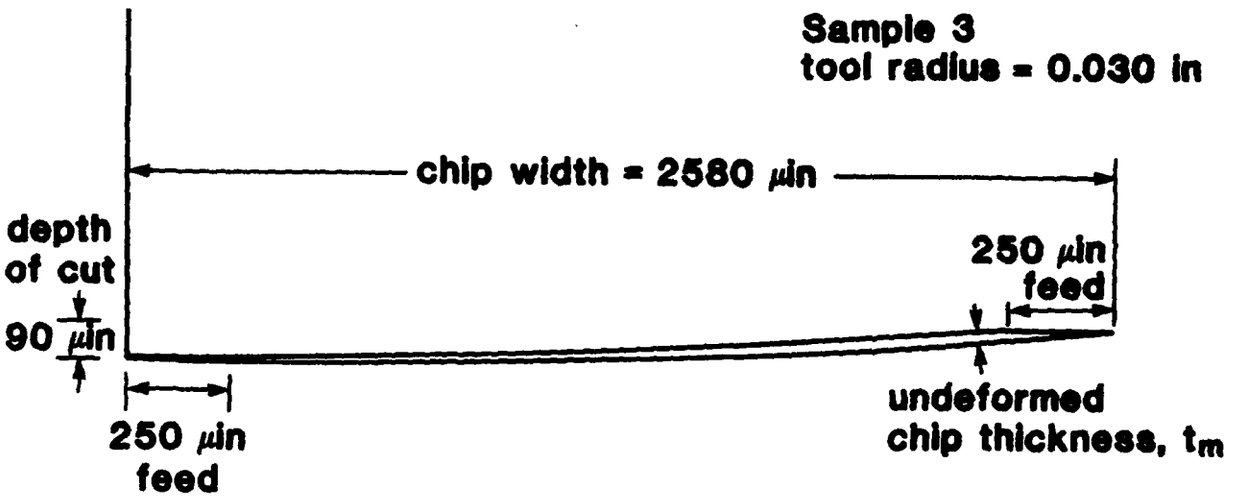

Figure 4. Cross section of undeformed chip geometry

R = nose radius of the tool and x is measured from the center of the chip width

For the case of a 400 μin. maximum depth of cut, a 0.030 in tool radius and a feed rate of 100 μin./revolution, the width of the chip for the facing cout would be 12 times wider than for the plunge cut. But at the same time, the undeformed chip thickness for this facing cut would be only 4 percent of the chip thickness in the plunge cut. The thickness to width ratio of the chip may be an important parameter in the deformation process. For this example, this ratio would be 300 for the facing cut and only 25 for the plunge cut.

A plunge cut is created by lowering the tool into a stationary workpiece to a known depth and moving the workpiece, under microprocessor control, one revolution at a specified maximum speed. Various depth and speeds were tried -- both with lubrication and without.

RESULTS

Facing Cuts

Five samples of facing chips with varied chip thickness were cut from a single OFHC sample at a constant rotational speed. The cutting speed was 100 in./sec. ± 20 in./sec., depending on the radius at which the cut was made. Lubrication was with Shell Dialla-AX.

Micrographs of these chips are shown in Figure 5 (a-e). Table 1 illustrates the relationship between chip thickness and lamellae spacing for different depths of cut and feed rates. The resultant maximum thickness is about 6 times (6x) the undeformed chip thickness, t_m (see Figure 2). The spacing of the lamellae in the center of the chips was measured. The spacing was found to be proportional to the maximum chip thickness.

Table 1. Relationship between chip thickness and lamellae spacing

Sample #	Maximum Undeformed chip thickness t_m (μin.)	Maximum Thickness measured in SEM (μin.)	Lamellae Spacing (μin.)
1	1.8	Unable to measure	5
2	5	33	10
3	18	100	15
4	48	300 - 400	16-28
5	150		20-100

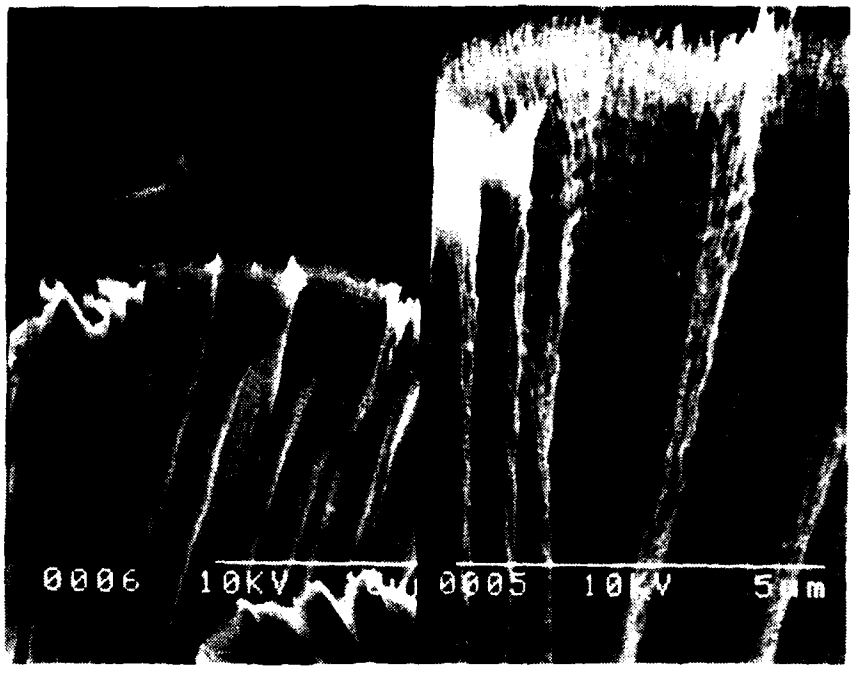

Figure 5a. Chip from facing cut. Sample #1
lamellae spacing: 5 µin.
magnification: right side: 10,000x
left side: 3000x

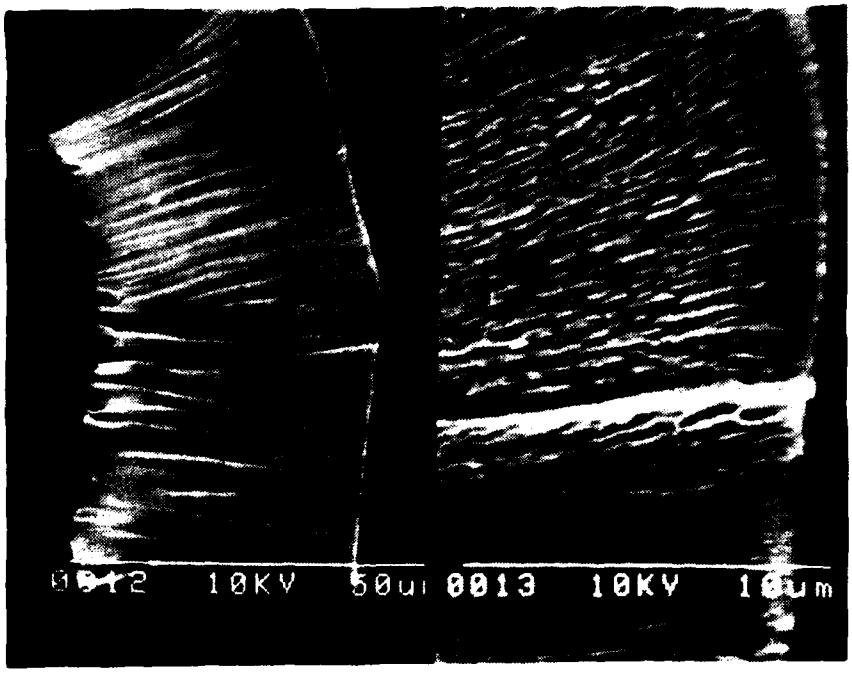

Figure 5b. Chip from facing cut. Sample #2
maximum undeformed chip thickness, t_m: 5µin.
lamellae spacing: 10 µin.
magnificaton: right side: 5000x
left side: 1000x

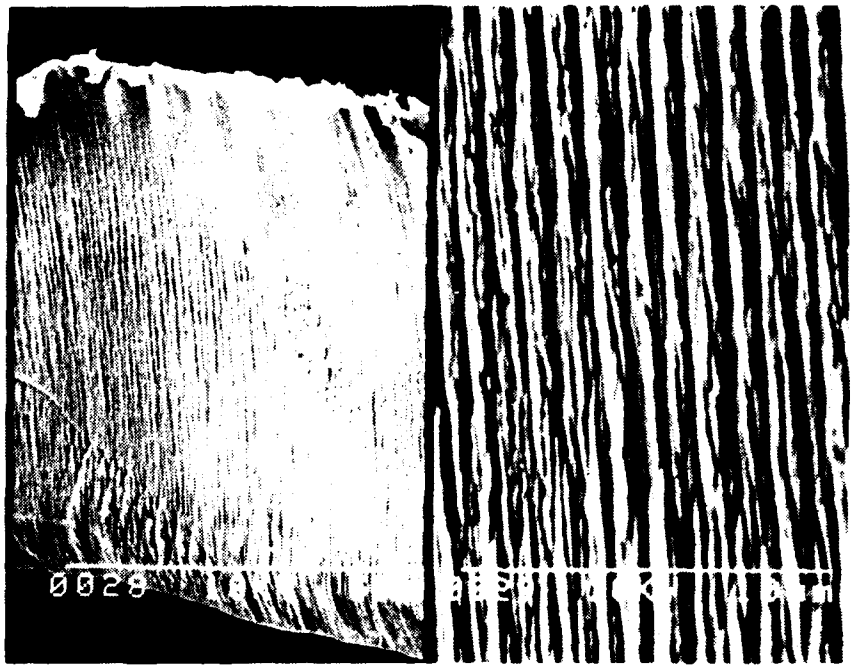

Figure 5c. Chip from facing cut. Sample #3
maximum undeformed chip thickness, t_m: 18 µin.
lamellae spacing: 15 µin.
magnification: right side: 5000x
left side: 1000x

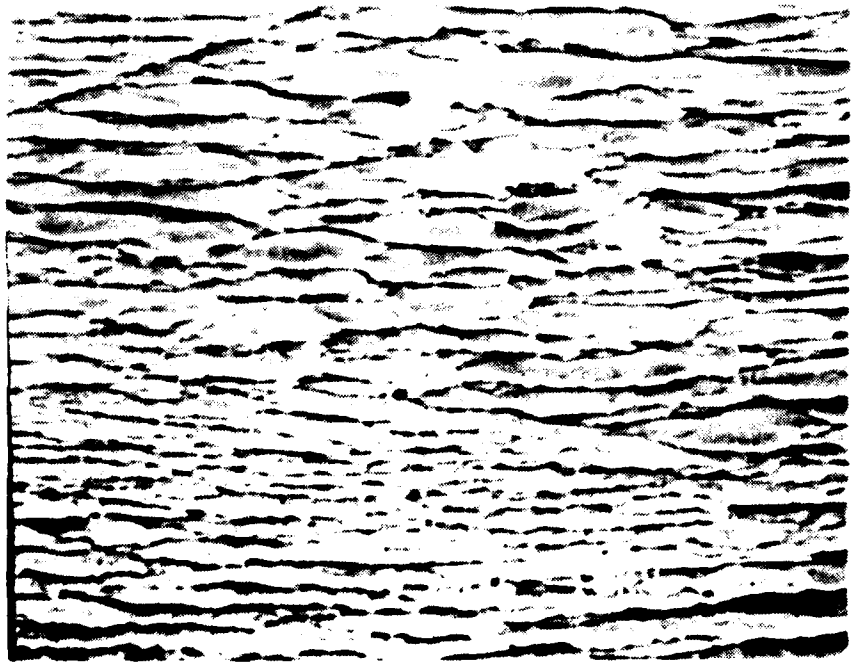

Figure 5d. Chip from facing cut. Sample #4
maximum undeformed chip thickness, t_m: 48 µin.
lamellae spacing: 16-28 µin.
magnification: 5000x

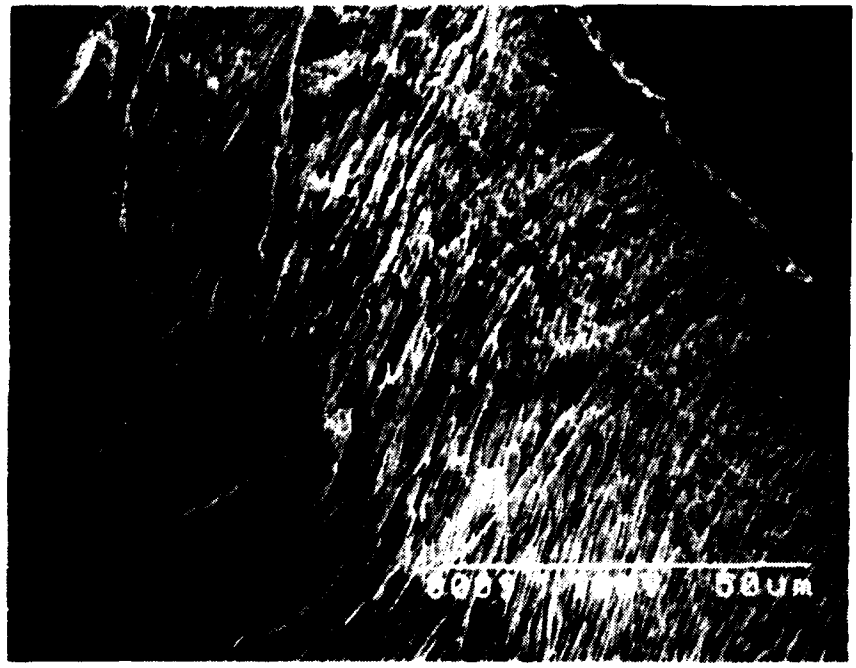

Figure 5e. Chip from facing cut. Sample #5
maximum undeformed chip thickness, 150 µm.
lamellae spacing 20-100 µin.
magnification: upper photo: 1000x
lower photo: 5000x

The spacing of the lamellae also varies across the chip width, increasing as the chip thickness decreases. Furthermore, for the largest chip thicknesses, there appear to be a number of different lamellae spacings superimposed on each other. Figure 5c shows lamellae of spacing 15 μin. imposed on larger scale lamellae of spacing 40 μin. Figure 5e, micrographs of the thickest chips (sample 5) shows a non-uniform superposition of lamellae of very different spacings.

Better processed images and statistical analysis will soon clarify the chip thickness -- lamellar spacing relationships.

Chips that were torn after collection often give a unique view of the lamellae. Figure 6 (and several other unpublished micrographs) show that at the thin edge of the chip, at least, the lamellae extend deep into the chip and are easily separated. Figure 7 appears to show that underlying the lamellae is a smooth membrane-like layer. Further work with stereoscopy and higher resolution microscopes is needed to confirm the validity of these initial observations.

Plunge Cuts

A second series of cuts, the plunge cuts, illustrates the effects of a significant variation in depth of cut across the width of the chip. For a chip from a lubricated cut of depth 400 μin. (Figure 8), only the center of the chip actually has this depth of cut; the edges approach zero thickness (the width of the chip is about 25 times the depth). The lamellae are spaced very tightly near the edges, increase in size near the center; and superimposed are larger blocks of material.

Several variations of this cut were tried. When the cut was unlubricated (Figure 9), the large blocks of material dominate the deformation process. They are clearly separated and show extreme tortuosity. Lamellae of the scale shown in Table 1 are present as part of the deformation of each block. The blocks appear at a frequency of about 150 Hz., so they could be due to vibration or stick/slip; they could also be due to heating effects.

When the cutting speed was increased by approximately 10 times (since the sample had to accelerate and deccelerate in the single revolution, the speed cannot be specified exactly) and the cut lubricated (Figure 10), a chip similar to that of the slower lubricated cut (Figure 8) was produced, but with more of the deformation occurring through the pushing out of large blocks.

Figures 11 and 12 illustrate chips machined for shallower depth of cut. The depth of cut for Figure 11 was 115 microinches and for Figure 12, 18 microinches

Decreasing the depth of cut causes a decrease in block-forming, until at the very shallow cut of 18 μin., the lamellae appear as they do in the facing cuts -- increasing in size towards the thicker part of the chip (the center). Figure 12 shows a change in lamellae spacing across

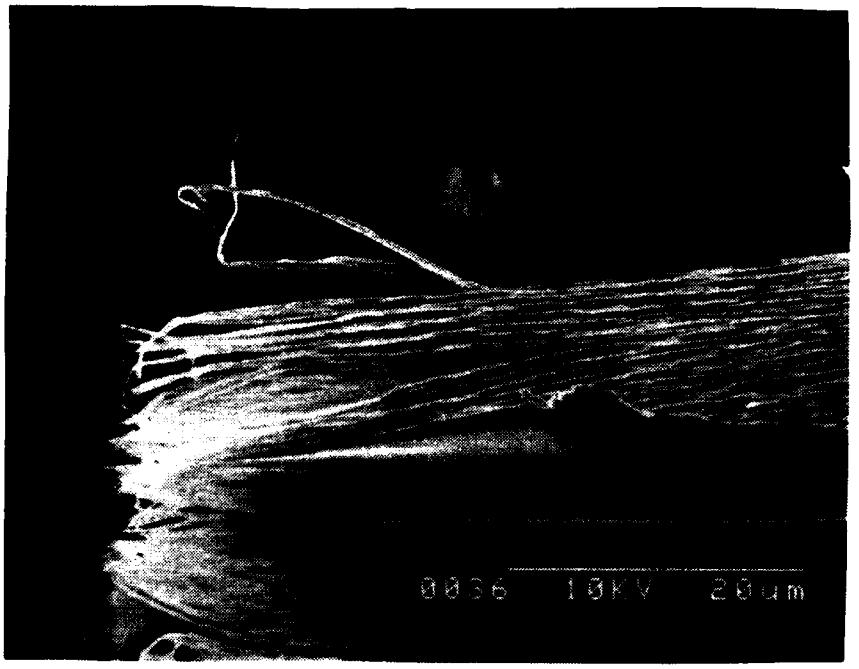

Figure 6. Thin edge of chip at 2000x

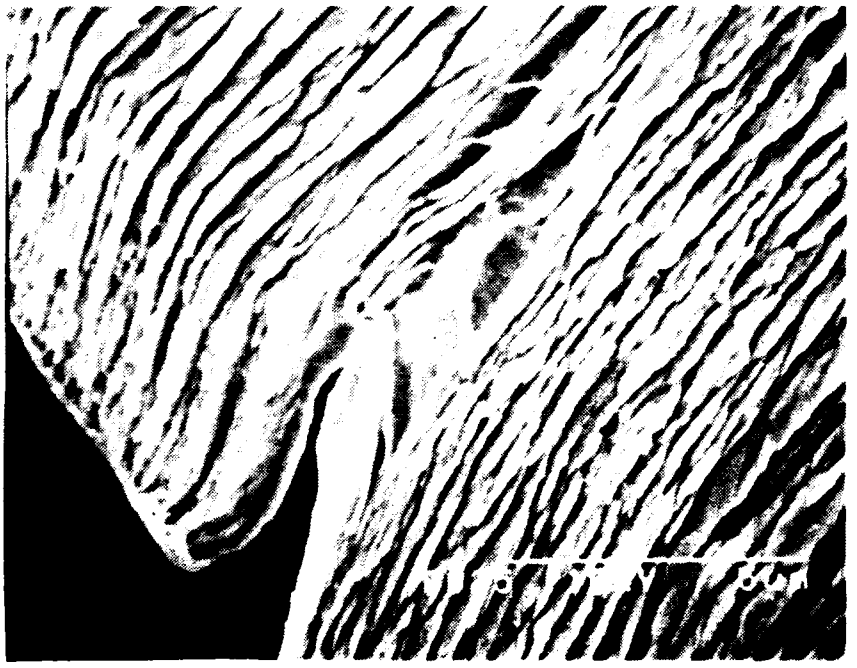

Figure 7. Thick edge of chip

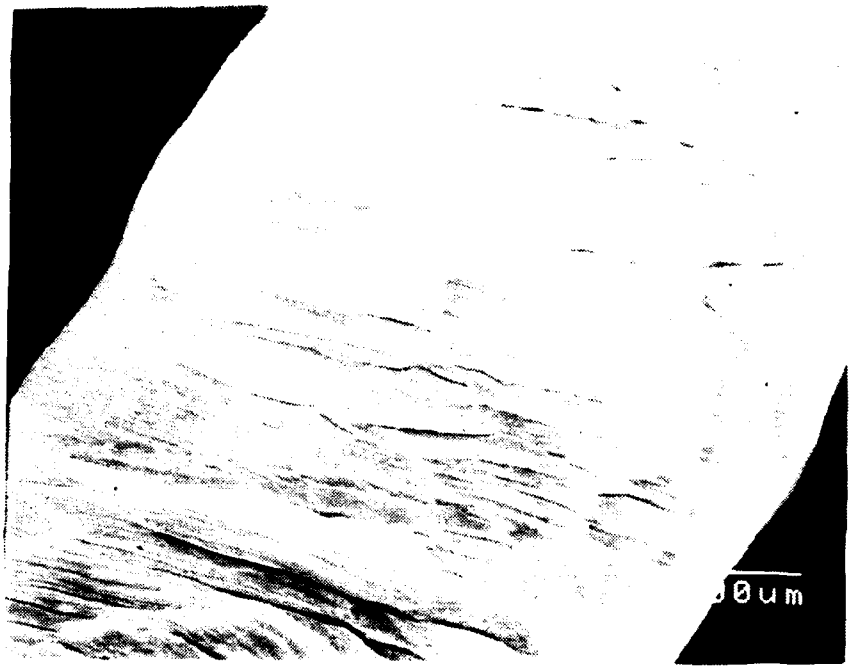

Figure 8. Chip from a lubricated plunge cut
Depth of cut: 400 µin.
cutting speed; .1 in/sec.
magnification: 2000x

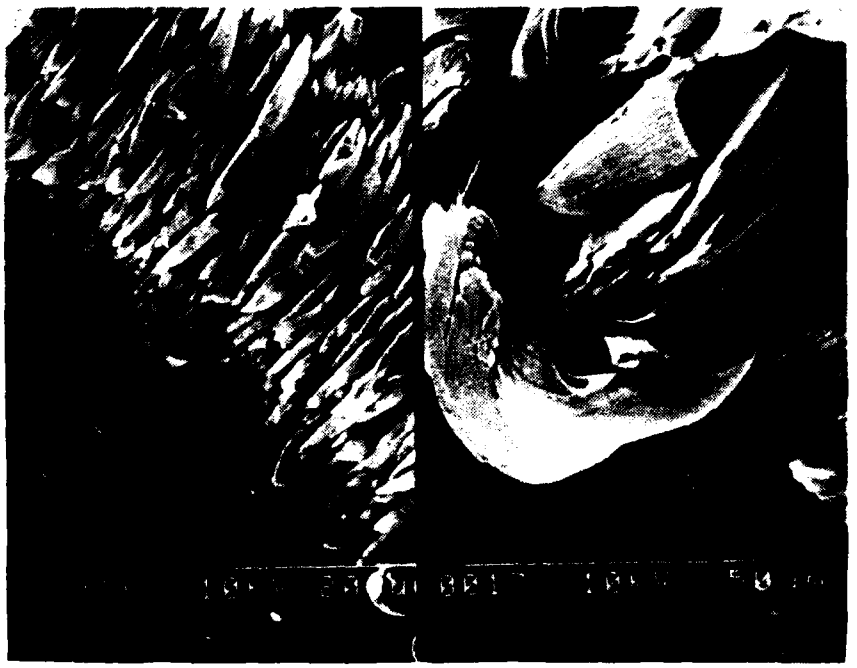

Figure 9. Chip from an unlubricated plunge cut
Depth: 600 µin.
cutting speed: .1 in/sec.
magnification: right side 1000x
left side: 150x

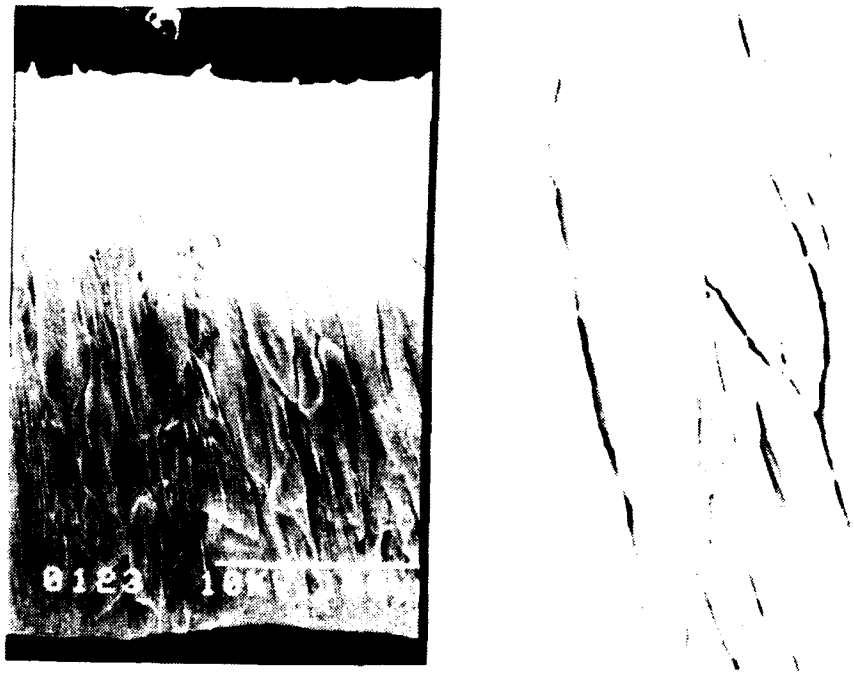

Figure 10: Chip from a lubricated plunge cut
Depth of cut: 440 µin.
cutting speed: 10 in/sec.
magnification: right side: 1500x
left side: 300x

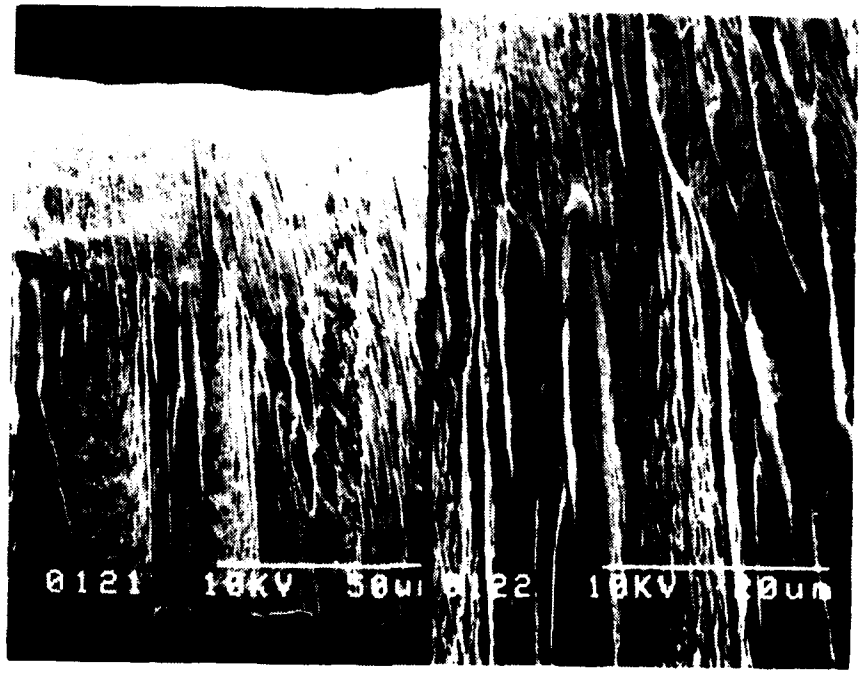

Figure 11. Chip from a lubricated plunge cut
Depth of cut: 115 µin.
cutting seed: 10 in/sec.
magnification: right side: 1500x
left side: 600x

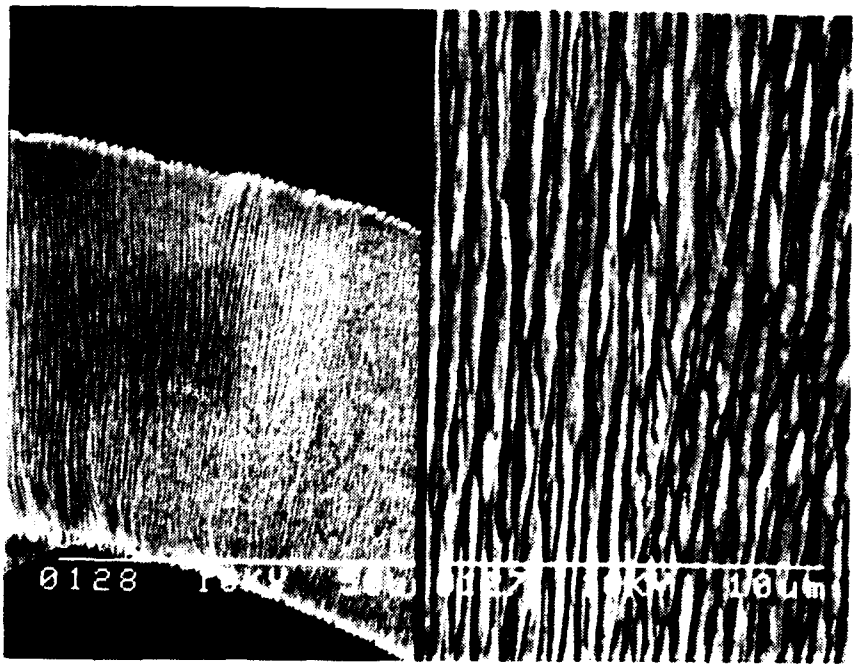

Figure 12. Chip from lubricated plunge cut
Depth of cut: 18 µin
cutting speed: 10 in/sec.
magnification: right side: 5000x
left side: 1000x

some boundary -- perhaps a grain boundary. Similar boundaries are seen in most micrographs of the facing chips (e.g., Figure 5c and d).

CONCLUSION

The preliminary conclusions from the observations of machining chip structure are that the lamellae spacings are proportional to chip thickness; and that the greater the variation of thickness with chip width, the greater the inhomogeneous extrusion of blocks of material from the free surface. Further studies will be carried out to provide further verification of these results.

REFERENCES

1. Walker, T. J. and M. C. Shaw, "On Deformation at Large Strains," Advances in Tool Design and Research, Pergamon Press, Oxford, 1970, pp. 241-252.

2. Von Turkovich, B. F., "Shear Stress in Metal Cutting," in Journal of Engineering for Industry, Trans. ASME, Series B, Vol. 92, No. 1, 1970, p. 151.

3. Black, J. T., "Shear Front-Lamella Structure in Large Strain Plastic Deformation Processes," Journal of Engineering for Industry, Vol. 94, No. 1, Feb. 1972, p. 307.

4. Rice, James R., "The Localization of Plastic Deformation," in Theoretical Appl. Mech., W. T. Koiter, ed., North Holland Publishing, 1976, p. 207.

TOOL FORCE MEASUREMENT EXPERIMENT

By

John T. Carroll, III
Graduate Student
Precision Engineering Laboratory

And

Thomas A. Dow
Professor
Mechanical and Aerospace Engineering

ABSTRACT

An experiment has been performed in the Precision Engineering Laboratory to measure cutting forces at slow speeds. Computer modeling efforts by members of the Precision Engineering team have been concerned with advancing an understanding of material removal on the micro-scale via cutting. This work has progressed to a point where reliable experimental observations are needed to further validate and direct the research effort. In response to this need, a force measurement apparatus was fabricated and installed on the Parallel Axis Ultraprecision Lathe (PAUL). Preliminary results obtained at a cutting velocity of 1.2 mm/sec (0.048 in/sec) for cutting depths that ranged between 3 and 22 micrometers (125 and 875 microinches) showed the cutting force to be directly proportional to cutting area. Photomicrographs of the specimen revealed clean, sharply defined cuts of uniform depth.

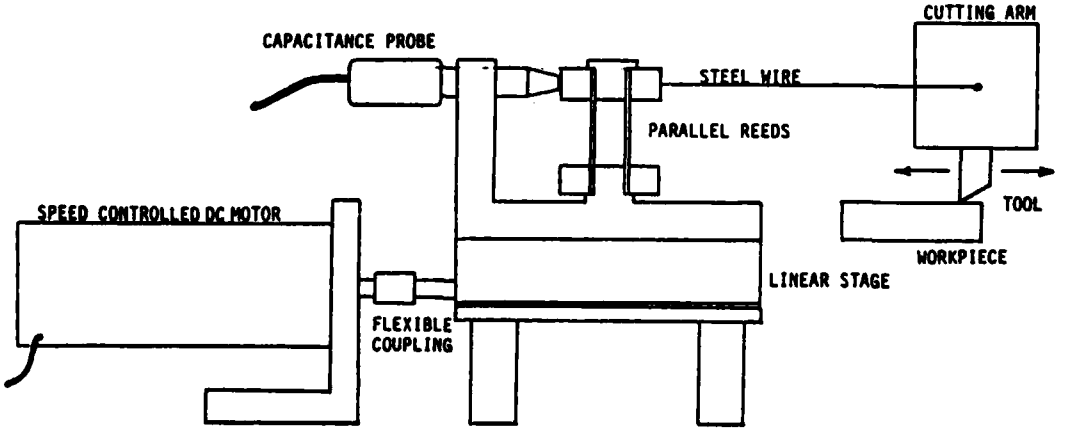

INTRODUCTION

The force on a cutting tool is a measurable process parameter that is sensitive to a number of material and geometric variables. The understanding of this sensitivity has been a goal of the Precision Engineering team working in the area of Material Removal. An earlier effort [1] to measure forces on the cutting tool was designed to

1. establish the magnitude of the tangential tool force for depths of cut less than 2 micrometers (80 microinches)

2. study the nature of the chip formation at slow speed

3. establish design parameters for a dynamometer to be used on the laboratory's diamond turning machine.

This experiment measured the force required to cut 2024-T3 aluminum with diamond tools (of different nose radii and rake angle) at depths of cut ranging from 0.25 micrometers (10 microinches) to 1.5 micrometers (60 microinches) for speeds less than 0.0254 cm/sec (0.01 in/sec). The results of this investigation were largely qualitative but showed with repeatability that the cutting force increases with an increase in the material removal rate (increased cutting depth and/or cutting radius holding speed constant) and greater negative rake angle orientations of the tool. The current experiment is intended to be a refinement of this work from which both qualitative and quantitative information can be obtained. Details of the cutting geometry are shown in Figures 1 and 2. The first figure defines the cutting depth, tool rake angle, and cutting force while the second defines the cutting area.

APPARATUS

The apparatus used to measure cutting force (F_c) is shown schematically in Figure 3. It consists of a pair of parallel reeds and a capacitance gage force measurement assembly mounted on a motorized linear stage. The parallel reeds have a stiffness of 10,000 N/cm (5600 lbf/in.) and are attached to the cutting arm of the Parallel Axis Ultraprecision Lathe (PAUL) [2] with 0.375 mm (0.015 in.) steel wire. The stage is driven through a flexible coupling by a speed-controlled DC motor. The stage/motor combination provides a range of steady, vibration isolated cutting velocities (V_c) from 0.01 to 5 mm/sec. (0.0004 to 0.2 in/sec). As the stage is advanced in the cutting direction, the displacement of the parallel reeds is measured with the capacitance gage and later converted to a force value using a calibrated stiffness factor.

The process of measuring cutting force with this apparatus begins with the preparation of a specimen as shown in Figure 4. The specimen is placed in the PAUL and finished with a diamond tool to a flatness of approximately 0.05 micrometer (2.0 microinch) and a surface roughness better than 0.025 micrometer (1 microinch). The cutting tool is then turned 90 degrees in its holder and the spindle locked so that radial

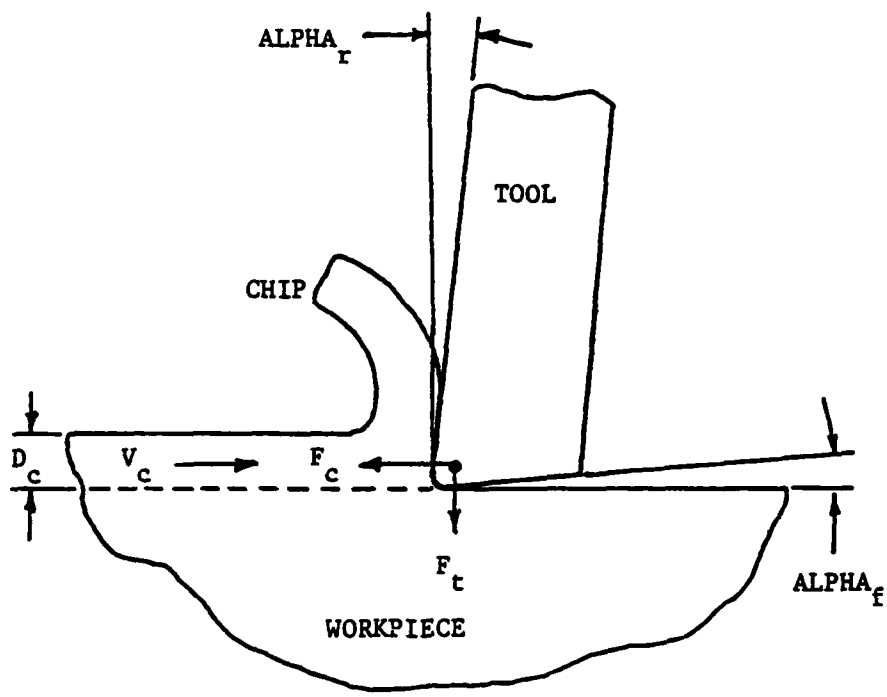

Figure 1. Detail of cutting geometry showing cutting depth (D_c), velocity (V_c), rake angle ($ALPHA_r$) and force (F_c).

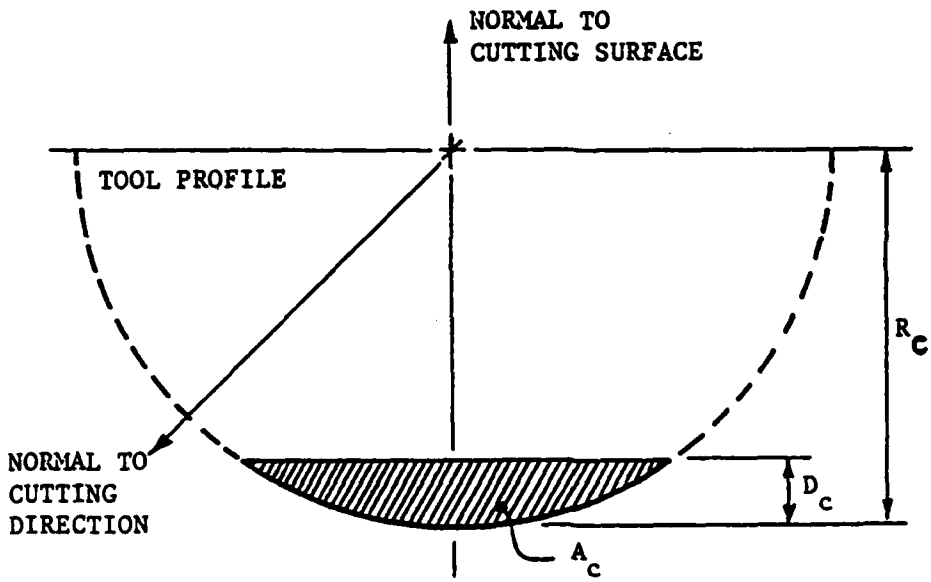

Figure 2. Detail of cutting geometry showing cutting area (A_C) and radius (R_C).

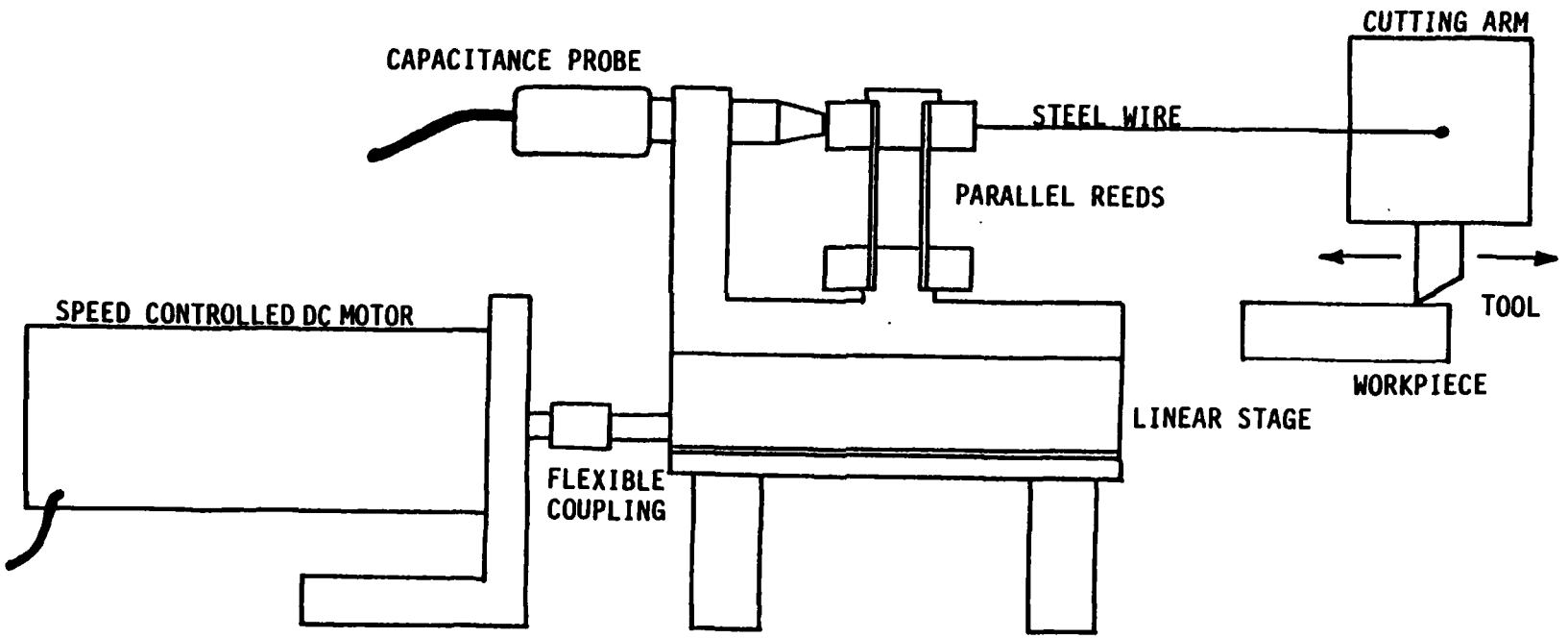

Figure 3. Tool Force Measurement Apparatus

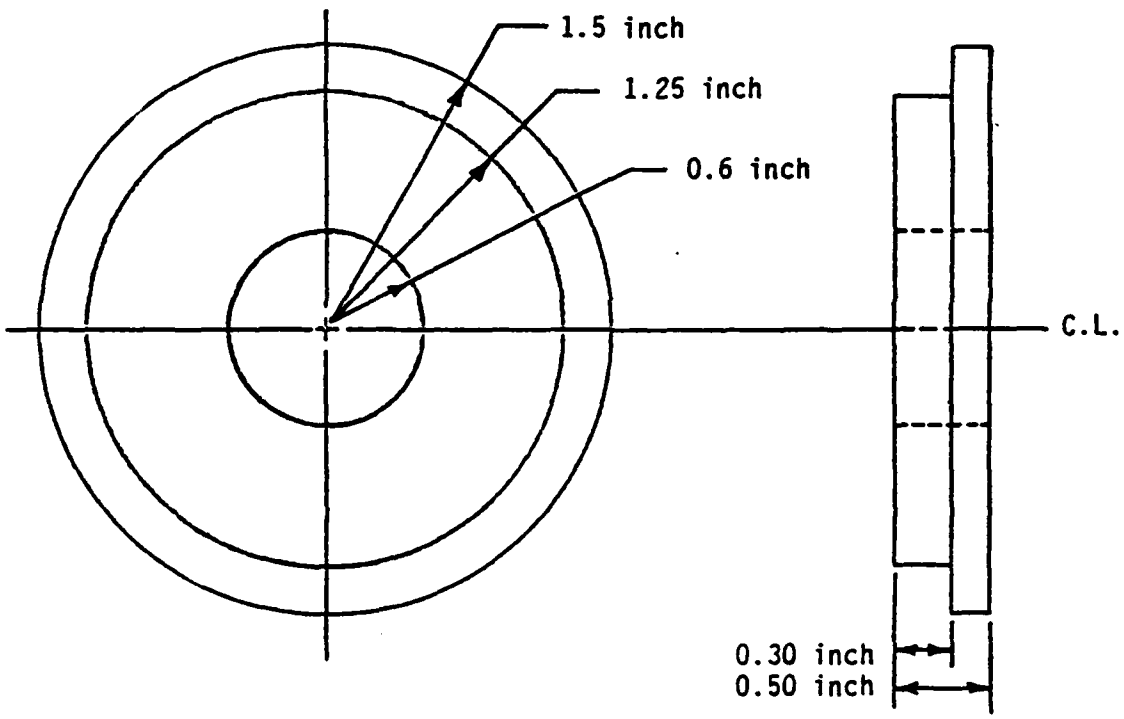

Figure 4. Specimen geometry

cuts can be made by pulling the cutting arm across the specimen with the force measurement assembly discussed above.

Design Considerations

The tool force measurement apparatus was designed to provide accurate cutting force information under controlled conditions. The previous effort to measure tool forces in the Precision Engineering Laboratory [1] showed that it is essential to begin with a smooth specimen, maintain a uniform cutting depth and to limit vibrations. The PAUL was chosen as the basis of the current experiment for its high stiffness and low error motion. With this lathe, specimens can be turned and left on the spindle for the tool force experiment. Preparing the specimen in this way insures a uniform cutting depth.

PRELIMINARY RESULTS

To test the tool force measurement apparatus, an aluminum (2024) specimen was fixtured in the PAUL and turned to a surface roughness of 0.03 micrometers (1.2 microinches) C.L.A. A series of successively deeper radial cuts were then made at a cutting velocity of 1.2 mm/sec. (0.048 in/sec). The shallowest cut was 3 micrometers (125 microinches) and the deepest was 22 micrometers (875 microinches).

Figures 5, 6 and 7 are Nomarsky photomicrographs showing the beginning, middle and end of a typical cut. In each case, the material appears to have been removed cleanly. Figure 5 shows evidence of tool chatter that is not present in the other photos suggesting a transient oscillation (256 Hz) accompanies the initiation of a cut. Figure 6 shows evidence of small inclusions or other contaminants being pulled out and dragged along the finished surface. The peculiar looking termination of the cut in Figure 7 is the result of lifting the tool in preparation for the next cut. As the tool is lifted, the depth of cut is gradually reduced to zero and tool advances in the direction of the cut. Tool height adjustment is made by manually adjusting the input to the piezoelectric transducer and results in the stepped pattern.

Figure 8 contains a plot of cutting force versus cutting time. It shows a clean transition to a average cutting force of 4.5 N (1 lbf).

Figures 9 and 10 contain plots of cutting force versus cutting depth and cutting area. The first shows that the cutting force is proportional to the depth of cut raised to the 3/2 power (less than 0.1 percent deviation). In the second figure, the force varies linearly with cutting area (less than 0.1 percent deviation). These results are mutually consistent with the geometry of the cut shown in Figure 2.

Figure 5. Nomarsky photomicrograph of a typical cut at the point of entry into the specimen.

material..... aluminum-2024
cutting depth ... 17.5 micrometers (700 microinches)
cutting speed ... 1.28 mm/sec (0.051 in/sec)
cutting radius .. 0.75 mm (0.03 in)
rake angle ..... 0 degrees
lubricant ..... unlubricated
magnification ... 400

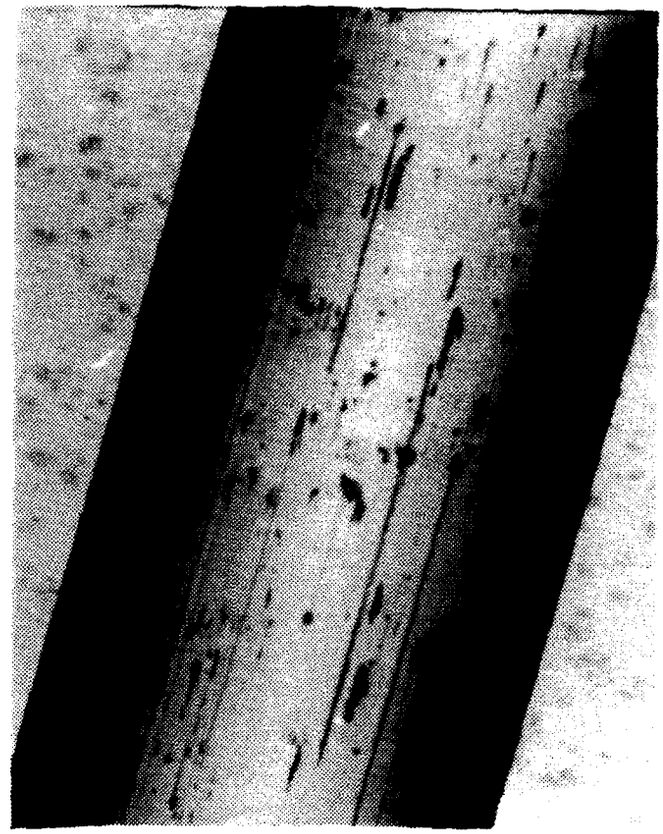

Figure 6. Nomarsky photomicrograph of a typical cut at a point midway through the specimen.

material..... aluminum-2024
cutting depth ... 17.5 micrometers (700 microinches)
cutting speed ... 1.28 mm/sec (0.051 in/sec)
cutting radius .. 0.75 mm (0.03 in)
rake angle ..... 0 degrees
lubricant ..... unlubricated
magnification ... 400

Figure 7. Nomarsky photomicrograph of a typical cut at the point of termination.

material..... aluminum-2024
cutting depth ... 17.5 micrometers (700 microinches)
cutting speed ... 1.28 mm/sec (0.051 in/sec)
cutting radius .. 0.75 mm (0.03 in)
rake angle ..... 0 degrees
lubricant ..... unlubricated

magnification ... 400

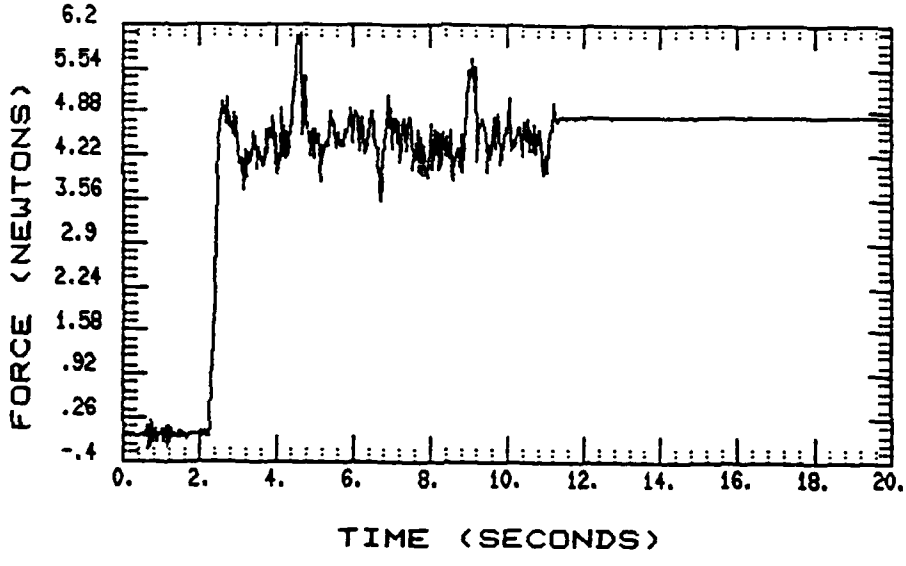

Figure 8. Plot of cutting force versus cutting time for a typical cut.

material..... aluminum-2024
cutting speed ... 1.28 mm/sec (0.051 in/sec)
cutting radius .. 0.75 mm (0.03 in)
rake angle ..... 0 degrees
lubricant ..... unlubricated

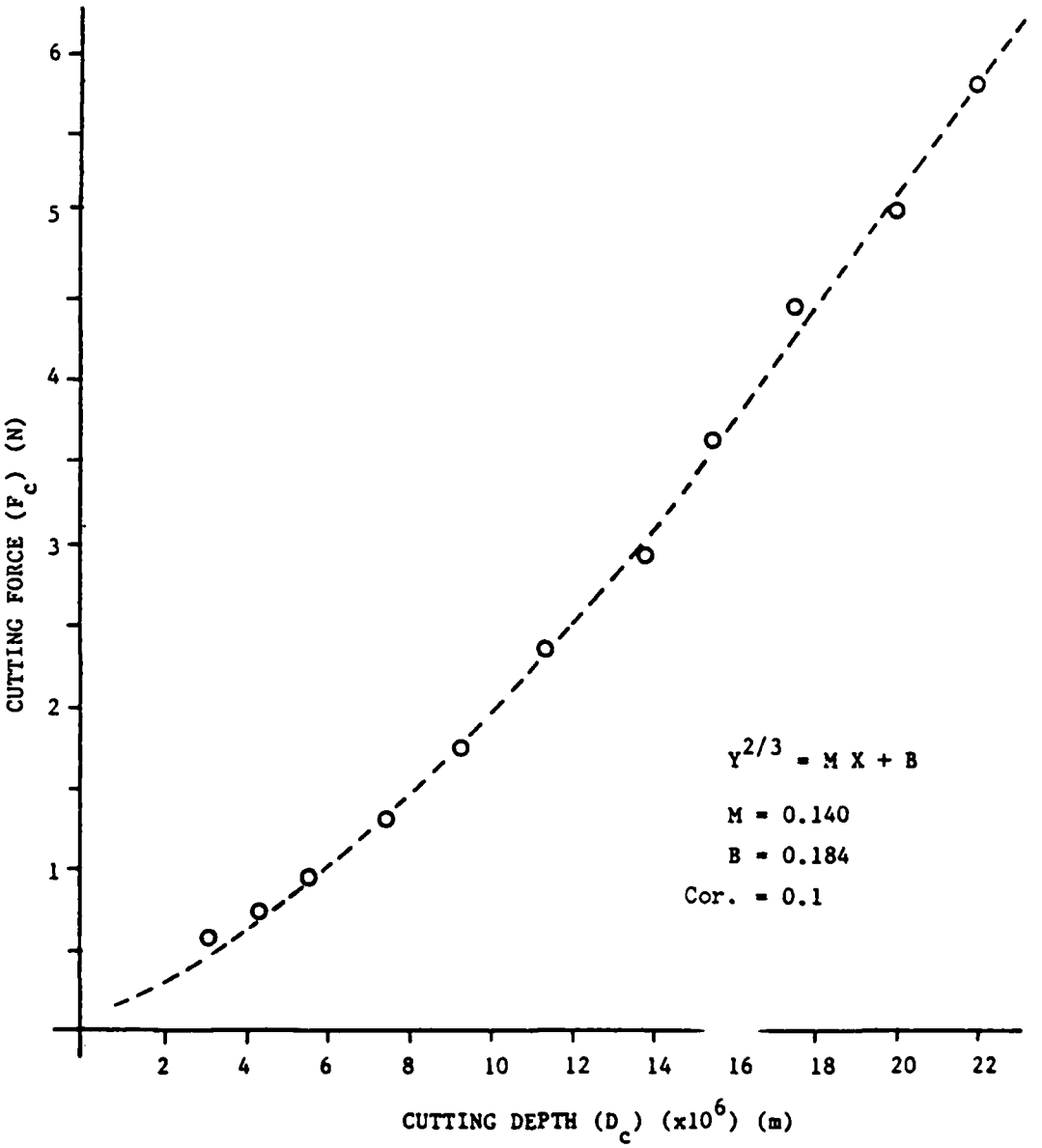

Figure 9. Plot of cutting force versus cutting depth.

material..... aluminum-2024
cutting speed ... 1.28 mm/sec (0.051 in/sec)
cutting radius .. 0.75 mm (0.03 in)
rake angle ..... 0 degrees
lubricant ..... unlubricated

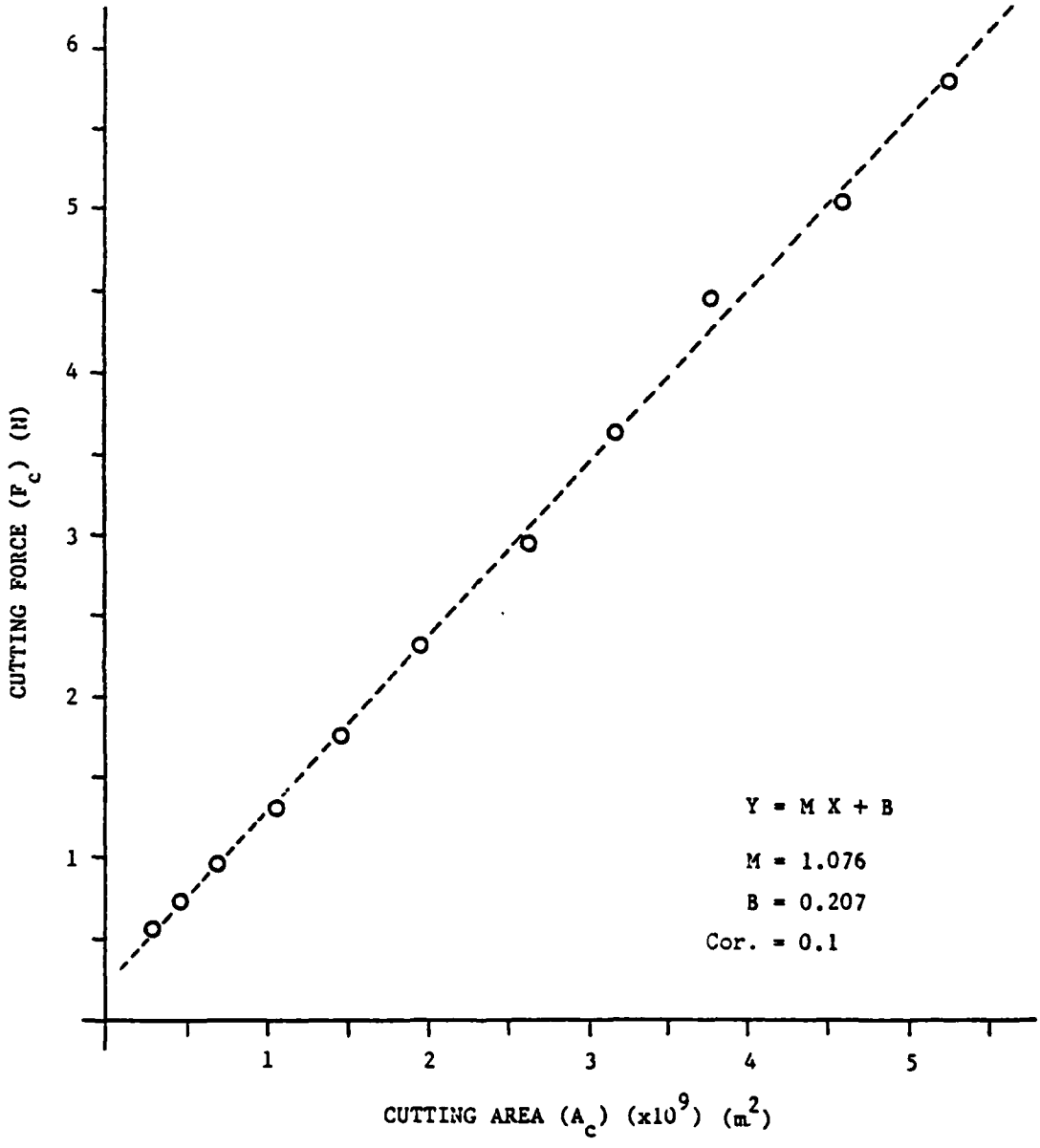

Figure 10. Plot of cutting force versus cutting area.

material..... aluminum-2024
cutting speed ... 1.28 mm/sec (0.051 in/sec)
cutting radius .. 0.75 mm (0.03 in)
rake angle ..... 0 degrees
lubricant ..... unlubricated

FUTURE WORK

The preliminary results obtained with the tool force measurement apparatus are both interesting and encouraging. A complete series of tool force measurements will be performed to study the effect of changes in cutting velocity, depth, radius, rake angle, lubricant and workpiece material. Details of these process variables are as follows:

1. Velocity ..... 0.01 to 5 mm/sec. (0.0004 to 0.2 in./sec.)
2. Depth ..... 2 to 20 micrometers (80 to 800 microinches)
3. Radius ..... 0.75 mm (0.03 in.) and 3.125 mm (0.125 in.)
4. Rake angle ..... -45 to +2 degrees
5. Lubricant ..... lubricated and unlubricated
6. Material ..... aluminum, OFHC copper and electroless nickel

The results of this study will form a valuable data base for comparison with other experimental and theoretical work.

REFERENCES

1. Burton, R. A., D. L. Christenbury, and T. A. Dow, "Measurement of Tool Forces for Precision Diamond Cutting," Second Annual Report on Precision Engineering, North Carolina State University, January 1985.

2. Falter, P. J. and T. A. Dow, "PAUL - Parallel Axis Ultraprecision Lathe," Third Annual Report on Precision Engineering - SRO 154 North Carolina State University at Raleigh, January 1986, p. 163.

COMPUTER SIMULATION OF ORTHOGONAL METAL CUTTING EMPLOYING THE FINITE ELEMENT METHOD WITHIN AN EULERIAN COORDINATE REFERENCE FRAME

By

John T. Carroll III
Graduate Student
Precision Engineering Laboratory

And

John S. Strenkowski
Associate Professor
Mechanical and Aerospace Engineering Department

ABSTRACT

A computer model for simulating orthogonal metal cutting has been developed in the Precision Engineering Laboratory. The model is the result of continuing efforts in the area of material removal to study the effect that different cutting conditions have on chip formation, tool forces, and surface damage. Results obtained for a series of metal extrusion problems show agreement with other published work. Further, the results of a preliminary metal cutting simulation are presented.

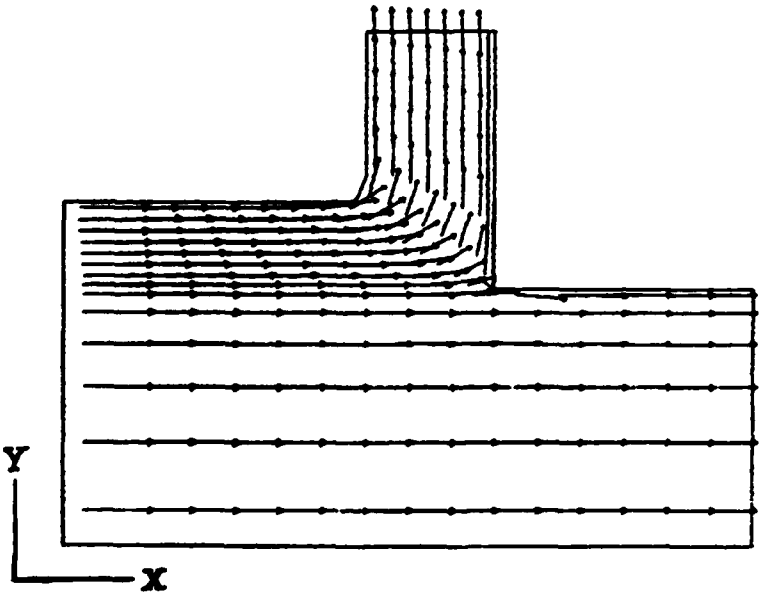

INTRODUCTION

The Precision Engineering Laboratory has been and continues to be involved in research efforts to understand the material removal process through the development and use of advanced computer assisted simulations. To date, considerable progress has been made toward modeling orthogonal (two dimensional, plane strain) metal cutting with the NIKE2D code.

NIKE2D is an implicit, finite deformation, large strain, finite-element code for analyzing the response of two-dimensional axisymmetric and plane strain solids [1]. The code was acquired from the Lawrence Livermore National Laboratory and modified to simulate the cutting process [2]. Sample results from a typical simulation are shown in Figures 1 through 4. For this simulation, a sharp, frictionless, tool oriented at a zero degree rake angle was moved into an aluminum workpiece at a 10 microinch depth of cut. Figures 1, 2, and 3 show the distorted finite element grid prior to cutting and at two successive tool positions, respectively. Figure 4 is a contour plot of the total effective plastic strain in the chip and finished surface. Simulations of this kind are run to study the effect different cutting conditions have on chip formation, tool forces and surface damage. Recently, the process by which segmented chips are formed was modeled [3]. This work has provided new insights into the material removal process and demonstrates the feasibility of using advanced computer assisted simulations as research tools.

The successes achieved with the NIKE2D code and the desire to model cutting conditions for which it is not well suited has lead to the development of a new code called MCS (Metal Cutting Simulation). MCS is a finite element code applicable to two-dimensional, plane-strain, metal-forming problems. The code is largely based on information presented in a series of papers by O. C. Zienkiewicz treating the subject of metal forming and extrusion. Details of the simulation methodology, preliminary results, and future work are discussed in this section.

SIMULATION METHODOLOGY

The MCS code was developed to eliminate some of the modeling limitations imposed by NIKE2D. In particular, the objectives behind this development were to:

1. reduce the time required to perform a simulation
2. eliminate the need to deal with a material separation criterion
3. better resolve the flow of material in the vicinity of the tool tip where a built-up edge may be present.

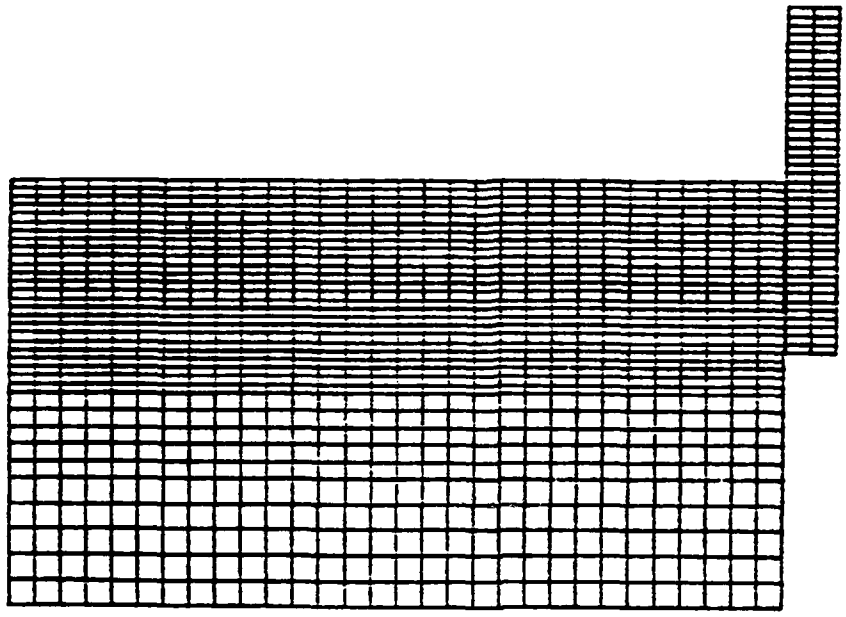

Figure 1. Finite element mesh prior to cutting. (results from a NIKE2D simulation)

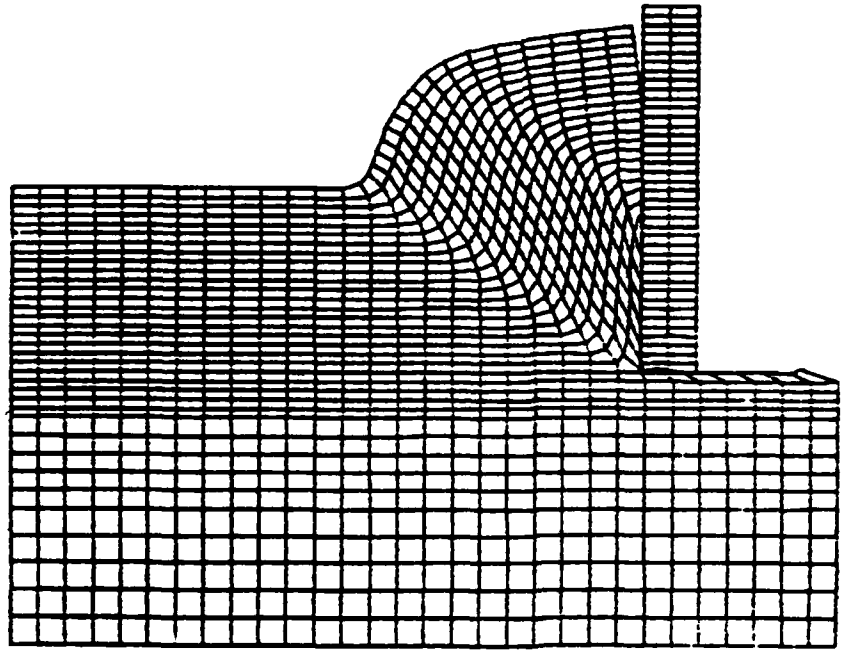

Figure 2. Finite element mesh at an intermediate tool position. (results from a NIKE2D simulation)

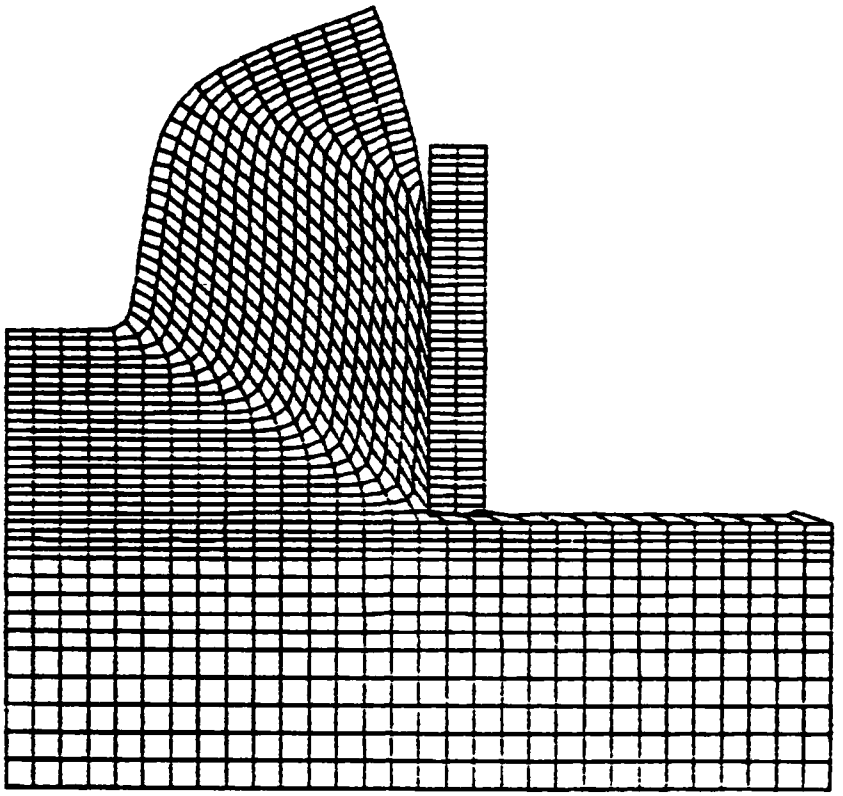

Figure 3. Finite element mesh at final tool position. (results from a NIKE2D simulation)

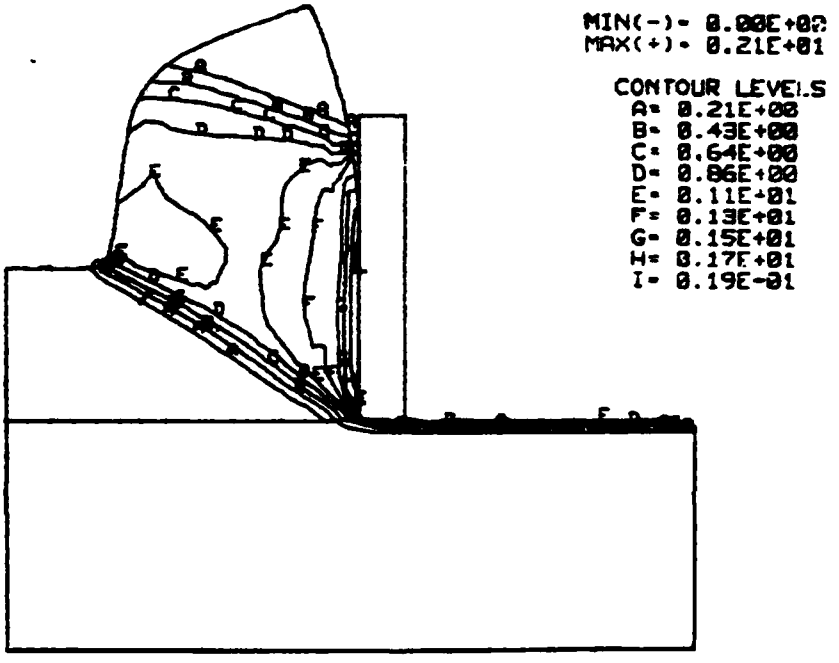

Figure 4. Contour plot of total effective plastic strain at final tool position. (results from NIKE2D simulation)

Eulerian Coordinate Reference Frame

NIKE2D employs a Lagrangian coordinate reference frame in which the finite element mesh is attached to the workpiece and chip. To produce a chip, it is necessary to advance the tool a considerable distance into the workpiece using a material failure criterion to define the conditions under which the chip is allowed to part from the finished surface. This process requires a tremendous computational effort and cannot be applied to conditions where mesh distortions are severe (i.e. large negative tool rake angles and built-up edge formations). MCS uses an Eulerian coordinate reference frame where the finite element grid defines a control volume through which the material flows. While this approach requires that the boundary geometries be known in advance or iteratively adjusted during the simulation, it eliminates the transition to steady cutting and the need for a material parting criterion. Other advantages of the Eulerian formulation are that

1. fewer finite elements (reduced computational effort) are required
2. the presence of a built-up edge or other stagnation in the flow presents no special problem
3. the line along which the chip separates from the finished surface can be observed with respect to the nose of the tool rather than having to be defined in advance.

Mechanical Considerations

The most important aspect of the MCS code is the constitutive law that relates deformation to applied load. In a series of papers on metal forming and extrusion [4,5,6,7], O. C. Zienkiewicz presents a simple means of dealing with large deformation processes involving plastic or visco-plastic materials where elastic deformation and inertial effects are negligible. For such problems, the constitutive law becomes a viscous flow relation linking stresses to instantaneous strain rates in an Eulerian coordinate reference frame. Consequently, the viscosity is dependent on the strain rates and the material behaves as a viscous, non-Newtonian, incompressible fluid [4]. Expressing this constitutive law in tensor notation,

$$\dot{e}_{ij} = \frac{1}{2\mu} S_{ij} \qquad (1)$$

where $\dot{e}_{ij}$ are the strain rates, μ is the viscosity and S_{ij} are the deviatoric stress components. If the material satisfies the Von Mises Flow Criterion, the viscosity has the form

$$\mu = \frac{Y}{3^{1/2}\,\dot{\bar{e}}} + \bar{\mu} \quad . \tag{2}$$

where $\dot{\bar{e}}$ is the second invariant of the strain rate tensor, Y is the uniaxial yield stress, and $\bar{\mu}$ is a viscous coefficient that becomes zero in the case of ideal plasticity.

An analogy can be drawn between the problem of pure visco-plastic flow and that of infinitesimal strain elasticity by replacing strains with strain rates, displacements with velocities and allowing the elastic constants to be dependent on the strain rate. This analogy makes it possible to solve the visco-plastic flow problem with the same techniques used in elasticity problems. In particular, solutions can be obtained with a Finite Element code written to solve problems in isotropic linear elasticity provided it can accommodate incompressibility, the material properties can be assigned on an elemental basis, and prescribed displacement boundary conditions are allowed [7].

The MCS code was developed with these requirements in mind to specifically study metal cutting. The structure of the code allows the material properties of each element to depend on strain, strain rate, stress and temperature. Therefore, the code is not limited to a single constitutive law but could conceivably accommodate several. Incompressibility is treated using a Poisson's ratio of 0.4999 coupled with a reduced integration technique described in [8] for both four and eight noded elements. A novel "friction element" suggested by Zienkiewicz [7] has been implemented that simplifies the specification of boundary conditions and the calculation of heat generation terms. Also, an upwind marching algorithm is used to compute total strain values anywhere in the flow field. Finally, MCS produces plot files compatible with ORION [9] allowing full color graphic presentation of results.

Thermal Considerations

Heat generated during the metal cutting process is thought to have a significant effect on chip formation, tool forces and surface damage. The MCS code includes a comprehensive Finite Element algorithm for modeling two dimensional, steady state, conductive-advective heat transfer. Features of this algorithm include

1. heat generation due to sliding friction and plastic working
2. heat transport within the modeled region due to conduction and advection (no up-winding)
3. heat transport across the boundaries of the modeled region due to a specified normal flux and/or convection

4. insulated surfaces

5. specified temperatures.

This algorithm computes temperatures everywhere in the modeled region and the information is used to update material properties.

RESULTS

A validation process was conducted to be sure the MCS code generated results consistent with other observations. To date, two validation exercises have been performed.

Plane Strain Extrusion

As a first validation exercise, the problem of plane strain extrusion through single hole symmetric dies was studied. Figures 5 and 6 show the problem geometry for a square and tapered die, respectively. In each case, the material to be extruded enters the die cavity at a constant velocity where it is constrained by the die and centerline to exit through a smaller opening at the opposite end. The reduction that occurs is expressed as $(1 - A_e/A_b)$ where A_b and A_e are the billet and extrusion areas, respectively.

Table 1 contains the results of a series of cases involving a square die where the reduction was 0.50 and frictionless die surfaces were assumed. Cases were run with both four and eight noded finite elements with mesh sizes of 16, 64 and 144 elements. The extrusion pressure computed with the four noded elements is seen to be insensitive to mesh refinements (2.40*K, 2.40*K, 2.38*K) and closely matches the theoretical values of 2.50*K obtained from Slipline Theory and reported by W. Johnson [10]. The extrusion pressure computed with the eight noded element, however, is sensitive to mesh refinement (3.53*K, 3.00*K, 2.73*K) but is converging toward the theoretical value.

Figure 7 contains the results of a second series of cases involving a square die where the reduction was 0.67 and the die surfaces were modeled with several friction conditions. As in the previous series, both four and eight noded elements were used; however, the mesh size was fixed at 66 elements. The plotted extrusion pressures for the eight noded elements closely match the theoretical values reported by Johnson [10] while less agreement is seen in the four noded cases. Recall that in the previous series, the four noded elements came closer to matching the theoretical extension pressure. The relative accuracy of the two formulations is sensitive to the number of elements used to model a problem. For a fixed number of elements the eight noded elements will generally give more accurate results but the computational effort per element is nearly three times greater than that for the four noded elements. Consequently, a trade-off between accuracy and computational effort must be made.

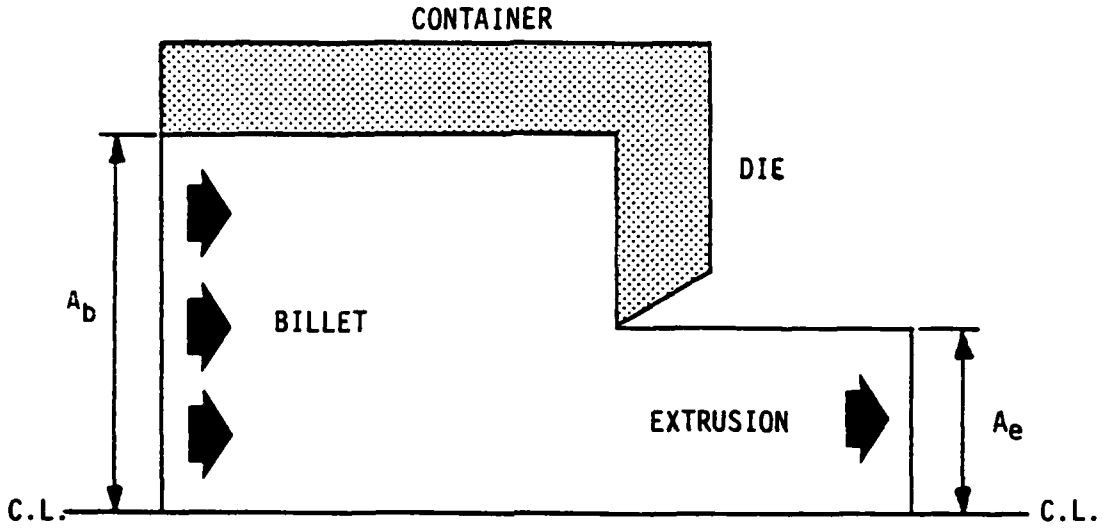

Figure 5. Geometry for plane strain extrusion through a single hole symmetric square die. (reduction = 1 - A_e/A_b)

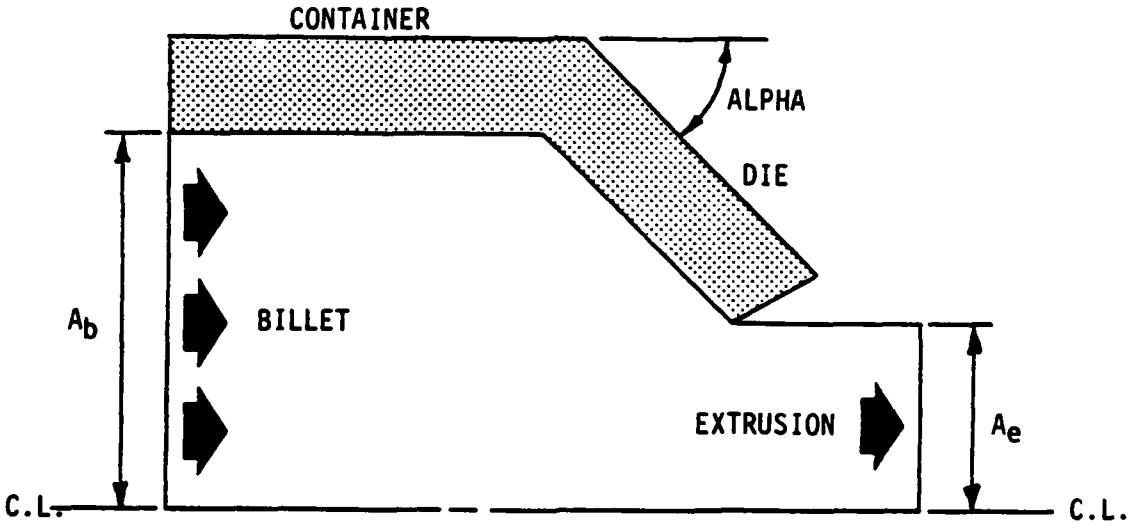

Figure 6. Geometry for plane strain extrusion through a single hole symmetric tapered die. (reduction = A_e/A_b)

Table 1. Square Die Extrusion (reduction = 0.50)

CASE	REDUCTION	ELEMENTS	NODES	FRICTION COEFFICENT	EXTRUSION PRESSURE
1	0.50	16	4	FULL-SLIP	2.40 * K
2	0.50	64	4	FULL-SLIP	2.40 * K
3	0.50	144	4	FULL-SLIP	2.38 * K
4	0.50	16	8	FULL-SLIP	3.53 * K
5	0.50	64	8	FULL-SLIP	3.00 * K
6	0.50	144	8	FULL-SLIP	2.73 * K

(slipline solution, full-slip = 2.50 * K, K = yield strength in shear)

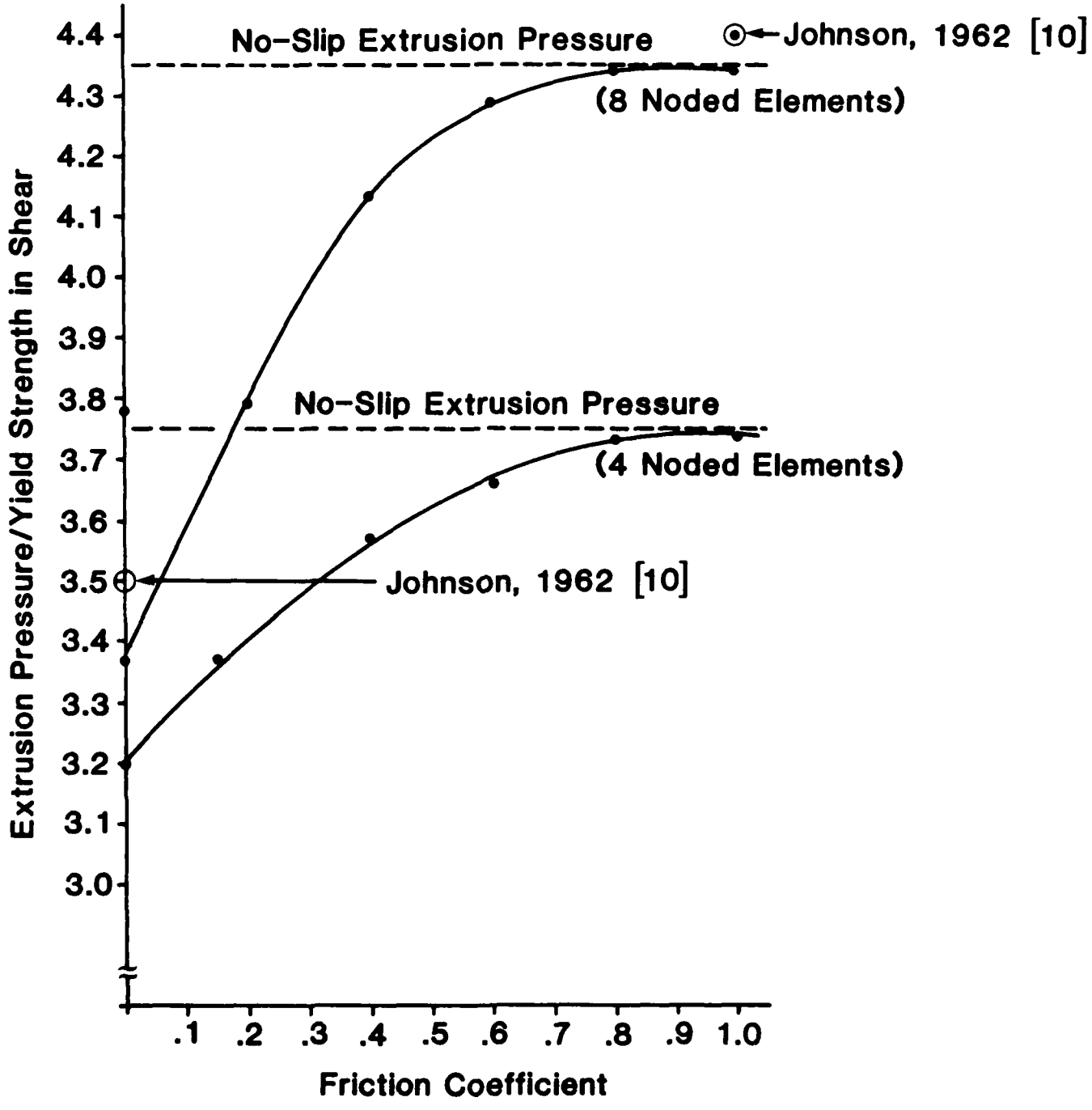

Figure 7. Normalized extrusion pressure versus friction coefficient for square die extrusion. (elements = 66, reduction = 0.67)

Figures 8 and 9 contain velocity vector plots showing the magnitude and direction of the material flow for two cases: in the first case, the friction coefficient is zero and the material flows through the corner formed by the container walls and die face. In the second case, the friction coefficient is 1.0 and a stagnation or "dead zone" is formed in this region.

Figure 10 contains the results of a third series of cases involving a tapered die where the reduction was 0.50, the die angle was 45 degrees and the die surfaces were modeled with several friction conditions. For this series of cases, the four noded element and two mesh sizes (55 and 150 elements) were used. The computed zero friction extrusion pressures (1.66*K and 1.72*K) closely match the theoretical value of 1.8*K reported by Johnson [10] and the shape of the curves is similar to those obtained for a square die.

Metal Cutting

The results of simulating metal cutting using MCS and NIKE2D have been compared. Each model was used to study two-dimensional, plane strain, frictionless, cutting of aluminum for several tool rake angles between -5 and +20 degrees. Figures 11 and 12 contain the problem geometries specific to each code. Figure 11 corresponds to the MCS code where the steady state chip geometry must be specified in advance. Note that the depth of cut, chip ratio (chip thickness/cutting depth) and tool rake angle define the geometry. Figure 12 is for the NIKE2D code where the tool must be advanced into the undeformed workpiece to form the steady state chip. Note that the depth of cut (tool position and location of parting line) and rake angle define the geometry.

A list of pertinent modeling parameters for each code are given in Table 2. The results obtained using these parameters are presented in Figure 13. The cutting variable of interest is the force normal to the cutting direction and is expressed as a force per unit width of cut. The dashed line in Figure 13 indicates the NIKE2D results while the remaining lines correspond to those obtained with MCS (using 4 noded elements) for chip ratios of 1.5, 1.25 and 1.0 which correspond to shear angles of 34, 39 and 45 degrees. The following observations can be made from these results:

1. Cutting forces computed with MCS are not particularly sensitive to changes in chip ratio

2. the MCS results most closely correlate with NIKE2D for a zero degree rake angle

3. the relationship between cutting force and rake angle appears to be linear for the MCS code while the NIKE2D results indicate a higher order behavior.

Figure 14 shows the material flow pattern for the case of zero degree rake angle and a chip ratio of 1.5. Note that along the back side of

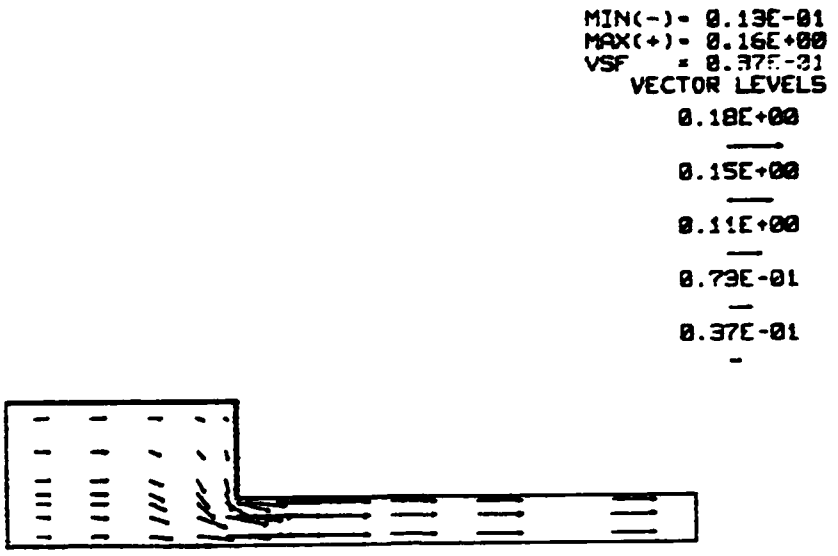

Figure 8. Velocity vector plot showing the magnitude and direction of material flow. (friction coefficient = 0.0)

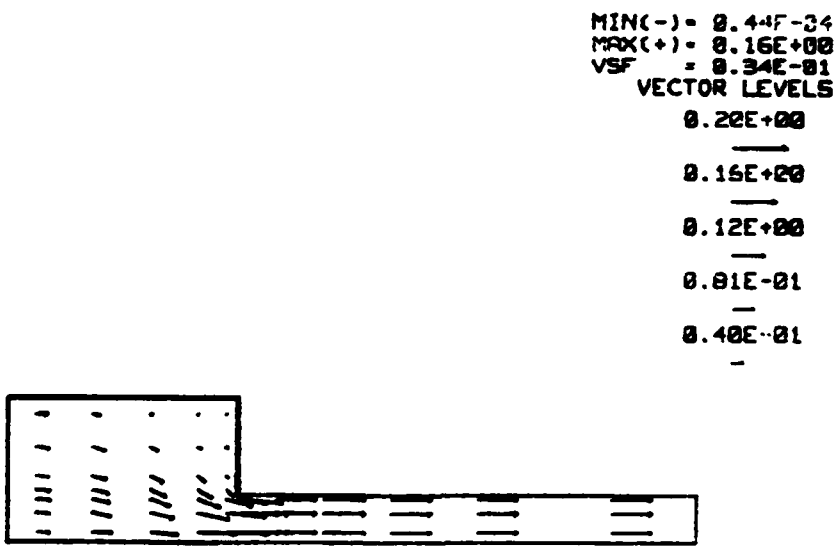

Figure 9. Velocity vector plot showing the magnitude and direction of material flow. (friction coefficient = 1.0)

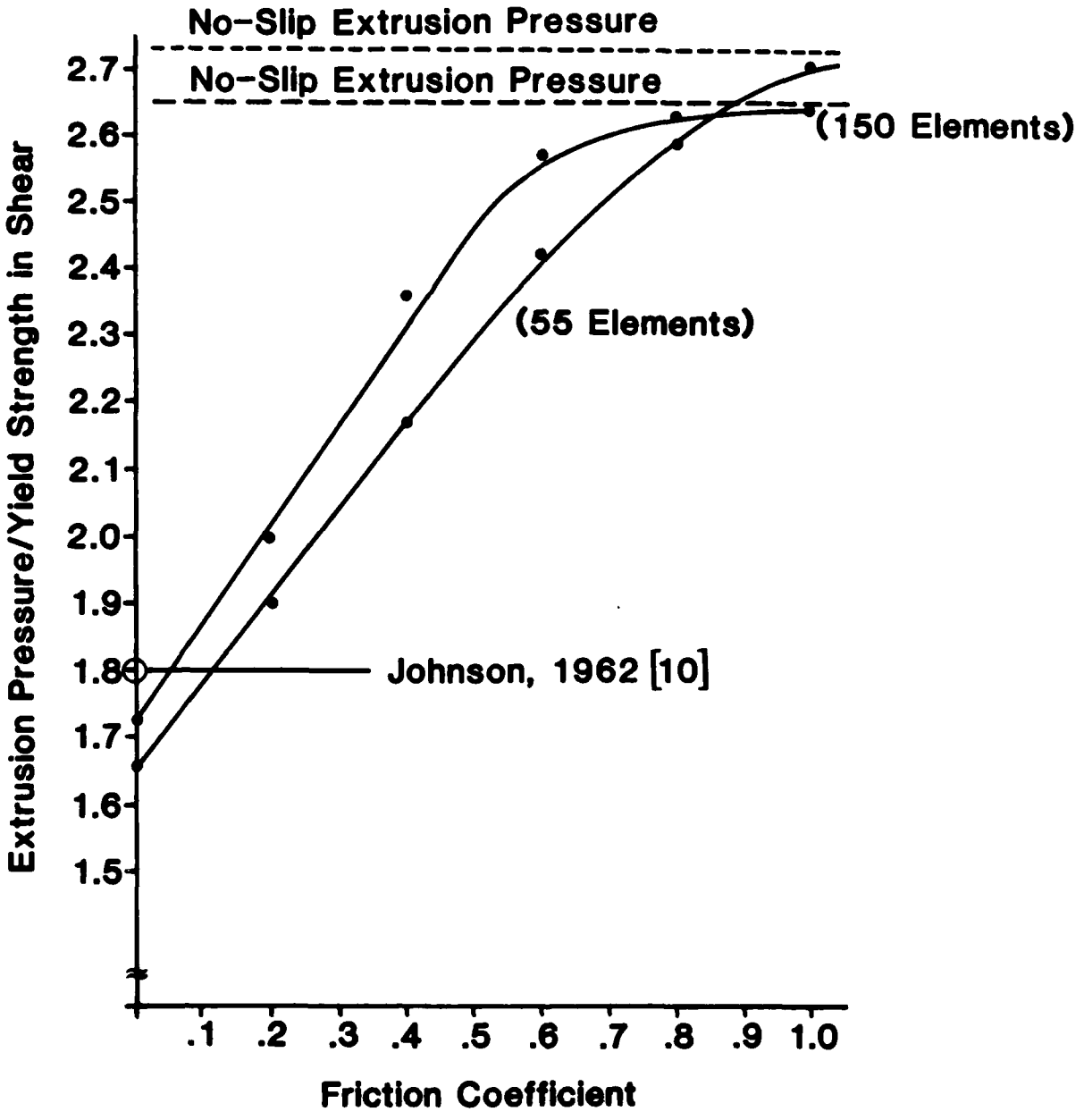

Figure 10. Normalized extrusion pressure versus friction coefficient for tapered die extrusion. (die angle = 45 degrees, reduction = 0.50, 4-noded elements)

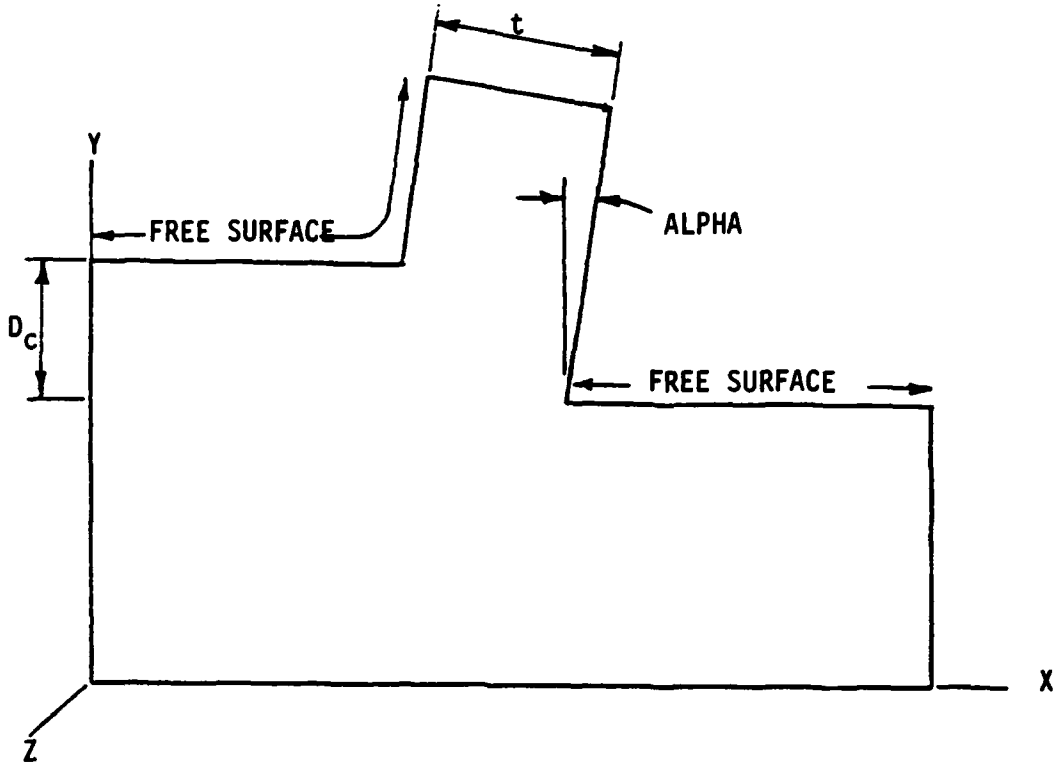

Figure 11. Problem geometry for MCS simulations. (D_c = cutting depth, t = chip thickness, alpha = rake angle)

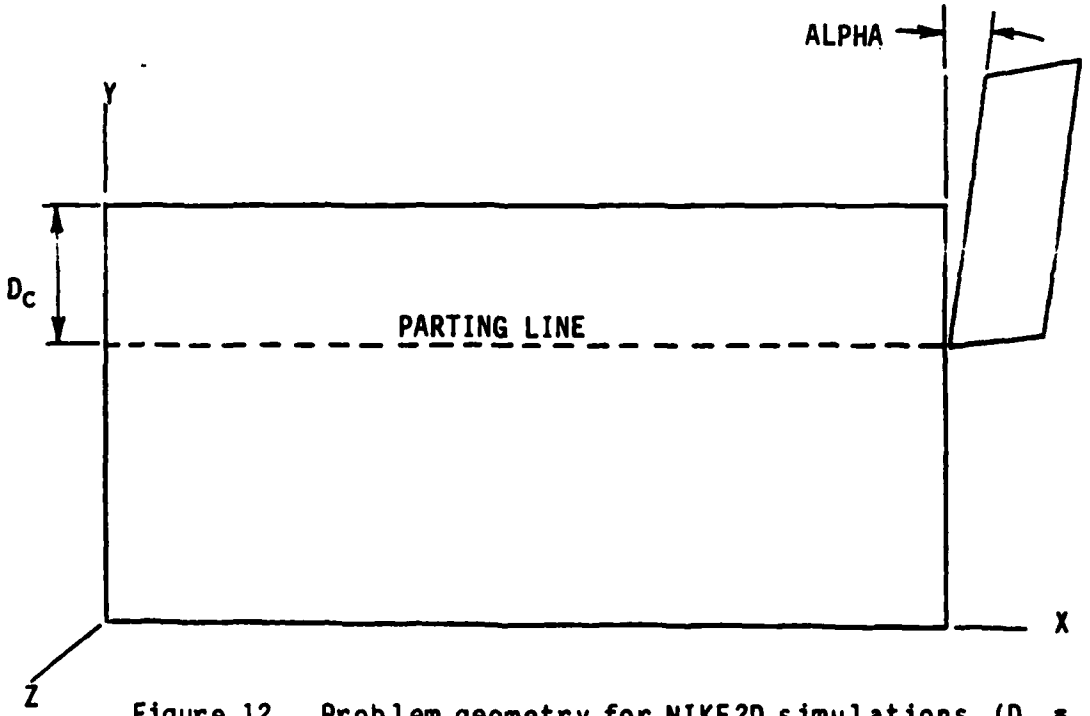

Figure 12. Problem geometry for NIKE2D simulations. (D_c = cutting depth, alpha = rake angle)

Table 2. Simulation Parameters

MATERIAL PARAMETERS

type = aluminum
yield strength = 3.0338×10^8 N/m^2 (44.0×10^3 lbf/in^2)
elastic modulus = 7.3087×10^{10} N/m^2 (10.6×10^6 lbf/in^2)

MCS3 SPECIFIC PARAMETERS

cutting depth = 0.25 micrometers (10 microinches)
cutting speed = 0.01 micrometers/sec (0.04 microinches/sec)
rake face friction coefficient = 0.0
convergence tolerance = 0.01 (relative)
number of elements = 224
element type = 4 node isoparametric quadrilateral
integration order = 1 point Gauss Quadrature
material model = incompressible visco-plastic

NIKE2D SPECIFIC PARAMETERS

cutting depth = 0.25 micrometers (10 microinches)
cutting speed = static
rake face friction coefficient = 0.0
convergence tolerance = 0.001 (relative)
number of elements = 400
element type = 4 node isoparametric quadrilateral
integration order = 1 point Gauss Quadrature
material model = elastic-plastic
separation criterion = 100 percent total effective plastic strain

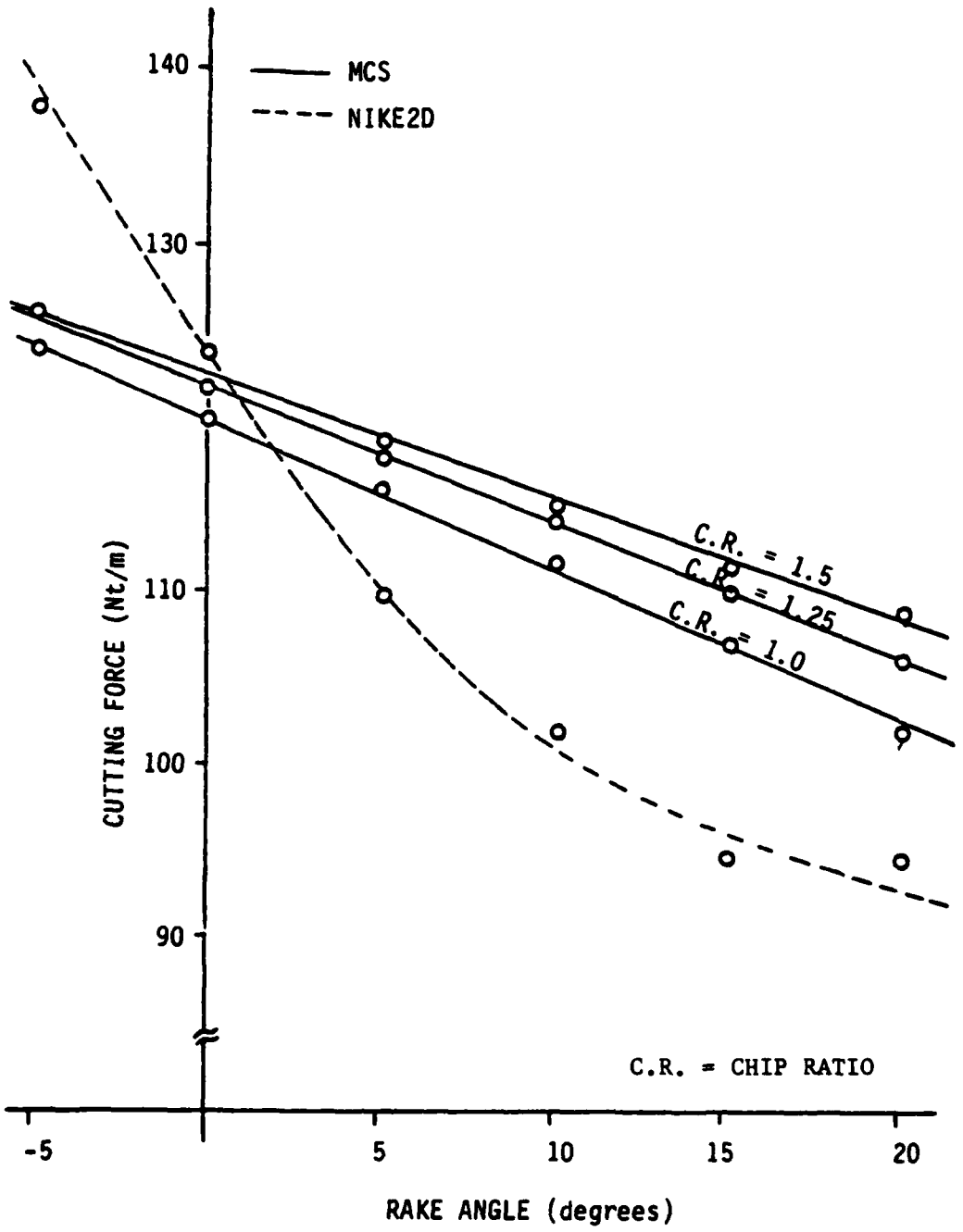

Figure 13. Graph of cutting force vs. rake angle. (results obtained from MCS and NIKE2D simulations)

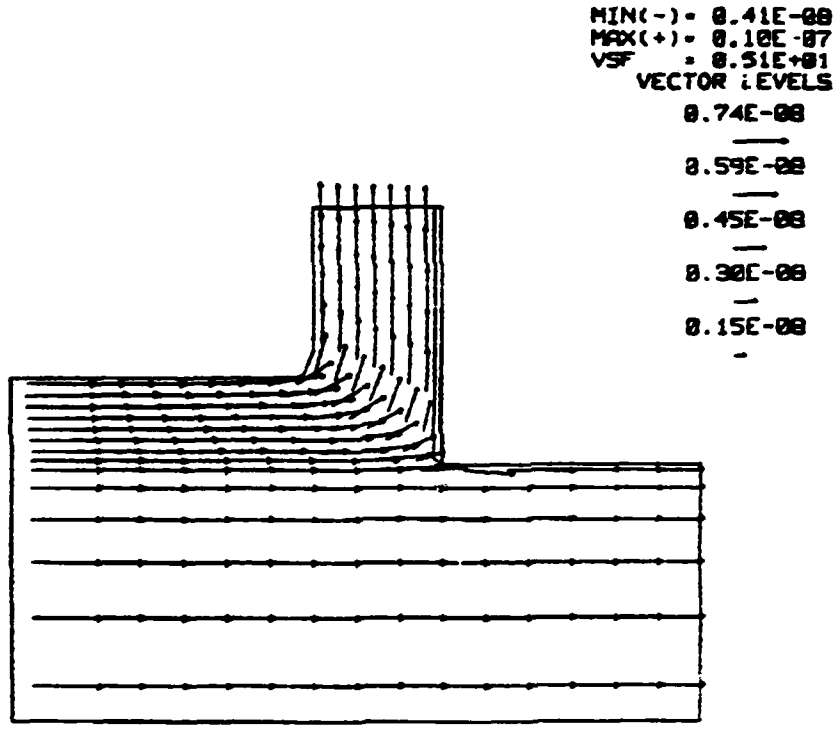

Figure 14. Velocity vector plot showing the magnitude and direction of material flow. (zero degree rake angle, 1.5 chip ratio)

the chip and the finished surface, the material does not cross the boundary even though it is not prevented from doing so. This gives some indication that the assumed geometry is close to being correct. Figure 15 contains a contour plot of total effective plastic strain showing the intense straining that occurs along the rake face and below the tool. It is felt that these results demonstrate metal cutting with the MCS code.

FUTURE WORK

The preliminary results obtained with the MCS code are encouraging but continued development and validation efforts are required. Initially these efforts will focus on experimental validation (see next section on Measurement of Tool Forces) and modifications to the material model. As work progresses, additional features will be added and the code refined in general.

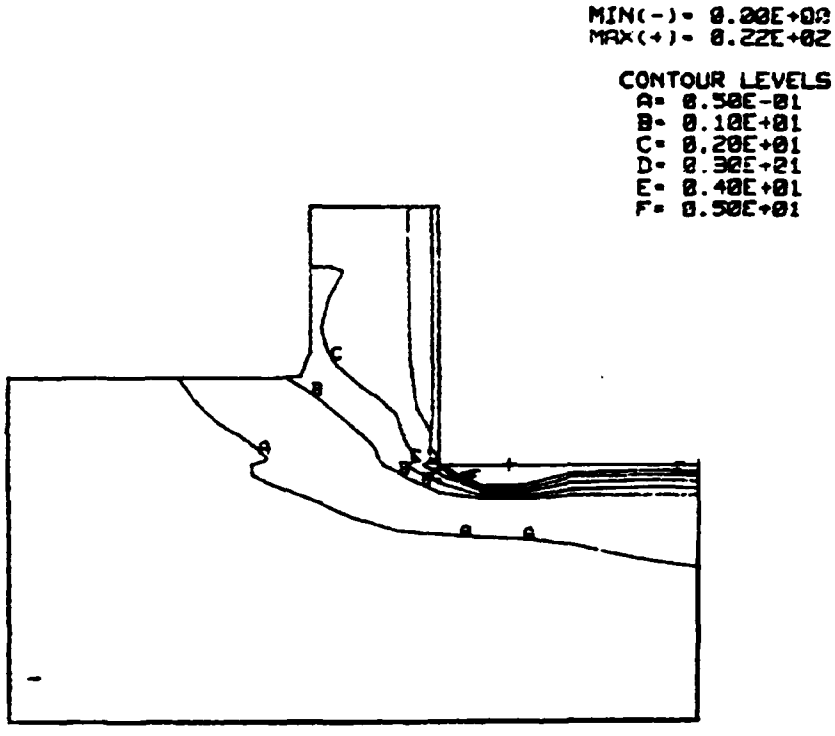

Figure 15. Contour plot of total effective plastic strain showing the intense straining that occurs along the rake face and below the tool. (zero degree rake angle, 1.5 chip ratio)

REFERENCES

1. Hallquist, J. O. "NIKE2D: A Vectorized, Implicit Finite Deformation, Finite Element Code for Analyzing the Static and Dynamic Response of 2-D Solids," Lawerence Livermore National Laboratory Report No. UCID-19677.

2. Strenkowski, J. S. and J. T. Carroll, III, "A Finite Element Model of Orthogonal Metal Cutting," Journal of Engineering for Industry, Vol. 107, November 1985, pp. 349-354.

3. Mitchum, G. L., "Phenomenon of Shear Banding in Orthogonal Metal Cutting using the Finite Element Method," Third Annual Report on Precision Engineering - SRO 154, North Carolina State University at Raleigh, January 1986, p. 248.

4. Zienkiewicz, O. C. and P. N. Godbole, "Flow of Plastic and Visco-Plastic Solids with Special Reference to Extrusion and Forming Processes," International Journal for Numerical Methods in Engineering, Vol. 8, 1974, pp. 3-16.

5. Zienkiewicz, O. C. and I. C. Cormeau, "Visco-Plasticity - Plasticity and Creep in Elastic Solids - A Unified Numerical Solution Approach," International Journal for Numerical Methods in Engineering, Vol. 8, 1974, pp. 821-845.

6. Zienkiewicz, O. C. and P. N. Godbole, "A Penalty Function approach to Problems of Plastic Flow of Metals with Large Surface Deformations," Journal of Strain Analysis, Vol. 10, No. 3, 1975, pp. 180-183.

7. Zienkiewicz, O. C., P. C. Jain and E. Onate, "Flow of Solids During Forming and Extrusion: Some Aspects of Numerical Solutions," International Journal of Solids and Structures, Vol. 13, 1978, pp. 15-38.

8. Naylor, D. J., "Stresses in Nearly Incompressible Materials by Finite Elements with Application to the Calculation of Excess Pore Pressures," International Journal for Numerical Methods in Engineering, Vol. 8, 1974, pp. 443-460.

9. Hallquist, J. O., "ORION: An Interactive Post-Processor for the Analysis Codes NIKE2D, DYNA2D and TACO2D," Lawrence Livermore National Laboratory Report No. UCID-19310, Rev. 1.

10. Johnson, W., The Mechanics of Metal Extrusion, Manchester University Press, England, 1962.

THERMAL EFFECTS IN FINITE ELEMENT ANALYSIS OF ORTHOGONAL METAL CUTTING

By

Stephen A. Lehrman
Graduate Student
Precision Engineering Laboratory

And

Dr. John S. Strenkowski
Associate Professor
Mechanical and Aerospace Engineering

ABSTRACT

The temperature dependent material behavior of a metal subjected to orthogonal cutting was evaluated using the finite element method. A two-dimensional, plane strain, finite element model of orthogonal metal cutting has been analyzed using the NIKE2D computer program. The Elastic-Plastic material properties were input to the finite element code. The model predicted the temperature distribution in the chip and workpiece based on adiabatic thermal conditions. The temperature dependance of the material properties due to thermal softening was shown to oppose the work hardening of the material. The residual stress in the workpiece were illustrated from a curve relating effective stress and tool position.

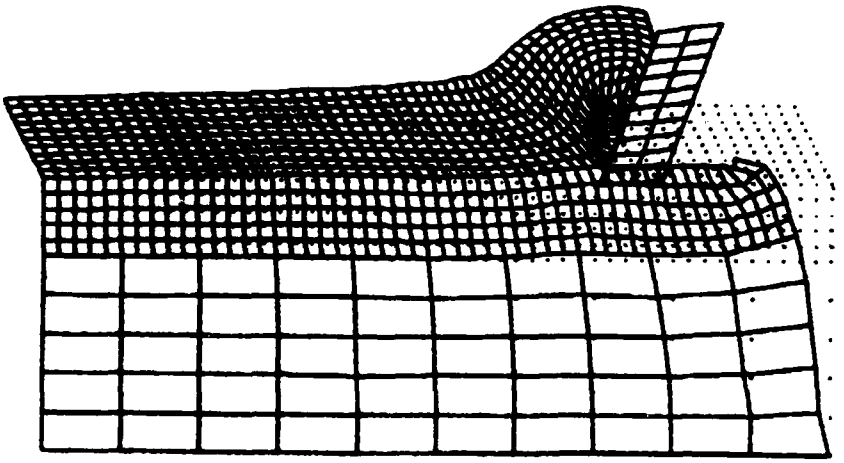

INTRODUCTION

Orthogonal cutting causes large strain, strain rate and temperature rise in the primary and secondary shear zones. Effective strain of hundreds of percent with associated strain rate of thousands per second have been reported for normal machining. The temperature rise due to deformation and friction may exceed 800 C.

Temperature has a very significant effect on the machining of metals. In the primary shear zone, the large strain rate results in plastic deformation at adiabatic thermal conditions. The metal yield strength decreases and ductility increases as the temperature increases. This behavior makes the metal easier to machine. However, some metals such at Titanium alloys, develop a chemical reaction with the tool at high temperatures resulting in excessive tool wear.

The literature contains many solutions to the calculation of the temperature in the primary shear zone. Some of these can be found in references [1-3]. These approaches look at the shear zone as a plane with an applied temperature distribution. The temperature rise is calculated using heat transfer equations subject to assumed boundary conditions. More recently, the finite element method has been used to calculate the temperature distribution in metal machining. The results of these analyses are discussed in references [4-6].

The finite element method is a very powerful numerical analysis procedure applicable to non-uniform geometries and boundary conditions. The temperature dependent material behavior of metal subjected to orthogonal cutting can be evaluated using the finite element method.

The finite element model of orthogonal metal cutting is based on an updated Lagrangian formulation for plane strain conditions as provided by NIKE2D [7]. NIKE2D is a structural analysis program. Subroutines are incorporated into NIKE2D to calculate the temperature rise under adiabatic conditions due to plastic deformation. The program accepts Thermo-Elastic-Plastic material properties. Strenkowski and Carroll [8] describe the NIKE2D program method of analysis.

Thermal Dependence of Material Flow Stress

An equation of state can be written relating the workpiece material flow stress (σ) to strain (ε), strain rate ($\dot{\varepsilon}$), and temperature (T). This equation is of the form

$$\sigma = f(\varepsilon, \dot{\varepsilon}, T)$$

The flow stress increases with increasing strain rate at constant strain and temperature and decreases with increasing temperature at constant strain and strain rate.

The development of empirical equations for the flow stress as a function of strain, strain rate, and temperature is a critical element in the analysis of orthogonal metal cutting. Without these relations, the true Thermo-Elastic-Plastic behavior of the workpiece cannot be modeled.

The torsion test of hollow tubes has proved to be the most suitable test method for developing the necessary empirical equations. Large strains can be generated without developing local instabilities such as necking in tensile testing. Also, strain rates up to 1000 sec^{-1} can be developed.

Johnson reported the results of a series of torsion tests on ductile metals [9,10]. An empirical relation was developed for the shear stress as a function of shear strain, shear strain rate, and temperature. Johnson's equation is of the form

$$\tau = (A + B\gamma^n)[1 + C\ \ell n(\dot{\gamma}/\dot{\gamma}_0)]\ K_T$$

where

τ = the shear stress,
A,B,C = material dependent constants
γ = the shear strain
n = the strain hardening exponent
$\dot{\gamma}$ = the shear strain rate
$\dot{\gamma}_0 = 1\ sec^{-1}$

The final term, K_T, is a factor used to adjust the shear stress due to temperature effects. Johnson shows that the form of K_T is material dependent. A linear softening expression of the form

$$K_T = 1 - \frac{T}{T_M}$$

where

T = the material temperature
T_M = the material melting point

is shown to be acceptable.

The flow stress, σ, and effective strain, ϵ, can be determined from Johnson's equation and the Von Mises Yield Criterion. The appropriate relations are

$$\sigma = \sqrt{3}\ \tau, \text{ and}$$

$$\epsilon = \frac{\gamma}{\sqrt{3}}$$

Costin reported the results of Kolsky bar torsion tests using 1018 CR and 1020 HR steel [11]. The dynamic strain rates were 500 sec^{-1} and 1000 sec^{-1}, respectively. The maximum test temperature was 250 F.

Costin also developed an empirical equation for the shear stress of the form

$$\tau = C(1 - aT)(1 + b\dot{\gamma})^m \gamma^n$$

where

τ = shear stress
C, a, b = material dependent constants
T = material temperature
γ = shear strain
n = strain hardening exponent
$\dot{\gamma}$ = shear strain rate
m = strain rate hardening exponent.

It can be seen that Costin's equation uses a linear thermal softening model.

Olsen developed an adiabatic shear stress-shear strain relation that implicity incorporates thermal softening [12]. Olsen's equation is of the form

$$\tau = \tau_o(1 + \alpha\gamma)e^{-\beta\gamma}$$

where

τ_o = shear yield stress
α = strain hardening parameter
β = thermal softening parameter

An alternative to the development of empirical equations is to present the experimental data in tabular or graphical form. The temperature dependent material properties for Stainless Steel Type 304 are shown in Figure 1. These material properties are independent of strain rate. Otherwise, an empirical equation relating the flow stress to strain, strain rate, and temperature could be developed. Data such as shown in Figure 1 are suitable input to the NIKE2D program.

Thermal Instability Strain

Culver [1], Recht [2], and Staker [13] have discussed the instability in the flow stress under certain conditions. Starting with the equation of state, the total derivative of the flow stress is

$$\frac{d\sigma}{d\varepsilon} = \left(\frac{\partial\sigma}{\partial\varepsilon}\right) + \left(\frac{\partial\sigma}{\partial\dot{\varepsilon}}\right)\frac{d\dot{\varepsilon}}{d\varepsilon} + \left(\frac{\partial\sigma}{\partial T}\right)\frac{dT}{d\varepsilon}$$

where each partial derivative is taken with the other variables held constant. Each of these terms has a particular physical significance. The first represents isothermal strain hardening, the second isothermal strain rate hardening, and the last term is a measure of thermal softening.

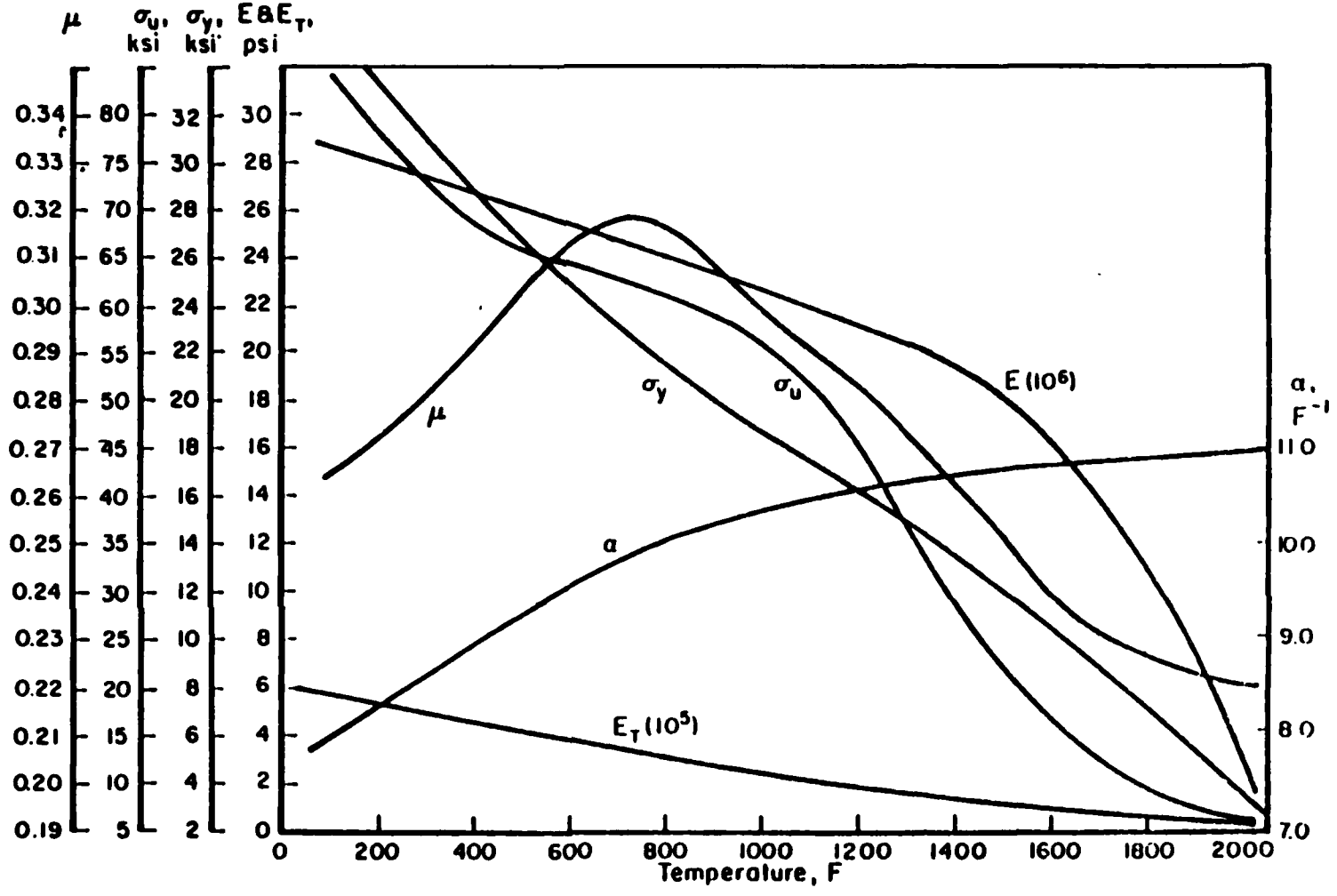

Figure 1. 304 stainless steel temperature dependent properties used for finite element stress analysis*

*E. F. Rybicki, et al., "Residual Stresses at Girth-Butt Welds in Pipes and Pressure Vessels," Final Report to the U.S. Nuclear Regulatory Commission, 1977.

An instability in the flow stress occurs when

$$\frac{d\sigma}{d\varepsilon} < 0$$

At this instability, the slope of the true flow stress versus true strain curve is zero. Strains can continue to develop to very large values without increasing flow stress. In fact, the flow stress generally will decrease. It is noted that the isothermal strain rate hardening is commonly neglected in evaluating the instability condition.

Recht [2] termed this instability condition "catastrophic shear." Because the strain rates in metal cutting are very large in the shear zone, adiabatic temperature conditions are approximated. The instability condition has also been called Adiabatic Shear Deformation.

Calculation of Workpiece Temperature in NIKE2D

The temperature of the workpiece is calculated for adiabatic conditions on an element-by-element basis. Consider each element of the finite element model to be a thermodynamic system. The First Law of Thermodynamics states that

$$dU = dq + dW$$

where

dU = change in the system internal energy
dq = change in heat absorbed by the system
dW = is the change in work done to the system

All changes are per unit volume. The adiabatic boundary conditions require dq = 0.

The change in work done to the system is

$$dW = \sigma d\bar{\varepsilon}$$

where

σ = effective stress

$d\bar{\varepsilon}$ = effective strain increment

For small elastic strains, the effective strain increment can be replaced by the effective plastic strain increment, $d\bar{\varepsilon}_p$. A subroutine incorporated into NIKE2D computes the effective stress and effective plastic strain increments.

The change in the system internal energy per unit volume gives rise to a temperature change. If adiabatic heating is assumed, the temperature change can be expressed as follows:

$$dT = \frac{dU}{\rho C_p}$$

where

dT = temperature change per unit volume
ρ = material density
Cp = material specific heat

The change in internal energy and work per unit volume are related by the equation

$$dU = f_1 * f_2 * dW$$

where

f_1 = work to heat conversion factor (1.0717×10^{-4})
f_2 = conversion efficiency factor (0.9 - 1.0)

The conversion efficiency factor is required because a portion of the plastic work developed in the workpiece is retained by the workpiece as latent energy. The latent energy is the internal energy due to plastic work associated with the build-up of dislocations [14].

NIKE2D calculates stresses and strains at the element integration points. The adiabatic temperature subroutine uses a bilinear least square extrapolation algorithm to compute the nodal temperature changes. The new nodal temperatures are given by the equation

$$T_{new} = T_{old} + dT$$

Numerical Results

The finite element model shown in Figure 2 was used to simulate the machining of Stainless Steel Type 304. The finite element model consists of 966 nodes and 820 elements. Figure 3 illustrates the final position of the chip and tool after 60 incremental steps. Thermo-Elastic-Plastic material properties were used to represent the chip and workpiece. The input to the NIKE2D Thermo-Elastic-Plastic model consists of temperature dependent values for Young's Modulus, Poisson's Ratio, Yield Strength, and Plastic Hardening Modulus. The data in Figure 1 was used in the analysis because the data was more complete than using the empirical equations.

Figure 4 shows the temperature contours for the final configuration. The temperatue is a maximum near the tool tip and radiates outward. The temperature contour gradient is largest for the finite elements representing the chip material that are entering the shear zone. The finite elements representing the workpiece material do not exhibit significant temperature changes. This result tends to validate the assumption of adiabatic conditions throughout the finite element model even though the adiabatic conditions are true only for the shear zone.

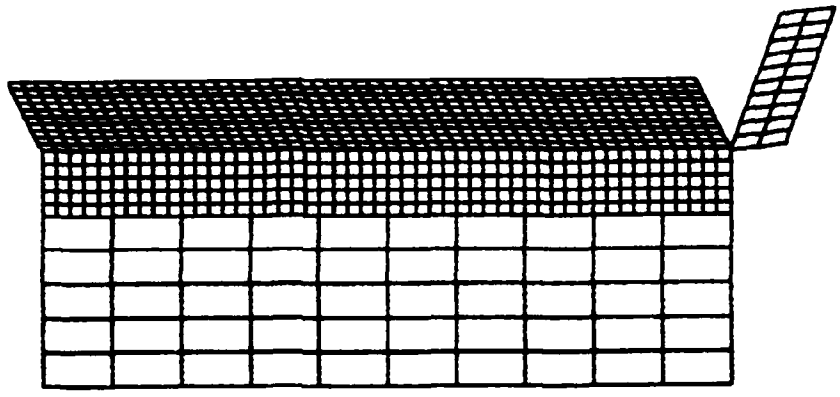

Figure 2. Initial geometry

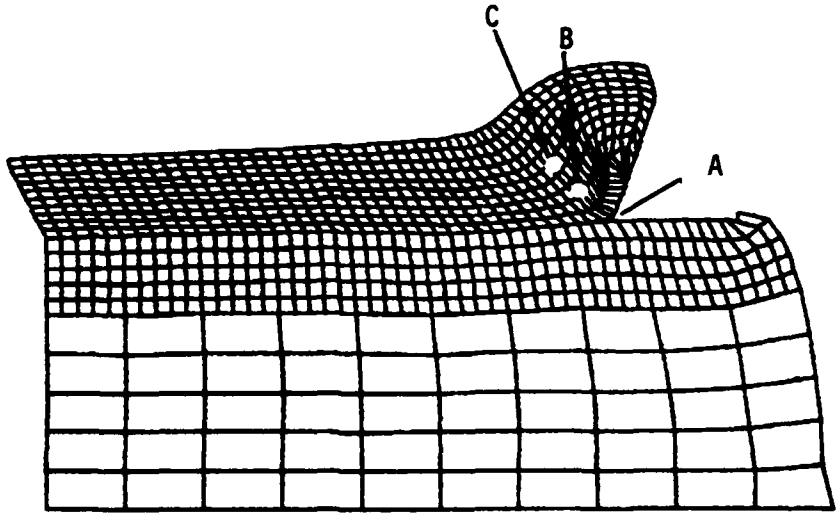

Figure 3. Final geometry at state 60

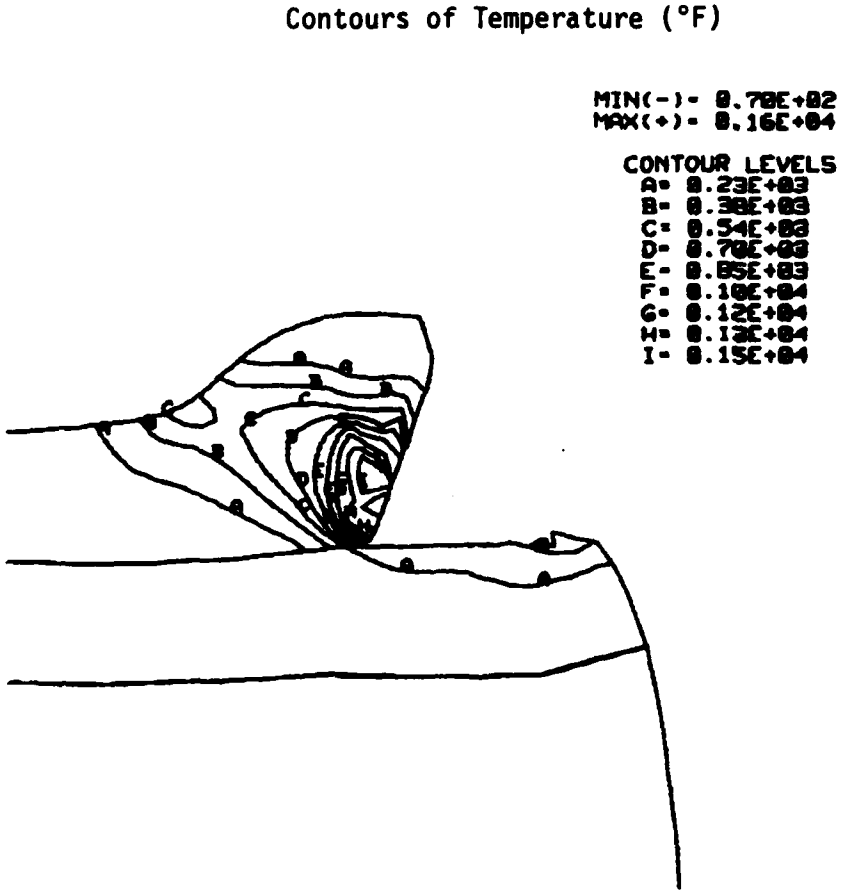

Figure 4. Temperature contours for portion of finite element model at state 60

The temperature as a function of position for three nodes is shown in Figure 5. Node A is at the tip of the tool in the final configuration. Nodes B and C are two and four layers above node A. All three nodes are in the shear zone. The figure shows the temperature building up as the nodes approach the shear zone.

The effective stress versus effective plastic strain for element number 490 is shown in Figure 6. This element lies on the interface between the chip and the workpiece. The plot shows a decrease in stress at the maximum strain. This decrease is not attributed to the onset of a thermal instability. Figure 7 shows a plot of the effective stress versus position for this element. The element separates from the workpiece at time 56. An unloading occurs and the stress decreases even though the element continues to plastically deform. Figure 6 illustrates the opposing effects of work hardening and thermal softening. At moderate strains up to 1.0, work hardening dominates. At larger strains, the effect of thermal softening is more pronounced.

The residual stress in the workpiece is illustrated in Figure 8. Element number 549 is the first element in the top layer of the workpiece. The effective stress increases until the tool completely passes the element. The stress drops precipitously to the residual stress level.

CONCLUSIONS

The finite element structural analysis program NIKE2D has been modified to calculate the adiabatic temperature distribution of a model of orthogonal metal cutting. The thermal analysis predicts a significant temperature rise as material passes through the shear zone. Temperature rises up to 1200 F. have been calculated for cutting of stainless steel material.

The effective stress versus effective plastic strain can be plotted for finite elements modeling the chip and workpiece. These plots can be used to predict the development of adiabatic shear bands in the chip. The stainless steel Thermo-Elastic-Plastic material model was shown not to develop adiabatic shear bands. The opposing effects of work hardening and thermal softening are shown to result in a flattening of the effective stress versus effective plastic strain curve at large deflections.

The NIKE2D computer program has been shown to predict the residual stress in the workpiece after orthogonal cutting. The effective stress in the workpiece is shown to drop precipitously after the tool passes. The remaining stress is the residual stress.

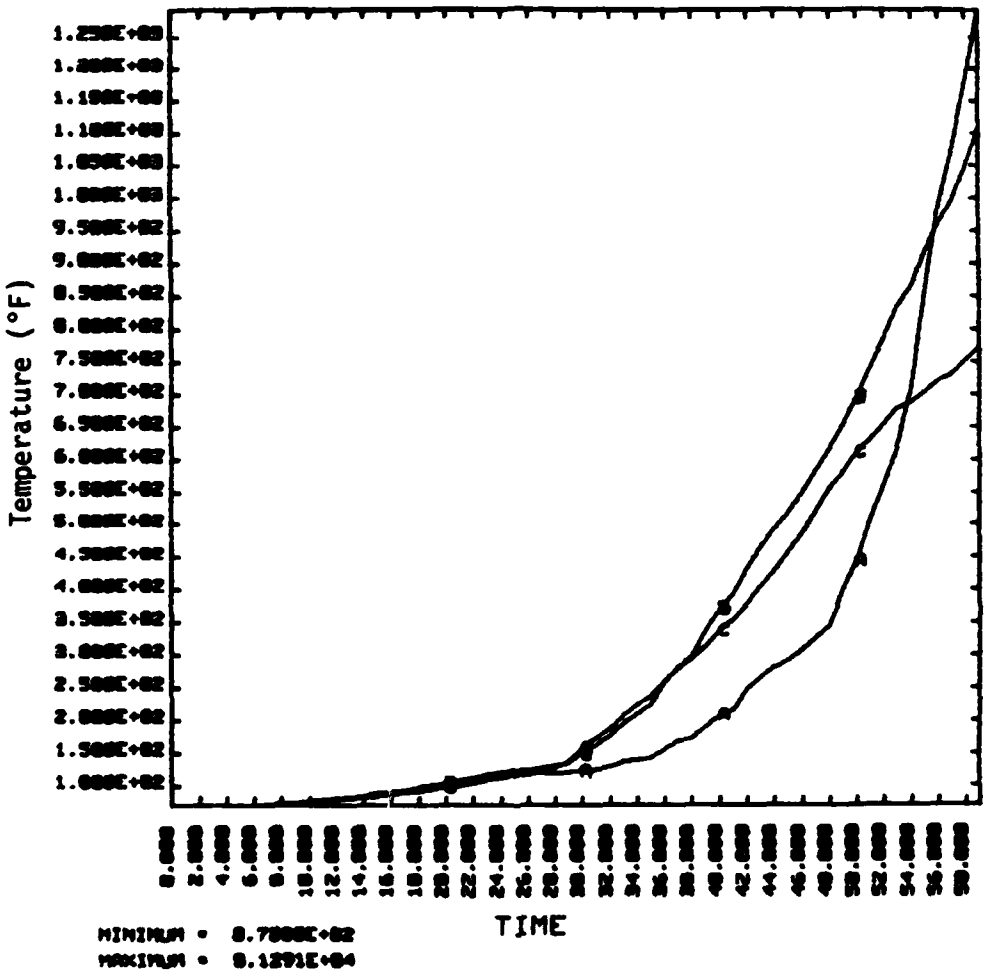

Figure 5. Temperature versus position for nodes A, B, and C

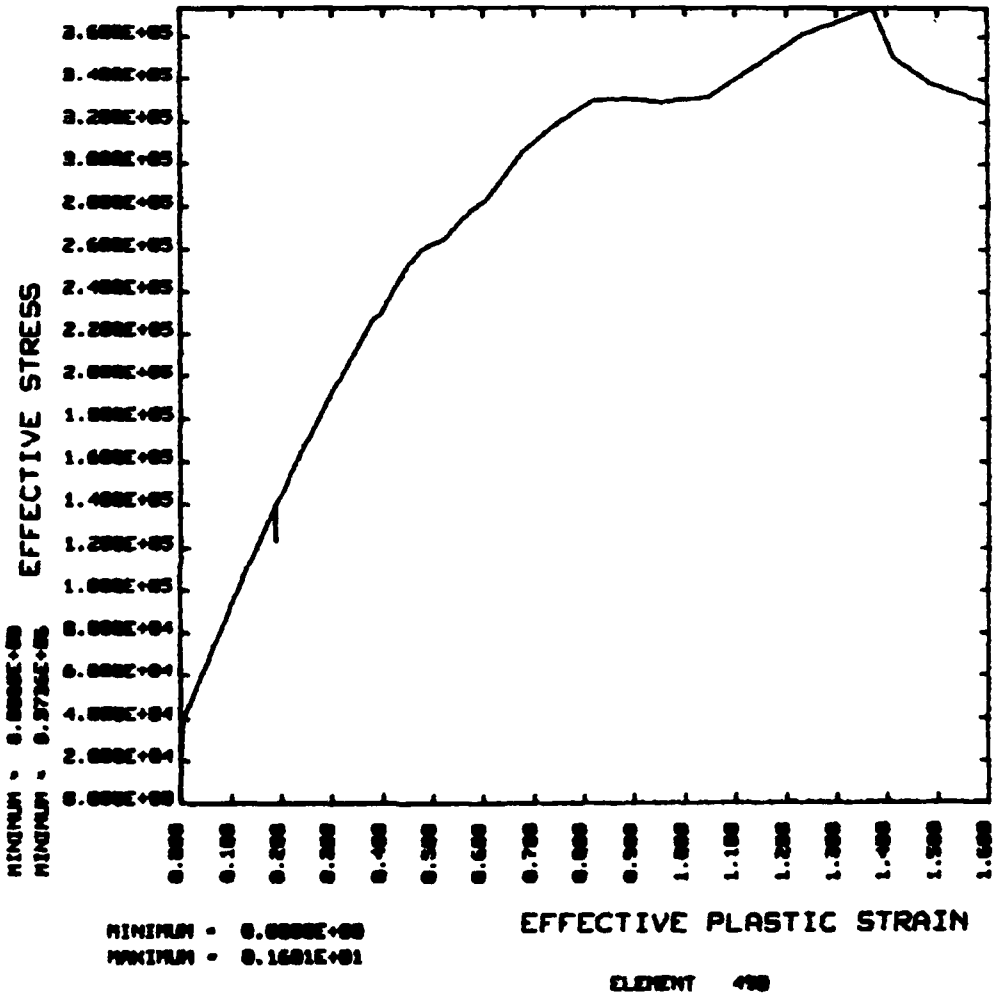

Figure 6. Effective stress versus effective plastic strain for element 490

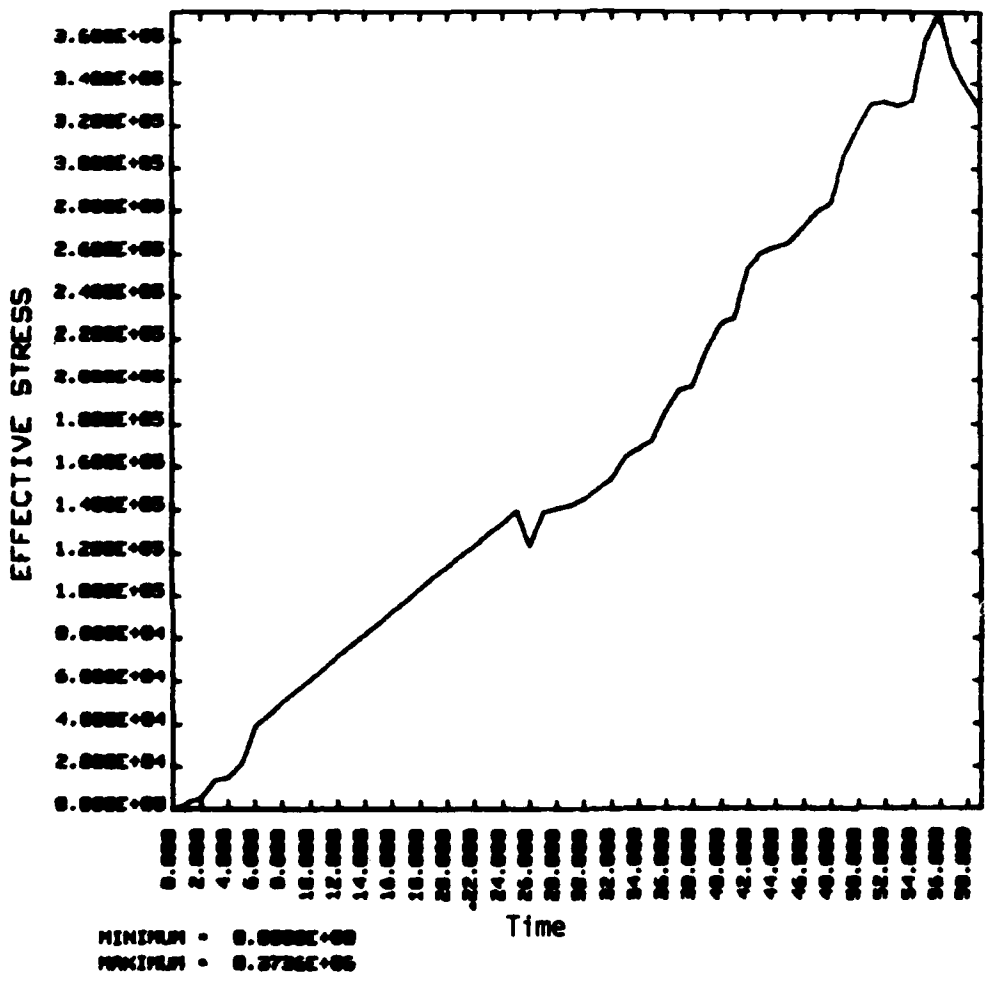

Figure 7. Effective stress versus position for element 490

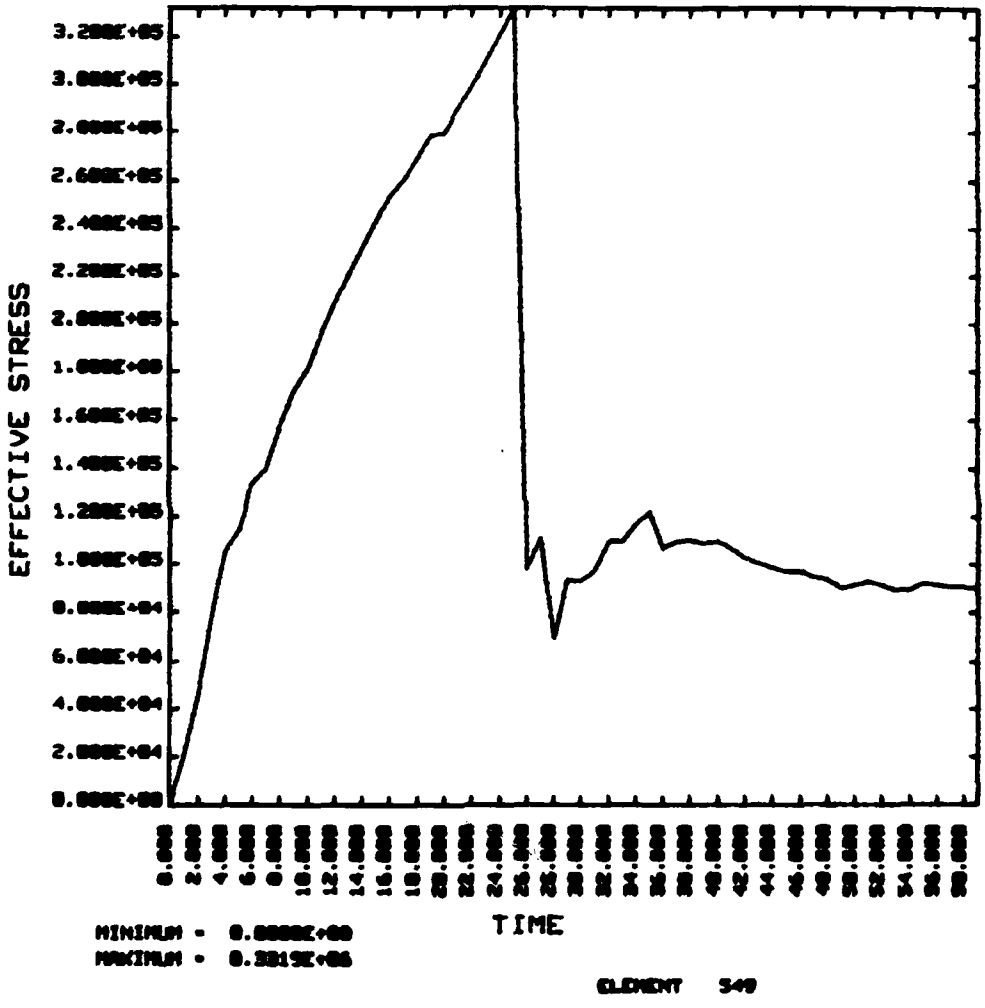

Figure 8. Effective stress versus position for element 549

REFERENCES

1. Culver, R. S., "Thermal Instability Strain in Dynamic Plastic Deformation," Metallurgical Effects at High Strain Rates, edited by R. W. Rohde, Plenum Press, New York, 1973, p. 519.

2. Recht, R. F., "Catastrophic Thermoplastic Shear," ASME Journal of Applied Mechanics, Vol. 86, 1964.

3. Leone, W. C., "Distribution of Shear-Zone Heat in Metal Cutting," Transactions of the ASME, Vol. 76, 1954.

4. Tay, A. O., M. G. Stevenson, and G. de Vahl Davis, "Using the Finite Element Method to Determine Temperature Distributions in Orthogonal Machining," Proc. Inst. of Mech. Engrs. Vol. 188, 1974, pp. 627-638.

5. Tay, A. O., M. G. Stevenson, G. de Vahl Davis, and P. L. B. Oxley, "A Numerical Method for Calculating Temperature Distributions in Machining, From Force and Shear Angle Measurements," International Journal of Machine Tool Design and Research, Vol. 16, 1976, pp. 335-349.

6. Stevenson, M. G., P. K. Wright, and J. G. Chow, "Further Developments in Applying the Finite Element Method to the Calculation of Temperature Distributions in Machining and Comparisons with Experiments," ASME Journal of Engineering for Industry, Vol. 105, 1983, pp. 149-154.

7. Hallquist, J. O., "NIKE2D-A Vectorized, Implicit Finite Deformation, Finite Element Code for Analyzing the Static and Dynamic Response of 2-D Solids," Lawrence Livermore National Laboratory Report No. UCID-19677.

8. Strenkowski, J. S. and J. T. Carroll, "A Finite Element Model of Orthogonal Metal Cutting," Second Annual Report on Precision Engineering - SRO 154, 1985, p. 118.

9. Johnson, G. R., J. M. Hoegfeldt, U. S. Lindholm, and A. Nagy, "Response of Various Metals to Large Torsional Strains Over a Large Range of Strain Rates -Part 1: Ductile Metals," Transactions of the ASME, Vol. 105, January 1983, pp. 42-47.

10. Johnson, G. R., J. M. Hoegfeldt, U. S. Lindholm, A. Nagy, "Response of Various Metals to Large Torsional Strains Over a Large Range of Strain Rates -Part 2: Less Ductile Metals," Transactions of the ASME, Vol. 105, January 1983, pp. 48-53.

11. Costin, L. S., E. E. Crisman, R. H. Hawley and J. Duffy, "On the Location of Plastic Flow in Mild Steel Tubes Under Dynamic Torsional Loading," Institute of Physics Conference Series Number 47, Chapter 1, pp. 90-100.

References (Continued)

12. Olson, G. B., Mescall, J. F., and Azrin, M., "Adiabatic Deformation and Strain Localization," Army Materials and Mechanics Research Center Report AMMRC TR 82-48, 1982.

13. Staker, M. R., "The Relation Between Adiabatic Shear Instability Strain and Material Properties," Acta Metallurgica, Vol. 29, 1981.

14. Zener, C. and J. H. Holloman, "Effect of Strain Rate Upon Plastic Flow of Steel," Journal of Applied Physics, Vol. 15, 1944.

PHENOMENON OF SHEAR BANDING IN ORTHOGONAL CUTTING USING THE FINITE ELEMENT METHOD

By

Gary L. Mitchum
Graduate Student
Precision Engineering Laboratory

And

John S. Strenkowski
Associate Professor
Mechanical and Aerospace Engineering Department

ABSTRACT

A computer simulation of shear band behavior in orthogonal metal cutting is presented. The simulation is performed by utilizing a finite element analysis. The results indicate that shear bands form in materials whose stress-strain curve is characterized by a small amount of strain hardening at low strains followed by significant strain softening at higher values of strain. Thermal changes in material properties during the deformation process would be an important contributor to the strain-softening.

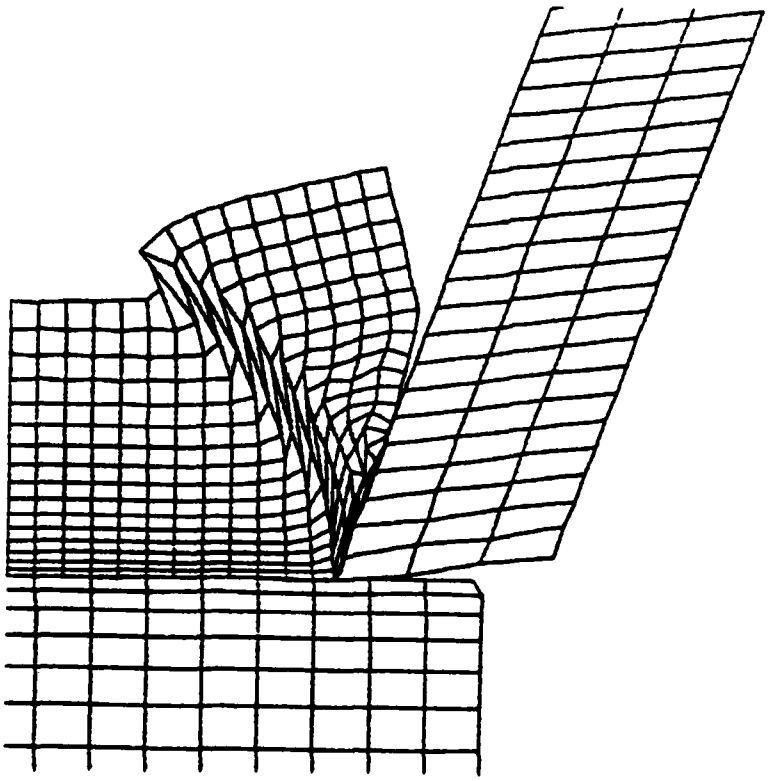

INTRODUCTION

The presence of shear bands in metal cutting produces discontinuous chips or chips with serrated edges. Shear banding is a phenomenon that can be described as a thermal instability that occurs when the heat generated by plastic deformation sufficiently softens the material so that the strain-hardening effects of the material are overcome. A band of intense shear strain can then occur, which is localized just ahead of the tool cutting edge.

Shear bands are more likely to form in less ductile materials, in ductile materials that exhibit strain-softening behavior, and for small positive or negative rake angles. For example, titanium alloys are known to exhibit serrated or even discontinuous chips [1] which may be related to shear banding. Other materials, such as HY-TUF steel, also show a tendency to form shear bands under large strain and high strain-rate loading conditions [2]. OHFC copper exhibits thermal softening at high strain rates [3] which is a criteria for shear band formation. Beta-Brass exhibits shear band formation for small positive or negative rake angles [4]. Recognition of the role that shear banding behavior plays in serrated and discontinuous chip formation has led to its study in metal cutting.

In spite of this attention, the stress distribution in the workpiece ahead of the tool has not been thoroughly investigated. This is due to the complexity of the cutting process mechanisms, even for continuous chip formation; and the fact that experimental stress measurements are difficult in the area ahead of the cutting edge.

This paper investigates the incipient occurrence of shear bands in metal cutting by studying the shear stress distribution using a finite element model of the cutting process. It is demonstrated that shear bands form in a material (HY-TUF steel) that exhibits strain-softening behavior after slight strain-hardening. For identical cutting conditions but with a material which has more strain-hardening and less strain-softening; no shear bands formed.

MODEL OF SHEAR BANDING

Material Properties

As a first approximation, high speed metal cutting can be considered to be an adiabatic process. The temperature rise accompanying plastic deformation under adiabatic conditions contributes to the strain-softening behavior. In graphical terms strain-hardening is indicated by a positive slope on the effective stress-strain curve and strain-softening is indicated by a negative slope on the effective stress-strain curve (Figure 1). A material shown to exhibit this softening effect at small strain is HY-TUF steel. High strain-rate adiabatic torsion tests indicate that the effective stress-strain (S-e) curve for the high strength steel can be described by an expression of the form:[2]

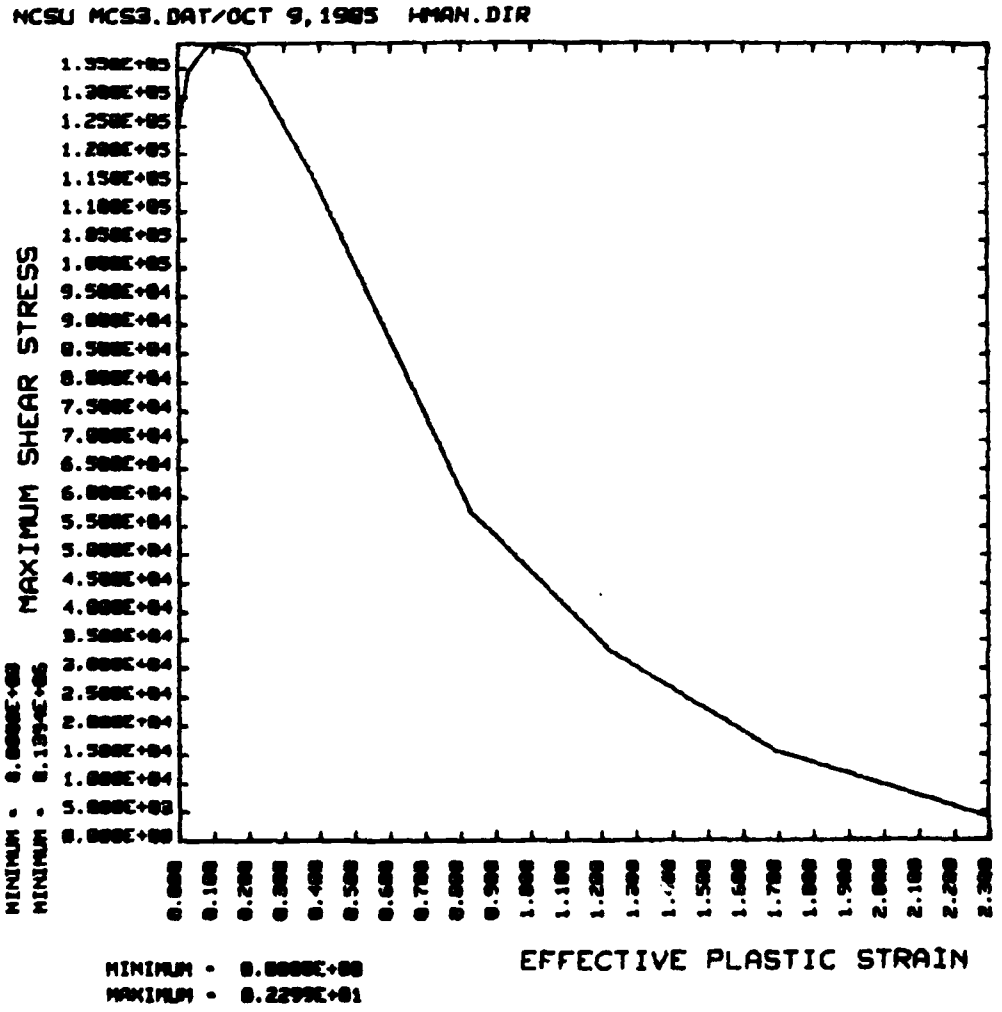

Figure 1. Effective stress-strain curve for HY-TUF steel

$$S = S_0(1 + Ae) \exp(-Be) \quad (1)$$

where

$S_0 = (\sqrt{3} \times 132 \text{ ksi})$:a constant representing the yield stress of the material

$A = (\sqrt{3} \times 2.36)$:a dimensionless hardening parameter for vacuum-arc-remelted (VAR) conditions

$B = (\sqrt{3} \times 1.61)$:a dimensionless softening parameter for VAR

The variables S and e represent the effective stress and strain respectively based on a Von Mises flow criterion.

The instability strain occurs when the slope of the stress-strain curve is zero. Therefore taking the derivative of the stress with respect to the strain and setting this derivative to zero yields the instability strain:

$$e_i = B^{-1} - A^{-1}. \quad (2)$$

With properties listed above for the HY-TUF steel the instability strain is 0.12. This corresponds to a maximum effective stress of 244 ksi.

Discontinuous Chip Model

The finite element model of orthogonal metal cutting is based on an updated Lagrangian formulation for plane strain conditions as provided by NIKE2D [5]. Reference [6] describes the method by which the program is capable of simulating the cutting process. Both the workpiece and the tool were modeled with a total of 1040 nodes and 940 linear isoparametric quadrilateral elements. The workpiece was modeled as an elastic-plastic material and the tool as an elastic material.

HY-TUF steel was selected as the workpiece material to simulate the shear banding. The material plastically yields at 0.2% strain with a yield stress of 229 ksi. The other stress-strain properties are given by equation (1). Eight points on the stress-strain curve are input values used to define the material properties in the analysis.

The separation of the chip from the workpiece was modeled by allowing nodes to part along a slide-line when the effective plastic strain (EPS) of the nodes on the slide-line reach a predetermined value. The EPS value appears not to affect the stresses in the chip region, but plays an important role in the determination of the residual stresses in the machined surface [6]. The EPS value for this model was set at 0.12 since it was the value of the instability strain from equation (2).

The model shown in Figure 2 was used to simulate the machining of HY-TUF steel to show the effects of thermal softening on the metal cutting process. The tool was moved ahead from the unstressed initial position for twenty-two states before excessive distortion of the elements in the zone of the shear band (Figure 3) terminated the program.

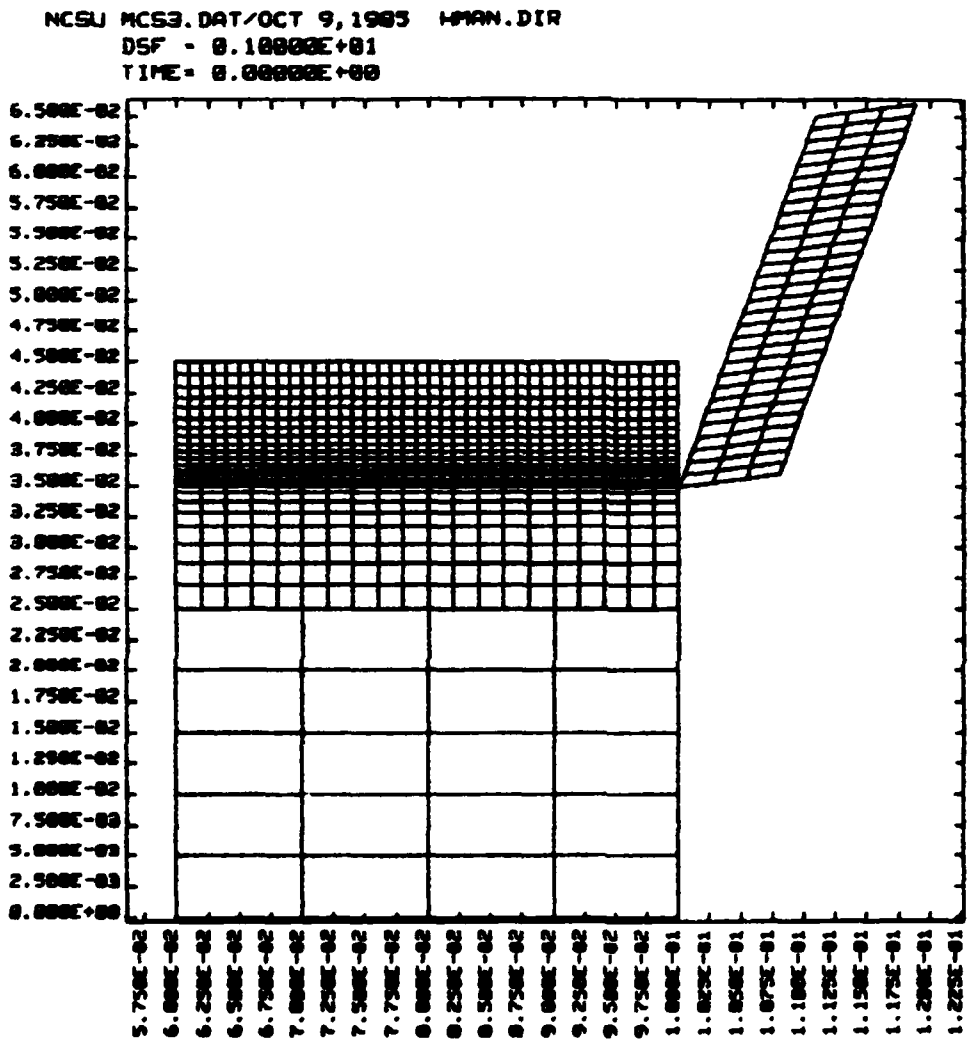

Figure 2. Initial finite element grid for cutting simulation

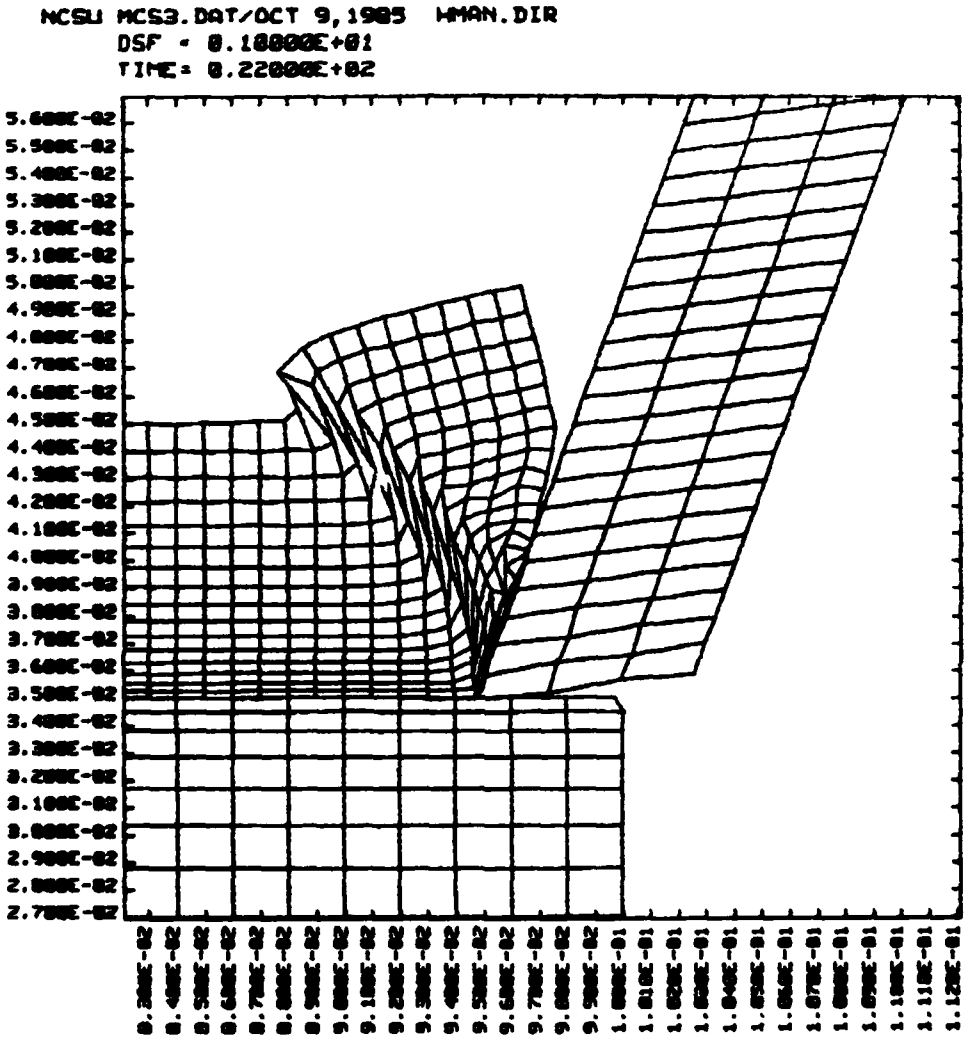

Figure 3. Grid indicating the shear band

The cutting forces exhibited a dramatic decrease during the tool increments. A maximum plane strain force of 1700 lbs./in. occurred at state 10. The strains in the material completely through the chip formation region (shear zone) up to state 10 were below the instability strain. After state 10 the strains at each point along the shear zone were higher than the instability strain and the cutting forces decreased for the remainder of the simulation (Figure 4).

The effective strain contour (Figure 5) indicates the zone of the shear banding where the maximum strain reached a value of six times the instability strain. The shear band started to form in the part of the chip nearest the tool tip and emanated to the free surface. The maximum shear stress contour (Figure 6) indicates that the stress distribution in the region just ahead of the shear-band zone exhibits the maximum shear stress. This region is where the workpiece begins to form into a chip. The additional plastic work past this region forces the material into the thermal softening regime thus resulting in the shear-banding.

Continuous Chip Model

If the stress-strain model that produced the discontinuous chip described above were modified, a continuous chip could result. The key changes would be an increased region of strain hardening and a reduced strain softening coefficient. For example, if the yield strength was kept the same but the material continued to harden up to a strain of .25 and the strain softening coefficient was cut by a factor of 4, no shear banding would occur. As the strain through the chip increased past the instability strain there was no drop in cutting force. The plane strain cutting force reached a steady state value of 2400 lb./in. in 30 time states (Figure 7).

The maximum shear stress contour (Figure 8) indicates a zone of maximum shear stress emanating from the tool tip to the free surface. The strain along this section is equal to the instability strain of the material. The maximum shear stresses in a fixed section of the chip with respect to the tool do not change after the cutting forces have reached steady state (Time 30).

Comparison of Continuous and Discontinuous Chip Models

The results of the shear banding model showed a dramatic decrease in the cutting force, whereas the continuous chip model exhibited a steady state value. The zone of maximum shear stress in both models was similar, indicating that the formation of both continuous and discontinuous chips is related to the same mechanism. The greater amount of total work-hardening in the continuous chip model appears to allow for a uniform stress distribution across the chip. Therefore the difference in whether a continuous or discontinuous chip is formed depends on the amount of work-hardening incurred before the strain instability is reached as well as the degree of strain-softening afterwards.

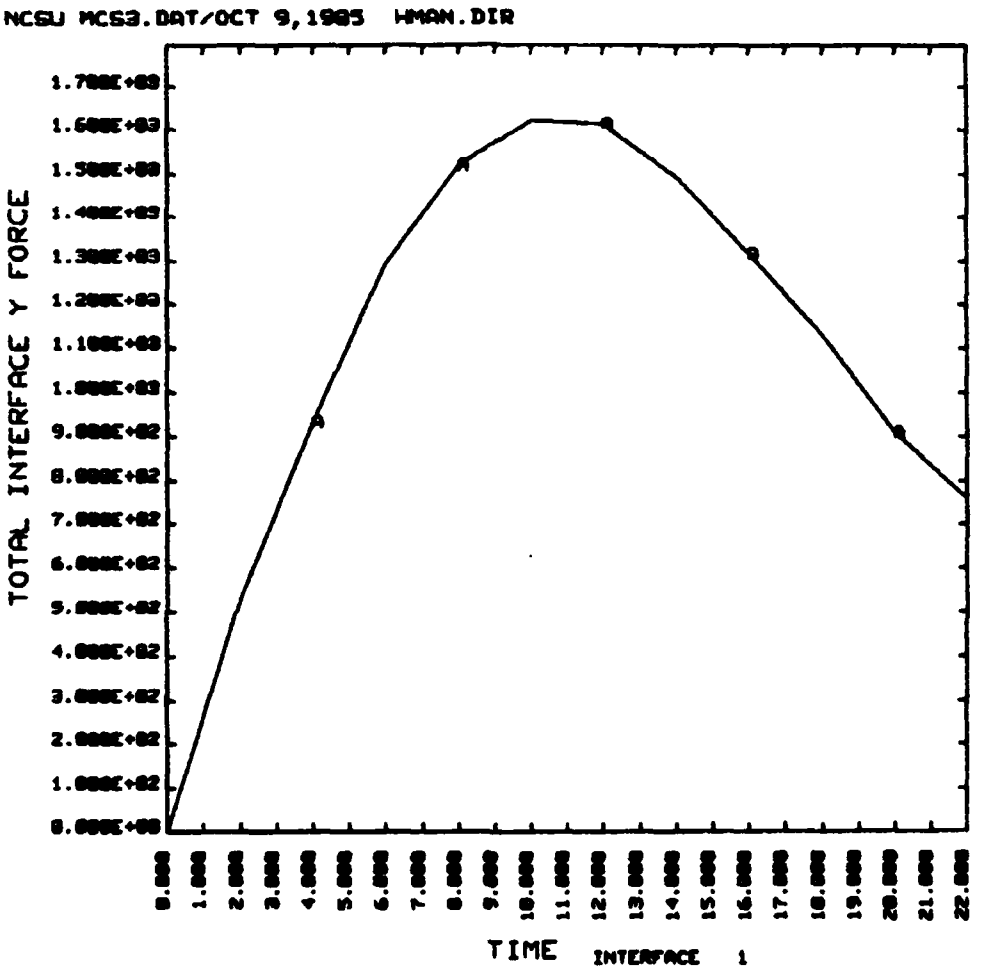

Figure 4. Horizontal plane strain cutting force

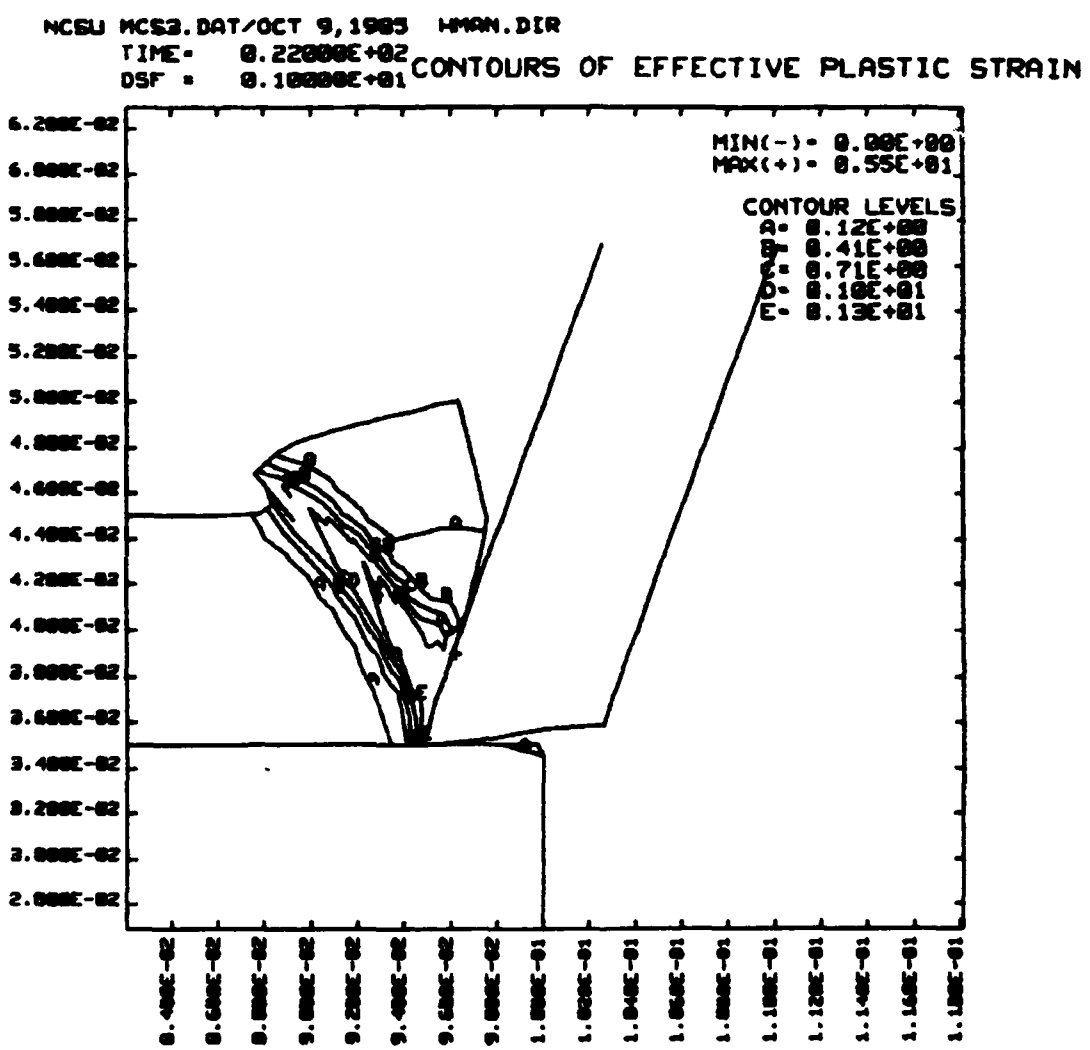

Figure 5. Effective plastic strain in shear band region

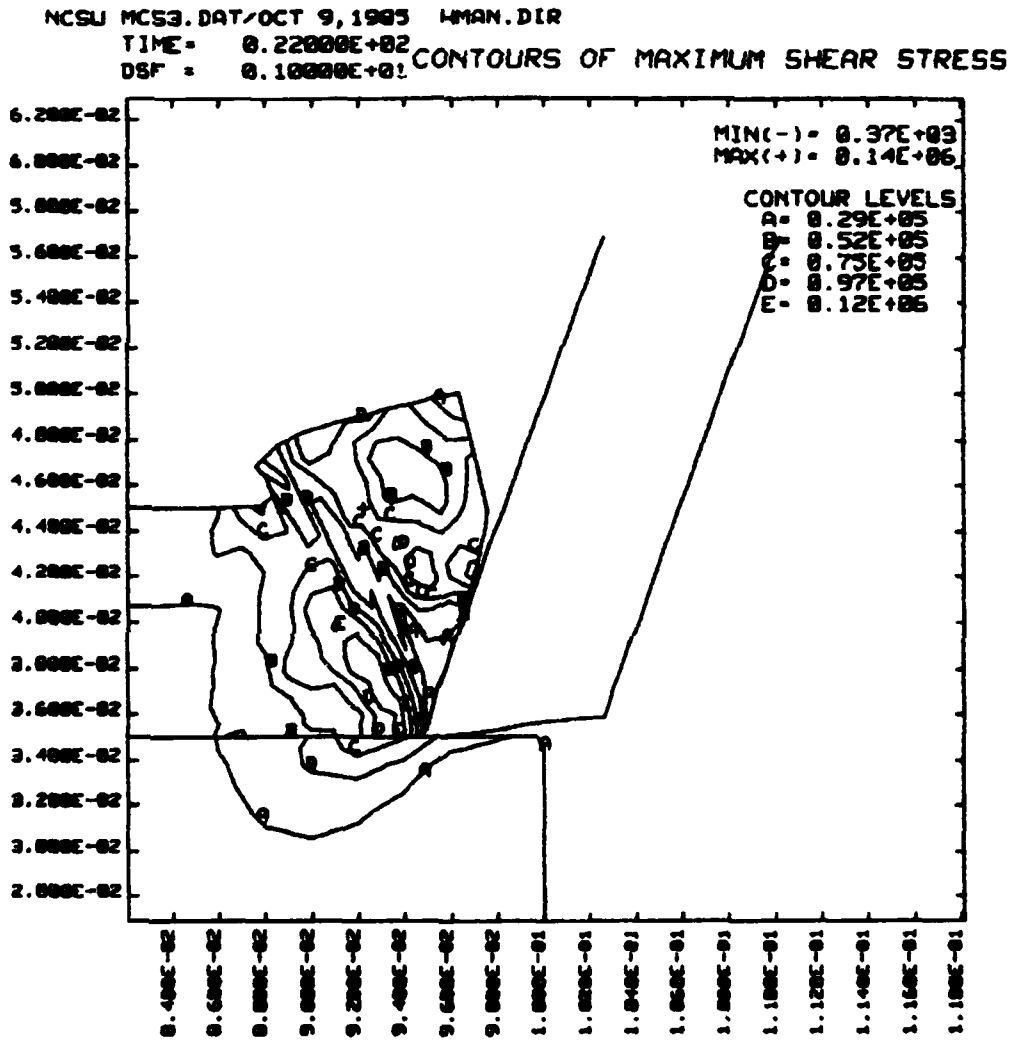

Figure 6. Maximum shear stress in work-piece and shear zone

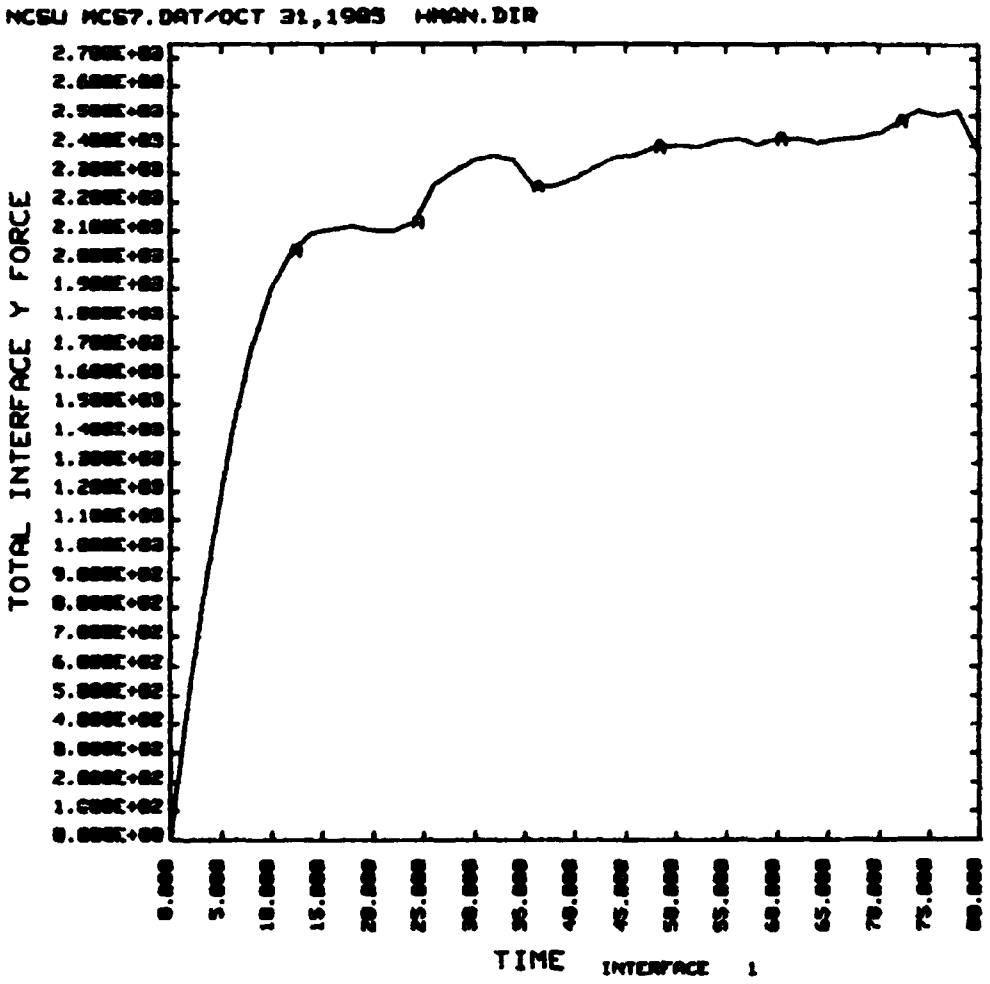

Figure 7. Plane strain cutting force for continuous chip formation

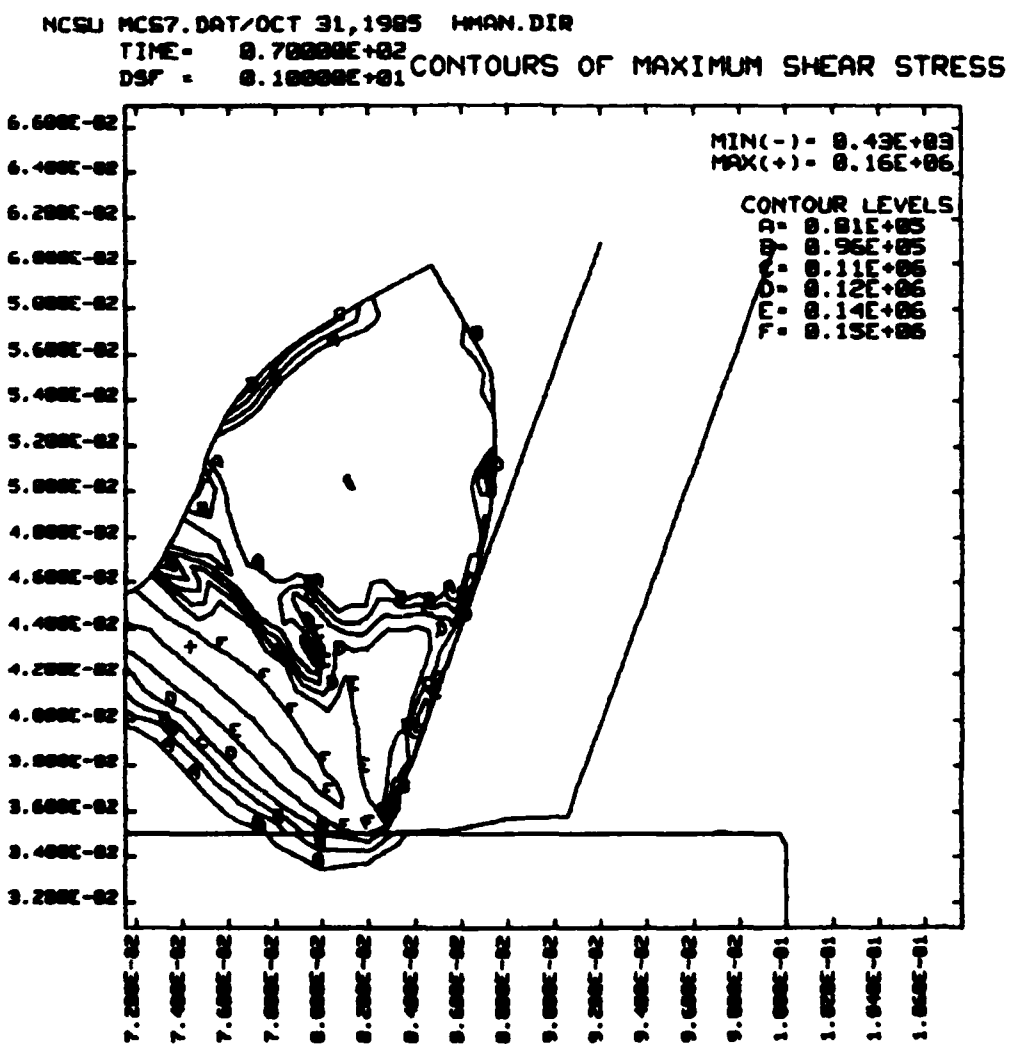

Figure 8. Maximum shear stress for continuous chip formation

CONCLUSION

A finite element model of material undergoing orthogonal metal cutting process which exhibits shear banding or a discontinuous chip has been described and compared to a material which exhibits a continuous chip. The material properties for HY-TUF steel which forms a shear-band were described along with the modified material properties which resulted in a continuous chip. The shear zone in both material models was described and it seems to indicate that the same mechanism of cutting occurs in both cases. The amount of strain-hardening, the magnitude of the instability strain, and the strain-softening effects seem to determine whether a chip is continuous or discontinuous.

REFERENCES

1. Von Turkovich, B. F. and D. R. Durham, "Machining of Titanium and Its Alloys," Advanced Processing Methods for Titanium, the Metallurgical Society of AIME.

2. Olson, G. B., J. F. Mescall, and A. Azrin, "Adiabatic Deformation and Strain Localization," Army Materials and Mechanics Research Center, Watertown, MA 02172, Report No. AMMRC TR 82-48, August 1982.

3. Johnson, G. R., "Dynamic Analysis of a Torsion Test Specimen Including Heat Conduction and Plastic Flow," Journal of Eng. Mat. and Tech., Vol. 103, July 1981, pp. 201-206.

4. Finnie, I., "Review of the Metal-Cutting Analyses of the Past Hundred Years," Mechanical Engineering, August 1956, p. 715-719.

5. Hallquist, J. O, "NIKE2D--A Vectorized, Implicit Finite Deformation, Finite Element Code For Analyzing the Static and Dynamic REsponse of 2-D Solids," Lawrence Livermore National Laboratory, Report No. UCID-19677.

6. Strenkowski, J. S. and J. T. Carroll, III, "A Finite Element Model of Orthogonal Metal Cutting," Journal of Engineering for Industry, Vol. 107, November 1985, pp. 349-354.

SECTION 4. TECHNOLOGY TRANSFER

ACADEMIC PROGRAM

Problems and limitations associated with precision manufacturing can originate in the machine, the process, or the material. In fact, most problems will probably be caused by a combination of these factors. Therefore, improvement of current processes and development of new manufacturing methods will require knowledge of a multi-disciplinary array of subjects. The educational goal of the Precision Engineering Center is to develop an academic program which will educate scientists and engineers in metrology, control, materials, and the manufacturing methods of precision engineering.

Over the past several years, an academic course schedule has been designed for a PhD degree in Precision Engineering. The emphasis on the PhD was a result of the multi-disciplinary aspects of the subject and the broad range of courses necessary. However, to expedite research, MS degree candidates have also been involved in the program. The course plan for the MS students is not as multi-disciplinary as the PhD but their research tasks are real problems in precision engineering. In the future, the educational program to be expanded to include more MS and PhD students as well as offering stimulating undergraduate programs to acquaint them with the methods, capabilities, and potential for precision manufacturing.

The graduate students involved in the Precision Engineering Center have an annual stipend as research assistants. They can take up to 3 classes each semester while spending about 20 hours per week on their research projects. These students will also work in the Center full-time during the summer months.

PhD Degree Program

The PhD program in Precision Engineering has been set up as a multi-disciplinary program--drawing upon courses throughout the University to provide background and expertise for the students. It contains required courses to insure solid grounding in the fundamentals plus electives to prepare the student in his area of specialization.

Because Precision Engineering is concerned with an integrated manufacturing process, students interested in computer control, materials, machine structure, and measurement and actuation systems are involved in the program. Student research projects currently include analysis of plastic flow of material in a cutting process, development of a high-speed control system for error correction in a rotating spindle, and the design of a general algorithm for multi-input, multi-output control systems. Each student's thesis has an experimental component because Precision Engineering is basically a hands-on technology. However, for these students to contribute to development of precision devices, they must also have a solid grounding in mathematics, mechanics, fluid flow, and heat transfer as well as precision measurement and fabrication.

Required Courses

Electrical Engineering

EE 513 Digital Signal Processing
EE 613 Advanced Feedback Control

Materials Science

MAT 500 Modern Concepts in Materials Science

Mathematics

MA 501/502 Advanced Mathematics for Engineers and Scientist
MA 511 Advanced Mathematics
MA 524/525 Math Methods in the Physical Sciences
MA 529/530 Numerical Analysis I/II

Mechanical Engineering

MAE 513 Vibration of Mechanical and Structured Components
MAE 533 Finite Element Analysis of Mechanical Systems
MAE 541 Advanced Machine Design
MAE 505 Heat Transfer Theory & Applications
MAE 557 Dynamics of Internal Fluid Flow
MAE 589 Metrology in Precision Engineering

Physics

PY 516 Physical Optics

These required courses will take the student beyond the MS degree, which requires 30 credits including 6 credits for the thesis. PhD students can elect to take an oral exam and receive the MME (a non-thesis MS) after 33 credits of course work. The PhD degree does not have a specific credit hour requirement beyond the MS, but a minor area of study with at least 21 credit hours is necessary. The minor area could be mathematics, materials, electrical engineering, or computer science.

Elective Courses

Elective courses can be drawn from any curriculum of science or engineering. Examples of possible elective courses include:

1. Computer Science

CSC 511/532 Artificial Intelligence I/II
CSC 583 Special Topics in the Numerical Solution of Ordinary Differential Equations
CSC 427 Introduction to Numerical Analysis I
CSC 428 Introduction to Numerical Analysis II
CSC 635 Functional Analysis and Numerical Analysis

2. Electrical Engineering

EE 435 Elements of Control
EE 436 Digital Control Systems
EE 443 Digital System Design
EE 441 Introduction to Solid State Devices
EE 533 Digital Electronics
EE 624 Electronic Properties of Solid State Devices
EE 540 Electromagnetic Fields & Waves
EE 559 Pattern Recognition

3. Materials Science

MAT 510 Structure of Crystalline Materials
MAT 520 Theory and Structure of Materials
MAT 530/630 Phase Transformation in Materials I/II
MAT 550 Dislocation Theory
MAT 633 Advanced Mechanical Properties of Materials

4. Mathematics

MA 523 Topics in Applied Mathematics
MA 532 Theory of Ordinary Differential Equations
MA 641/642 Calculus of Variations & Theory of Optimal Control I/II
MA 632/633 Operational Mathematics I/II

5. Mechanical Engineering

MAE 553 Mechanics of Ideal Fluids
MAE 608 Advanced Conductive Heat Transfer
MAE 609 Advanced Corrective Heat Transfer
MAE 610 Advanced Radiative Heat Transfer
MAE 545/646 Variational Methods in Optimization Techniques I/II
MAE 513 Vibration of Mechanical and Structural Components
MAE/MAT 531 Materials Processing by Deformation
MAE/MAT 532 Fundamentals of Metal Machining Theory
MAE 535 Experimental Stress Analysis
MAE 581 Computer Aided Design I
MAE 623 Mechanics of Machinery
MAE 614 Mechanical Transients and Machine Vibrations
MAE 615 Non-Linear Vibrations
MAE 619 Random Vibrations
MAE 642 Mechanical Design Analysis
MAE 643 Mechanical Design Synthesis

6. Operations Research

OR 531 Dynamical Systems and Multivariable Control
OR 650 Algorithmic Methods in Optimal Control

MS Degree Program

The Master of Science degree will have a higher percentage of application courses than the PhD degree previously described. The emphasis will be to develop the foundation for involvement in precision engineering research and development. Because of the limited course load for this degree, there is little flexibility in the plan. However, exceptions can always be made to accommodate a specific student's needs and interest.

The MS thesis, while less comprehensive than the PhD dissertation, will be directed at important problems in Precision Engineering. Typically the MS program will take four semesters including one summer.

Required Courses	Credits
Electrical Engineering	
ECE 516 System Control Engineering	3
Materials Engineering	
MAT 500 Modern Concepts in Materials Science	3
Mathematics	
MA 427 or 428 Introduction to Numerical Analysis	3
MA 501 Advanced Mathematics for Engineers and Scientist	3
Mechanical Engineering	
MAE 513 Vibration of Mechanical and Structural Components	3
MAE 533 Finite Element Analysis of Mechanical Systems	3
MAE 541 Advanced Machine Design	3
Physics	
PY 516 Physical Optics	3
Thesis	6
	30

Undergraduate Program

The undergraduate degree in engineering broadly prepares the engineering student for industrial activities ranging from power generation, product design, and engineering sales to production implementation. Because a disproportionately large share of engineers only have the BS degree, these will be the people who must implement the new technology developed in research programs like the Precision Engineering Center. Therefore, a way must be found to acquaint engineers at the BS level with the techniques, problems, and potential of precision manufacturing.

The undergraduate degree program in Mechanical Engineering is typical of those offered in many engineering curriculums in that only limited time is available for technical electives. However, these electives offer the student the opportunity to expand his knowledge in many different directions. Specific lecture and laboratory courses are being planned for the University undergraduate curriculum. These will be offered by the Physics, Mechanical, and Materials Engineering Departments and will include:

* structural vibrations
* control practice
* instrumentation
* optics
* metrology

The capstone course in Mechanical Engineering Design (MAE 416) is intended to provide a way for students to taste the satisfaction and frustration of having to implement an engineering design. Typically, one or two projects are tackled by teams of 6 to 7 seniors. Specific projects relating to Precison Engineering are an option for that course. This procedure was implemented several years ago when two undergraduate students successfully designed and built a laser interferometer as their senior design project.

New Course Offerings

During the last several years, the research effort in Precision Engineering has lead to new graduate courses being developed. During 1985, the following two new courses were presented. The metrology course will again be offered in 1986.

MAE 589 Metrology in Precision Engineering

Instructor: T. A. Dow

Objective

Measurement plays a key role in Precision Engineering. About 100 years ago, Lord Kelvin said:

"I often say that when you can measure what you are speaking about and express it in numbers you know something about it; but when you cannot measure it, when you cannot express it in numbers, your knowledge is of a meagre and unsatisfactory kind."

This knowledge has been put to much more use in modern machines which utilize measurement in an automatic control scheme. Thus, measurement becomes an integral part of a manufacturing process. This course is designed to familiarize students with the broad range of measurement techniques currently available and the basic principles which govern their operation. An attempt is also made to present a philosophy of design which can be applied to a broad range of measuring instruments and precision machine tools.

Topics Discussed

History of Metrology
Design of precision machines
Methods of magnification
Error analysis
Surface profilometry
Standards of length
Standards of angular measurement
Vibration isolation
Temperature control
Bearing design
Methods of manufacturing standard shapes

MAE 586 Engineering Applications of Symbolic Algebraic Manipulation Languages

Instructor: C. J. Maday

Objective

Computers have been used in engineering and engineering education primarily for number crunching. Finite element methods, finite difference methods, and optimization techniques have been implemented to solve "real-world" problems. These techniques were little more than curiosities before the availability of high speed computers. A similar situation exists today for any technique that requires much symbolic and algebraic manipulation. Over the past few years, symbolic and algebraic manipulation (SAM) languages have become available to do these operations as well as some number crunching. SAMs are examples of applied artificial intelligence (AI). There is an exciting potential for application in automatic control, and force and deflection analyses in elastic structures. A striking parallel exists between numerical methods that require much number crunching for complex problems and analytical methods (non-numerical) that require significant symbolic and algebraic manipulation. Today numerical methods are implemented as a matter of course. In the near future, SAMs will permit the implementation of the non-numerical techniques.

PRECISION ENGINEERING CONFERENCE

The first international Precision Engineering Conference was held in Raleigh, North Carolina on November 14 & 15, 1985. It was attended by over 100 conferees from the US and Japan. There were two technical sessions chaired by Dr. Clayton Teague of the National Bureau of Standards (NBS) and Dr. Daniel Thompson of Lawrence Livermore National Laboratory (LLNL). There were also two round table discussions: the first, chaired by Dr. Ray McClure of LLNL, concerned the creation of a US Precision Engineering Society; and the second, chaired by Dr. Robert Hocken of NBS, involved the education of a precision engineer. These latter sessions turned out to be lively affairs with many different viewpoints discussed.

Technical Points

The conference was jointly organized by the Precision Engineering Laboratory at North Carolina State University and the Precision Engineering Program at Lawrence Livermore National Laboratory. It began with a request from the Japanese to present several technical papers at LLNL and to learn of US technical progress in Precision Engineering. Because of the growing interest in this field in the US, it was decided to expand the scope of the meeting to include a greater audience than the LLNL community. The meeting was planned for Raleigh to take advantage of the Precision Engineering Laboratory and to use that facility for a laboratory tour. The Japanese selected six papers for presentation and six complementary papers were selected from US authors. These papers are not meant to be the only work of note currently in progress but to be representative of the range of research being pursued. The schedule for the conference is attached.

The papers were of excellent quality and each presented significant results. Of special mention are the following.

1) Polishing Research - Norm Brown (LLNL)

The removal of material from a surface by polishing is not simply an abrasive process but involves chemistry, structure, and thermodynamics in the surface layer. Dr. Brown showed evidence of glass polishing as far back as 2500 BC; but even with this considerable experience, there is much unknown in polishing. Many of the problems are related to the fact that the surface represents a transition region; physically there is a transition from the kinetics of the interior to those on the surface. Chemically, on the surface, bonding no longer extends outward. In addition there are often chemical differences due to diffusion that can extend to considerable depths. There are possibilities of reversible chemical reactions between the base material and diffusing species triggered by changes in the state of strain of the material. During these reactions, structural reorderings can take place, manifested by the appearance of ductility in an otherwise brittle material.

This paper points to the multidisciplinary nature of the field of Precision Engineering. The problems of producing surfaces that have roughness on the order of the molecular size of the material requires a thorough understanding of all aspects of the chemistry and the wear processes involved.

2) Micro-grooving for molds for plastic grating lenses - Katsunobu Ueda (Toshiba Machine K K)

Consumer electronics is an area where much of the need for precision engineering is evidenced in Japan. Video casette recorders and optical audio disks (compact disc) require high precision in their manufacture, but because of their cost and the competition, the manufacturing costs must be kept low. The paper by Dr. Ueda described their work in producing molded grating lenses for optical disc systems. Diamond turning is used to produce the master disc which in turn is used to electroform the molding dies. The plastic lenses are then molded in these dies. It takes about one hour to machine the 220 saw shaped grooves in the 5.2 mm (0.2 in.) diameter master disc. The groove depth is 1.6 m (64 in.) and the width varies with a minimum of 6 m (240 in.). The author reported excellent performance of the molded lenses.

3) Diamond grinding of Brittle Materials

Two papers were presented on this subject and both indicated that the state-of-the-art is rapidly expanding. The first by Mr. Leonard Chaloux of Pneumo Precision described their newest machine for grinding ceramics. One important application is the grinding of tungsten carbide and silicon carbide lens molds. Surface finishes of 0.2 m (8 in.) have been achieved using this apparatus. The paper by Dr. Miyashita of Citizen Watch K K described their work in grinding of brittle materials. He pointed out that traditional machining processes for these materials have serious shortcomings from the viewpoint of mass production. Design specifications of the grinding machine, trueing accuracy of the wheel, and wheel wear characteristics have to be considered using the idea of plastic regime grinding. Concepts of microgrinding, microtrueing/dressing and plastic failure regime wear characteristics of the grinding wheel were proposed. Dr. Miyashita indicated that to take advantage of this potential the position resolution must be on the order of the chip removal rate. He pointed to achievable surface roughnesses of 0.15 m (6 in.) for silicon carbide and an incredible 20 angstrom (0.1 in.) for quartz.

4) Shear band behavior in diamond turning-Dr. J. Strenkowski (NCSU)

The surface finish that will exist as a result of a turning operation will depend upon the diamond tool and the feed rate. In addition, changes in the material structure or the tool force can appear as a signature in the final finish. Dr. Strenkowski's work is directed toward finding the relationship which controls the development of a chip and the parameters that lead to the transition to a discontinuous chip.

Round Table Discussions

Organization of An American Precision Engineering Society

A meeting of the conference attendees was moderated by R. McClure with panel members:

* Mr. Fred Parsons, Federal Products
* Dr. K. Yamamoto, President, Japan Society of Precision Engineering
* Dr. C. Teague, National Bureau of Standards
* Mr. W. Moore, Chief Executive Officer, Moore Special Tool Co.
* Mr. J. Howell, Managing Director, Technical Affairs, ASME

The panel was introduced by Ray and each had a prepared statement. In general, there was agreement on the need for a society, but disagreement on the way it should be formed. A suggestion was made by Jack Howell of ASME to initially form the society as a division of ASME and a statement of scope for the society written by Dr. T. Dow was passed out along with a support statement for ASME members to sign. Only one was returned. There was much discussion concerning the need for a parent organization and what that organization should be to encompass the full breadth of the field.

The consensus of the group at the afternoon meeting and also at the dinner meeting was to defer the decision of a parent organization until the potential members of a Precision Engineering Society could be identified and polled. A committee volunteered to prepare a questionnaire to be sent out to potential members of an ASPE. This committee included:

T. Dow, N. C. State University
J. Gleeson, Battelle Memorial Institute
R. McClure, Lawrence Livermore National Laboratory
C. Teague, National Bureau of Standards
F. Parsons, Federal Products

Bob Hocken of National Bureau of Standards offered their services to mail out such a questionnaire. Clayton Teague will coordinate the design of the questionnaire and its mailing.

The Education of a Precision Engineer

Moderator: Dr. R. Hocken

Members: T. Dow, North Carolina State University
C. Evans, University of Wisconsin
G. Beni, University of California, Santa Barbara
A. Kobayashi, Saitama University

Dr. Hocken began the session with a description of his ideal educational program. It would consist of :

a) Basic Science
   * Physics
   * Chemistry

b) Basic Technology
   * Mechanical Engineering
   * Electrical Engineering
   * Computers
   * Materials
   * Optics

c) Design Tools
   * Finite Element Modeling
   * Statistics (Error budgeting)
   * Design

d) Culture
   * History of PE

e) Ability to
   * reason
   * think
   * learn

Clearly this education would take some time to complete, and the latter topics may not be teachable. However, the program represents a thorough background in the foundation necessary to be a precision engineer. Given this introduction, Dr. Hocken opened the floor for discussion. The conferees responded according to their own educational and practical experience, which is to say that there were as many ideas as there were people.

The next speaker was Professor Kobayashi of Saitama University in Japan. Dr. Kobayashi described the impetus for precision engineering in Japan. He showed that the fastest growing segment of industry is electric and electronic machinery. From 1982-1984, this area grew 43% compared to 19% for the transportation industry. Thus the main industry in Japan now is the manufacture of electronic and electronic/mechanical devices known as "mechatronics." This area represents annual sales of $110 Billion compared to $90 Billion for transportation related sales. In the areas of mechatronics, there are many devices which require ultra-precision manufacturing techniques. These include:

Video casette recorder (VCR)
Video disk
Memory disk for electronic computer
Magnetic recorder
Copying machinery
Facsimile machine

For the VCR, the production has tripled from 1981 to 1984 reaching 30 million units. The mechanical accuracy required is impressive. The radial and axial runout of the spindle which rotates the magnetic head

is 60 in. The magnetic head which has overall dimensions of .1 x .075 x .004 in. but the actual reading area is:

Track width	.00076 ± .00008 in.
Gap length	000012 ± .000001 in.

The last dimension is ± one millionth of an inch. This, in mass production at a rate of 30 x million units per year, is truly precision engineering.

Dr. Kobayashi went on to discuss other applications which currently require such high precision. He also projected into the future and predicted the rise in output of the high-precision optical industry. From 1980 to 1985, this industry has grown from annual sales of $500 million to $5 billion. He projected that by the year 2000, this industry would have annual sales of $60 billion.

Dr. Kobayashi state that new manufacturing methods must be found to produce high precision parts which emphasize:

* Quality
* Cost
* Delivery
* Repeatability

The research areas of interest include the fabrication processes of grinding, lapping, polishing, diamond machining and electrochemical material removal. The annual meeting of the Japan Society of Precision Engineering emphasized the direction of precision research in Japan to meet these needs. Of the 144 papers presented, the three largest categories were:

1) Grinding & polishing brittle materials (59)
2) High precision movements & machine elements (17)
3) Ultra precision diamond cutting (13).

The Japanese have set their sights on "mechatronics" as the growth area for their manufacturing industry.

The next speaker was Dr. G. Beni of the University of California at Santa Barbara. Dr. Beni is the Technical Directory for the Center for Robotic Systems in Microelectronics (CRSM). This center is an Engineering Research Center funded by the National Science Foundation. Through detailed analysis of the needs of US to retain competitiveness with Japan, he cited mechatronics as the technology which will be given emphasis at the CRSM. The program at Santa Barbara is both research and education, and courses in robots have been set up combining the electrical and mechanical engineering area. The mechanical skills for building electrical engineering components will be stressed by the Center.

The final speaker was Dr. T. Dow, Director of the Precision Engineering Laboratory at North Carolina State University. Dr. Dow

described the course of study suggested for a M.S. and PhD. degree in Mechanical Engineering with an emphasis in Precision Engineering.

Dr. Dow noted the broad range of interests discussed in the technical presentations and the problems of fitting one specific curriculum to this multidisciplinary area. However, he emphasized that there is some commonality to the field--a background shared by all. The required courses should guarantee new entrants this foundation from which they can specialize in their area of research.

PRECISION ENGINEERING
FACULTY

THOMAS A. DOW

Director, Precision Engineering Laboratory
Professor, Departmentof Mechanical and Aerospace Engineering

BS, Mechanical Engineering, Virginia Polytechnical Institute, 1966
MS, Engineering Design, Case Institute of Technology, 1968
PhD, Mechanical Engineering, Northwestern University, 1972

After receiving his PhD degree from Northwestern University in 1972, Dr. Dow joined the Tribology Section of Battelle Columbus Laboratories. For the next ten years, his sponsored research programs ranged from the study of the wet-effectiveness of bicycle brakes to oil-in-water emulsions for large steel rolling mills to film thickness generated in a concentrated contact bearing. He has developed test apparatuses, established analytical models, and corroborated those analysis with experimental measurements. Since joining the faculty at North Carolina State University in 1982, Dr. Dow has remained involved in Tribology research (he is the chairman of the Tribology Division of ASME and a member of the planning committee of the Annual ASME/ASLE Tribology Conference) and has become extremely active in the field of Precision Engineering.

During the coming year of the program, Dr. Dow will act as principal investigator in the area of metrology and real-time control. This research area within the Precision Engineering Center has the long term goal of basic and applied research on measurement systems, control algorithms, digital and analog controllers, and actuator systems for positioning of mechanical system. Specifically, the research focuses on systems and devices which can make rapid corrections in the microinch range.

The strategy for approaching the research in 1986 is to study specific problems within this overall area. The specific tasks to be pursued include the following:

Project 1 - High-Speed Sensor Development (Dan Luttrell)

Task 1 - Develop low-cost, high-speed laser interferometer with 3 microinch resolution and 100 Kz. bandwidth.

AD-A166 084 PRECISION ENGINEERING - SRO 154(U) NORTH CAROLINA STATE 4/4
UNIV AT RALEIGH PRECISION ENGINEERING LAB
T A DOW ET AL. JAN 86 N00014-83-K-0064

UNCLASSIFIED F/G 13/8 NL

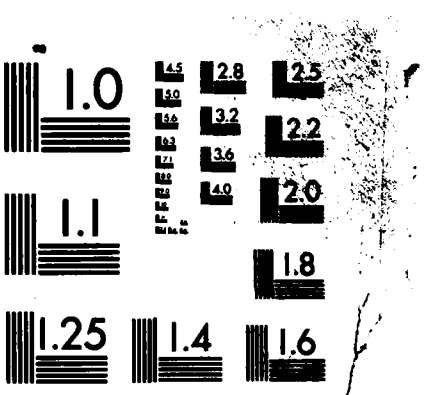

Task 2 - Integrate the interferometer into digital control scheme to correct linear motion errors in real-time.

Project 2 - Control of Error Motions in a Machine Slide (Mark Landy)

Task 1 - Linear position correction and dynamic motion control of linear stage.

Task 2 - Feasibility of laser beam as straightness reference.

Task 3 - Development of sensors and metrology frame for controlling six-degrees of freedom.

Project 3 - High-Speed Tool Positioning in DiamondTurning(Peter Falter)

Task 1 - Dynamic characterization of DTM - PAUL.

Task 2 - Development of metrology reference for tool position.

Task 3 - Development of control scheme for dynamic tool positioning as a function of tool radial position and angular rotation of part.

RICHARD F. KELTIE

Associate Professor, Mechanical and
Aerospace Engineering Department

BS, Mechanical Engineering, North Carolina State University, 1973
MS, Mechanical Engineering, North Carolina State University, 1975
PhD, Mechanical Engineering, North Carolina State University, 1978

Dr. Keltie has a strong background in the study of the dynamics of elastic structures and their interaction either with other structures or with their surroundings. His research topics in this area have ranged from the study of the aerodynamic excitation of saw blades to analytical modelling of truck tire carcass vibration and sound radiation to the coupled vibro-acoustic response of elastic structures underwater. From 1978 to 1981, he was a member of the Senior Professional staff at the Applied Physics Laboratory of the Johns Hopkins University. Among his duties there, he initiated several studies regarding signal detection and tracking algorithms for use in sonar data processing. In 1981 he joined the faculty at North Carolina State University where he is an active member of the Center for Sound and Vibration, an interdisciplinary research group. Dr. Keltie's sponsored research activities have been in the areas of investigating the dynamic response of shells underwater and energy propagation and dissipation in large structures.

During 1986, Dr. Keltie will head the research effort in machine tool structural dynamics. Development of precision machining processes has placed new demands on the ability to characterize and control the relative motion between the tool and workpiece. One important aspect concerns the control of machine tool structural vibration. This problem is being addressed through understanding of the processes and mechanisms responsible for the generation and propagation of vibrational energy in complex built-up structures.

The research plan to be implemented includes measurement of the structural power flow, identification of the important parameters of this phenomenon, and techniques for its control.

Specific tasks include the following:

Project 1 - Structural Power Flow Measurement (Kelly Allred)

Task 1 - Development of data acquisition and analysis system for structural power flow measurements.

Task 2 - Parametric investigation of energy transmission through structural elements and connections.

Task 3 - Power flow measurements on machine tool structure.

Project 2 - Acoustic Emission Monitoring

Task 1 - Feasibility study of using spectral analysis of acoustic emissions for tool wear monitoring and tool breakage prediction.

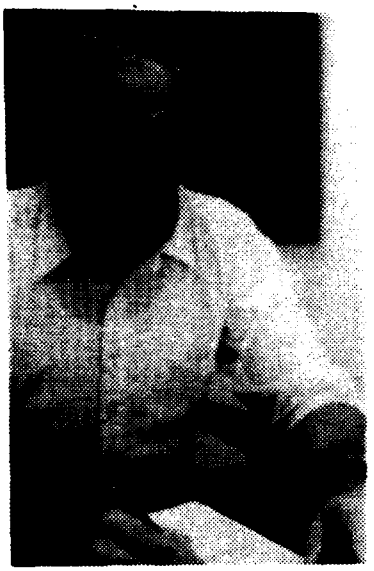

RONALD O. SCATTERGOOD

Professor, Materials Engineering
Department

BS, Metallurgial Engineering, LeHigh University, 1961
MS, Metallurgy, Massachusetts Institute of Technology, 1963
PhD, Metallurgy, Massachusetts Institute of Technology, 1968

Dr. Scattergood has a continuing interest in the mechanics of materials, with special emphasis on defects and their role in structure-property relationships. He has contributed to the modern theory of defects, as it has been developed in the nonisotropic elastic continuum framework, and also in the application of the theory to important problems in materials science. His current areas of interest include the role of defects and diffusion-related processes in semiconductor and nuclear-related materials, erosion and wear in single and multiphase materials (metals and ceramics), and the role of defects in the advance processing of ceramic materials. In addition to a broad background in the theoretical framework of the mechanics of materials, he has experience in computer methods, electron microscopy and mechanical testing procedures.

During 1986, Dr. Scattergood will be principle investigator in the area of precision finishing. The research on precision machining and finishing operations within the Precision Engineering Center has the goal of establishing the relationship between machine-tool parameters and surface finish or surface damage parameters. Central to this theme is the understanding of the role of material microstructure and material removal mechanisms in surface finishing processes. An area of emphasis to be developed at the Center will be the precision surface finishing of hard, brittle materials. This includes both simple model materials and complex, advanced commercial ceramics. Single-point diamond turning and diamond grinding will be the two finishing methods studied in the initial research projects. In the longer term other finishing methods will be considered.

The specific tasks to be addressed during 1986 include the following:

Project 1 - Single-Point Diamond Turning (Peter Blake)

Task 1 - Modify Precision Engineering Laboratory diamond turning machine for rake angle adjustment and chip collection.

Task 2 - Start machining studies on Ge and Si.

Task 3 - Start characterization studies on Si and Ge - profilometry, optical microscopy, scanning microscopy and x-ray topography.

Project 2 - Diamond Grinding (Thomas Bifano)

Task 1 - Complete design and construction of laboratory-scale diamond grinding machine for Precision Engineering Laboratory.

Task 2 - Carry out performance evaluation of diamond grinding machine.

Task 3 - Select material systems for initial diamond grinding studies.

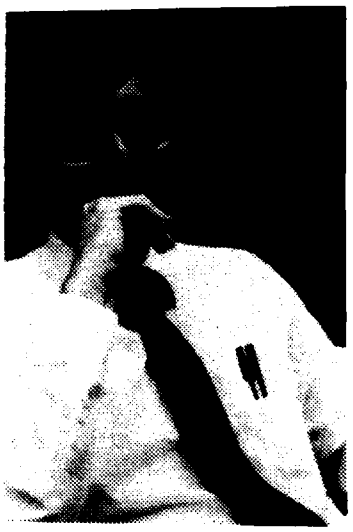

JOHN S. STRENKOWSKI

Associate Professor, Mechanical and
Aerospace Engineering Department

BS, Aerospace Engineering, University of Virginia, 1972
MS, Astronautics and Aeronautics, Massachusetts Institute of Technology, 1973
PhD, Applied Mechanics, University of Virginia, 1976

Dr. Strenkowski has an extensive background in the development of advanced computational techniques for structural analysis, interactive graphics for computer-aided design (CAD), and finite element stress and vibration analysis. He has analyzed numerous designs for structural integrity and fatigue life using general purpose finite element codes, such as Nastran, Adina, and Sap IV. In many cases these analyses entailed modification of existing codes, which required an in-depth understanding of the code. Dr. Strenkowski assisted in the development of an analytical model and nonlinear finite element program to predict residual stresses in girth-butt welds in pipes. His understanding of vibration theory has been used to analyze pipeline dynamics in severe ocean environments, and to reduce noise and vibration levels in punch presses.

For the coming year, Dr. Strenkowski will direct the development of advanced cutting models for precision machining. To produce a precision machined surface, it is essential that the functional relationships between cutting conditions and subsurface residual stresses and the machined surface deformation be know. This research will focus on the development of models and verification with cutting test data.

The specific tasks to be addressed in 1986 include:

Project 1 - Development of Cutting Models (John Carroll)

Task 1 - Develop an Eulerian-based model of the cutting process for steady-state conditions.

Task 2 - Investigate the potential of the Boundary Integral Element Method for simulating cutting.

Project 2 - Cutting Model Verification (Stephen Lehrman and Gary Mitchum)

Task 1 - Conduct material tests for ductile materials to establish stress vs. strain data at high strain-rates, large strain, and high temperature.

Task 2 - Perform cutting tests to verify tool force and possible residual stress calculations from the cutting model.

Task 3 - Evaluate the accuracy of the stress distribution predicted by the cutting models.

MICHAEL D. BRYANT

Assistant Professor, Mechanical and Aerospace Engineering Department

BS, Information Engineering, University of Illinois, 1972
MS, Mechanical and Nuclear Engineering, Northwestern University, 1980
PhD, Engineering Science and Applied Mathematics, Northwestern University, 1981

Dr. Bryant joined the faculty at North Carolina State University in 1981. He possesses a broad background in mechanical and electrical engineering, computer science, and mathematics. Dr. Bryant has conducted research on stress, fatigue, and wear of rolling elements; wear and heating of electrical brushes; and the control systems governing eye movements. He is a 1985 recipient of the National Science Foundation's Presidential Young Investigator Award.

RALPH A. BURTON

Professor Emeritus, Department of Mechanical and Aerospace Engineering
Co-Principal Investigator, ONR-SRO 154

Dr. Burton's experience encompasses academic research as a professor at Northwestern (1969-1980) and contact research as a section manager at Southwest Research Institute (1958-1969). He has served as Liaison Scientist, ONR London (1967-1969 on leave) and IPA, ONR Arlington (1978-1980 on leave. His early research was in optical techniques for measurement of gas properties. At SWRI he was drawn into Tribology and established programs on friction and wear in vacuum, high temperature friction wear, liquid metal bearings and contact fatigue. His section designed and constructed numerous precision apparatuses. Several of these were operated for more than a decade at WPAFB. One gas-bearing supported contact fatigue machine is presently in operation at NBS.

CLARENCE J. MADAY

Associate Professor, Mechanical and Aerospace Engineering Department

BS, Mechanical Engineering, Illinois Institute of Technology, 1951
MS, Mechanical Engineering, Illinois Institute of Technology, 1954
PhD, Mechanical Engineering, Northwestern University, 1960

Dr. Maday's twenty-two years of research experience in system dynamics, lubrication, automatic control systems, design optimization,

heat transfer, and computer aided analysis have spanned a wide variety of projects that required the development of innovative techniques to reach a successful conclusion. He carried out analog computer simulations of hot-gas servo systems and hydraulic servo systems. Results of these investigations were successfully implemented in hardware applications. He applied optimal control theory to the design of a feedback system to control instability in a two phase flow system with boiling heat transfer. This was recognized as one of the first applications of control techniques to such processes. He also used variational techniques to obtain optimum designs of cooling fins, shaft-disk system, and hydrodynamic bearings. Extensive use has been made of analog and digital computers for system simulation and the solution of nonlinear boundary value problems. He has developed and taught graduate courses in design optimization, automatic control, and mechanical engineering analysis.

Precision Engineering Staff and Students:

(Left to right, back row) - Mark Cagle, Steve Lehrman, John Carroll, Mark Landy, Kelly Allred, and Dan Luttrell. (Seated left to right) - Gary Mithcum, Peter Blake, Tom Bifano and Annie Kauffman. Not pictured - Peter Falter.

PRECISION ENGINEERING STAFF

CAROL A. KAUFFMAN

Secretary and Administrative Assistant, Precision Engineering Laboratory

BS, Home Economics Education, Messiah College, 1978
MS, Early Childhood Education, Purdue University, 1983

Mrs. Kauffman was a secretary and public relations assistant for the Academic Counseling and Student Services office of the School of Consumer and Family Sciences during her academic career at Purdue University. This experience enabled Mrs. Kauffman to become proficient in word processing and data entry with a variety of computer systems. Mrs. Kauffman's background provides the Precision Engineering Laboratory with expertise in university policy and regulations, word processing, public relations, bookkeeping, and conference planning.

GRADUATE STUDENTS

C. KELLY ALLRED, an MS candidate currently engaged in research on machine vibrations involving power flow measurements. He received his BS degree in Biological and Agricultural Engineering from NC State University in 1981. Mr. Allred worked for three years as an Agricultural Engineer and Commercial Power Engineer with Duke Power Company before enrolling in the graduate program. He is also a registered Engineer in North Carolina. His interests include structural analysis and vibrations.

THOMAS G. BIFANO, a PhD student currently studying ductile regime ultraprecision grinding of hard materials. He received both BS (1980) and MS (1983) degrees in Mechanical Engineering from Duke University. For the 2 1/2 years prior to his enrollment into the graduate program, Mr. Bifano was a full-time research engineer for the North Carolina State Precision Engineering Laboratory.

PETER N. BLAKE, a PhD student in Materials Engineering, is currently studying material removal mechanisms in the machinery of brittle substances. After completing his BA at the University of Michigan (1969) and MA at Duke University (1972), he taught school and operated a construction and maintenance business. His interests include X-ray and electron beam characterization of materials.

CHRISTOPHER M. CAGLE, an MS candidate currently completing a thesis involving the real-time control of spindle runout. Mr. Cagle graduated with a BS degree in Mechanical Engineering from North Carolina State University in 1984. As an undergraduate cooperative education student, he worked at the NASA-Langley Research Center. His work there involved thermal and structural analysis using finite elements and mechanical design using CAD. Mr. Cagle's interest includes automated manufacturing, precision machining, and mechanical design.

JOHN T. CARROLL, III, a PhD student studying finite element modelling of orthogonal metal cutting. He received both his BS (1982) and his MS (1983) in Mechanical Engineering from North Carolina State University. For an MS thesis, Mr. Carroll developed a computer simulation for residential heat pump systems. His areas of interest span the thermal and mechanical sciences with special emphasis on numerical computation and simulation. Mr. Carroll's experience includes summer employment at IBM assisting in mechanical aspects of testing, failure analysis, and automated manufacturing.

PETER J. FALTER, a PhD student in Mechanical Engineering. Mr. Falter received the BS in Mechanical Engineering from North Carolina State University in 1983. In the Precision Engineering Laboratory he has developed a statistical characterization using a stylus profilometer, and designed a research lathe to study diamond turning. Mr. Falter's dissertation will examine the relationship between the machine structure and the surface finish produced in a precision machining operation.

MARK S. LANDY, received his BS in Mechanical Engineering from North Carolina State University (1984). Mr. Landy is presently working on his PhD in Mechanical Engineering in the fields of control and machine design. He is studying the control of a PZT actuated cantilever beam through the use of classical analog controls.

STEPHEN A. LEHRMAN, a PhD student engaged in the analytical study of the material removal process. Mr. Lehrman received his BS in Engineering from Brown University and an MS in Mechanical Engineering from Northeastern University in 1978. Mr. Lehrman has over 11 years of experience in consulting engineering firms and has broad expertise in analysis of vibration and failure problems. He is a registered Professional Engineer in North Carolina, Massachusetts and Texas.

DAN E. LUTTRELL, a graduate student pursuing the MS and PhD degree in Mechanical Engineering. Mr. Luttrell received his BS degree in Mechanical Engineering from the University of Tennessee in 1977. After serving for six years in the U.S. Navy, he worked as a mechanical engineer at DOE's Y-12 plant in Oak Ridge, Tennessee. His current research involves the development of the polarized laser inferometer for use as a position sensor in computer controlled systems. His future research interests include microprocessor control of dynamic systems, precision actuators and measurement systems, and optics.

GARY L. MITCHUM, currently an MS candidate, received his BS in Mechanical Engineering in 1985 from North Carolina State University. Mr. Mitchum is presently working on the finite element study of the orthogonal metal cutting process. As an undergraduate, he worked at Duke Power Company in Charlotte, North Carolina for the Mechanical/Nuclear Design department performing piping stress analysis.

LIST OF AUTHORS BY VOLUME

INDEX OF TOPICS OF VOLUMES

Volume 1

Volume 2

(Volume 2 continued)

(Volume 3 continued)

END

DTIC

5-86